Oceanologia

Official Journal of the Polish Academy of Sciences: Institute of Oceanology and Committee on Maritime Research

This journal is supported by the Ministry of Science and Higher Education, Warsaw, Poland

Indexed in: ISI Journal Master List, Science Citation Index Expanded, Scopus, Current Contents, Zoological Record, Thomson Scientific SSCI, Aquatic Sciences and Fisheries Abstracts, DOAJ

IMPACT FACTOR ANNOUNCED FOR 2014 IN THE 'JOURNAL CITATION REPORTS' IS 1.000; 5-year IF — 1.346

Publisher
Elsevier Sp. z o.o. 4/59,
02-796 Warsaw, Poland
Tel. +48 22 546 38 20, Fax. +48 22 546 38 21

Director of Journals Publishing
Ewa Kittel-Prejs

Publishing Manager
Agnieszka Pawłowska
a.pawlowska@elsevier.com

Marketing & Promotion Manager
Anna Szkolut
a.szkolut@elsevier.com
48 22 546 38 40, 48 515 090 174

Publishing Editor
Joanna Lewczuk
j.lewczuk@elsevier.com
48 515 082 585, 48 22 546 38 24

Subscription and Distribution Manager
Jacek Sołtyk
prenumerata@elsevier.com
48 22 546 38 27, 48 510 134 282

Advertising Pharma Solutions
Monika Giergielewicz
m.giergielewicz@elsevier.com
48 519 130 280

ISSN 0078-3234

Oceanologia (2016) 58, 59—70

Available online at www.sciencedirect.com

ScienceDirect

journal homepage: www.elsevier.com/locate/oceano

ORIGINAL RESEARCH ARTICLE

On the nonlinear internal waves propagating in an inhomogeneous shallow sea

Stanisław R. Massel *

Institute of Oceanology of the Polish Academy of Sciences, Sopot, Poland

Received 6 November 2015; accepted 22 January 2016
Available online 16 February 2016

KEYWORDS
Internal waves;
Energy flux conservation;
Bottom friction;
Shearing instability;
Wave breaking

Summary A concept of conservation of energy flux for the internal waves propagating in an inhomogeneous shallow water is examined. The emphasis is put on an application of solution of the Korteweg—de Vries (KdV) equation in a prescribed form of the cnoidal and solitary waves. Numerical simulations were applied for the southern Baltic Sea, along a transect from the Bornholm Basin, through the Słupsk Sill and Słupsk Furrow to the Gdańsk Basin. Three-layer density structure typical for the Baltic Sea has been considered. An increase of wave height and decrease of phase speed with shallowing water depth was clearly demonstrated. The internal wave dynamics on both sides of the Słupsk Sill was found to be different due to different vertical density stratification in these areas. The bottom friction has only negligible influence on dynamics of internal waves, while shearing instability may be important only for very high waves. Area of possible instability, expressed in terms of the Richardson number *Ri*, is very small, and located within the non-uniform density layer, close to the interface with upper uniform layer. Kinematic breaking criteria have been examined and critical internal wave heights have been determined.

1. Introduction

A sea bottom is only seldom horizontal and usually water depth and vertical density structure are varying in space and time. Observations of internal waves in the Andaman Sea, Sulu Sea, Australian North West Shelf and the South China Sea, as well as in other sea basins, show that shoaling effects and local bottom changes may influence essentially the

* Correspondence to: Institute of Oceanology of the Polish Academy of Sciences, 81-712 Sopot, Poland. Tel.: +48 587311815.
E-mail address: smas@iopan.gda.pl.
Peer review under the responsibility of Institute of Oceanology of the Polish Academy of Sciences.

Production and hosting by Elsevier

http://dx.doi.org/10.1016/j.oceano.2016.01.005

internal wave evolution. At present, the South China Sea is known as a "hot spot" for observations of the internal waves generated by tides in deep sea and propagating on the ocean shelf (Lien et al., 2014). A large-amplitude depression of the first mode of the internal solitary waves has been observed during spring tide using both shipboard and mooring ADCP and CTD measurements. Maximum negative vertical displacement approached the value of 100–150 m, nearly half of the water depth, and observed phase velocity was equal to about 2 m s^{-1}. Comprehensive observations of the internal tides by Holloway (1994, 1996) in a region of shelf-break on the Australian North West Shelf showed that internal tides exhibit a three-dimensional structure. Waves of depression are observed during summer, while in winter they are weaker and are waves of positive elevation.

Satellite SAR images provided an excellent tool for observation and recording of the internal waves in the ocean. The Indonesian Throughflow, the Middle Atlantic Bight, the Gulf of Aden and the White Sea are only a few examples of such locations. Other examples have been collected and discussed by Massel (2015).

Except the observations in nature, several attempts of modelling of the internal waves have been reported. Vlasenko and Hutter (2002) using numerical simulations, studied transformation of large amplitude internal solitary waves over a slope-shelf topography. Grimshaw et al. (2004) employed the extended Korteweg-de Vries (eKdV) equation to simulate propagation of internal solitary waves taking into account a real variability of wave parameters for several oceanic shelves. It was shown that if the background environment varies sufficiently slowly in comparison with an individual solitary wave, then the wave has a soliton-like form with varying amplitude and phase for large distances.

Combined effect of the Earth rotation and varying bathymetry on the solitary internal waves propagating on long distances was described by Grimshaw et al. (2014) using an extension of the KdV equation in the form of the Ostrovsky equation. The main finding of this study is that the Earth rotation induces a formation of a secondary wave packet, trailing behind the leading wave. These results correspond to bottom topography and density stratification for the cross section on the South China Sea. However, as the authors argued, they are rather typical for many other continental slopes.

In contrast to the deep sea there are not numerous papers on the internal waves dynamics in the shallow water. The application of the concept of conservation of energy flux to study the long internal wave dynamics in the horizontally inhomogeneous ocean was reported by Pelinovsky and Shavratsky (1976) and Pelinovsky et al. (1994), however without any connections to the real bathymetry and density stratification. Laboratory experiments and theoretical studies have been conducted by Helfrich and Melville (1986) and Helfrich (1992) to explore shoaling of the internal solitary waves of depression in a two-layer system on a uniform slope. An extended Korteweg-de Vries (eKdV) equation, including the nonlinearity, dispersion and dissipation was solved numerically for single and rank-ordered pairs of solitary waves incident on the slope-shelf topography of large dimension when the topographic effects dominate nonlinearity and dispersion. The authors discussed an application of the developed theoretical models for the real oceanographic situations, however expressing some doubts to which extent a laminar damping in the laboratory tanks properly reflects turbulent eddy viscosity in the real ocean.

In this paper, numerical simulations of long internal waves motion over a slowly changing bathymetry and density stratification in the southern Baltic Sea are considered. For analysis, the typical temperature and salinity vertical structure, recorded during the cruise of the research vessel s/v *Oceania* in February 2003 along the transect from Bornholm Basin, through Słupsk Sill and Słupsk Furrow to Gdańsk Basins (see Fig. 1) was used. This period corresponded to one of the major inflows of saline water from the North Sea to the Baltic Sea and high dynamics of the pycnocline motions (Massel, 2015; Piechura and Beszczyńska-Möller, 2004).

A concept of the energy flux conservation was considered under the assumption that the internal wave maintains its cnoidal-like shape with varying wave parameters. Also, the limiting cases of the cnoidal wave, namely the solitary and sinusoidal waves are taken into account. In the numerical simulations, the non-dissipative motion, as well as motion with several dissipative mechanisms, such as bottom friction, shearing instability with mixing and wave breaking, have been taken into account.

The paper is organised as follows. In Section 2, the concept of energy flux conservation for internal waves is introduced. In Section 3, motion of the internal waves of prescribed form is discussed and governing equations are solved. Finally, variation of the wave height and wave shape are determined and illustrated for given locations along the transect in the southern Baltic Sea. The major conclusions are formulated in Section 4.

2. Concept of the energy flux conservation

We would like to consider a long internal wave motion in two-dimensional vertical plane (x, z) with z-axis positive upward. Water depth is slowly varying in the x direction and the refraction effects are omitted. The background density $\overline{\rho}(x,z)$ is a known slowly varying function of x and z coordinates. Under the Boussinesq approximation, the rate of wave energy change can be presented as follows (Kundu et al., 2016; Massel, 2015):

$$\frac{\partial}{\partial t}\left[\frac{1}{2}\overline{\rho}(x,z)(u^2+w^2)\right]+g\rho(z)w+\nabla\cdot(pu)=0, \tag{1}$$

where u and w are the velocity components in x and z direction, respectively, p is the water pressure and $\rho(z)$ is the perturbation of density component due to wave action. The first term in Eq. (1) represents a rate of change of the kinetic energy and the second term can be considered as the rate of change of potential energy. The last term is the net work done by the pressure forces and it can be interpreted as the divergence of the energy flux pu (Gill, 1982).

Therefore, the energy flux integrated over water depth and averaged over wave period can be written as follows:

$$\overline{F_E(x)}=\frac{1}{T}\int_0^T\int_{-h(x)}^0 p(x,z,t)u(x,z,t)\,dz\,dt, \tag{2}$$

in which $T=2\pi/\omega$ is the internal wave period and ω is the wave frequency.

To determine the energy flux $\overline{F_E(x)}$ we consider the vertical displacements of isopycnals due to long internal

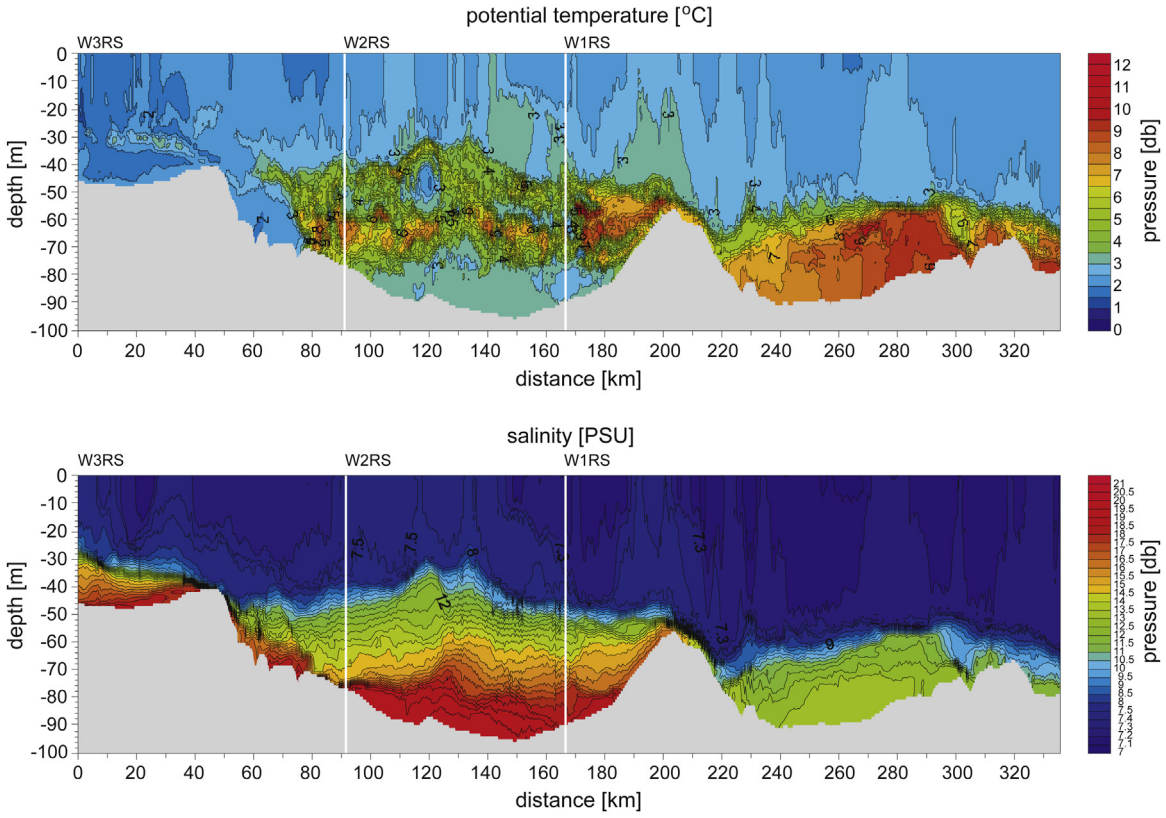

Figure 1 Water depths, water temperature and salinity in the Bornholm Basin, Słupsk Sill and Słupsk Furrow on February 4—6, 2003 (Piechura and Beszczyńska-Möller, 2004).

waves in the form (Grimshaw et al., 2004; Kurkina et al., 2011; Massel, 2015):

$$\zeta(x,z,t) = \eta(x,t)\Phi(x,z), \tag{3}$$

in which $\eta(x, t)$ describes an evolution of the internal wave shape in space and time, and function $\Phi(x, z)$ determines a vertical modal structure of the internal wave.

Among a variety of approaches to describe an evolution of the long periodic internal waves, the Korteweg-de Vries (KdV) theory (Korteweg and de Vries, 1895; Massel, 1989; Miles, 1981; Whitham, 1974) is applied where the balance between nonlinearity and dispersion of wave motion is included:

$$\frac{\partial\eta}{\partial t} + C_p\frac{\partial\eta}{\partial x} + \alpha\eta\frac{\partial\eta}{\partial x} + \beta\frac{\partial^3\eta}{\partial x^3} = 0, \tag{4}$$

in which C_p is the linear phase velocity, α is the nonlinearity parameter and β is the dispersion parameter.

The function $\Phi(x, z)$ in Eq. (3) is a solution of the eigenvalue problem which in the Boussinesq approximation becomes (Massel, 2015):

$$\frac{d^2\Phi(x,z)}{dz^2} + \frac{N^2(x,z)-\omega^2}{\omega^2-f^2}k^2(x)\Phi(x,z) = 0, \tag{5}$$

where $k(x)$ is the horizontal wavenumber, f is the inertial frequency and $N(x, z)$ is the Väisälä-Brunt frequency:

$$N^2(x,z) = -\frac{g}{\overline{\rho}(x,z)}\frac{d\overline{\rho}(x,z)}{dz}, \tag{6}$$

in which $\overline{\rho}(x,z)$ is the background density.

Function $\Phi(x, z)$ is defined for the water column ($-h \le z \le 0$) and the boundary conditions are:

$$\Phi(x,0) = \Phi(x,-h) = 0. \tag{7}$$

The above boundary value problem should be valid for each mode, n, and the wave frequency ω should be bounded above by the Väisälä-Brunt frequency, $N(x, z)$, and below by the inertial frequency, f, i.e.:

$$f^2 < \omega^2 < N^2(x,z). \tag{8}$$

For long periodic waves if $\omega^2 \ll N^2(x, z)$ and when the Earth rotation is neglected, we obtain:

$$N^2(x,z)-\omega^2 \approx N^2(x,z), \quad \omega^2-f^2 \approx \omega^2. \tag{9}$$

Thus, Eq. (5) for function $\Phi(x, z)$ can be rewritten as follows:

$$\frac{d^2\Phi(x,z)}{dz^2} + q(x,z)\lambda\Phi(x,z) = 0, \tag{10}$$

where

$$q(x,z) = N^2(x,z), \qquad \lambda = \frac{1}{C_p^2(x)}. \tag{11}$$

The solution of Eq. (10) is described fully in Section 3.2.3 for an inhomogeneous three-layer density stratification. Here we only note that the function $\Phi(x, z)$ is normalised so that maximum value of the function $\Phi(x, z)$ is equal to 1 at some level z, and $\Phi(x, z)$ vanishes at the sea surface and sea bottom. For a given frequency ω, solution of Eq. (10) shows

that an initial disturbance is decomposed into a set of propagating modes λ_n with corresponding phase velocities $C_p^{(n)}$. However for further analysis, the first most energetic mode (eigenvalue) $\lambda = \lambda_1$ is retained, with the phase velocity given by Eq. (11). It should be noted here that phase velocity $C_p(x)$ is totally dependent on the vertical water stratification and Väisälä-Brunt frequency, and it does not depend on the internal wave amplitude.

From the following expressions for the dynamic pressure p and horizontal velocity u (Krauss, 1966; Kurkina et al., 2011; Kundu et al., 2016):

$$p(x,z) = -\overline{\rho}(x,z)C_p(x)u(x,z) \quad \text{and} \quad u(x,z) = -C_p(x)\eta(x,t)\frac{d\Phi(x,z)}{dz}, \tag{12}$$

the energy flux integrated over water depth and averaged over wave period becomes:

$$\overline{F_E(x)} = \frac{1}{T}\int_0^T\int_{-h(x)}^0 C_p^3(x)\overline{\rho}(x,z)\eta^2(x,t)\left(\frac{d\Phi(x,z)}{dz}\right)^2 dz\,dt, \tag{13}$$

or:

$$\overline{F_E(x)} = C_p^3(x)\Pi(x)\frac{1}{T}\int_0^T \eta^2(x,t)\,dt, \tag{14}$$

where

$$\Pi(x) = \int_{-h(x)}^0 \overline{\rho}(x,z)\left(\frac{d\Phi(x,z)}{dz}\right)^2 dz. \tag{15}$$

Functions $C_p(x)$ and $\Pi(x)$ depend totally on the vertical stratification of water masses at a given distance x and they do not depend on time.

Now we assume the conservation of energy flux for a given dissipation mechanisms in the general form:

$$\frac{\partial\overline{F_E(x)}}{\partial x} + D(x) = 0, \tag{16}$$

in which $D(x)$ is the dissipation term. This term obeys the possible energy losses due to bottom friction, percolation within the sea bottom, shearing instability and mixing in water column, and wave breaking.

3. Propagation of long internal waves on slowly varying water depth

3.1. Governing equations

In general, the energy flux conservation concept should be valid for arbitrary internal wave shape $\eta(x, t)$. However, determination of initial $\eta(x_0, t)$ function is very difficult to achieve in the natural conditions. Therefore we will consider an evolution of long internal waves with isopycnal displacements given in a prescribed form of the periodic cnoidal waves. The cnoidal waves resulting from the KdV equation were chosen as they provide an opportunity to study dynamics of the simple linear sinusoidal waves as well as solitary waves within the same framework of the Jacobian elliptic functions (Abramowitz and Stegun, 1975).

Thus we assume the wave shape as follows (Massel, 1989, 2015):

$$\eta(x,t) = H(x)\left\{\frac{1}{m}\left(1-\frac{\mathbf{E}}{\mathbf{K}}-m\right) + cn^2\left[\frac{2\mathbf{K}}{L}(x-Ut)\right]\right\}, \tag{17}$$

in which $H(x)$ is the wave height, L is the wave length, $cn(x)$ is the Jacobian elliptic function, and $\mathbf{K}$ and $\mathbf{E}$ are the complete elliptic integrals of the first and second kind, respectively. They are functions of the elliptic parameter m from the range $0 \le m \le 1$ (Abramowitz and Stegun, 1975). The phase speed U is given by:

$$U = C_p(x)\left[1 + \frac{\hat{\alpha}H(x)}{3m}\left(2-3\frac{\mathbf{E}}{\mathbf{K}}-m\right)\right]. \tag{18}$$

The wave height $H(x)$ corresponds to the maximum isopycnal displacement ζ at a level z where the normalised function $\Phi(x, z) = 1$. Due to boundary conditions (7), the isopycnal displacements at sea surface and sea bottom are equal to zero.

To define an unknown elliptic parameter m, the following relationship is applied (Massel, 1989, 2015):

$$\left(\frac{\hat{\alpha}}{\hat{\beta}}\right)\frac{H(x)L^2}{48} = m\mathbf{K}^2, \tag{19}$$

or

$$\left(\frac{\hat{\alpha}(x)}{\hat{\beta}(x)}\right)\frac{H(x)(C_p(x)\,T)^2}{48} = \frac{m\mathbf{K}^2}{\left[1+\frac{\hat{\alpha}(x)H(x)}{3m}\left(2-3\frac{\mathbf{E}}{\mathbf{K}}-m\right)\right]^2}, \tag{20}$$

in which nonlinearity and dispersion parameters $\hat{\alpha}$ and $\hat{\beta}$ are:

$$\hat{\alpha}(x) = \frac{\alpha(x)}{C_p(x)} = \frac{3}{2}\frac{\int_{-h(x)}^0\left(\frac{d\Phi(x,z)}{dz}\right)^3 dz}{\int_{-h(x)}^0\left(\frac{d\Phi(x,z)}{dz}\right)^2 dz}, \tag{21}$$

$$\hat{\beta}(x) = \frac{\beta}{C_p(x)} = \frac{1}{2}\frac{\int_{-h(x)}^0\Phi^2(x,z)\,dz}{\int_{-h(x)}^0\left(\frac{d\Phi(x,z)}{dz}\right)^2 dz}. \tag{22}$$

To get the energy flux we have to solve the integral in Eq. (14) for $\eta(x, t)$ given by Eq. (17). The calculations are facilitated by a recursion relations from Gradshteyn and Ryzhik (1965):

$$I(l) = \frac{1}{\mathbf{K}}\int_0^K [m\,cn^2(\theta)]^l d\theta; \tag{23}$$

then:

$$I(0) = 1 \quad \text{and} \quad I(1) = -1 + m + \frac{\mathbf{E}}{\mathbf{K}}, \tag{24}$$

and:

$$I(l+2) = \left(\frac{2l+2}{2l+3}\right)(2m-1)I(l+1) + \left(\frac{2l+1}{2l+3}\right) \times (m-m^2)I(l). \tag{25}$$

Using these relationships an evolution equation for wave height becomes:

$$\frac{\partial}{\partial x}\left(C_p^3(x)\Pi(x)\sum_{i=1}^{i=3}A_i(x)H^2(x)\right)+D(x)=0, \tag{26}$$

or

$$\frac{dH(x)}{dx}+\frac{1}{2}\frac{\frac{dP_1(x)}{dx}}{P_1(x)}H(x)+\frac{1}{2}\frac{D(x)}{P_1(x)H(x)}=0, \tag{27}$$

in which

$$P_1(x)=C_p^3(x)\Pi(x)\sum_{i=1}^{i=3}A_i(x), \tag{28}$$

$$A_1(x)=\left[\frac{1}{m}\left(1-\frac{\mathbf{E}}{\mathbf{K}}-m\right)\right]^2, \tag{29}$$

$$A_2(x)=-\frac{2}{m^2}\left(1-\frac{\mathbf{E}}{\mathbf{K}}-m\right)^2, \tag{30}$$

$$A_3(x)=\frac{1}{3m^2}\left[2(1-2m)\left(1-m-\frac{\mathbf{E}}{\mathbf{K}}\right)+m(1-m)\right]. \tag{31}$$

Prior to solving Eq. (27), the dissipation term $D(x)$ should be determined. In the following reasoning, various dissipation mechanisms are discussed. However, it will be useful to start with case of the non-dissipative motion.

3.2. Wave motion without energy dissipation

When dissipation is totally neglected, i.e. $D(x) = 0$, solution of Eq. (27) takes the form:

$$H(x)=\left(\frac{C_p(x_0)}{C_p(x)}\right)^{3/2}\left(\frac{\Pi(x_0)}{\Pi(x)}\right)^{1/2}\left[\frac{\sum_{i=1}^{i=3}A_i(x_0)}{\sum_{i=1}^{i=3}A_i(x)}\right]^{1/2}H(x_0), \tag{32}$$

where x_0 denotes the reference point where the values $C_p(x_0)$, $\Pi(x_0)$ and $A_i(x_0)$ are assumed to be known.

3.2.1. Solitary wave

The above formula for the cnoidal waves is simplified considerably for extreme values of the elliptic parameter m, namely for $m = 1$ and $m = 0$. When $m \to 1$, we have $\mathbf{E} = 1$ and $\mathbf{K} \to \infty$. Consequently $L \to \infty$, and function $cn^2(u) \to \cosh^{-2}(u)$. Thus the solitary wave shape becomes:

$$\eta(x,t)=H(x)\cosh^{-2}\left[\left(\frac{H(x)}{12}\frac{\hat{\alpha}(x)}{\hat{\beta}(x)}\right)^{1/2}(x-Ut)\right], \tag{33}$$

where

$$U=C_p(x)\left(1+\frac{1}{3}\hat{\alpha}(x)H(x)\right)\approx C_p(x). \tag{34}$$

For averaged energy flux for the solitary waves we have:

$$\overline{F_E(x)}=\frac{4}{\sqrt{3}}C_p^2(x)\Pi(x)\left(\frac{\beta(x)}{\alpha(x)}\right)^{1/2}H^{3/2}. \tag{35}$$

Thus, if $D(x) = 0$ from Eq. (27) we find:

$$H(x)=E_1(x)\,E_2(x)\,E_3(x)\,H(x_0), \tag{36}$$

where:

$$\left.\begin{aligned}E_1(x)&=\left(\frac{C_p(x)(x_0)}{C_p(x)(x)}\right)^{4/3}\\ E_2(x)&=\left[\left(\frac{\hat{\alpha}(x)}{\hat{\alpha}(x_0)}\right)\left(\frac{\hat{\beta}(x_0)}{\hat{\beta}(x)}\right)\right]^{1/3}\\ E_3(x)&=\left(\frac{\Pi(x_0)}{\Pi(x)}\right)^{2/3}\end{aligned}\right\}. \tag{37}$$

Let us rewrite Eq. (36) as follows:

$$H(x)=C_p^{-4/3}(x)\,\Pi^{-2/3}(x)q^{1/3}(x)\,D_{\mathrm{ref}}, \tag{38}$$

in which:

$$q(x)=\frac{\int_{-h}^{0}\left(\frac{d\Phi(x,z)}{dz}\right)^3dz}{\int_{-h}^{0}\Phi^2(x,z)\,dz}, \tag{39}$$

and

$$D_{\mathrm{ref}}=C_p^{4/3}(x_0)\,\Pi^{2/3}(x_0)q^{-1/3}(x_0)H(x_0). \tag{40}$$

Expression (40) is in full agreement with results of Pelinovsky and Shavratsky (1976) obtained by another methods.

In a similar way we can determine the amplitudes of velocities and water density, i.e.:

$$\left.\begin{aligned}&\text{vertical velocity}\approx C_p^{-4/3}(x)\Pi^{-2/3}(x)q^{1/3}(x)\\ &\text{horizontal velocity}\approx C_p^{-1/3}(x)\Pi^{-2/3}(x)q^{1/3}(x)\frac{d\Phi(x,z)}{dz}\\ &\text{water density}\approx C_p^{-4/3}(x)\Pi^{-2/3}(x)q^{1/3}(x)\Phi(x,z)\frac{d\overline{\rho}(x,z)}{dz}\end{aligned}\right\}. \tag{41}$$

3.2.2. Linear wave

In the second extreme case when the parameter $m \to 0$, the complete elliptic integrals $\mathbf{E} = \mathbf{K} = \pi/2$. Therefore the first term in Eq. (17) becomes:

$$\lim\left[\frac{1}{m}\left(1-\frac{\mathbf{E}}{\mathbf{K}}-m\right)\right]=-1/2, \tag{42}$$

and

$$cn^2\left[\frac{2\mathbf{K}}{L}Ut\right]\to\cos^2\left[\frac{\pi}{L}C_p(x)t\right]. \tag{43}$$

Now the wave shape becomes:

$$\begin{aligned}\eta(x,t)&=-\frac{H(x)}{2}+H(x)\cos^2\left[\frac{\pi}{L}C_p(x)t\right]\\ &=\frac{H(x)}{2}\cos\left[\frac{2\pi}{L}C_p(x)t\right],\end{aligned} \tag{44}$$

and for wave height $H(x)$ we have:

$$H(x)=\left(\frac{C_p(x)(x_0)}{C_p(x)(x)}\right)^{3/2}\left(\frac{\Pi(x_0)}{\Pi(x)}\right)^{1/2}H(x_0). \tag{45}$$

3.2.3. Numerical simulation for an inhomogeneous three-layer water density structure

To illustrate the applicability of above formulae we assume for a moment that the dissipation energy is absent and the

internal waves are propagating over slowly changing water depth in the southern Baltic Sea. Two sections of the sloping bottom in region of the Słupsk Sill and the Słupsk Furrow have been chosen for numerical simulation. The first section of length of about 27 km extends from Stations 172 till Station 199. Numbers of Stations correspond to the distances given in Fig. 1. Water depth is changing from about 90 m in the Bornholm Basin to about 55 m close to the Słupsk Sill. Thus, the mean bottom slope is ~0.0011. The experimental data on the density stratification $\overline{\rho}(x,z)$ were obtained from the s/v *Oceania* cruises in February 2003. They confirm that the three-layer vertical density distribution dominates in the Baltic Sea (Krauss, 1966; Massel, 2015). The upper and bottom layers are usually uniform and the non-uniform layer between them is characterised by slowly changing density as follows:

$$\overline{\rho}(z)=\begin{cases}\rho_1 & \text{for } -h_1\le z\le 0\\ \rho_1\exp\left[-\dfrac{N_0^2(x)}{g}(z+h_1)\right] & \text{for } -h_2\le z\le -h_1\\ \rho_2 & \text{for } -h\le z\le -h_2\end{cases}, \tag{46}$$

in which h is total water depth, h_1 is the thickness of upper layer, (h_2-h_1) is the thickness of the non-uniform layer, $(h-h_2)$ is the thickness of bottom uniform layer and $N_0(x)$ is the Väisälä-Brunt frequency given as:

$$N_0^2(x)=\begin{cases}0 & \text{for } -h_1\le z\le 0\\ \dfrac{g\ln\left(\frac{\varrho_1}{\varrho_2}\right)}{h_1-h_2} & \text{for } -h_2\le z\le -h_1\\ 0 & \text{for } -h\le z\le -h_2\end{cases} \tag{47}$$

Solution of the linear eigenvalue problem (see Eq. (10)) for long internal waves with a given density distribution can be obtained by an analytical method. In particular, we adopt the function $\Phi(x,z)$ in the form:

$$\Phi(x,z)=\begin{cases}B(x)z & -h_1\le z\le 0\\ C(x)\cos(\gamma z)+D(x)\sin(\gamma z) & -h_2\le z\le -h_1\\ E(x)(z+h) & -h\le z\le -h_2\end{cases} \tag{48}$$

where $\gamma=N_0(x)/C_p(x)$.

The functions $B(x)$, $C(x)$, $D(x)$ and $E(x)$ are obtained from the continuity conditions at the sublayers boundaries. These conditions are expressed in the form of continuity of function $\Phi(x,z)$ and its gradient $d\Phi(x,z)/dz$ across the boundaries (Massel, 2015). The resulted set of equations has a non-trivial solution only when the following determinant Δ becomes zero:

$$\Delta=\begin{vmatrix}a_{11} & a_{12} & a_{13} & a_{14}\\ a_{21} & a_{22} & a_{23} & a_{24}\\ a_{31} & a_{32} & a_{33} & a_{34}\\ a_{41} & a_{42} & a_{43} & a_{44}\end{vmatrix}=0, \tag{49}$$

in which:

$$\left.\begin{array}{llll}a_{11}=h_1, & a_{12}=\cos(\gamma h_1), & a_{13}=-\sin(\gamma h_1), & a_{14}=0\\ a_{21}=1, & a_{22}=-\gamma\sin(\gamma h_1), & a_{23}=-\gamma\cos(\gamma h_1), & a_{24}=0\\ a_{31}=0, & a_{32}=-\cos(\gamma h_2), & a_{33}=\sin(\gamma h_2), & a_{34}=h-h_2\\ a_{41}=0, & a_{42}=-\gamma\sin(\gamma h_2), & a_{43}=-\gamma\cos(\gamma h_2), & a_{44}=1\end{array}\right\}. \tag{50}$$

For a given value of the Väisälä-Brunt frequency $N_0(x)$, Eq. (49) allows to determine the phase velocities $C_p(x)$ for an infinite number of modes, n, and corresponding functions for a given mode are:

$$\left.\begin{aligned}C(x)&=\frac{a_{13}a_{21}-a_{11}a_{23}}{a_{12}a_{23}-a_{13}a_{22}}B(x)\\ D(x)&=\frac{a_{11}a_{22}-a_{12}a_{21}}{a_{12}a_{23}-a_{13}a_{22}}B(x)\\ E(x)&=\frac{-(a_{32}C(x)+a_{33}D(x))}{a_{34}}\end{aligned}\right\}. \tag{51}$$

Now we apply above formulae for the first mode of the internal solitary wave moving over the west slope of the Słupsk Sill. The scattered rhombuses in Fig. 2 show the solitary wave height increase with a distance x, when approaching to the Słupsk Sill, what should be expected. Spreading of dots results from the variation in space of the experimental temperature and salinity values which are initial ones for determination of density stratification according to UNESCO formula (Massel, 2015). Solid line represent the best fitting of the simulation data. These remarks also apply for other figures in the paper.

It should be noted that on the distance of about 30 km, the non-dimensional wave height has increased more than two times with respect to wave height at the reference point. In the same time, the circular dots demonstrate a slower decrease of the non-dimensional phase velocity $C_p(x)$.

Fig. 3 illustrates an important dependence of the solitary non-dimensional wave height and phase velocity on water depth. Non-dimensional wave height is decreasing approximately as the function $H(x)/H(x_0)\approx h^{-2.67}$ while the phase velocity increase is approximated by the linear function of $C_p(x)/C_p(x_0)\approx 0.015h-0.21$. In Fig. 4 the known fact that the dispersion parameter β depends mostly on the water depth h is confirmed. For both regions under consideration, parameter β is almost a linear function of water depth. However values of parameter β for the same water depths are different for both slopes what suggests that the dispersion parameter β possibly depends also on another factors. For deeper waters in the Gotland Deep in the Baltic Sea,

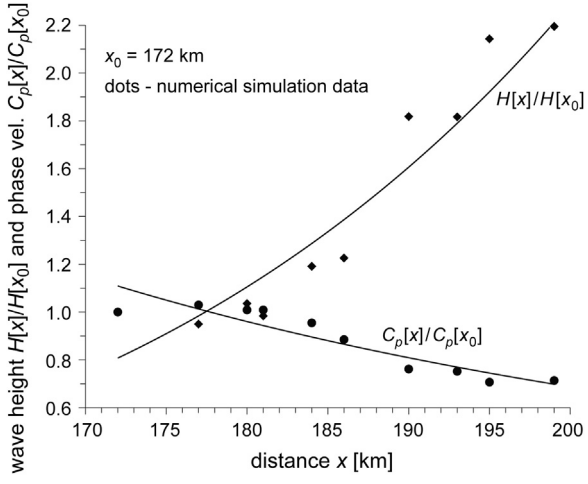

Figure 2 Non-dimensional wave height and phase velocity as a function of distance for the west slope of the Słupsk Sill. Solid curves denote the best fitting of simulation data.

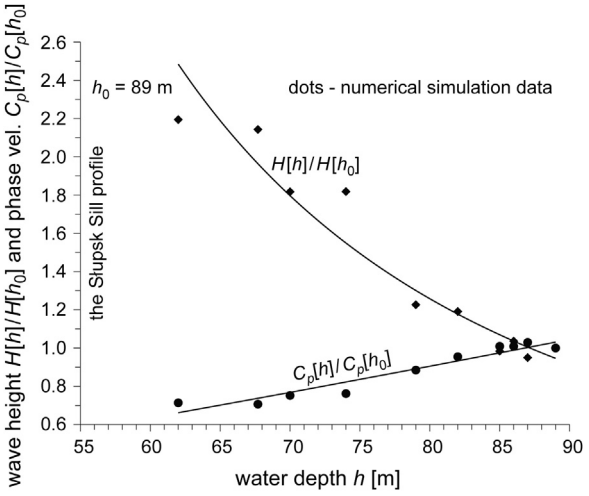

Figure 3 Non-dimensional wave height and phase velocity as a function of water depth for the west slope of the Słupsk Sill. Solid curves denote the best fitting of simulation data.

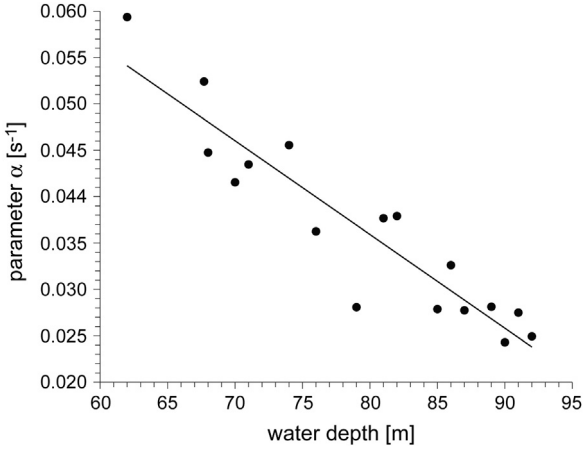

Figure 5 Nonlinear parameter α as a function of water depth. Solid curves denote the best fitting of simulation data.

Talipova et al. (1998) showed that $\beta = 2.12 \cdot 10^{-6} h^{3.86}$ and phase velocity $C_p = 0.82 \ln(h) - 3.4$.

As shown in Fig. 5, the nonlinear parameter α linearly attenuates with the water depth for both regions under consideration, i.e. $\alpha \approx -0.001h + 0.117$. It means that internal waves climbing on the west slope of the Słupsk Sill and on the east slope of the Słupsk Furrow become more and more nonlinear, what should be expected. Moreover, Fig. 6 shows a linear relationship between wave height H and the function $C_p^{-4/3}(x)$ (see Eq. (38). From this equation it follows that under assumption of constant energy flux, when water depth decreases, the solitary wave height increases and the crest of a solitary wave becomes higher and wave shape becomes thinner as shown in Fig. 7).

Similar numerical simulations have been performed for east slope of the Słupsk Furrow for Stations 244—318 (see Fig. 1). Comparison of the phase velocities given in Fig. 8 showed that $C_p(x)$ for this slope is smaller than phase velocity on west slope of the Słupsk Sill.

From Eq. (10) follows that except water depth, the phase velocity $C_p(x)$ depends on the Väisälä-Brunt frequency $N_0(x)$ which is a function of the vertical stratification of water density. So, let us write:

$$\frac{C_p(x)}{\sqrt{gh(x)}} = f\left(\frac{\rho_2 - \rho_1}{\rho_1 + \rho_2}\right), \tag{52}$$

where the ratio $(\rho_2 - \rho_1)/(\rho_1 + \rho_2)$ can be called as a density parameter. Function (52) is shown in Fig. 9 for both regions under consideration. The non-dimensional phase velocities form two separated groups depending on the density parameter. Larger value of this parameter yields the higher value of the phase velocity for the west slope of the Słupsk Sill than for the other region. However within each group of data, the non-dimensional phase velocity is almost linearly dependent on the density parameter:

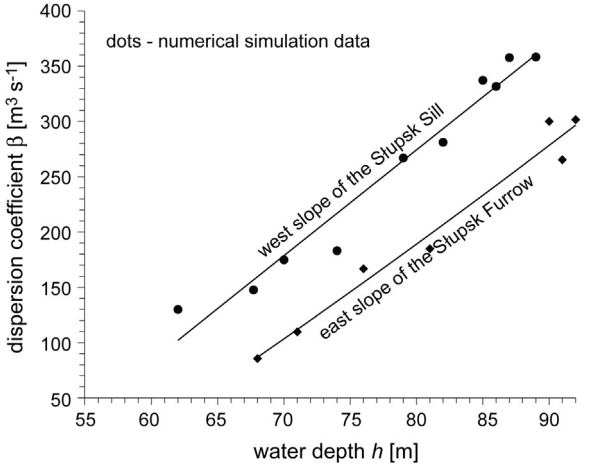

Figure 4 Dispersion parameter β as a function of water depth. Solid curve denotes the best fitting of simulation data.

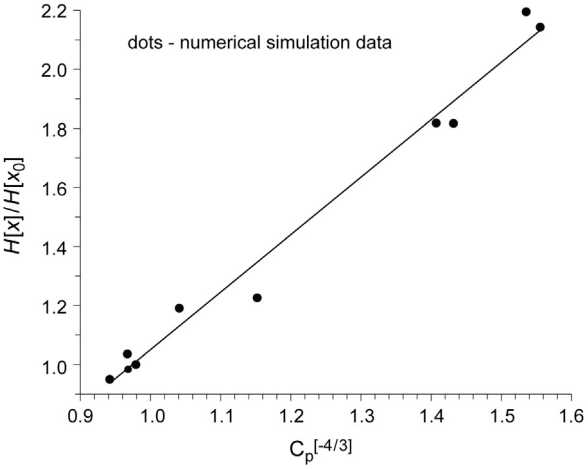

Figure 6 Non-dimensional wave height as a function of phase velocity for the west slope of the Słupsk Sill. Solid curve denotes the best fitting of simulation data.

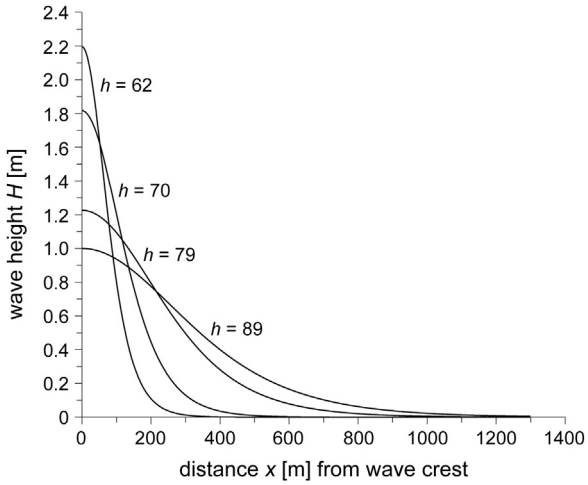

Figure 7 Internal wave shape as a function of distance from wave crest for chosen water depths.

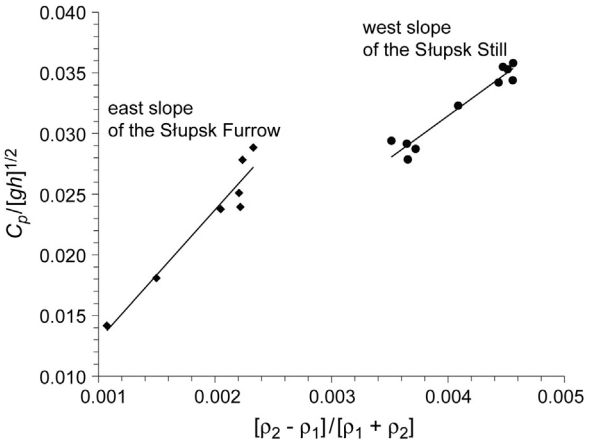

Figure 9 Non-dimensional phase velocity as a function of density parameter for the west slope of the Słupsk Sill and the east slope of the Słupsk Furrow. Solid curves denote the best fitting of simulation data.

$$\frac{C_p(x)}{\sqrt{gh(x)}} = \begin{cases} 7.0\left(\dfrac{\rho_2-\rho_1}{\rho_1+\rho_2}\right) & \text{for west slope of the Słupsk Sill} \\ 10.7\left(\dfrac{\rho_2-\rho_1}{\rho_1+\rho_2}\right) & \text{for east slope of the Słupsk Furrow} \end{cases} \tag{53}$$

From the above analysis it follows that the Słupsk Sill separates regions of different phase velocities of the solitary waves. This difference is mostly due to different density structure of a water column. The density ρ_1 at the top of a pycnocline remains the same for both regions and it is equal to $\rho_1 \approx 1005.65$ kg m^{-3}. On the other hand, the bottom layer density for the west slope of the Słupsk Sill is equal $\rho_2 \approx 1013-1014$ kg m^{-3} while for the east slope of the Słupsk Furrow it is equal only $\rho_2 \approx 1008-1010$ kg m^{-3}. It means that dense bottom water from the Bornholm Basin is not able to overflow through the Słupsk Sill, being blocked at the west slope of the Słupsk Sill.

Eq. (38) indicates that internal wave height is proportional to the phase velocity as $H(x) \approx C_p^{-4/3}(x)$. Therefore for the same value of the density parameter $(\rho_2 - \rho_1)/(\rho_1 + \rho_2)$, smaller phase velocity corresponds to a higher wave. That is illustrated in Fig. 10 by comparison of two groups of data for the west slope of the Słupsk Sill and the east slope of the Słupsk Furrow. The following reference values of the wave heights for both regions have been used for calculations: $H(x_0 = 172) = 1$ m and $H(x_0 = 244) = 1$ m.

Another factor which can influence the phase speed and wave height is the thickness of a pycnocline. As it is shown in Fig. 11, thickness of the pycnoclines is changed linearly with water depth h in both regions under consideration. On the west slope of the Słupsk Sill, the thickness is bigger than on the east slope of the Słupsk Furrow. It should be noted that pycnocline thickness $(h_2 - h_1)$ is located in a denominator of fraction in the formula for Väisälä-Brent frequency $N_0(x)$ (see Eq. (47)). Therefore, the smaller pycnocline thickness should

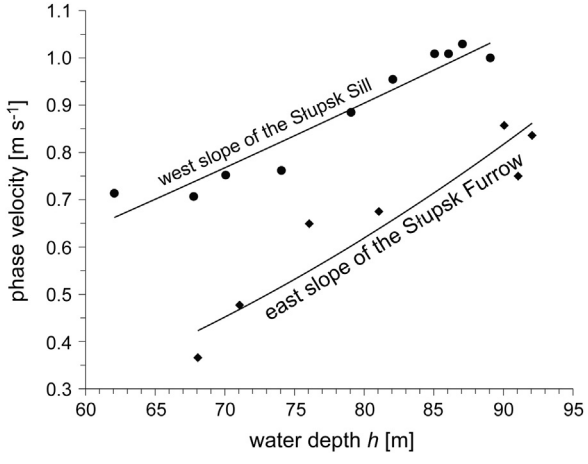

Figure 8 Comparison of phase velocity as a function of water depth for the west slope of the Słupsk Sill and the east slope of the Słupsk Furrow. Solid curves denote the best fitting of simulation data.

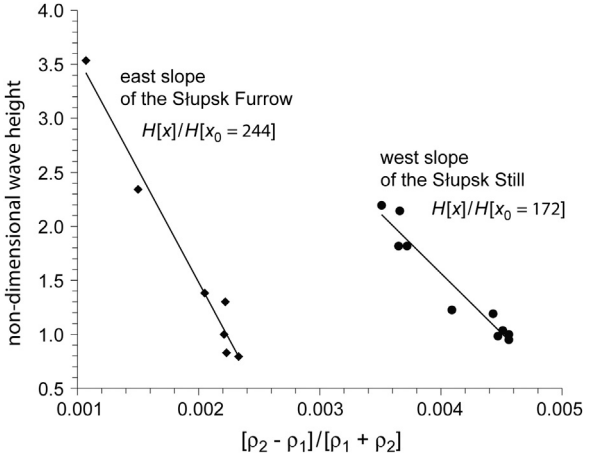

Figure 10 Non-dimensional wave height as a function of density parameter for the west slope of the Słupsk Sill and the east slope of Słupsk Furrow. Solid curves denote the best fitting of simulation data.

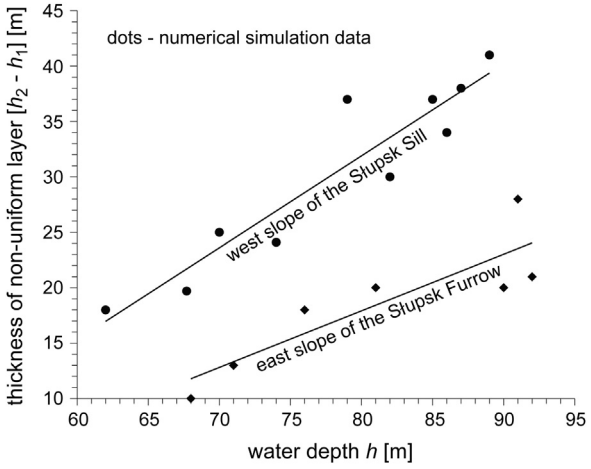

Figure 11 Thickness of non-uniform layer as a function of water depth. Solid curves denote the best fitting of simulation data.

give higher frequency $N_0(x)$ and *vice versa*. Despite this fact, the influence of the density ratio (ρ_2/ρ_1) on frequency $N_0(x)$ is much stronger resulting finally in the higher value of the Väisälä-Brunt frequency on the west slope of the Słupsk Sill.

Let us now consider a short cnoidal wave (T = 10 min) propagating on the west slope of the Słupsk Sill. In Fig. 12, the relationship of wave height and phase speed on the water depth is shown. Wave height of the short cnoidal wave increases much slower than the solitary wave height (see Fig. 3 for comparison). However, phase speed behaves in a similar way, being independent on the shape of an internal wave.

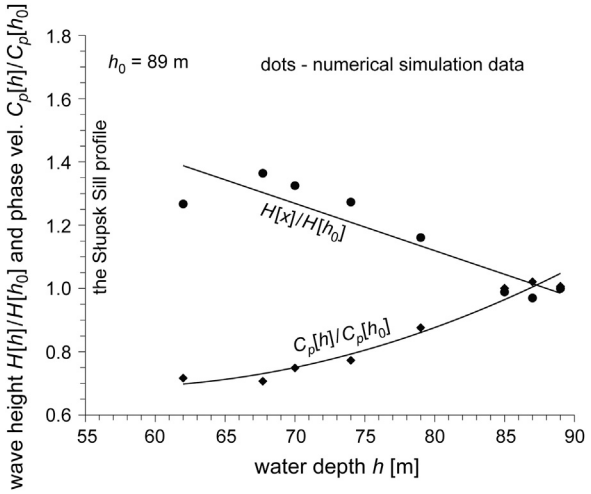

Figure 12 Internal wave height and phase velocity as a function of water depth for short internal wave. Solid curves denote the best fitting of simulation data.

3.3. Wave motion with energy dissipation

3.3.1. Influence of bottom friction

In the previous section, propagation of the internal waves over varying water depth was discussed under assumption that the energy dissipation is absent. When waves are non breaking and the energy loss by percolation is neglected, the only dissipation mechanism is the bottom friction, i.e. $D(x) = D_{fr}$. Then, the energy flux becomes:

$$\frac{d\overline{F_E(x)}}{dx} + D(x) = 0, \tag{54}$$

in which the average work done by friction stress for periodic wave per unit area is (Massel, 2012):

$$D = \overline{\tau u_b} = \frac{1}{T}\int_0^T \overline{\rho} f u_b^2 |u_b|\, dt, \tag{55}$$

where f_r is the friction factor ($f_r \approx 0.05$) and u_b is the bottom velocity due to internal waves:

$$u_b(x,t) = -C_p(x)(x)\eta(x,t)\left(\frac{d\Phi(x,z)}{dz}\right)_{z=-h}. \tag{56}$$

First let us apply above relationships for the cnoidal waves of arbitrary elliptic parameter m. Thus, the dissipation term D_{fr} becomes:

$$D(x) = -P_2(x)H^3(x), \tag{57}$$

in which:

$$P_2(x) = \overline{\rho}(-h) f_r C_p^3(x)\left(\frac{d\Phi(x,z)}{dz}\right)_{z=-h}^3 \sum_{i=1}^{4} B_i(x), \tag{58}$$

and

$$B_1(x) = \left[\frac{1}{m}\left(1-\frac{\mathbf{E}}{\mathbf{K}}-m\right)\right]^3, \tag{59}$$

$$B_2(x) = \frac{-3}{m^3}\left(1-\frac{\mathbf{E}}{\mathbf{K}}-m\right)^3, \tag{60}$$

$$B_3(x) = \frac{1}{m^3}\left(1-\frac{\mathbf{E}}{\mathbf{K}}-m\right) \times \left\{m(m-1)-2(2m-1)\left[1-\frac{\mathbf{E}}{\mathbf{K}}-m\right]\right\}, \tag{61}$$

$$B_4(x) = \frac{1}{5m^3}\left\{\frac{4}{3}(2m-1)\left[m(1-m)-2(2m-1)\left(1-\frac{\mathbf{E}}{\mathbf{K}}-m\right)\right] -3m(1-m)\left[1-\frac{\mathbf{E}}{\mathbf{K}}-m\right]\right\}. \tag{62}$$

Substituting Eq. (57) into Eq. (27) provides the governing equation for wave amplitude $H(x)$ in a form of the Bernoulli equation:

$$\frac{dH(x)}{dx} + \frac{1}{2}\frac{\frac{dP_1(x)}{dx}}{P_1(x)}H(x) + \frac{1}{2}\frac{P_2(x)}{P_1(x)}H^2(x) = 0, \tag{63}$$

which has the following solution:

$$H(x) = \left(\frac{P_1(x_0)}{P_1(x)}\right)^{1/2} G^{-1}(x, x_0) H(x_0), \tag{64}$$

where:

$$G(x) = 1 + \frac{1}{2}\overline{\rho}(-h) f_r H \times (x_0) P_1^{1/2}(x_0) \int_{x_0}^{x} P_1^{-3/2}(x) \hat{P}_2(x)\, dx \tag{65}$$

and

$$\hat{P}_2(x) = C_p^3(x) \left(\frac{d\Phi(x,z)}{dz}\right)^3_{z=-h} \sum_{i=1}^{4} B_i(x). \tag{66}$$

For the solitary waves, if $m = 1$, the energy flux, the dissipation term and the wave height become:

$$\overline{F_E(x)} = P_1(x) H^{3/2}(x) = \frac{4\sqrt{3}}{3} \times C_p^2(x) \Pi(x) \left(\frac{\hat{\beta}(x)}{\hat{\alpha}(x)}\right)^{1/2} H^{3/2}, \tag{67}$$

$$D_{fr} = P_2(x) H^{5/2}(x) = \frac{16\sqrt{3}}{15} C_p^2(x) \overline{\rho}(-h) f_r \times \left(\frac{d\Phi(x,z)}{dz}\right)_{z=-h} \left(\frac{\hat{\beta}(x)}{\hat{\alpha}(x)}\right)^{1/2} H^{5/2}, \tag{68}$$

$$H(x) = \left(\frac{P_1(x_0)}{P_1(x)}\right)^{2/3} G^{-1}(x, x_0) H(x_0), \tag{69}$$

where:

$$G(x, x_0) = 1 + \frac{2}{3}\overline{\rho}(-h) f_r H(x_0) P_1^{2/3}(x_0) \times \int_{x_0}^{x} P_1^{-5/3}(x) \hat{P}_2(x)\, dx \tag{70}$$

and

$$\hat{P}_2(x) = \frac{16\sqrt{3}}{15} C_p^2(x) \left(\frac{d\Phi(x,z)}{dz}\right)^3_{z=-h} \left(\frac{\hat{\beta}(x)}{\hat{\alpha}(x)}\right)^{1/2}. \tag{71}$$

We illustrate an influence of the bottom friction on the propagation of solitary waves on west slope of the Słupsk Sill for the initial wave height $H = 3$ m and friction factor $f_r = 0.05$. In Fig. 13, the ratio of the wave height $H_{fr}(x)/H(x)$ is shown, where H_{fr} is the wave height including the bottom friction and $H(x)$ is wave height without dissipation. Reduction of wave height due to bottom friction is very small, being less than 1.5% for water depth decreasing along the slope from 89 m till 62 m.

3.3.2. Shearing instability and mixing

Except the bottom friction, internal wave energy is decreasing by radial spreading and mixing in the water column where the passing wave generates high shear. The energy loss due to shear-induced mixing may be enhanced for shoaling internal waves on shelf. Following Bogucki and Garrett (1993), we examine an influence of the solitary wave height on attenuation of the Richardson number

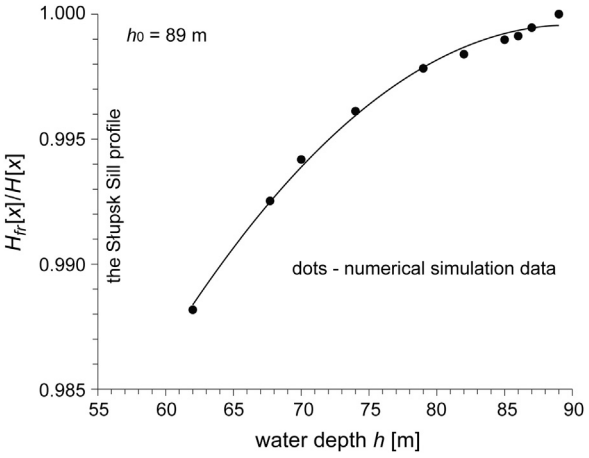

Figure 13 Influence of bottom friction on dynamics of solitary wave height. Solid curves denote the best fitting of simulation data.

Ri. Let the basic state consist steady, shearing flow with dominated horizontal flow. The governing equation for such flow is the Taylor–Goldstein equation for the vertical structure of a perturbation in a stratified flow. The question is now, what is the critical velocity shear below which the flow is stable and above which mixing occurs. This limiting velocity can be determined from the Richardson number (Kundu et al., 2016):

$$Ri(x,z) = \frac{N^2(x)}{\left(\frac{du(x)}{dz}\right)^2}. \tag{72}$$

When $Ri(x, z) > 1/4$ holds everywhere in the domain, the stratified shear flow is stable. On the other hand, criterion $Ri(x, z) < 1/4$ is a necessary but not sufficient condition for instability. In our case for the Richardson number we obtain:

$$Ri(x,z) = \frac{N^2(x)}{\left(C_p(x)(x)\eta(x)\frac{d^2\Phi(x,z)}{dz^2}\right)^2}, \tag{73}$$

where function $\Phi(x, z)$ is given in Eq. (48). For the three-layer vertical density distribution, Eq. (73) is applicable only in the non-uniform layer when $-h_2 < z - h_1$. In the upper uniform layer $(-h_1 \le z \le 0)$ and in the lower uniform layer $(-h \le z \le -h_2)$, the second derivative of function $\Phi(x, z)$ is equal to zero and the Richardson number $Ri(x, z)$ cannot be determined.

Fig. 14 shows distribution of the Richardson number in the non-uniform layer for Station 199 at west slope of the Słupsk Sill when internal wave height ~26 m. The area where the Richardson number $Ri(x, z) < 1/4$ is concentrated under the wave crest and below the upper level of non-uniform layer. This area is rather small, even for very big wave height. The minimum value of the Richardson number drops to about 0.17.

Bogucki and Garrett (1993) argued that for a two-layer system separated by a thin interface with a finite density gradient, the Richardson number in the interface falls below 1/4 if the internal wave height exceeds $2[(h_2 - h_1)\, h_1]^{1/2}$. For such wave height a two-layer system generates mixing by

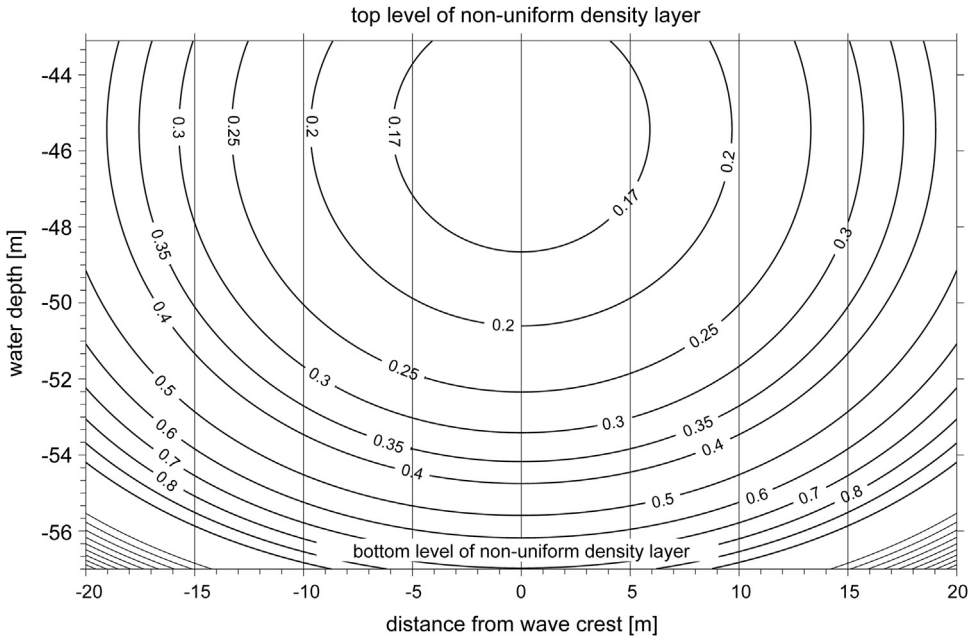

Figure 14 Area of possible shearing instability at the Station 199.

shear instability, and the interface is widening due to passing of internal wave. Bogucki and Garrett (1993), using the concept of interface widening developed a model describing internal wave dissipation and wave height attenuation. However, this model is not applicable as the interface thickness $(h_2 - h_1)$ in our case is not small.

3.3.3. Wave breaking

Numerical calculations by Vlasenko and Hutter (2002) showed that the kinematic instability is responsible for mechanism of strong wave breaking rather than a shearing instability, discussed above. They considered a two-layer system with a vertical fluid stratification. Amplitudes of waves and the bottom parameters were chosen to be close to those observed in the Andaman and Sulu Seas. A proposed breaking criterion for the internal solitary waves for sea bottom slope in the range $0.52^\circ < \beta < 21.8^\circ$ is:

$$\frac{H}{h_b - h_m} \geq \frac{0.8^\circ}{\beta} + 0.4, \tag{74}$$

where H is the maximum displacement at the centre of wave, β is the bottom slope, h_b is the water depth at point of wave breaking and h_m is the depth of an undisturbed position of the interface line. If the water depth on the shelf is less than h_b, a solitary wave breaks before it and penetrates into the shallow water zone, otherwise it passes into the shelf without breaking.

Laboratory experiments by Helfrich and Melville (1986) and Helfrich (1992) showed that wave breaking occurs when normalised maximal wave height $H/(h_b - h_m)$ exceeds 0.4 and does not depends on the bottom slope, i.e.:

$$\frac{H}{h_b - h_m} \geq 0.4. \tag{75}$$

Observations of Lien et al. (2014) on the Dougsha slope (about 0.4°) in the northern South China Sea confirmed that convective breaking of the solitary internal waves, with negative displacement, occurs at $H/(h - h_m) \geq 0.4$, in agreement with the Helfrich's laboratory results.

For typical three-layer density structure, discussed above, determination of the wave breaking criteria is more complicated. First, we apply criterion (75) and assume that depth h_m coincides with a level of the maximum eigenfunction $\Phi(x, z)$, defined by the linear boundary value problem (10) at which $d\Phi(x, z)/dz = 0$. At this level, the isopycnal displacement $\zeta(x)$, given in Eq. (3), has the maximum value.

The second breaking criterion follows from assumption that location of the wave breaking is defined at a position where the horizontal velocity u begins to surpass the phase speed $C_p(x)$ at some level z in water column, i.e.:

$$|u(x, z)| > C_p(x). \tag{76}$$

Numerical simulations showed that for the three-layer density structure, the velocity $|u(x, z)|$ reaches a maximum value close to the sea bottom. Therefore, this value was used for comparison with the phase speed. In Fig. 15 a comparison of the limiting wave heights for both breaking criteria is shown for some Stations on the west slope of the Słupsk Sill, starting from deeper water in the Bornholm Basin and going easterly up to the Słupsk Sill. At the deeper section of the slope, up to Station 193, criterion (76) requires much bigger wave height $H(x)$ than criterion (75). For smaller depths (from Section 193 till Section 199), waves break after reaching criterion (76) and before criterion (75) is satisfied. It should be noted that these results are based on the numerical simulation for real bathymetry and experimental density stratification. However, due to lack of the experimental data on the wave height, these conclusions should be taken only as some estimations of the real breaking process.

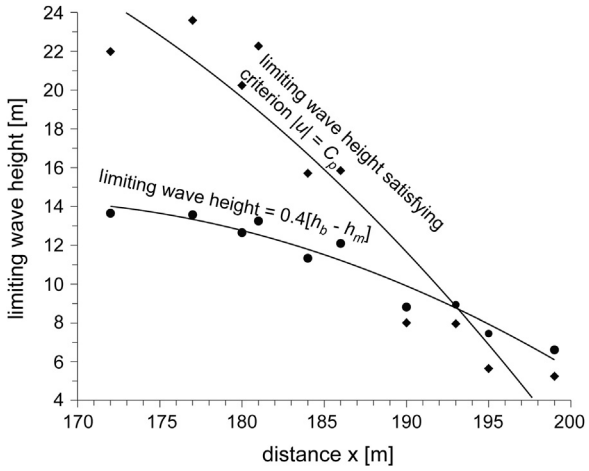

Figure 15 Comparison of two breaking criteria for the west slope of the Słupsk Sill. Solid curves denote the best fitting of simulation data.

4. Conclusions

In this paper, dynamics of the internal cnoidal and solitary waves propagating on horizontally inhomogeneous shallow water is studied. For slowly varying background environment (water depth and density stratification), the theoretical formulae for the wave height and wave shape parameters are derived in an explicit forms, based on the concept of the conservation of energy flux with various energy dissipation terms.

The numerical simulations were applied for the southern Baltic Sea, along the transect from the Bornholm Basin, through the Słupsk Sill and Słupsk Furrow to the Gdańsk Basin. An increase of wave height and decrease of the phase speed in shallowing water depth was illustrated. The bottom friction has only negligible influence on the dynamics of internal waves, while the shearing instability may be important only for very large wave heights. The area of the possible instability, expressed in terms of the Richardson number Ri, is very small and restricted to an area within the non-uniform density layer, close to the upper uniform layer. The kinematic breaking criteria, suggested by Helfrich and Vlasenko and Hutter, have been examined and critical internal wave heights for the three-layer density structure have been determined.

Acknowledgments

This work has been supported by the Programme *Natural and antropogenic variability of the Baltic Sea environment* of the Institute of Oceanology of the Polish Academy of Sciences. I am thankful to the reviewers for their suggestions and comments.

References

Abramowitz, M., Stegun, I.A., 1975. Handbook of Mathematical Functions with Formulas, Graphs, and Mathematical Tables. Dover Publ., New York, 1075 pp.

Bogucki, D., Garrett, Ch., 1993. A simple model for the shear-induced decay of an internal solitary wave. J. Phys. Oceanogr. 23 (8), 1767–1776.

Gill, A.E., 1982. Atmosphere-Ocean Dynamics. Academic Press, New York, 662 pp.

Gradshteyn, I.S., Ryzhik, I.M., 1965. Tables of Integrals, Series and Products. Academic Press, New York, 860 pp.

Grimshaw, R., Guo, Ch., Helfrich, K., Vlasenko, V., 2014. Combined effect of rotation and topography on shoaling oceanic internal solitary waves. J. Phys. Oceanogr. 44 (4), 1116–1132.

Grimshaw, R., Pelinovsky, E.N., Talipova, T., Kurkin, A., 2004. Simulation of the transformation of internal solitary waves on oceanic shelves. J. Phys. Oceanogr. 34 (1), 2774–2791.

Helfrich, K.R., 1992. Internal solitary wave breaking and run-up on a uniform slope. J. Fluid Mech. 243, 133–154.

Helfrich, K.R., Melville, W.K., 1986. On long nonlinear internal waves over slope-shelf topography. J. Fluid Mech. 167, 285–308.

Holloway, P.E., 1994. Observations of internal tide propagation on the Australian North West Shelf. J. Phys. Oceanogr. 24, 1706–1716.

Holloway, P.E., 1996. A numerical model of internal tides with application to the Australian North West Shelf. J. Phys. Oceanogr. 26, 21–37.

Korteweg, D.J., de Vries, G., 1895. On the change of form of long waves advancing in a rectangular canal, and on a new type of stationary waves. Phil. Mag. J. Sci. 39, 422–443.

Krauss, W., 1966. Interne Wellen. Gebruder Borntraeger, Berlin, 248 pp.

Kundu, P.K., Cohen, I.M., Dowling, D.R., 2016. Fluids Mechanics, sixth edition. Elsevier, Amsterdam, 921 pp.

Kurkina, O., Talipova, T.G., Pelinovsky, E.N., Soomere, T., 2011. Mapping the internal wave field in the Baltic Sea in the context of sediment transport in shallow water. J. Coast. Res. 64, 2042–2047.

Lien, R.C., Henyey, F., Ma, B., 2014. Large-amplitude internal solitary waves observed in the Northern South China Sea: properties and energetics. J. Phys. Oceanogr. 44 (4), 1095–1115.

Massel, S.R., 1989. Hydrodynamics of Coastal Zones. Elsevier, Amsterdam, 336 pp.

Massel, S.R., 2012. Tsunami in coastal zone due to meteorite impact. Coastal Eng. 66, 40–49.

Massel, S.R., 2015. Internal Gravity Waves in the Shallow Seas. GeoPlanet: Earth and Planetary Sciences. Springer Int. Publ, Switzerland, 163 pp.

Miles, J.W., 1981. The Korteweg-de Vries equation: a historic essay. J. Fluid Mech. 106, 131–147.

Pelinovsky, E.N., Shavratsky, S.Kh., 1976. Propagation of nonlinear internal waves in an inhomogeneous ocean. Izv. Atmos. Ocean. Phys. 12 (1), 41–44.

Pelinovsky, E.N., Stepanyants, Yu., Talipova, T.G., 1994. Modelling of the propagation of nonlinear internal waves horizontally inhomogeneous ocean. Izv. Atmos. Ocean. Phys. 30 (1), 79–85.

Piechura, J., Beszczyńska-Möller, A., 2004. Inflow waters in the deep regions of the southern Baltic Sea — transport and transformations. Oceanologia 46 (1), 113–141.

Talipova, T.G., Pelinovsky, E.N., Kouts, T., 1998. Kinematic characteristics of an internal wave field in the Gotland Deep in the Baltic Sea. Oceanology, Translated from Okeanologiya 38, 33–42.

Vlasenko, V., Hutter, K., 2002. Numerical experiments on the breaking of solitary internal waves over a slope-shelf topography. J. Phys. Oceanogr. 32 (6), 1779–1793.

Whitham, G.B., 1974. Linear and Nonlinear Waves. Wiley, New York, 636 pp.

Oceanologia (2016) 58, 71—89

Available online at www.sciencedirect.com

ScienceDirect

journal homepage: www.elsevier.com/locate/oceano

ORIGINAL RESEARCH ARTICLE

An integrated wave modelling framework for extreme and rare events for climate change in coastal areas — the case of Rethymno, Crete☆

Vasiliki K. Tsoukala [a,*], Michalis Chondros [a], Zacharias G. Kapelonis [b], Nikolaos Martzikos [a], Archodia Lykou [c], Kostas Belibassakis [b], Christos Makropoulos [c]

[a] *Laboratory of Harbor Works, National Technical University of Athens, Athens, Greece*
[b] *School of Naval Architecture and Marine Engineering, National Technical University of Athens, Athens, Greece*
[c] *Laboratory of Hydrology & Water Resources Utilization, National Technical University of Athens, Athens, Greece*

Received 23 July 2015; accepted 8 January 2016
Available online 29 January 2016

KEYWORDS
Climate change;
Wave run-up;
Wave overtopping;
Storm events;
Coastal flooding

Summary Coastal floods are regarded as among the most dangerous and harmful of all natural disasters affecting urban areas adjacent to the shorelines. Rapid urbanization combined with climate change and poor governance often results in significant increase of flood risk, especially for coastal communities. Wave overtopping and wave run-up are the key mechanisms for monitoring the results of coastal flooding and as such, significant efforts are currently focusing on their predicting. In this paper, an integrated methodology is proposed, accounting for wave overtopping and wave run-up under extreme wave scenarios caused by storm surges. By taking advantage of past and future climatic projections of wind data, a downscaling approach is proposed,

☆ The research leading to these results has received funding from the European Union Seventh Framework Programme (FP7/2007-2013) under Grant agreement n° 603663 for the research project PEARL (Preparing for Extreme And Rare events in coastaL regions). The research and its conclusions reflect only the views of the authors and the European Union is not liable for any use that may be made of the information contained herein.

* Corresponding author at: Laboratory of Harbor Works, School of Civil Engineering, NTUA, 5, Iroon Polytechniou St., 15780 Zografou, Greece. Tel.: +30 693 246 0540; fax: +30 210 772 2372.
E-mail addresses: vtsouk@hydro.civil.ntua.gr (V.K. Tsoukala), chondros@hydro.ntua.gr (M. Chondros), zkapel@central.ntua.gr (Z.G. Kapelonis), nmartzikos@central.ntua.gr (N. Martzikos), alykou@central.ntua.gr (A. Lykou), kbel@fluid.mech.ntua.gr (K. Belibassakis), cmakro@chi.civil.ntua.gr (C. Makropoulos).

Peer review under the responsibility of Institute of Oceanology of the Polish Academy of Sciences.

ELSEVIER Production and hosting by Elsevier

http://dx.doi.org/10.1016/j.oceano.2016.01.002

utilizing a number of appropriate numerical models than can simulate the wave propagation from offshore up to the swash zone. The coastal zone of Rethymno in Greece is selected as a case study area and simulations of wave characteristics with the model SWAN for the period 1960–2100 in the offshore region are presented. These data are given as boundary conditions to further numerical models (MIKE21 PMS and HD) in order to investigate the spatial evolution of the wave and the hydrodynamic field in intermediate and shallow waters. Finally, the calculated wave height serves as input to empirical formulas and time dependent wave propagation models (MIKE21 BW) to estimate the wave run-up and wave overtopping (EurOtop). It is suggested that the proposed procedure is generic enough to be applicable to any similar region.

1. Introduction

In recent years research efforts from several disciplines have focused on the long-term prediction of climate change and its effects, including prediction of wind and wave climate changes, intensity and frequency of rainfalls as well as changes in temperature and increase in sea level. This paper focuses on the effects of climate change on coastal zones and specifically examines the occurrence of coastal floods under climate change scenarios.

Coastal floods are complex phenomena influenced by a series of factors including the bathymetry of sea bottom, existing port and coastal works, erosion and sea level rise phenomena geometry of the urban environments (e.g. roads, buildings, drainage systems, etc.). Recent research has contributed to the development of useful tools to predict and calculate the causes of coastal flood events (Kundzewicz, 2014) arising from e.g. storms and storm surges (Anselme et al., 2011; Breilh et al., 2014; Long et al., 2014), sea level rise (Warner and Tissot, 2012; Wiśniewski and Wolski, 2011) and tsunami (McCabe et al., 2014). These phenomena eventually result in wave overtopping and wave run-up (Laudier et al., 2011; Lynett et al., 2010; Matias et al., 2012; Plant and Stockdon, 2015; Senechal et al., 2011; Smith et al., 2012; Stockdon and Holman, 2011) on shore and thus result in coastal flooding. During the last years the impacts of climate change on coastal flooding and on the stability and operation of ports and coastal defense structures has risen in attention, looking specifically on disaster risk resilience (Karambas, 2015; Koftis et al., 2015; Kokkinos et al., 2014).

Moving closer to numerical modelling of coastal flood components discussed above, Chini and Stansby (2012) presented a modelling system for determining wave overtopping discharge depending on water level and nearshore wave height. Kokkinos et al. (2014) assessed wave run-up and storm surge in the Aegean Sea using large wave data characteristics proving the vulnerability to flooding for the examined coastal areas. Gallien et al. (2014) took advantage of flood field observations in order to evaluate the accuracy of two urban flood prediction models. The first one, termed static, compares water level to land elevation while the second one, and more sophisticated, is based on a hydrodynamic model using time-dependent overtopping rates and estimating the overland flow.

The issue of flood risk management in coastal regions has been on the research agendas of several national and EU funded projects (Oumeraci et al., 2015; RISC-KIT, 2015). The present research, undertaken within the framework of the project PEARL (Preparing for Extreme And Rare events in coastaL regions) is funded under the 7th Framework Programme for Research of the European Union (FP7/2007-2013). The main goal of PEARL is to develop adaptive, socio-technical risk management measures and strategies for coastal communities against extreme hydro-meteorological events minimizing social, economic and environmental impacts and increasing the resilience of coastal regions in Europe (Makropoulos et al., 2014, 2015).

The approach presented in this paper is an integrated methodology for long-term prediction of climate changes and their respective impacts on coastal zones, starting from the wind climate change ending with the calculation of wave overtopping and run-up. This is achieved by the combination and cooperation of various numerical models for predicting and simulating the related natural phenomena. The case study in which the proposed methodology is demonstrated is the coastal region of Rethymno in the island of Crete, Greece. The results can be used in future plans of local authorities in order to take appropriate measures to inform the residents and to support optimum design of future protection works. Due to the methodology's generic nature, it can be applied to any coastal region. Section 2 presents the complexities of the selected area of research (Rethymno) and introduces the framework of the methodology by specifying the chain of numerical models implemented. Section 3 highlights the main assumptions and the available data used for past and future projections of local wave climate data obtained for SWAN model (Booij et al., 1999; Ris et al., 1999), a third-generation wave model that computes random, short-crested, wind generated waves in open sea, coastal regions and inland waters. With offshore wave data available, definition and categorization of the storm events is accomplished in order to distinguish the severity of each event. Registered flood events in the port area of Rethymno, as reported by residents' testimonials, are categorized according to wind measurements conducted by the National Weather Service. This action verifies the storm characteristics arising from the suggested approach. The simulations are then fed, as boundary conditions, into a wave propagation model (Section 4) to simulate the wave characteristics and the hydrodynamic field nearshore (MIKE21 PMS, HD (DHI, 2007a,b,c)). Subsequently the characteristic wave height, as transformed through various physical processes (shoaling, refraction, breaking, etc.), is used to simulate wave run-up with an improved Boussinesq-type model MIKE21BW (DHI,

2007a,b,c), and to estimate the wave overtopping (EurOtop, 2007) in selected reaches along the coastal zone of Rethymno (Section 5). Section 6 discusses the methodology and presents the main conclusions, important results obtained and suggested areas for further investigation.

2. Methodology

2.1. Rethymno site description

The area under study (Fig. 1) is located at the Prefecture of Rethymno, which is one of the four Prefectures of Crete in Greece. Rethymno city's population stands at 32,468 inhabitants, which characterize it as the third most populous urban area in Crete. Rethymno is the centre of commercial, administrative and cultural activities of the homonymous Regional Unit where most of the human activities are being developed along the coastline of the harbour area. The area, where the methodology will be tested, includes the Port of Rethymno and the adjacent coastal area (a total area of about 14 km^2 with a coastline length of approximately 8 km).

Flooding has always been a serious problem for Rethymno. Major flood events have been encountered throughout the years, resulting in serious damages mainly in the Old Town of Rethymno and the east low-lying areas (Figs. 2—5). Furthermore, changes in wind conditions — potentially due to climatic changes — have resulted in more frequent occurrence of storm events. Extreme weather conditions of strong winds resulting in the creation of storm waves are combined sometimes with flash floods from ephemeral streams. Dire consequence of the extreme waves formulation were the violent wave overtopping along the windward breakwaters of the harbour, as shown in Fig. 5, threatening the stability of breakwaters and port facilities as well as the safety of human population. An additional severe result of wave overtopping is the flood inundation of the harbour's surface area and the surrounding roads. The quantities of seawater (see figure) that penetrates from the west (Parking area) during those storm events, overflows the harbour's surface area, as well as the wider coastal area, causing disruption to loading and unloading operations, damage to the port facilities and the cargo, traffic problems and damage to coastal shops and restaurants. The adjacent recreational beaches are also exposed to erosion, spoiling the coastal site and affecting the tourism's contribution to local economy.

The combined occurrence of extreme hydro-meteorological events poses a real threat to Rethymno's community and emphasizes the need for specific actionable roadmaps that will enhance the existing infrastructure and operational strategies against the danger of flood by helping stakeholders to identify areas that are sensitive to floods and also to define efficient flood management strategies including engineering, environmental and socio-economic measures for Rethymno.

2.2. Description of methodology followed and numerical models chain

The SWAN model is initially used to simulate the offshore wave characteristics (directional spectrum) taking into account the changes of wind climate, followed by the MIKE21 PMS model which is applied for the transformation of the offshore information to shallower regions, up to the coast. Finally, a combination of MIKE21 BW, EurOtop and empirical formulas are utilized for the computation of wave overtopping

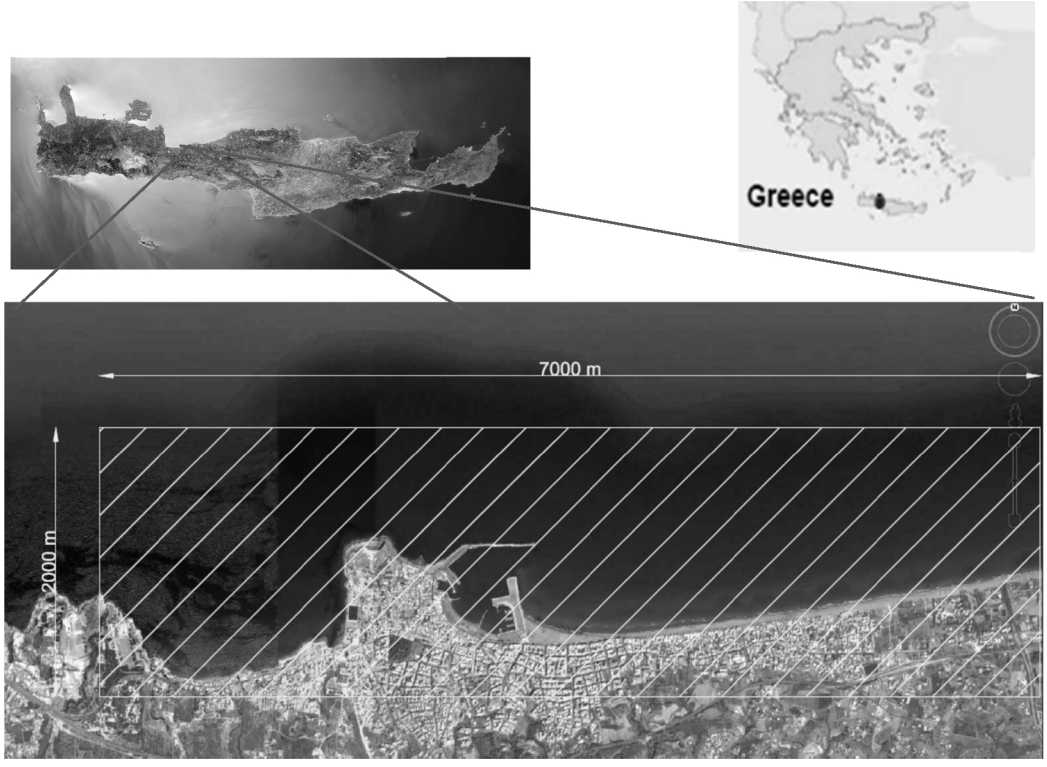

Figure 1 Rethymno city, Crete, Greece and area of interest.

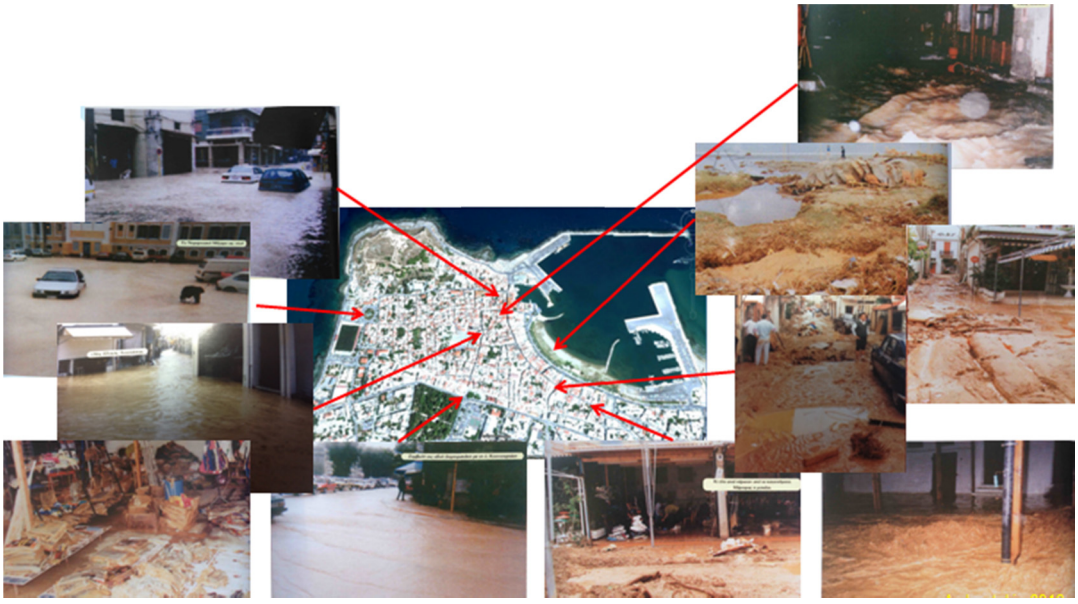

Figure 2 Historic flood in Rethymno, October 28th 1991 (Archontakis, 2013).

and run-up. The necessary wave condition at the offshore boundary of the local geographical area were derived from a downscaling approach, based on the transformation of global wind fields carrying the effect of climate change and affecting nearshore wave conditions. The latter are subsequently exploited for calculating the changes of wave overtopping and run-up which ultimately causes inland flooding of the coastal region of Rethymno's area.

The offshore wave simulations utilize a 3-level SWAN-based scheme (Athanassoulis et al., 2014) illustrated in

Figure 3 Recent floods at the harbour area of Rethymno (2010—2013).

Figure 4 Damages of the base of windward wave breakwater: (a) previous damages, photograph taken on January 4th, 2014; (b) new damages after structural repairs, photograph taken on January 14th, 2015.

Figure 5 Penetration of seawater through overtopping to the wider area of port facilities and debris from the windward wave breakwater damages.

Fig. 6 which was developed in the framework of Thales project CCSEAWAVS (Prinos, 2014) which aimed to estimate the effects of climate change on sea level and wave climate of the Greek seas, the coastal vulnerability and the safety of coastal and marine structures. This simulation scheme uses past and future projections climatic wind fields (also produced in the context of CCSEAWAVS) for the estimation of wave characteristics with resolution 0.2 × 0.2 degrees in the Mediterranean basin (Level 1). These data provide boundary information for repeating the simulation using a finer mesh 0.05 × 0.05 degrees inside an Eastern Mediterranean subsection (Level 2); see Fig. 6. Then, a high-resolution 0.005 × 0.005 degrees mesh is applied in the frames of the present work in the selected coastal region (Level 3). Details of the methodology are described in Athanassoulis et al. (2015). For evaluation purposes, systematic comparisons with results from the operational WAM-Cycle 4 implementation (courtesy of the Atmospheric Modelling & Weather Forecasting Group, University of Athens) were performed.

Within the present work, the Level 3 results of the offshore wave height, period, and direction are used to distinguish the usual incident waves from the storm surges. This is a

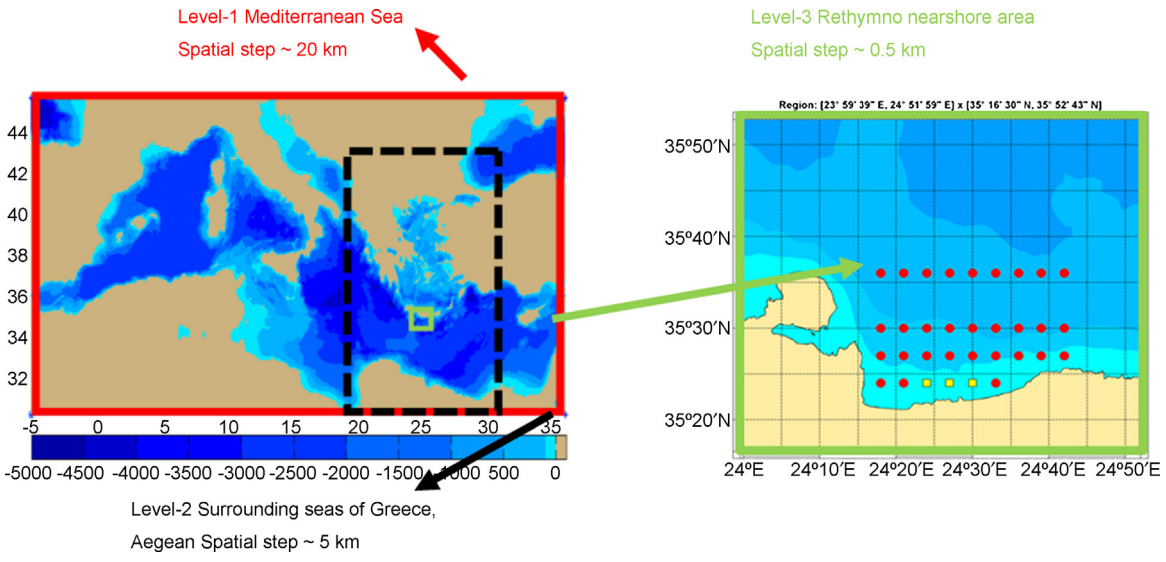

Figure 6 Estimation of offshore wave characteristics using a 3-level downscaling approach.

crucial step of the whole procedure, since the goal of this paper is to predict the extreme values of wave characteristics. The basic idea is to group storms into classes based on similar characteristics in order to apply the desired simulations for each category. Additionally, this will become valuable information for a future research dealing with the evaluation of coastal vulnerability for each class. Thus, many scientists of coastal study have made efforts to this direction. According to Dean and Dalrymple (2004) the destructiveness of a storm surge depends inter alia on its magnitude and duration and the wind-driven waves. Several attempts have been made after the Saffir-Simpson Scale (Saffir, 1977; Simpson, 1979) for storm intensity in the United States where hurricanes are placed in five classes depending on their central pressure, the maximum wind speed and the surge elevation. Halsey (1986) proposed a classification of Atlantic coast extratropical storms based on damage potential index. Dolan and Davis (1992, 1994) developed a classification of extratropical storms, or northeasters for the middle Atlantic coast, where an index of storm power was based on wave height and storm duration. They grouped and ranked the storms into five classes from weak to extreme, analogous to the Saffir—Simpson scale, using an average linkage clustering method. Concerning recent studies in Mediterranean Sea, Mendoza and Jiménez (2006, 2009) and Mendoza et al. (2011) provided a storm classification based on the beach erosion potential in Catalonian Coast and later for the Yucatan Peninsula (Mendoza et al., 2013) taking into consideration the storm energy and using the cluster analysis. The classification adopted here, is one of the most well-documented and it is based on the concept of the energy content (Dolan and Davis, 1992, 1994).

The above results are further exploited as boundary conditions for a coastal region phase-resolving simulation including the Rethymno area by means of a numerical wave model, based on the Parabolic Mild Slope equations (PMS, MIKE21). In this way the offshore wave characteristics are further downscaled in Level 4 taking into account additional local phenomena such as shoaling, refraction, bottom friction and wave breaking that take place in shallower water regions. The latter phenomena are well represented in the fine spatio-temporal mesh of Level 4 (as shown in Section 4, Fig. 16). The output of the above calculation provides subsequently the input to the hydrodynamic module through which the wave-induced current in the near shore area is calculated.

Ultimate step within Level 4 is the implementation of the empirical formulas and the MIKE21 BW wave model, so that computation of wave overtopping and run-up shall be achieved across the coastline. The latter model solves the so-called Boussinesq type equations in the time domain. It also resolves the wave propagation in detail and is best suited for simulation of nonlinear wave interactions, capable of reproducing the wave transformation across an arbitrary profile from intermediate waters up to the shoreline for the study of surf zone and swash zone dynamics. Herein, the 1D version is used to simulate the combination of setup and run-up whereas the empirical formulas are called for comparison. Additionally EurOtop, a widely accepted tool, is utilized incorporating techniques to investigate flood risk and predict wave overtopping at seawalls, breakwaters and other shoreline structures. This approach including the numerical chain is proposed in the present paper and the chart in Fig. 7 summarizes the above procedure in four discrete steps.

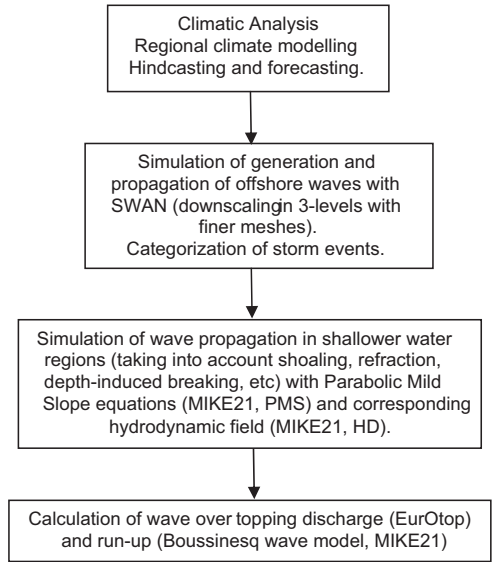

Figure 7 Flow chart depicting the proposed procedure.

Chini and Stansby (2012), as mentioned in Section 1, presented a similar downscaling procedure for determining wave overtopping depending on water level and nearshore wave height from global climate modelling. From offshore conditions to nearshore, waves were simulated using WAM (WAMDI-Group, 1988) and surges were modelled with the continental shelf tide and surge model CS3 (Williams and Flather, 2004). The nearshore wave propagation was achieved by using the third generation wave spectral model TOMAWAC, solving for the conservation of wave action on an unstructured mesh using the finite element method (Benoit et al., 1996). Finally, a neural network approach was used from EurOtop to calculate the overtopping discharge at a specific example of a vertical wall. The present approach provides a more integrated approach, providing results for both wave run-up and overtopping.

3. Projections of past and future wave climate (SWAN)

3.1. Atmospheric variables and climate change scenario

The wind data used as forcing of the SWAN simulation over Rethymno were also one of the outcomes of the CCSEAWAVS project (Velikou et al., 2014). Over the northeast Atlantic and Europe, the regional atmospheric model REMO, which is based on the Europamodel/Deutschland model system (Majewski and Schrodin, 1994), was used in order to get a high resolution atmospheric forcing. Climatic analysis of the Mediterranean and the Greek sea area and eventually estimation of atmospheric variables was achieved by utilizing the RegCM regional model (RegCNET: regional climate network, 2003). Its spatial analysis is 25 km $\times$ 25 km and for the future projections of atmospheric (10 m wind, atmospheric pressure, air temperature) data the model is using the AR4-A1B emission scenario. Past projections for 1960—2000 are based on input from measured carbon dioxide emissions. Enhanced

simulated data in the Greek Sea region have also been derived from the new version of RegCM3_10 regional model, with 10 km × 10 km spatial resolution (Velikou et al., 2014). RegCM3_25 model uses 18 vertical levels on a horizontal 192 × 108 grid and a time step of 60 s. RegCM3_10 model is nested inside the RegCM3_25 model and uses 18 vertical levels on a horizontal 128 × 160 grid and a time step of 30 s.

3.2. Study area, bathymetry and computational grid

The Level 3 SWAN simulation was performed in a rectangular frame with limits 35.3E, 35.7E Latitude and 24.25N, 24.75N Longitude. With a regular resolution of 0.005 × 0.005 degrees for Level 3, the produced computational grid consists of 8181 grid points of which 6471 are wet-points and the rest fall on land. The bathymetry was obtained from the combination of the General Bathymetric Chart of the Oceans database (GEBCO, 2009) and a nautical chart from the Hellenic Navy Hydrographic Service. In particular, the GEBCO database was used for depths higher than 500 m and digitized nautical chart contours for depths lower or equal to 500 m, along with the digitized coastline (Fig. 8).

The distribution of significant wave height, wave peak period and mean wave direction at points n depicted in Fig. 8, for one past (1961–2000) and two bi-centurial future periods (2001–2050, 2051–2100) is shown in Fig. 9. In general, the projected future distributions remain very close to those of the past period. Some weak but noticeable variations are observed during period 2051–2100, with higher occurrence of waves originating from the North sector. Although relatively small, this probability shift towards southward waves can be significant due to the North-facing orientation of Rethymno coast.

The seasonal pattern (mean value for each month) for the same time-periods is illustrated in Fig. 10. The seasonal pattern is similar for the two parameters, which is expected due to the high correlation between wave height and wave period. Mean values for period 2051–2100 are generally equal or higher to that of the other two periods with the exception of 3 months (October–December). The higher mean value during the last period is also noticeable in

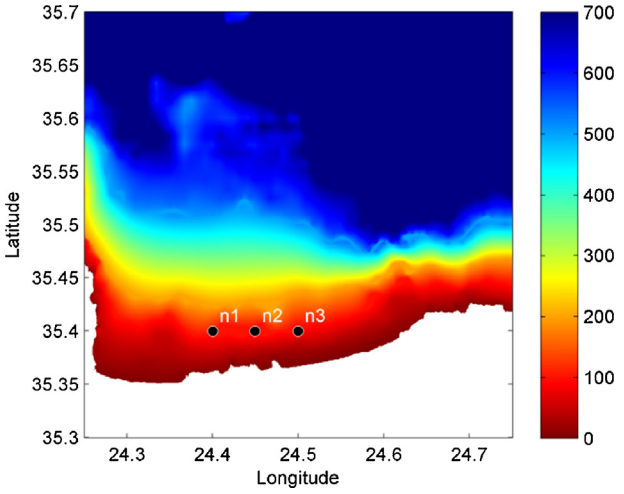

Figure 8 Bathymetric map used for Level 3 simulation.

Fig. 9, where a small reduction of the distribution peak is observed for both the significant wave height and peak period, implying an increased mean value due to the log-normal probability form.

3.3. Categorization of storm surge events, joint probability of significant wave height and period, sea level rise

With offshore wave data available, a definition and categorization of storm events can be derived, in order to treat the storm surges in group and not individually and to link them with respective factors of coastal vulnerability in a future research. This is done by following the definition and identification of the storms through the energy content as proposed by Dolan and Davis (1992). The classification is accomplished into five classes: I – weak, II – moderate, III – significant, IV – severe and V – extreme. The first step before applying this approach is the characterization of the forcing. A storm is defined as the event exceeding a minimum significant wave height (e.g. $H_s > 2$ m) and with a minimum duration of 6 h (Li et al., 2014; Michele et al., 2007). The

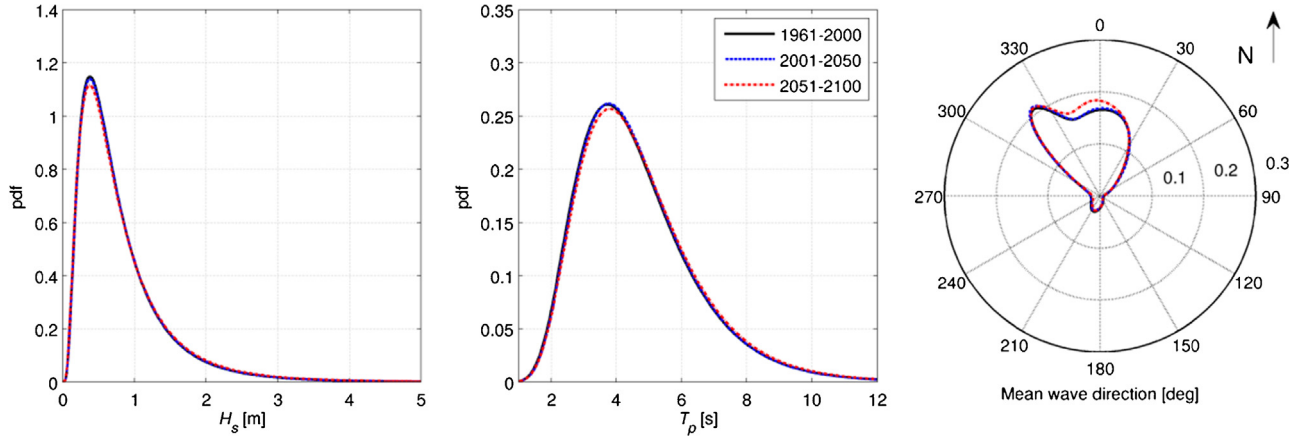

Figure 9 Probability density functions for the significant wave height H_s (left panel), peak wave period T_p (central panel) and mean wave direction (right panel), for three time periods, at points n*i* (*i* = 1–3) (shown in Fig. 8).

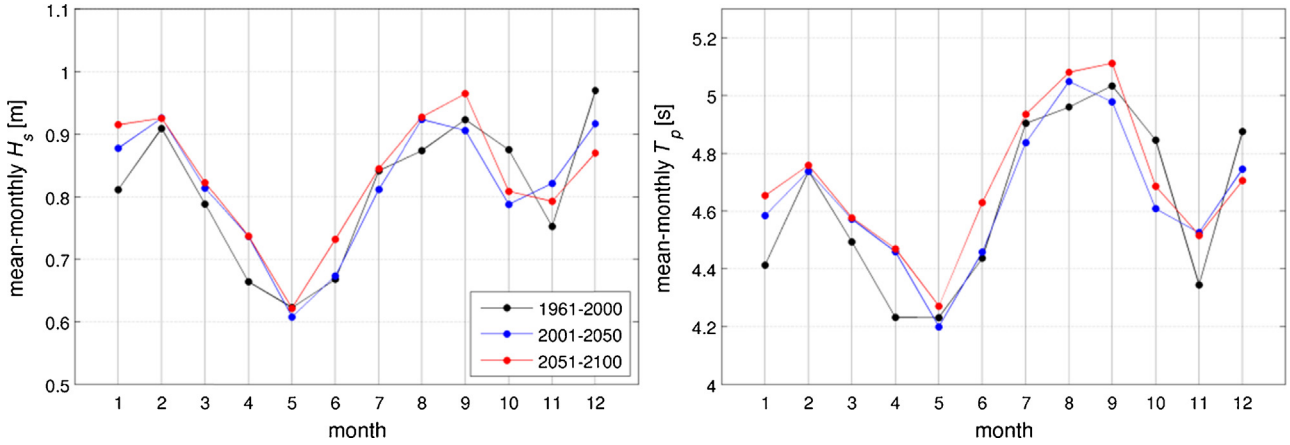

Figure 10 Seasonal pattern of the significant wave height H_s (left panel) and peak wave period (right panel) T_p for three time periods, at points n*i* (i = 1–3) (shown in Fig. 8).

threshold of significant wave height (H_s) is considered to be 2 m in order to describe rare events with only 10% of total wave heights and thus defined as the 90th percentile of the data set (Rangel-Buitrago and Anfuso, 2011). The energy content of each event is then calculated as follows:

$$E = \int_{t_1}^{t_2} H_s^2 \, dt, \tag{1}$$

where (t_1–t_2) is the storm duration and H_s is always greater than H_s threshold.

The above analysis has been divided into two periods: 1960–2000 (past climate) and 2000–2100 (future climate). It has to be noted here that this technique has also been applied by other researchers in regions close to Rethymno (e.g. Chania, Crete Island, Kokkinos et al., 2014). The analysis is done for the North wind direction since it is the dominant one that generates incident waves to the Rethymno coast.

The results of the average wave height, period and duration in n2 grid point, in Fig. 8, for each storm class are given in the following Tables 1 and 2 for the North wind direction and in Tables 3 and 4 for the Northwest wind direction. The extracted results came from n2 and n1 grid points, of Fig. 8, respectively for the two incident directions. Although the result of SWAN program gives an accuracy of 7 decimals for both variables, an accuracy of 1 decimal was selected herein, since it is answered in many engineering applications as well.

Inspection of the below provided results presents that the range of the wave height lies between 2 m (which is the minimum value that has been determined in this paper in order to have a storm event) up to almost 6 m. The specific range appears the same in any storm class which can be attributed to the fact that a storm event can consist of a sequence of small wave heights e.g. 2 or 3 m for long time

Table 1 Storm events for the period 1960–2000 N direction.

North wind direction 1960–2000							
Storm class		H_s range [m]	T_p range [s]	Average H_s [m]	Average T_p [s]	Average duration [h]	No. of events
I	Weak	2.0–4.6	6.2–9.4	2.5	7.7	14.20	318
II	Moderate	2.0–5.7	6.5–10.0	2.9	8.1	34.50	27
III	Significant	2.0–4.6	7.5–9.6	3.6	8.1	44.25	4
IV	Severe	2.0–5.6	6.7–10.7	3.3	8.3	72.50	6
V	Extreme	–	–	–	–	–	0

Table 2 Storm events for the period 2000–2100 N direction.

North wind direction 2000–2100							
Storm class		H_s range [m]	T_p range [s]	Average H_s [m]	Average T_p [s]	Average duration [h]	No. of events
I	Weak	2.0–5.3	6.4–10.1	2.5	7.7	14.13	823
II	Moderate	2.0–5.0	6.7–9.9	2.7	8.0	42.03	94
III	Significant	2.0–6.0	6.9–10.3	3.0	8.2	61.84	13
IV	Severe	2.0–5.4	6.4–10.0	3.2	8.2	81.38	8
V	Extreme	2.0–5.0	7.8–9.7	4.2	9.1	72.00	1

Table 3 Storm events for the period 1960–2000 NW direction.

Northwest wind direction 1960–2000							
Storm class		H_s range [m]	T_p range [s]	Average H_s [m]	Average T_p [s]	Average duration [h]	No. of events
I	Weak	2.5–4.6	6.2–9.4	2.5	7.7	11.40	10

Table 4 Storm events for the period 2000–2100 NW direction.

North wind direction 2000–2100							
Storm class		H_s range [m]	T_p range [s]	Average H_s [m]	Average T_p [s]	Average duration [h]	No. of events
I	Weak	2–4.6	6.2–9.4	2.5	7.7	10.55	33
II	Moderate	2–5.7	6.5–10.0	3.0	8.1	39.00	1

duration or in a sequence of large wave heights for a small duration. Besides, during the evolution of every storm event, small or large wave heights can appear. Obviously, by climbing storm class there is a tendency of the average wave heights and periods to be increased. As could be observed in Table 1 the upper limits of H_s and T_p ranges are greater in class IV in comparison with class III. The average values though remain smaller. This can be attributed to the small population of storm events for both categories.

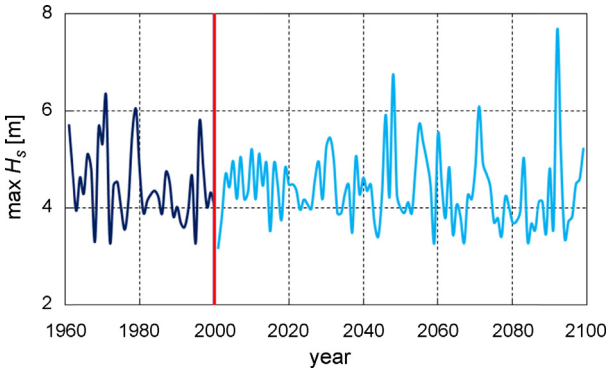

Figure 11 Maximum wave height (max H_s) per year for the two periods (1960–2000, blue line and 2000–2100, light blue line). (For interpretation of the references to colour in this figure legend, the reader is referred to the web version of this article.)

In order to gain a more integrated view of the future wave climate in the offshore region of Rethymno, the maximum wave height (max H_s) per year for the two periods is also depicted in Fig. 11 as obtained by the wave data in n2 grid point. One can observe that the maximum wave height is close to 8 m. However, this value appears in different wind direction than the North one which is of the greatest interest in the present paper. The maximum wave height coming from North was calculated at 5.95 m as presented in the above table.

Additionally the joint distributions of significant wave height H_s and peak wave period T_p at n2 grid point of Fig. 8, normalized to the respective average values of them (H_m and T_m) are given for the two examined different periods: 1960–2000 in Fig. 12 and 2000–2100 in Fig. 13 respectively. It is observed, through the high values of the corresponding correlation factor $r(H_s, T_p)$ that these two wave parameters are well correlated for extreme wave

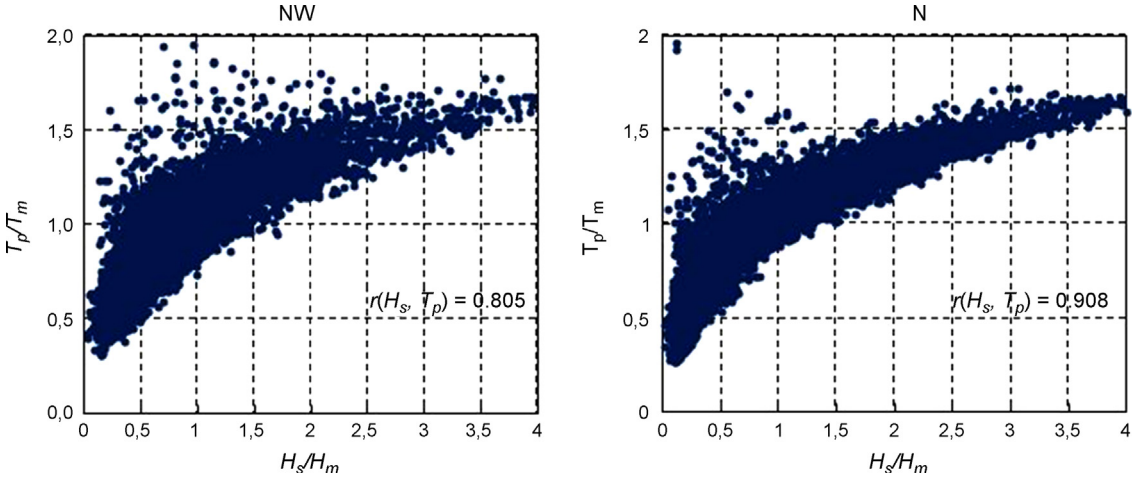

Figure 12 Scatter plots of normalized significant wave heights (H_s/H_m) and peak periods (T_p/T_m) for period 1960–2000 and for NW and N wind directions.

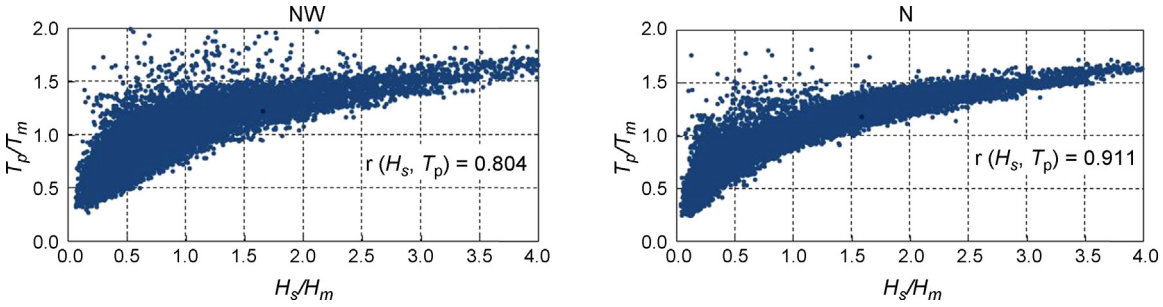

Figure 13 Scatter plots of normalized significant wave heights (H_s/H_m) and peak periods (T_p/T_m) for period 2000–2100 and for NW and N wind directions.

heights. Full dependence between extreme significant wave height and peak wave period is therefore assumed.

3.4. Observed storm surge and flood events

Recorded historical wave overtopping events (Galanis, 2010) include events that developed mainly in the port area, whose respective dates are presented in Table 5.

In order to distinguish the class of each of the above storm events the following procedure is applied. Firstly, the fetch effective F_{eff}, is calculated through CEM (2008) for the two dominant directions of wind i.e. North and Northwest, yielding to 281.8 km and 224.5 km respectively. The next step takes advantage of the continuous measurements of wind velocity and wind direction in the area of Rethymno every 3 h by the National Weather Service. These field measurements hold from 1958 up to date. However, the manageable data is limited until the year 2008. Thus, only the first three events of Table 5 can be categorized. In Figs. 14–16 the measured wind characteristics are illustrated.

The mean values of the above events are summarized in Table 6. It has to be mentioned that 360° denote the north wind direction, hence the first case is included to the northwest direction while the rest in the north.

Finally, having in mind the F_{eff} and the wind speed, along with the respective duration, the developed characteristic of wave e.g. wave height H_s and peak wave period T_p were calculated using the SMB wave prediction method (Bretschneider, 1952, 1958). Each storm event is then classified by applying Eq. (1). The results are given in Table 7.

As it is observed, the reported storm events are up to the third (III) class for north wind direction and to the first (I) for the northwest, proving that the above classification respond satisfactorily to reality. However, the storm class that derived herein are five (Table 1) and two respectively (Table 3) for the two directions, but it should be kept in mind that the above flood events, reported from the residents, are limited and indisputably cannot capture all the events that took place.

Table 5 Dates of flood events in the port area of Rethymno.

No.	Date	Year
1	20/11–21/11	1964
2	05/10–07/10	1989
3	28/11–29/11	2000
4	11/12	2010
5	28/02	2012
6	03/12	2013
7	11/12	2013

4. Numerical simulation of wave and hydrodynamic field

The bathymetry of Rethymno coastal area is constructed into a grid (Fig. 17) with dimensions 5.5 km × 6.2 km in x and y axes respectively. The spatial step is chosen $dx = dy = 5$ m. The bathymetry has been rotated counter clockwise at 90° due to requirements of MIKE21 PMS.

The average values of wave height and period of each storm class are adopted as input data and numerical simulations with MIKE21 PMS are carried out to estimate the spatial evolution of these quantities in the whole coastal area. Consequently, the resulting radiation stresses serve as input to the hydrodynamic module with MIKE21 HD to investigate the spatial evolution of the velocity. The results are depicted in Figs. 18 and 19 for the spatial distribution of significant wave height and in Figs. 20 and 21, for the hydrodynamic field for the total of five storm categories (I–V) in case of north wind direction and for the two storm categories in case of northwest wind direction (I, II). Furthermore, simulations have been carried out for the maximum incident wave as derived by the above analysis. The wave height of it equals to $H_s = 6.0$ m and the peak period is $T_p = 10$ s. These results are also presented in Figs. 18 and 20 for the spatial distribution of significant wave height and the hydrodynamic field respectively.

As it is obvious, from the above figures, one can notice the effect of refraction, as waves approaching the shallower region and the mean wave direction (represented by arrows) tend to be perpendicular to the coastline. Furthermore, diffraction phenomenon is satisfactorily simulated inside the port basin (denoted e.g. by red circle in the bottom, Fig. 20) providing the respective wave disturbance in that area for each storm class intensity. The coloured contours give information for the spatial evolution of wave height and for the breaking line that moves away from the shoreline as the storm class increase since the incident wave height increase as well. In any scenario of the above eight (for each storm class – including the maximum occurred incident wave $H_s = 6.0$ m and for each direction), the magnitude of wave

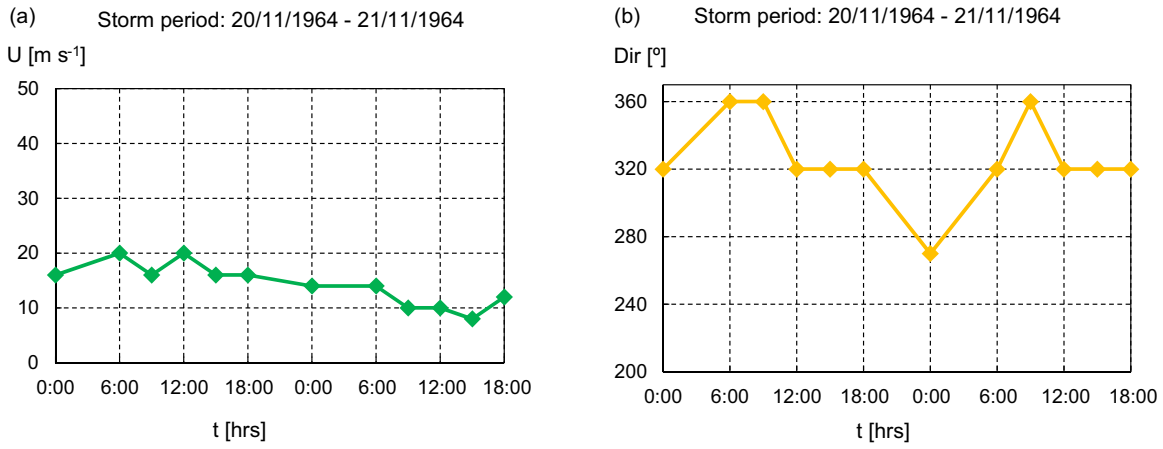

Figure 14 Wind characteristics: (a) wind velocity and (b) wind direction for Case No. 1 of Table 5.

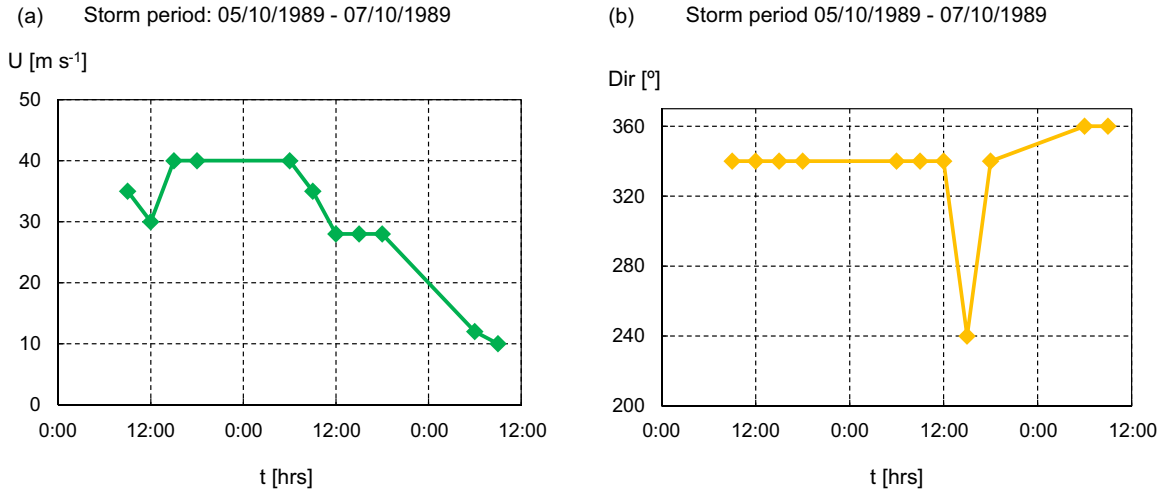

Figure 15 Wind characteristics: (a) wind velocity and (b) wind direction for Case No. 2 of Table 5.

heights in the area of the windward breakwater of the port is significantly greater than the respective approaching the shoreline. This was expected since the energy dissipation from depth-induced breaking in the first case is smaller than the second one. It will be shown in the next section that information about the wave height in this area, calculated by PMS, is essential for the proper calculation of overtopping.

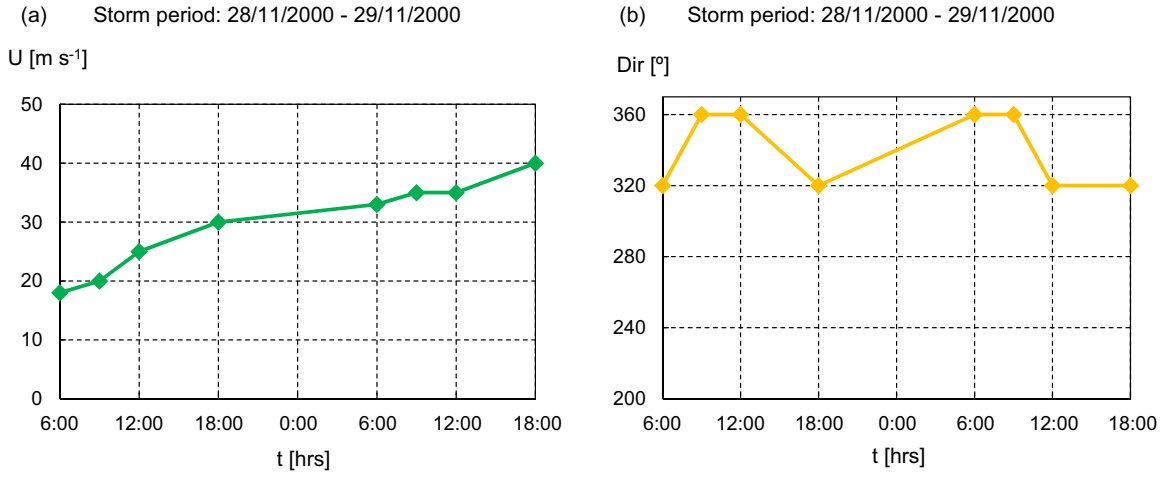

Figure 16 Wind characteristics: (a) wind velocity and (b) wind direction for Case No. 3 of Table 5.

Table 6 Mean characteristics of storm events as extracted by field measurements.

No.	Year	Wind velocity [m s^{-1}]	Wind direction [°]	Duration [h]
1	1964	7.4	326	42
2	1989	15.3	335	48
3	2000	15.2	340	36

Table 7 Classification of storm events by field measurements.

No.	Wind direction	H_s [m]	T_p [s]	Storm class
1	NW	1.6	6.6	I
2	N	3.8	7.8	III
3	N	3.8	7.8	II

As the storm intensity increases, the wave heights increase in the whole domain, generating strongest currents. The basic conclusion of the above figures depicting the hydrodynamic field, lies on the illustration of the most vulnerable sub areas where the magnitude of velocity components increase. Thus, in the sub area of the port and the area west of it, (denoted e.g. by red circles in the bottom above, Fig. 20) strongest movement of the currents are observed. This is in accordance with the physical observations where the most flood events are taking place in the respective locations of Rethymno as shown in Figs. 2—5. Another interesting point, that was expected and it is well simulated by the hydrodynamic model, is the generation of more dominant long-shore currents in the case of northwest direction, since the oblique wave incidence lead to greater values of radiation stresses (denoted e.g. by red circle in the right of Fig. 21). Unfortunately, these valuable results of the hydrodynamic field certainly affecting run-up and overtopping cannot be incorporated in the majority of numerical models, capable of predicting these processes, as boundary conditions, especially in one horizontal dimension models. Nonetheless, the simulation of spatial evolution of current velocities in one hand give a more integrated picture of the physical processes taking part in

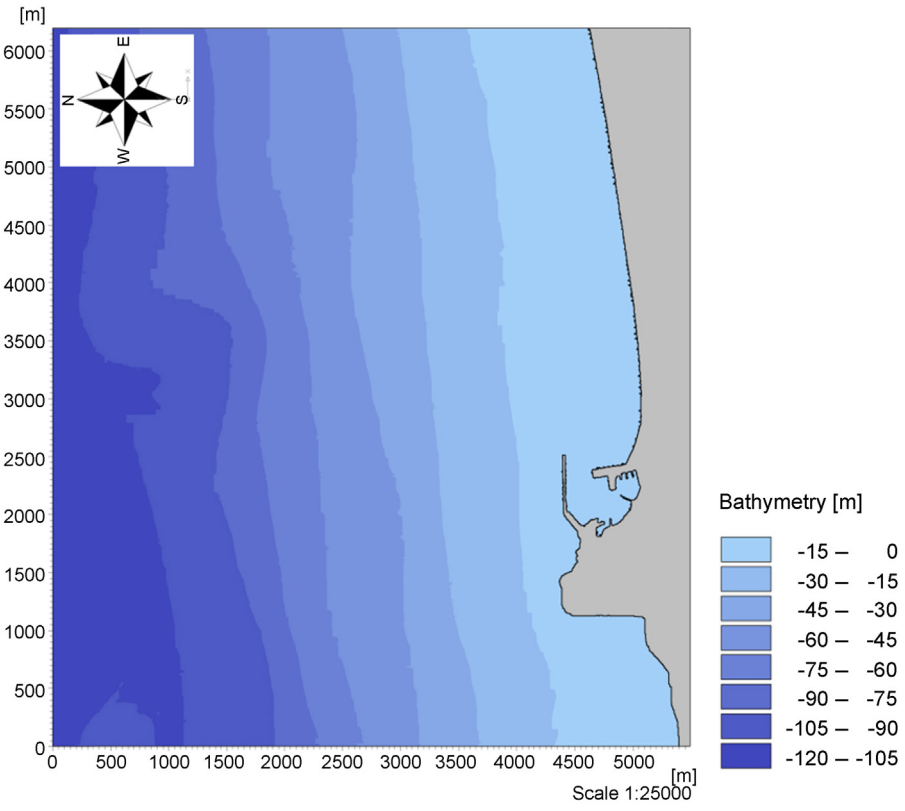

Figure 17 Numerical grid of Rethymno's bathymetry.

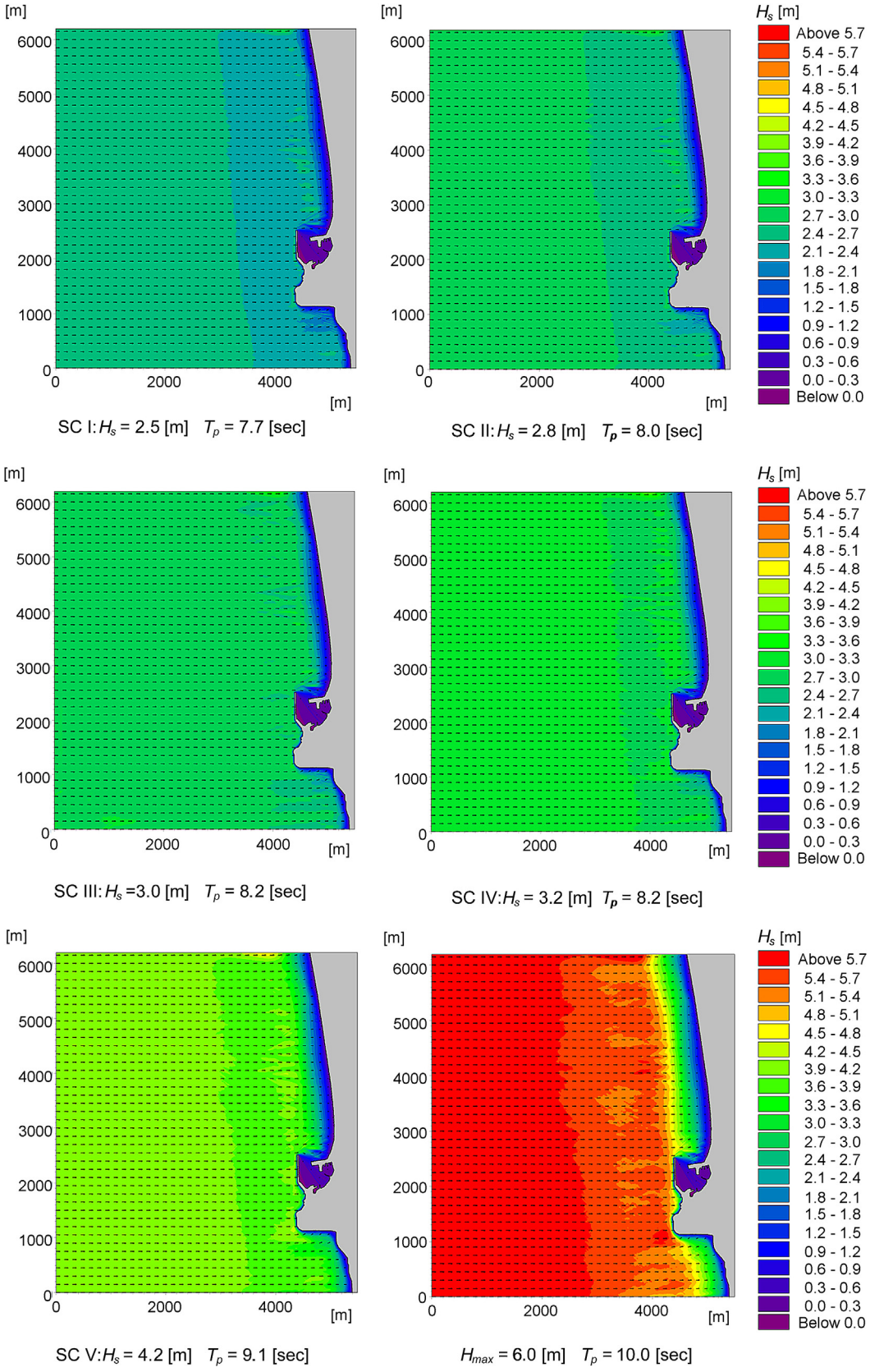

Figure 18 Spatial distribution of significant wave height (H_s) for storm classes (SC) I to V and for the maximum occurred incident wave H_{max} = 6.0 m for the north direction. Arrows denote the mean wave direction. The colour legend of wave height contours is identical for all classes.

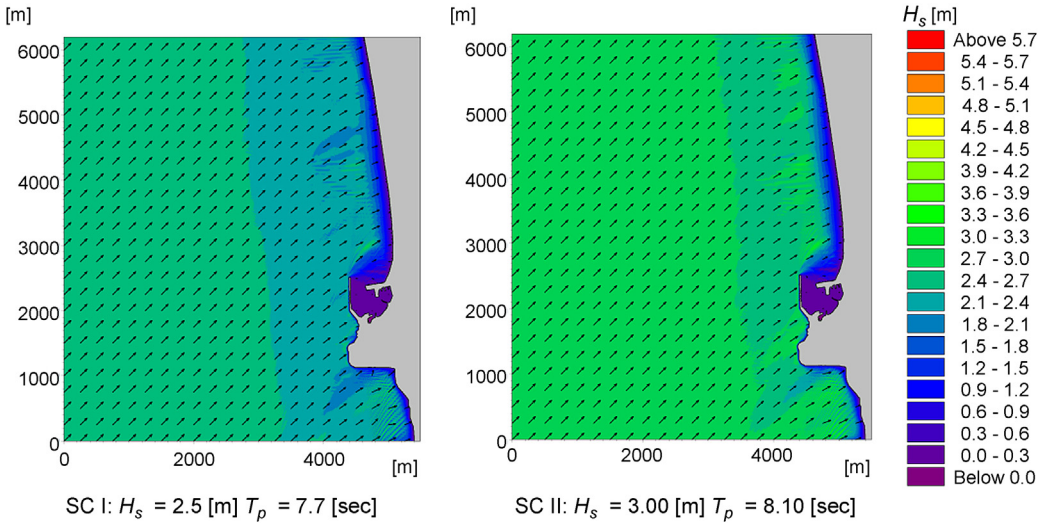

Figure 19 Spatial distribution of significant wave height (H_s) for storm classes (SC) I and II for the northwest direction. Arrows denote the mean wave direction.

the real field and cannot be avoided and on the other hand it is necessary for prediction of sediment transport in the area, which is a work on progress.

5. Wave overtopping and run-up

By taking advantage of the simulated wave propagation into shallower water regions and the corresponding nearshore wave characteristics, the wave overtopping and run-up can be estimated at any desired profile of the whole field under study.

5.1. Bathymetric profiles and chosen section

The wave run-up is calculated at two bathymetric profiles, arbitrarily chosen but representative of the mean profile of sea bottom in the area of interest, east and west of the port (Fig. 22) with a mean bottom slope equals to 3%. While the overtopping is calculated at section A-A′ of the port (Fig. 23) which is a characteristic section of the current port constructions, consisting of an upwind breakwater and a vertical quay wall in the leeside, it must be underlined that the proposed methodology can be proved really useful for redesigning future protection projects since the estimation of overtopping and run-up is available, with no extra time or computational cost.

5.2. Wave run-up

Wave run-up, *Ru* [m] is the extreme vertical height of the wave on a beach, and it is affected by the wave setup and swash. This quantity can be estimated through the following ways:

1. *Empirical formula as derived by* Stockdon et al. (2006)

$$Ru = 1.1 \times \left(0.35\tan\beta(H_s L_0)^{1/2} + \left(H_s L_0 \frac{(0.536\tan\beta^2 + 0.004)^{1/2}}{2}\right)\right), \quad (2)$$

where tan β is the beach slope and L_0 is the deep water wave length associated to the wave peak period T_p for each storm (all values are in m). The final *Ru* for each storm class is obtained by taking the average wave height calculated for all storms.

2. *Irregular wave run-up Equation of Coastal Engineering Manual* (CEM, 2008)

$$\frac{Ru}{H_s} = \begin{cases} 0.96\xi & \text{for } 1.0 < \xi < 1.5 \\ 1.17\xi^{0.46} & \text{for } 1.5 < \xi \end{cases}, \quad (3)$$

where ξ is the Irribaren number defined as: $\xi = \frac{\tan a}{\sqrt{H_s/L_0}}$.

3. *Numerical simulation with the 1D version of a Boussinesq-type wave model (MIKE21 BW).*

The wave characteristics (H_s, T_p), as calculated by PMS in intermediate water are fed into the time-dependant model as irregular time series of surface elevation along with the bathymetric profile. The recommended values (DHI, 2007a,b,c) are used in MKE21 BW for simulation of wave breaking and bottom friction.

The results for the five different storm classes for the three different approaches are given in Table 8. Inspection of the above results proves a deviation between the methods of run-up calculation for each storm class. In the present paper the latter method of numerical modelling is proposed, since it is based on a Boussinesq model simulating the time-dependent propagation of the wave train taking into account the changes in bathymetric profile and not just the bottom slope, thus, it is closer to real life sea state.

5.3. Wave overtopping

Calculation of mean overtopping discharge rate is the last step of the methodology, but of primary importance since it enables further estimation of the inland flooding due to storm events. By inserting wave characteristics i.g: wave height at the toe of the structure (H_{m0}) and wave period (T) and geometrical characteristics i.g: the height of the crest of the wall above still water (R_c); the width of the structure crest G_c; the coefficient for reduction factors (γ) depending

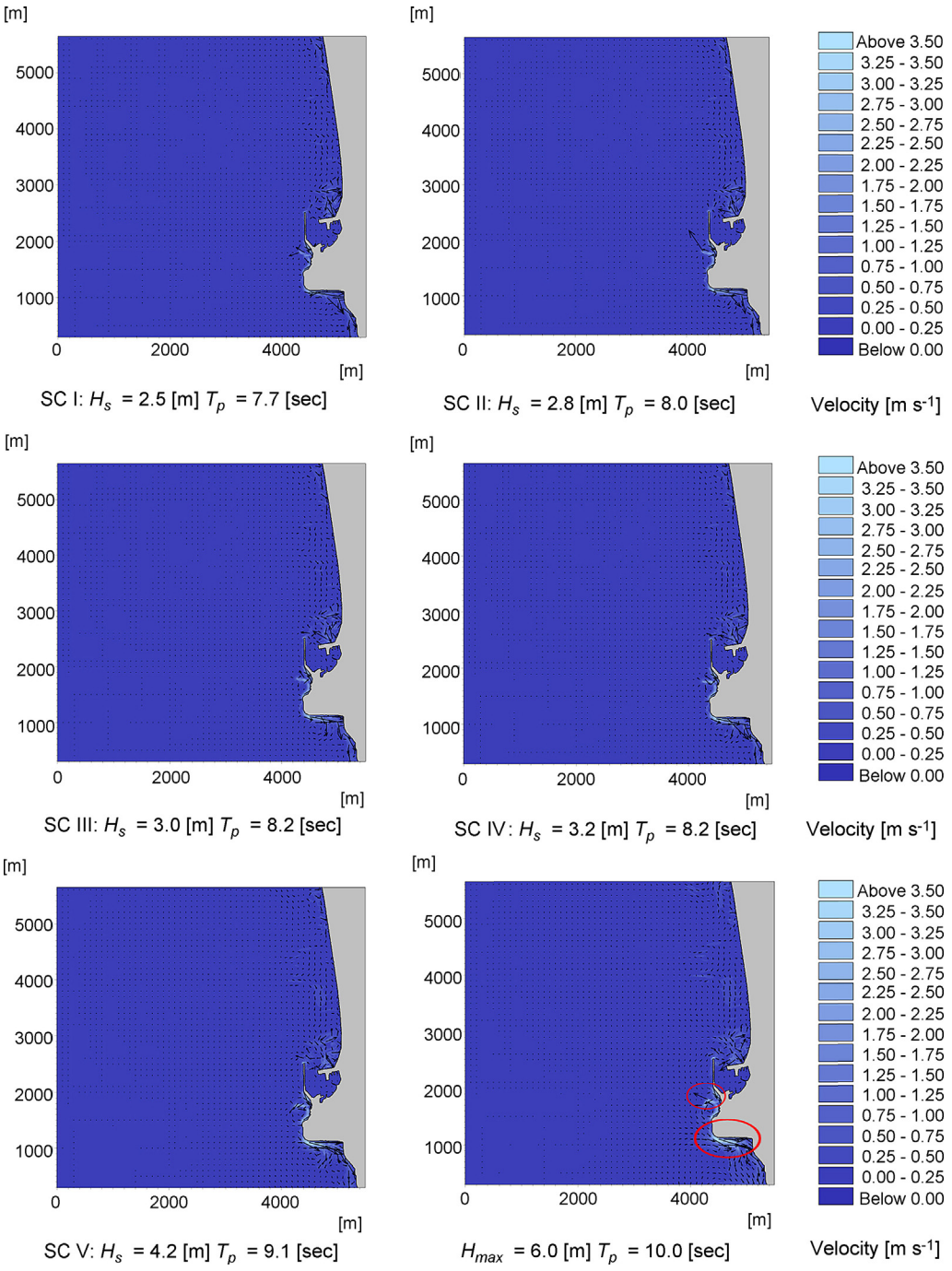

Figure 20 Hydrodynamic field for storm classes (SC) I to V and for the maximum occurred incident wave H_{max} = 6.0 m for the north direction. Arrows denote the current direction. The colour legend of wave height contours is identical for all classes.

on the permeability, into the EurOtop tools (EurOtop, 2007), such as parametric equations and artificial neural networks one can calculate the overtopping. The section A-A′ depicted in Fig. 22 is similar to the one of Fig. 24 and thus one can calculate the mean discharge rate per metre run of seawall Q [l s^{-1} m^{-1}] as shown in Table 9.

As it was expected, wave run-up and overtopping discharge increase as the intensity of the phenomenon increases. Nonetheless, the rapid increase of the overtopping for the extreme class (V) of the storm is worth of mentioning.

6. Discussion and conclusions

There is a growing interest in the development of reliable scenarios (future projections) for climate change affecting inter alia the frequency of storm surge events, the magnitude

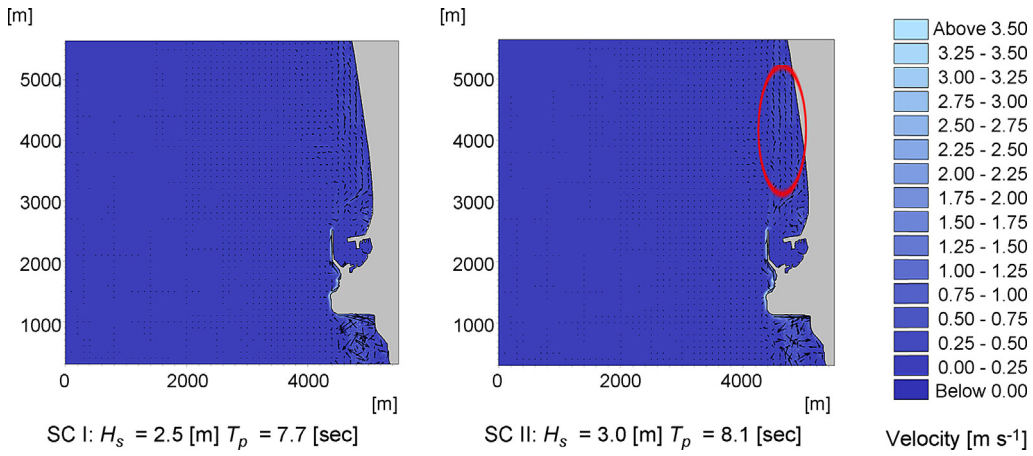

Figure 21 Hydrodynamic field for storm classes (SC) I and II for the northwest direction. Arrows denote the current direction.

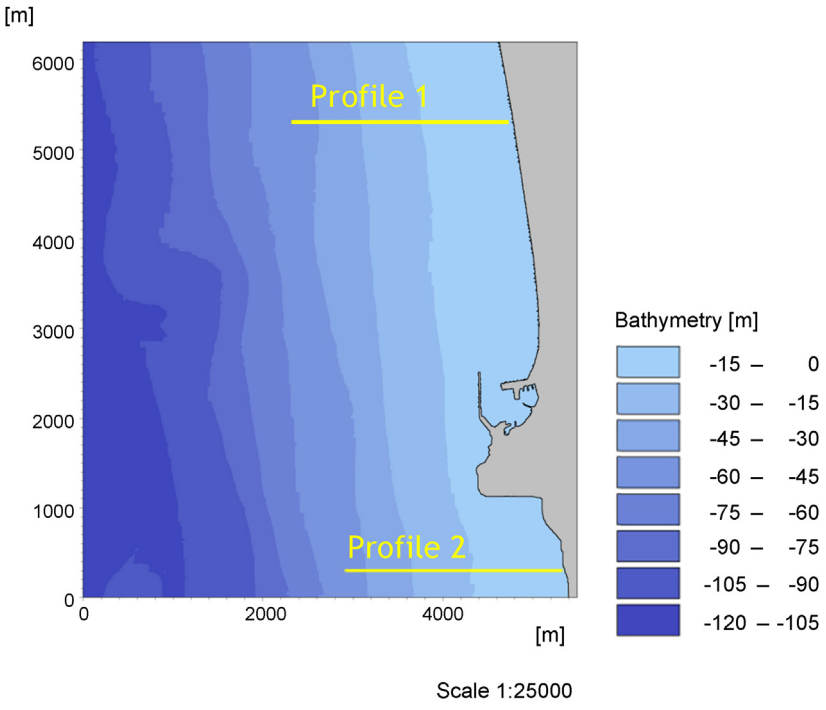

Figure 22 Selected bathymetric profiles for estimation of wave run-up.

Table 8 Calculation of wave run-up *Ru* [m] for the 2 different beach profiles of Fig. 22.

Storm class		*Ru* [m] for Profile 1			*Ru* [m] for Profile 2		
		Empirical Stockdon et al. (2006)	Empirical CEM (2006)	Numerical Boussinesq (MIKE21)	Empirical Stockdon et al. (2006)	Empirical CEM (2006)	Numerical Boussinesq (MIKE21)
I	Weak	0.84	1.14	0.57	0.84	1.14	0.67
II	Moderate	1.01	1.26	0.64	1.01	1.26	0.71
III	Significant	1.14	1.34	0.69	1.14	1.34	0.72
IV	Severe	1.24	1.42	0.7	1.24	1.42	0.75
V	Extreme	1.94	1.78	0.78	1.94	1.78	0.90

Figure 23 Selected cross section of the breakwater for estimation of wave overtopping.

Table 9 Mean overtopping discharge rate Q (Section A-A′).

Storm class	Input data					Output data
	H_{m0} [m]	T_p [s]	R_c [m]	G_c [m]	γ	Q [l s^{-1} m^{-1}]
I	2.33	7.68	6.1	4	0.55	0.002
II	2.64	7.99	6.1	4	0.55	0.015
III	2.85	8.19	6.1	4	0.55	0.045
IV	3.00	8.24	6.1	4	0.55	0.090
V	4.04	9.08	6.1	4	0.55	2.801

of wave heights, stronger currents and sea level rise. The above phenomena increase the flood risk for coastal areas and induce morphodynamic changes and as such their study is crucial for design and construction of climate resilient protection works.

In this paper, an integrated approach is proposed to calculate the wave overtopping and run-up through a chain of numerical tools starting from regional climate change models and ending nearshore. The first discrete step consists of climatic projections of wind forcing based on a potential emission scenario (e.g. AR4-A1B) and afterwards the simulation of offshore wave generation and propagation. It is expected that further emission scenarios will be selected and applied in the future to provide a more comprehensive picture of the future situation.

The proposed approach includes the categorization of storm events to avoid (i) individually handling of every event and (ii) to arrive at consolidated results. This was undertaken using an energy concept. Field data measurements of wind velocities and direction up to year 2008 were used to verify

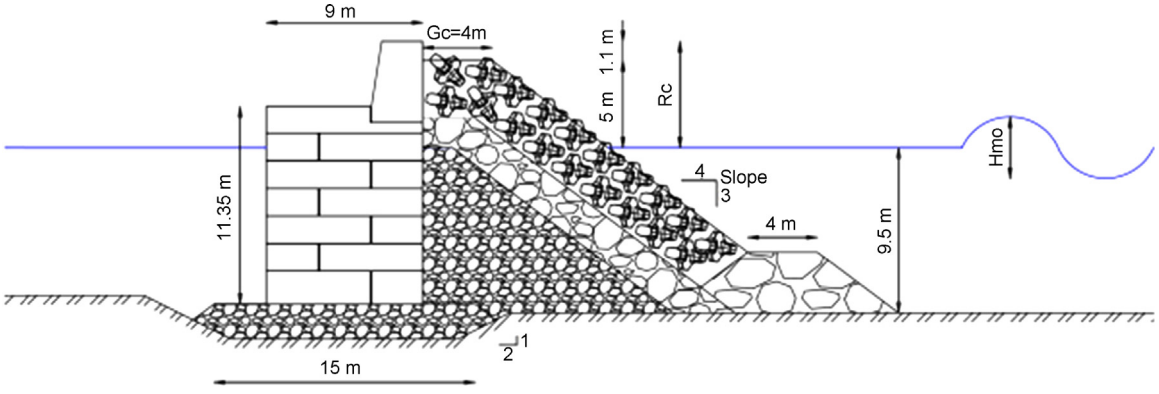

Figure 24 Definition sketch of breakwater cross section A-A′.

the outcomes of the model, showing a satisfactory correspondence concerning the classification of storm events. However, more reported storm events from 2008 up to date must be taken into consideration as soon as the relevant wind data are available from the National Weather Service.

The results of wave and hydrodynamic field simulations, by the means of a Parabolic Mild Slope model and a Hydrodynamic model, showed a good performance able to account for the spatial evolution of wave heights and velocity currents respectively. The modelled area, where wave breaking is more intense (on vertical fronts) and the generated currents become stronger, agrees fairly well with the field observations i.e. the port area of Rethymno, where the majority of coastal floods are reported. Finally, the implementation of Boussinesq model and EurOtop provides an advantage towards the accurate calculation of wave run up and overtopping respectively.

It can be argued that this procedure has a broader application range and can be adopted in any coastal region. The discrete steps, described in the methodology, can be adapted for any climate change scenario, bathymetry and topography of the potential coastal area of interest. We suggest that further research efforts should follow two main, interesting, directions: The first one would include the simulation of flooding within the urban areas by means of a hydrodynamic model, based on wave overtopping and run up results, and by taking into account current urban geometry (buildings, drainage, topography, etc.) but also possibly future urban form resulting from urban growth simulations (Bouziotas et al., 2015). The second direction is to embed the results into National and/or Local authorities planning policies, possibly using a collaborative knowledge co-production approach (Evers et al., 2012) to investigate options for flood risk management practices based on the calculated vulnerability of the coastal area.

References

Anselme, B., Durand, P., Thomas, Y.-F., Nicolae Lerma, A., 2011. Storm extreme levels and coastal flood hazards: a parametric approach on the French coast of Languedoc (district of Leucate). C. R. Geosci. 343 (10), 677—690, http://dx.doi.org/10.1016/j.crte.2011.07.006.

Archontakis, D., 2013. The Old Town of Rethymno: from a run down gheto to growth leverage of Rethymno. Rethymno, 12—18.

Athanassoulis, G.A., Belibassakis, K.A., Gerostathis, Th.P., Kapelonis, Z.G., 2014. Application of SWAN wave model for climatic simulation of sea condition at coastal areas of the Mediterranean. In: 6th Panhellenic Conf. Coastal Zones Manage. Improvement, 24—27 November 2014, Athens, Greece, 345—364.

Athanassoulis, G.A., Belibassakis, K.A., Gerostathis, Th.P., Kapelonis, Z.G., 2015. Wave climate analysis in the Mediterranean Sea based on wave model simulation driven by climatological winds. Technical Report WP 2.2. Res. Program CCSEAWAVS. (in Greek).

Benoit, M., Marcos, F., Becq, F., 1996. Development of a third generation shallow-water wave model with unstructured spatial meshing. In: 25th Int. Conf. Coastal Eng., Orlando, 465—478.

Booij, N., Ris, R.C., Holthuijsen, L.H., 1999. A third-generation wave model for coastal regions: 1. Model description and validation. J. Geophys. Res. 104 (C4), 7649—7666, http://dx.doi.org/10.1029/98JC02622.

Bouziotas, D., Rozos, E., Makropoulos, C., 2015. Water and the city: exploring links between urban growth and water demand management. J. Hydroinform. 17 (2), 176—192, http://dx.doi.org/10.2166/hydro.2014.053.

Breilh, J.-F., Bertin, X., Chaumillon, E., Giloy, N., Sauzeau, T., 2014. How frequent is storm-induced flooding in the central part of the Bay of Biscay? Global Planet. Change 122, 161—175, http://dx.doi.org/10.1016/j.gloplacha.2014.08.013.

Bretschneider, C.L., 1952. Revised wave forecasting relationships. In: Proc. 2nd Int. Conf. Coast. Eng., ASCE, Council Wave Res., Eng. Foundation, Berkeley, CA, 1—5.

Bretschneider, C.L., 1958. Revisions in wave forecasting: deep and shallow water. In: Proc. 6th Int. Conf. Coast. Eng., Council on Wave research, University of California, Richmond, CA, 30—67.

CEM, 2008. Coastal Engineering Manual. Coast. Eng. Res. Centre, US Army Corps Eng., Vicksburg, Mississippi, Part II, Chapter 2, 37—50; Chapter 4, 14—19.

Chini, N., Stansby, P.K., 2012. Extreme values of coastal wave overtopping accounting for climate change and sea level rise. Coast. Eng. 65, 27—37, http://dx.doi.org/10.1016/j.coastaleng.2012.02.009.

De Michele, C., Salvadori, G., Passoni, G., Vezzoli, R., 2007. A multivariate model of sea storms using copulas. Coast. Eng. 54 (10), 734—751, http://dx.doi.org/10.1016/j.coastaleng.2007.05.007.

Dean, R.G., Dalrymple, R.A., 2004. Coastal Processes with Engineering Applications. Cambridge Univ. Press, 488 pp.

DHI, 2007a. MIKE 21Boussinesq waves module: Scientific doc. Danish Hydraul. Instit., 1—24, (in Danish).

DHI, 2007b. MIKE 21Parabolic Mild Slope module: Scientific doc. Danish Hydraul. Instit., 1—22.

DHI, 2007c. MIKE 21Flow Model, HydroDynamic module: Scientific doc. Danish Hydraul. Instit., 1—60.

Dolan, R., Davis, R.E., 1992. An intensity scale for Atlantic coast northeast storms. J. Coast. Res. 8 (4), 840—853, http://www.jstor.org/stable/4298040.

Dolan, R., Davis, R.E., 1994. Coastal storm hazards. J. Coast. Res. (SI 12), 103—114, http://www.jstor.org/stable/25735593.

EurOtop Manual, 2007. In: Allsop, N.W.H., Pullen, T., Bruce, T., van der Meer, J.W., Schüttrumpf, H., Kortenhaus, A (Eds.), Overtopping Manual; Wave Overtopping of Sea Defences and Related Structures — Assessment Manual, http://www.overtopping-manual.com/manual.html (accessed 10 December 2015).

Evers, M., Jonoski, A., Maksimovic, C., Lange, L., Ochoa, S., Dinkneh, A.J., Cortés, Almoradie, A., van Andel, S.J., Simoes, N., Wang, L. P., Makropoulos, C., 2012. Collaborative modelling for active involvement of stakeholders in urban flood risk management. Nat. Hazards Earth Syst. Sci. 12 (9), 2821—2842, http://dx.doi.org/10.5194/nhess-12-2821-2012.

Galanis, D., 2010. Registration and control of the meteorological facts of the Meteorogical Station of Chania. (Dipl. Thesis). Tech. Edu. Instit. Chania, http://nefeli.lib.teicrete.gr/browse/sefe/sdfp/2010/GalanisDimitrios/attached-document-1277730043-268059-19836/2010galanis.pdf (accessed 10 December 2015).

Gallien, T.W., Sanders, B.F., Flick, R.E., 2014. Urban coastal flood prediction: integrating wave overtopping, flood defenses and drainage. Coast. Eng. 91, 18—28, http://dx.doi.org/10.1016/j.coastaleng.2014.04.007.

GEBCO, 2009. Gridded Global Bathymetry Data. British Oceanographic Data Centre, Liverpool, https://www.bodc.ac.uk/data/online_delivery/gebco/ (accessed 10 December 2015).

Halsey, S.D., 1986. Proposed Classification Scale for Major Northeast Storms: East Coast USA, Based on Extent of Damage. Geol. Soc. Am., abstracts with programs (Northeastern section), 18, 21 pp.

Karambas, T.V., 2015. Modelling of climate change impacts on coastal flooding/erosion, ports and coastal defence structures. Desalinat. Water Treat. 54 (8), 2130—2137, http://dx.doi.org/10.1080/19443994.2014.934115.

Koftis, T.H., Prinos, P., Galiatsatou, P., Karambas, Th., 2015. An integrated methodological approach for the upgrading of coastal

structures due to climate effects. In: E-proceedings of the 36th IAHR World Conference, 28 June—3 July, The Hague, the Netherlands.

Kokkinos, D., Prinos, P., Galiatsatou, P., 2014. Assessment of coastal vulnerability for present and future climate conditions in coastal areas of the Aegean Sea. In: Paper Presented at the 11th International Conference on Hydroscience & Engineering: Hydro-Engineering for Environmental Challenges, http://www.thalis-ccseawavs.web.auth.gr/el/publications (accessed 10 December 2015).

Kundzewicz, Z.W., 2014. Adapting flood preparedness tools to changing flood risk conditions: the situation in Poland. Oceanologia 56 (2), 385—407, http://dx.doi.org/10.5697/oc.56-2.385.

Laudier, N.A., Thornton, E.B., MacMahan, J., 2011. Measured and modeled wave overtopping on a natural beach. Coast. Eng. 58 (9), 815—825, http://dx.doi.org/10.1016/j.coastaleng.2011.04.005.

Li, F., van Gelder, P.H.A.J.M., Ranasinghe, R., Callaghan, D.P., Jongejan, R.B., 2014. Probabilistic modelling of extreme storms along Dutch coast. Coast. Eng. 86, 1—13, http://dx.doi.org/10.1016/j.coastaleng.2013.12.009.

Long, J.W., Bakker, A.T.M., de Plant, N.G., 2014. Scaling coastal dune elevation changes across storm-impact regimes. Geophys. Res. Lett. 41 (8), 2899—2906, http://dx.doi.org/10.1002/2014GL059616.

Lynett, P., Melby, J., Kim, D., 2010. An application of Boussinesq modeling to Hurricane wave overtopping and inundation. Ocean Eng. 37 (1), 135—153, http://dx.doi.org/10.1016/j.oceaneng.2009.08.021.

Majewski, D., Schrodin, R., 1994. Short description of the Europa-Modell (EM) and Deutschland-Modell (DM) of the DWD. Quarterly Bull. 1—31.

Makropoulos, Ch., Tsoukala, V.K., Belibassakis, K., Lykoy, A., Chondros, M., Gougoura, P., 2015. Managing flood risk in coast cities through an integrated modelling framework supporting stakeholders' involvement: the case study of Rethymno. In: E-proceedings of the 36th IAHR World Conference, 28 June—3 July, The Hague, the Netherlands.

Makropoulos, Ch., Tsoukala, V.K., Lykou, A., Chondros, M., Manojlovic, N., Vojinovic, Z., 2014. Extreme and rare events in coastal regions due to climate change — a case study application in Rethymno. In: Int. Conf. ADAPTto CLIMATE. 27—28 March 2014, Nicosia, Cyprus (e-proceedings: http://adapttoclimate.uest.gr/index.php/proceedings1, last accessed 10 December 2015).

Matias, A., Williams, J.J., Masselink, G., Ferreira, O., 2012. Overwash threshold for gravel barriers. Coast. Eng. 63, 48—61, http://dx.doi.org/10.1016/j.coastaleng.2011.12.006.

McCabe, M., Stansby, P.K., Rogers, B.D., Cunningham, L.S., 2014. Boussinesq modelling of tsunami and storm wave impact. Proc. Inst. Civil Eng. — Eng. Comput. Mech. 167 (3), 106—116, http://dx.doi.org/10.1680/eacm.13.00025.

Mendoza, E.T., Jiménez, J.A., 2009. Regional vulnerability analysis of Catalan beaches to storms. Proc. Inst. Civil Eng. — Mar. En. 162 (3), 127—135, http://dx.doi.org/10.1680/maen.2009.162.3.127.

Mendoza, E.T., Jiménez, J.A., 2006. Storm-induced beach erosion potential on the Catalonian Coast. J. Coast. Res. SI 48 (Proc. 3rd Spanish Conf. Coast. Geomorphol.), 81—88, http://www.jstor.org/stable/25737386.

Mendoza, E.T., Jiménez, J.A., Mateo, J., 2011. A coastal storms intensity scale for the Catalan sea (NW Mediterranean). Nat. Hazards Earth Syst. Sci. 11 (9), 2453—2462, http://dx.doi.org/10.5194/nhess-11-2453-2011.

Mendoza, E.T., Trejo-Rangel, M.A., Salles, P., Appendini, C.M., González, J.L., Torres-Freyermuth, A., 2013. Storm characterization and coastal hazards in the Yucatan Peninsula. J. Coast. Res. SI 65, 790—795.

Oumeraci, H., Kortenhaus, A., Burzel, A., Naulin, M., Dassanayake, D.R., Jensen, J., Wahl, T., Mudersbach, C., Gönnert, G., Gerkensmeier, A.B., Fröhle, P., Ujeyl, G., 2015. XtremRisK — integrated flood risk analysis for extreme storm surges at open coasts and in estuaries: methodology, key results and lessons learned. Coast. Eng. J. 57 (1), 23 pp., http://dx.doi.org/10.1142/s057856341540001x.

Plant, N.G., Stockdon, H.F., 2015. How well can wave runup be predicted? Comment on Laudier et al. (2011) and Stockdon et al. (2006). J. Coast. Eng. 102, 44—48, http://dx.doi.org/10.1016/j.coastaleng.2015.05.001.

Prinos, P., 2014. Climate change effects on the Greek seas and coastal areas — the research project THALIS-CCSEAWAVS. In: 6th Panhellenic Conference on Coastal Zones Management and Improvement, 24—27 November 2014, Athens, 315—324.

Rangel-Buitrago, N., Anfuso, G., 2011. An application of Dolan and Davis (1992) classification to coastal storms in SW Spanish littoral. J. Coast. Res. SI 64, 1891—1895.

Ris, R.C., Holthuijsen, L.H., Booij, N., 1999. A third-generation wave model for coastal regions: 2. Verification. J. Geophys. Res. 104 (C4), 7667—7681, http://dx.doi.org/10.1029/1998JC900123.

RISC-KIT, 2015. Coastal Hazard Assessment Module, Deliverable No: D.2.1, Ref.: WP2 - Task 2.1, 113 pp., http://www.risckit.eu/np4/file/23/RISCKIT_D.2.1_Coastal_Hazard_Asssessment.pdf.

Saffir, H.S., 1977. Design and Construction Requirements for Hurricane Resistant Construction. ASCE, New York, Preprint No. 2830, 20 pp.

Senechal, N., Coco, G., Bryan, K.R., Holman, R.A., 2011. Wave runup during extreme storm conditions. J. Geophys. Res. 116 (C7), C07032, http://dx.doi.org/10.1029/2010JC006819.

Simpson, R.H., 1979. A proposed scale for ranking hurricanes by intensity. In: Minutes of the Eighth NOAA, NWS Hurricane Conference, Miami.

Smith, R., Bates, P., Hayes, D., 2012. Evaluation of a coastal flood inundation model using hard and soft data. Environ. Modell. Softw. 30, 35—46, http://dx.doi.org/10.1016/j.envsoft.2011.11.008.

Stockdon, H.F., Holman, R.A., 2011. Observations of wave runup, setup, and swash on natural beaches. USGS Data Ser. 602, http://pubs.usgs.gov/ds/602/ (accessed 10 December 2015).

Stockdon, H.F., Holman, R.A., Howd, P.A., Sallenger, A.H., 2006. Empirical parameterization of setup, swash, and runup. Coast. Eng. 53 (7), 573—588, http://dx.doi.org/10.1016/j.coastaleng.2005.12.005.

Velikou, K., Tolika, K., Anagnostopoulou, C., Tegoulias, I., Vagenas, C., 2014. High resolution climate over Greece: assessment and future projections. In: 12th International Conference on Meteorology, Climatology and Atmospheric Physics (COMECAP 2014), Heraklion.

WAMDI-Group, 1988. The WAM model — a third generation ocean wave prediction model. J. Phys. Oceanogr. 18 (12), 1775—1810, http://dx.doi.org/10.1175/1520-0485(1988)018<1775:twmtgo>2.0.co;2.

Warner, N., Tissot, P.E., 2012. Storm flooding sensitivity to sea level rise for Galveston Bay, Texas. Ocean Eng. 44, 23—32, http://dx.doi.org/10.1016/j.oceaneng.2012.01.011.

Williams, J.A., Flather, R.A., 2004. The Operational Storm Surge Model: maintenance, performance and development, January 2003—March 2004. Proudman Oceanogr. Lab., Internal Doc. No. 164, 68 pp.

Wiśniewski, B., Wolski, T., 2011. Physical aspects of extreme storm surges and falls on the Polish coast. Oceanologia 53 (1—TI), 373—390, http://dx.doi.org/10.5697/oc.53-1-TI.373.

Oceanologia (2016) 58, 90—102

Available online at www.sciencedirect.com

ScienceDirect

journal homepage: www.elsevier.com/locate/oceano

ORIGINAL RESEARCH ARTICLE

Curonian Lagoon drainage basin modelling and assessment of climate change impact☆

Natalja Čerkasova [a], Ali Ertürk [b,a], Petras Zemlys [a], Vitalij Denisov [c], Georg Umgiesser [d,a,*]

[a] Open Access Centre for Marine Research, Klaipeda, Lithuania
[b] Department of Freshwater Biology, Istanbul University, Istanbul, Turkey
[c] Faculty of Marine Technology and Natural Sciences, Klaipeda University, Klaipeda, Lithuania
[d] ISMAR-CNR, Institute of Marine Sciences, Venezia, Italy

Received 8 September 2015; accepted 12 January 2016
Available online 9 February 2016

KEYWORDS
Drainage basin modelling;
SWAT;
Curonian Lagoon;
Nemunas basin;
Climate change

Summary The Curonian Lagoon, which is the largest European coastal lagoon with a surface area of 1578 km^2 and a drainage area of 100,458 km^2, is facing a severe eutrophication problem. With its increasing water management difficulties, the need for a sophisticated hydrological model of the Curonian Lagoon's drainage area arose, in order to assess possible changes resulting from local and global processes. In this study, we developed and calibrated a sophisticated hydrological model with the required accuracy, as an initial step for the future development of a modelling framework that aims to correctly predict the movement of pesticides, sediments or nutrients, and to evaluate water-management practices. The Soil and Water Assessment Tool was used to implement a model of the study area and to assess the impact of climate-change scenarios on the run-off of the Nemunas River and the Minija River, which are located in the Curonian Lagoons drainage basin. The models calibration and validation were performed using monthly streamflow data, and evaluated using the coefficient of determination (R^2) and the Nash-Sutcliffe model efficiency coefficient (*NSE*). The calculated values of the R^2 and *NSE* for the Nemunas and Minija Rivers stations were 0.81 and 0.79 for the calibration, and 0.679 and 0.602 for the validation period. Two potential climate-change scenarios were developed within the general

☆ This study was funded by the European Social Fund under the Global Grant measure (CISOCUR project VP1-3.1-ŠMM-07-K-02-086).
* Corresponding author at: ISMAR-CNR, Institute of Marine Sciences, Arsenale — Tesa 104, Castello 2737/F, 30122 Venezia, Italy. Tel.: +39 339 4238653.
E-mail address: georg.umgiesser@ismar.cnr.it (G. Umgiesser).
Peer review under the responsibility of Institute of Oceanology of the Polish Academy of Sciences.

Production and hosting by Elsevier

http://dx.doi.org/10.1016/j.oceano.2016.01.003

patterns of near-term climate projections, as defined by the Intergovernmental Panel on Climate Change Fifth Assessment Report: both pessimistic (substantial changes in precipitation and temperature) and optimistic (insubstantial changes in precipitation and temperature). Both simulations produce similar general patterns in river-discharge change: a strong increase (up to 22%) in the winter months, especially in February, a decrease during the spring (up to 10%) and summer (up to 18%), and a slight increase during the autumn (up to 10%).

1. Introduction

The Curonian Lagoon is located at N 55°30′ latitude and E 21°15′ longitude. It is the largest European coastal lagoon, separated from the Baltic Sea by a narrow 0.5—4 km wide sandy Curonian spit and connected to the Baltic Sea through the Klaipeda Strait. Several small rivers — such as the Bolshaya and Malaya Morianka, Kalinovka, Deima, Rybnaya, Minija, Dane and Dreverna — and one large river (Nemunas) discharge into the Curonian Lagoon. The southern and central parts of the lagoon contain fresh water due to the discharge from those rivers. The run-off of rivers to the lagoon varies from 14 to 33 km^3 per year (444 m^3 s^{-1} to 1046 m^3 s^{-1}) and exhibits a strong seasonal pattern, peaking with snowmelt during the flood season of March to April (Dubra and Červinskas, 1968).

The area of land draining into the Curonian Lagoon covers 100,458 km^2, of which 48% lies in Belarus, 46% in Lithuania, and 6% in the Kaliningrad Oblast and Poland (Gailiušis et al., 1992) (see Fig. 1). The drainage area of the Curonian Lagoon consists of several river basins; however, the most important of them is the Nemunas River drainage basin in terms of flow rates and nutrient inputs, supplying about 98% of its inflows (Jakimavičius, 2012). The annual Nemunas River water inflow into the Curonian Lagoon is more than three times greater than the volume of water in the lagoon (Žilinskas et al., 2012). According to researchers, the average annual run-off during 1812 to 2002 was 22.054 km^3 (699 m^3 s^{-1}) (Gailiušis et al., 1992), and from 1960 to 2007 it was 21.847 km^3 (692 m^3 s^{-1}) (Jakimavičius and Kovalenkovienė, 2010). As a result, the lagoon's water level is usually higher than that of the Baltic Sea; therefore, the dominant currents are from the lagoon to the Baltic Sea.

Figure 1 Curonian Lagoon drainage area.

Over the years, the water discharge to the lagoon changed, and this led to a fluctuation of the water balance. Major changes have been observed in the last decade in the winter—spring period. In the winter months of January and February, due to observed warmer winters, the Nemunas' run-off has increased, while spring floods are decreasing; therefore, run-off levels over the year became more homogeneous (Žilinskas et al., 2012).

Agriculture has a significant impact on the status of water bodies in the Nemunas River basin, especially in the sub-basins of the Sesupe and Nevezis Rivers; this factor has a local, but serious, impact. Chemicals that enter the river from agriculture and fishponds are a major source of pollution. A substantial proportion of point-source pollution comes from industry. According to the Second Assessment of Transboundary Rivers, Lakes and Groundwaters by the United Nations Economic Commission for Europe (2011), there is room for development in the monitoring of the Nemunas River, as the current list of monitored pollutants is limited. There is a lack of biological observation and monitoring of pollutants in river-bottom sediments, and a joint, harmonized monitoring programme for the transboundary watercourses is needed. It is important to develop a model for nutrient and other biogeochemically significant dissolved-substance contributions that are altering and influencing the ecosystems of the Nemunas River and Curonian Lagoon.

The first step is the development of a hydrological model and analysis of changes in the Curonian Lagoon drainage basin due to global processes (climate change, etc.), as well as local anthropogenic activities, and forecasting possible changes in the future. Model hydrology calibration, uncertainty analysis and sensitivity analysis enables a broader understanding of key processes in the catchment area. Recent work conducted in the field of Curonian Lagoon drainage basin modelling is reported in the doctoral dissertation “Changes of water balance elements of the Curonian Lagoon and their forecast due to anthropogenic and natural factors” by Jakimavičius (2012). In this work, the author had created hydrological models for the separate Nemunas catchment areas using HBV (Hydrologiska Byråns Vattenbalansavdelning), before calibrating and validating them. The sensitivity and uncertainty of the Nemunas run-off model parameters were assessed using the SUSA (Software for Uncertainty and Sensitivity Analyses) package. Hydrometeorological information of the period 1961—1990 was used for the model's creation. The period 1961—1975 was selected for the model's calibration, whereas the period 1976—1990

was used for its validation. Prognostic data from 14 measurement stations, data from 1961 to 1990 and the downscaling method were applied to calculate the daily mean data from the mean monthly output data of climate-change scenarios. In this way, obtained prognostic values of precipitation and temperature data were used to simulate the Nemunas' inflow and to compute its water balance (Jakimavičius, 2012).

Projections of the temperature and precipitation of the Nemunas' river basin for the 21st century (according to conclusions of the Fourth Assessment Report of the United Nations Intergovernmental Panel on Climate Change, as well as the results of output data of ECHAM5 and HadCM3 global climate models under A2, A1B and B1 greenhouse gas emission scenarios) were used to create the climate-change scenarios. These data were used to compute the Nemunas' inflow to the lagoon during 2011–2100, the amount of precipitation entering the lagoon and water evaporation from the lagoon's surface (Jakimavičius, 2012).

The study conducted by Jakimavičius (2012) is quite comprehensive; however, it lacks some key points. The research mainly focuses on the changes of water-balance elements of the Curonian Lagoon, such as the Nemunas River's inflow to the lagoon, and the water exchange between the Baltic Sea and the Curonian Lagoon, with no focus on the smaller rivers', such as the Minija, run-off change. The precipitation amount used covered only the territory of Lithuania. The selected baseline period is outdated and does not fully represent the current conditions of the catchment area. The climate change scenarios covered the precipitation amount and temperature change, with no change to the relative humidity.

The SWAT (Soil and Water Assessment Tool) model is also used by Lithuania's Ministry of Environment in development of a method and modelling system for nitrogen and phosphorus load-calculation for the surface waters of Lithuania (ELLE and PAIC, 2012). The model covers only the territory of Lithuania, which is divided into more than 1200 sub-basins. The developed model uses high-resolution DEM (Digital Elevation Model), soil and land-use data layers in order to create Hydrologic Response Units (HRUs) with a resolution of 5 m × 5 m; therefore, the model's accuracy and predictive capability is reduced. Overall, the model's Nash-Sutcliffe efficiency coefficient (*NSE*) performance for the monthly median flow is 0.5. The model is primarily used for the development of methods and tools for multi-objective spatial optimization, and structural agriculture-change scenario assessments. With additional model set-up corrections and a more thorough calibration, this model can become state-of-the-art for Lithuania's territory; however, it is not open access, is unavailable for usage outside of the Lithuanian Environmental Protection Agency and results have not yet been published in peer-reviewed journals. These facts led to the necessity of producing a more flexible tool for analysing and predicting hydrological and biogeochemical cycles of the Curonian Lagoon's drainage basin. In addition, the created model could allow the exchange of modelling results and benefit development of large-scale modelling systems.

2. Material and methods

The Curonian Lagoon drainage basin model was set up using the SWAT: a physically based, continuous-time catchment model that operates on a daily time step and is designed to predict the impact of management on water, sediment, and agricultural chemical yields in ungauged drainage areas (Arnold et al., 1993).

The drainage basin area was divided into multiple sub-basins, which were then further subdivided into Hydrological Response Units that consist of homogeneous land-use, management and soil characteristics (Arnold et al., 1993). Using the SWAT, run-off was predicted for each HRU separately and routed to obtain the total run-off of a catchment area. This solution improves the model's accuracy and provides a much better physical description of the water balance (Neitsch et al., 2011).

A stable version of the SWAT from 2009 was used due to the fact that additional extensions and extra tools are available for this version, and also because this version has undergone much testing and correction.

For the calibration of the Curonian Lagoon drainage basin model, the SWAT-CUP (Soil and Water Assessment Tool Calibration and Uncertainty Programs) semi-automated SUFI-2 method (Sequential Uncertainty Fitting, version 2) was applied, as it is most commonly used, well-documented method, and is reported to produce satisfactory results (Arnold et al., 2012). Model calibration and validation were performed using monthly streamflow data.

Several publications (Arnold et al., 2012; Balascio et al., 1998; Moriasi et al., 2007) have examined the usage of different model-evaluation statistics; however, not many of them provide directions or advice on using acceptable ranges of values for these performance indicators. Some of the guidelines suggest using the *NSE* and the coefficient of determination (R^2), in addition to graphical techniques (Moriasi et al., 2007). Suggested guidelines were followed, and the Curonian Lagoon's drainage basin model was evaluated according to them.

2.1. SWAT model description and features

The development of the SWAT is a continuation of the United States Department of Agriculture Agricultural Research Service (USDA-ARS), a modelling experience that spans a period of roughly 30 years. The current SWAT model is a direct descendant of the Simulator for Water Resources in Rural Basins (SWRRB) model, which was designed to simulate management impacts on water and sediment movement for ungauged rural basins across the U.S. (Arnold et al., 2010). The SWAT has experienced constant reviews and an extension of its functionality since it was created in the early 1990s. The most significant improvements are listed in the official SWAT theoretical documentation (Neitsch et al., 2011) and include the following: incorporation of multiple HRUs, auto-fertilization and auto-irrigation management options, incorporation of the canopy storage of water, the Penman-Monteith potential evapotranspiration equation, in-stream water quality equations, improvement of snow melt routines, nutrient cycling routines, rice and wetland routines, bacteria transport routines, Green and Ampt infiltration, weather generator improvements and many other factors. The incorporation of the Curve Number (CN) method and non-spatial HRUs allow adaptation of the model to virtually any drainage basin with a wide variety of hydrological conditions (Gassman et al., 2007). Simulation of the

hydrology of a catchment area can be separated into two major points:

1. Land phase of the hydrological cycle: the amount of water, nutrient, sediment and pesticide loadings in the main channel in each sub-basin.
2. Water or routing phase of the hydrological cycle: the movement of water, sediments, etc., through the channel network of the drainage area to the outlet (Neitsch et al., 2011).

The hydrologic cycle simulated by SWAT is based on the water balance equation:

$$SW_{t+1t} = SW_{t0} + \sum_{i=1}^{t}(R_{day} - Q_{surf} - E_a - w_{seep} - Q_{gw}), \quad (1)$$

where SW_{t+1t} is the final soil water content at day t [mm H_2O], SW_{t0} the initial soil water content, R_{day} the amount of precipitation on day t [mm H_2O], Q_{surf} the amount of surface runoff on day t [mm H_2O], E_a the amount of evapotranspiration on day t [mm H_2O], w_{seep} the amount of water entering vadose zone from the soil profile on day t [mm H_2O], and Q_{gw} is the amount of return flow on day t [mm H_2O].

2.2. Model set-up and data

There are four main data sets that were used in the SWAT set-up:

1. Digital Elevation Model (DEM) data;
2. Land-use data;
3. Soil data;
4. Weather data.

There are many more optional datasets that can be used as inputs for the SWAT.

2.2.1. DEM

DEM data were obtained from the Consortium for Spatial Information (CGIAR-CSI) database (CGIAR — Consortium for Spatial Information, accessed: February 2014) based on the SRTM (Space Radar Topographic Mission) survey data provided by NASA (National Aeronautics and Space Administration) dating back to 2001. The resolution of the DEM is 51 m × 51 m. To use this DEM in the SWAT, the grid size had to be changed to a coarser resolution. This decision is based on studies of the DEM's resolution effects on the SWAT's output. Studies showed that run-off had little or no sensitivity to the resampled resolution, and the minimum DEM resolution should range from 100 m to 200 m in order to achieve a less than 10% error rate in the SWAT's output for flow, NO_3-N and total P predictions (Chaubey et al., 2005; Ghaffari, 2011; Lin et al., 2010). A coarser resolution results in a decrease of the computational needs by up to three times during model's set-up and run phases. The DEM grids were resampled to a size of 153 m x 153 m, which is within the recommended range (Chaubey et al., 2005).

Table 1 Land use type occurrence in the Curonian Lagoon drainage basin area.

Nr.	Class label	Land use type	Area [% of total]
1	CRWO	Cropland/woodland mosaic	64
2	CRDY	Dryland cropland and pasture	23
3	FOMI	Mixed forest	6
4	CRGR	Cropland/grassland mosaic	3
5	WATB	Water bodies	2
6	FOEN	Evergreen needleleaf forest	2
7	FODB	Deciduous broadleaf forest	1
8	URMD	Residential medium density	<1
9	GRAS	Grassland	<1
10	FODN	Deciduous needleleaf forest	<1
11	CRIR	Irrigated cropland and pasture	<1
12	TUWO	Wooded tundra	<1
13	SHRB	Shrubland	<1

2.2.2. Land-use data

Land-use data were acquired from the WaterBase project database (United Nations University, accessed: November 2014) based on the FAO's (Food and Agriculture Organization of the United Nations) land-use data. There are 13 classes of land-use types in the study area, which correspond to the ones used in the SWAT database (Table 1). The most dominant type of land-use in the area is CRWO (covering 64% of the study area), which is the abbreviation for “cropland, woodland mosaic”, followed by CRDY (23%) — “dryland, cropland and pasture” and FOMI (6%) — “mixed forest”. The information required to simulate plant growth is stored in the SWAT plant-growth database file according to plant species. The SWAT uses a plant-growing cycle in order to determine how much water is consumed by the canopy, and how much can be stored and released by it. The model takes into account growing seasons, harvesting and other parameters, which can be specified or modified by the user during the model's set-up stage.

2.2.3. Soil data

Soil data were acquired from the WaterBase project database of United Nations University (accessed: November 2014). Twenty-six classes of soil are present in the study area, which correspond to the ones used in the SWAT database (Table 2). Soil-class characteristics can be determined in the same way as for land-use classes, by using a database that is implemented in the tool, which contains the most common soil types and their properties.

Soil data used by the SWAT can be divided into two groups: physical characteristics and chemical characteristics. Physical properties of the soil govern the movement of water and air through the soil's profile, and have a major impact on the cycling of water within the HRU, whereas inputs for chemical characteristics are used to set the initial levels of chemicals that are present in the soil (Neitsch et al., 2011). Physical properties for each soil type are necessary for use of the model, while chemical ones are optional. The most widely presented soil layer in the study area is De18-2a-3049 (33%), which is categorized as “loam”, followed by Gm32-2-3a-3074 (10%) and Lg55-1a-31993199 (9%), which are “clay loam” and “sandy loam” respectively.

Table 2 Soil class occurrence in the Curonian Lagoon drainage basin area.

Nr.	Class label	Soil texture	Area [% of total]
1	De18-2a-3049	LOAM	33
2	Gm32-2-3a-3074	CLAY_LOAM	10
3	Lg55-1a-3199	SANDY_LOAM	9
4	De20-2ab-3052	LOAM	8
5	De18-1a-3048	SANDY_LOAM	6
6	De17-1-2a-3047	SANDY_LOAM	4
7	Pl5-1ab-3236	LOAMY_SAND	4
8	Lo78-1-2a-3204	SANDY_LOAM	3
9	Be144-2-3-3019	CLAY_LOAM	3
10	Dg5-1ab-3055	SANDY_LOAM	3
11	Dd8-1ab-3045	SANDY_LOAM	2
12	De13-1ab-3046	SANDY_LOAM	2
13	De19-1a-3050	SANDY_LOAM	2
14	De19-2a-3051	SANDY_LOAM	1
15	Je87-2-3a-3149	CLAY_LOAM	1
16	Lg41-2-3a-3194	LOAM	1
17	Lg43-2ab-3196	SANDY_LOAM	1
18	Lo69-2ab-3201	LOAM	1
19	Od22-a-3217	LOAM	1
20	Oe14-a-3223	LOAM	1
21	Pl5-1ab-3236	LOAMY_SAND	<1
22	Po30-1ab-3239	SANDY_LOAM	<1
23	Be126-2-3-6436	LOAM	<1
24	Lo79-2a-6572	LOAM	<1
25	Lo81-1a-6574	SANDY_LOAM	<1
26	Qc62-1a-6623	SAND	<1

2.2.4. Weather data

Historical weather data are usually gathered and archived by the countries' meteorological services. In Lithuania, such data are available from the Lithuanian Hydrometeorological Service, under the Ministry of Environment of the Republic of Lithuania (LHMS). However, the study area covers not only the territory of Lithuania, but also Kaliningrad Oblast and Belarus, meaning that data had to be acquired from global public resources. The weather data were acquired through Global Weather Data for the SWAT service (National Centers for Environmental Prediction, Accessed: November 2014). It provides data for the 35-year period between 1979 and 2014. The service allows the downloading of daily data for precipitation, wind, relative humidity and solar radiation in the SWAT's file format for a given location and time period. Weather data used for the Curonian Lagoon drainage basin model covered a period of 16 years, from 1995 to 2010; the first five years' data (1995—1999) were used for the model's warm-up stage, whereas the remaining data were used for the model's set-up, calibration and validation.

2.2.5. Observed data

The observed run-off data files had to be prepared for the model's output analysis and calibration. The available observed data were for two river discharges: Nemunas, near Smalininkai, and Minija, near Lankupiai (Fig. 2). The data files present the daily time series over 11 years (2000—2010) for measured discharges in $m^3\ s^{-1}$. These data were provided by the Klaipeda University Coastal Research and Planning Institute (KU CORPI).

2.2.6. Sub-basin set-up

The study area was delineated using the MapWindow Terrain Analysis Using Digital Elevation Models (TauDEM) tool, following the specification of the threshold drainage area, which is the minimum drainage area required to form the origin of the stream, and identification of the drainage basin outlets. The accuracy of the delineation process was influenced by the DEM's resolution. Several iterations were performed with different delineation threshold-values, thus creating models with different numbers of sub-basins. Each model's initial output performance was tested in order to analyse the delineation threshold-value's influence on its predictive flow capabilities. As a result, a total of 117 sub-basins were produced, which proved to be the best performing number of sub-basins for this study. Multiple HRUs were then created automatically with the MapWindow SWAT plug-in within each sub-basin, as a function of the dominant land-use and soil types.

2.3. Calibration procedure

The available period of observation data (2000—2010) was divided into the two groups of 2000—2007 for calibration and 2008—2010 for validation; this supplies a period of 8 years for calibration and 3 years for validation.

Various studies have reported different input parameters used in the SWAT model's calibration. Table 3 summarizes the most frequently used parameters in various studies (Abbaspour, 2011; Arnold et al., 2012). As the SWAT is a comprehensive model that simulates process interactions, many parameters will impact multiple processes. For instance, CN (Curve Number) directly impacts surface run-off; however, as surface run-off changes, all components of the hydrological balance change. The described feature is the primary reason for calibrating the model starting with the hydrological balance and streamflow, then moving to sediment and, finally, calibrating nutrients and pesticides (Arnold et al., 2012). All suggested parameters described in Table 3 were subjected to calibration and sensitivity analysis in order to regionalize the most sensitive parameters and make the necessary adjustments to their values. These steps were performed iteratively, as recommended in the SUFI-2 calibration procedure documentation (Abbaspour, 2011). The maximization of *NSE* for river discharge was used as an objective function:

$$NSE = 1 - \frac{\sum_i (Q_m - Q_s)_i^2}{\sum_i (Q_{m,i} - \overline{Q}_m)^2}, \quad (2)$$

where Q_m is the measured parameter value (e.g. river discharge), Q_s the simulated parameter value, and $\overline{Q}_m$ is the average value of measured parameter. *NSE* values ranges between $-\infty$ and 1.0, with 1.0 being the optimal value. Values between 0.0 and 1.0 are generally viewed as acceptable levels of performance, whereas values below 0.0 indicate unacceptable performance of the model (in this case the mean observed value is a better predictor than the simulated one) (Krause et al., 2005).

SWAT-CUP calibration iteration presumes the existence of a set of simulations with predefined parameters, uncertainty ranges for these parameter values, statistics of every

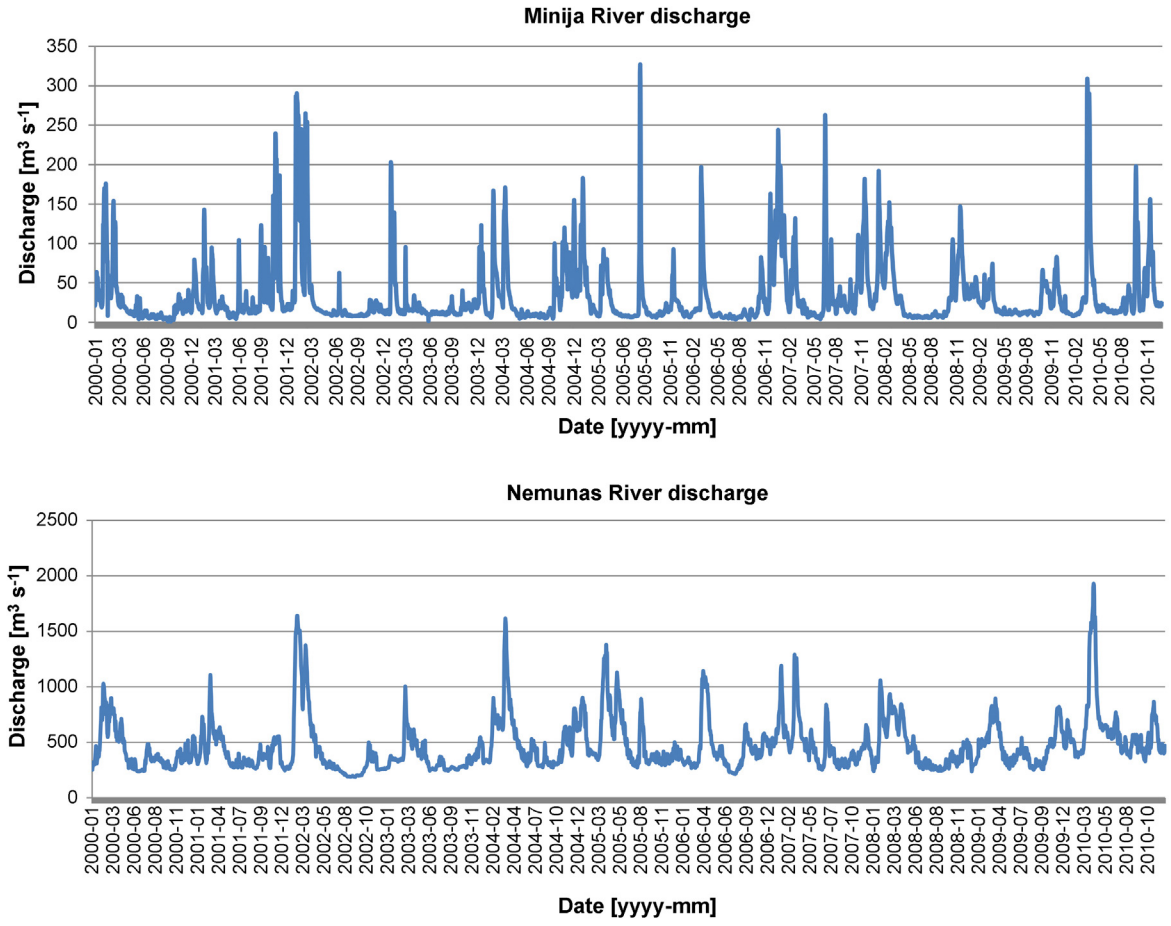

Figure 2 Minija and Nemunas river historical discharge.

simulation output and overall statistics of the calibration process. A simulation is a single execution of the SWAT model, with certain parameter values within a boundary of the uncertainty ranges, as defined in the iteration set-up process. The initial calibration run was carried out with 2000 model simulations. As the number of parameters and simulations was high, the time consumption of such a calibration iteration was demanding. To complete one iteration cycle on a standard laptop computer (with an Intel Core i7 2.4 GHz processor) with 2000 simulations, the calibration tool had to run for 36 h (for a model with 117 sub-basins). The speed performance of the calibration tool is strongly dependent on the complexity of the model (the number of sub-basins, HRUs, calibration parameters and simulated period), the processor's clock speed and some other factors, such as the speed of the hard drive and the architecture of the machine. Studies have shown that the calibration procedure's run time could be enhanced by enabling the parallel processing of the calibration tool (Rouholahnejad et al., 2012).

Calibration was carried out, accounting for spatial parameter variations in different basins (of the Minija and Nemunas Rivers) (see Fig. 3). Global model performance for the monthly run-off values of $NSE = 0.79$ and $R^2 = 0.81$ were achieved, which correspond to very good ratings (see Table 4). This model was subjected to further validation and used in the scenario assessment. SWAT-CUP produces a fitted parameter value table for the best simulation. Corresponding values are given in Table 5.

Some parameter values are similar for every sub-basin, whereas others differ substantially. This can be explained by the spatial distribution of sub-basins and their differences in soil, land-use and the topographic properties of the area. Since sub-basins and HRUs are spatial averaging over some area, the parameter values for the same catchment area will change as the sizes of sub-basins and HRUs change.

Defining proper parameter boundaries for parameters used in the calibration stage can be a challenging process. These ranges have a strong impact on the autocalibration outcome. In some SWAT model autocalibration studies (Arnold et al., 2012; Balascio et al., 1998; Moriasi et al., 2007), different parameter ranges are used for the same parameters that are subjected to calibration, but the explanation for such boundary usage is not always provided.

The high number of parameters complicates and prolongs the model's parameterization and calibration procedure, and can therefore be considered as a weakness of the model, especially if the soil and geological differences of the catchment area are not well known. This was the drawback for Curonian Lagoon basin model, as the soil and land-use data were acquired from public sources and not from local ones, which would be of better quality and backed-up by more recent observations. Different competences in various fields of study are required in order to fully assess the influence of each parameter and its value to the basin. A more detailed analysis of each parameter, not only those that are used in

Table 3 Most frequently used calibration parameters in various SWAT model calibration studies.

Parameter	Definition	Process
CN2	Initial Soil Conservation Service runoff curve number	Surface runoff
CH_K1	Effective hydraulic conductivity in tributary channel alluvium [mm h^{-1}]	
CH_K2	Effective hydraulic conductivity in main channel alluvium [mm h^{-1}]	
CH_N2	Manning's "*n*" value for the main channel	
ESCO	Soil evaporation compensation factor	
EPCO	Plant uptake compensation factor	
SURLAG	Surface runoff lag coefficient	
CANMX	Maximum canopy storage [mm H_2O]	
ALPHA_BF	Baseflow alpha factor [days]	Baseflow
GW_REVAP	Groundwater "revap" coefficient	
GW_DELAY	Groundwater delay time [days]	
GWQMN	Threshold depth of water in the shallow aquifer required for return flow to occur [mm H_2O]	
GWHT	Initial groundwater height [m]	
REVAPMN	Threshold depth of water in the shallow aquifer for "revap" or percolation to the deep aquifer to occur [mm H_2O]	
SFTMP	Snowfall temperature [°C]	Snow
SMFMN	Melt factor for snow on December 21 [mm H_2O °C-day^{-1}]	
SMFMX	Melt factor for snow on June 21 [mm H_2O °C-day^{-1}]	
SMTMP	Snowmelt base temperature [°C]	
TLAPS	Temperature laps rate [°C]	
SOL_Z	Depth from soil surface to bottom layer [mm]	Soil
SOL_AWC	Available water capacity of the soil layer	
SOL_ZMX	Maximum rooting depth of soil profile [mm]	
SOL_BD	Moist bulk density [Mg m^{-3}] or [g cm^{-3}]	
SOL_K	Saturated hydraulic conductivity [mm h^{-1}]	
SOL_ALB	Moist soil albedo for top layer	

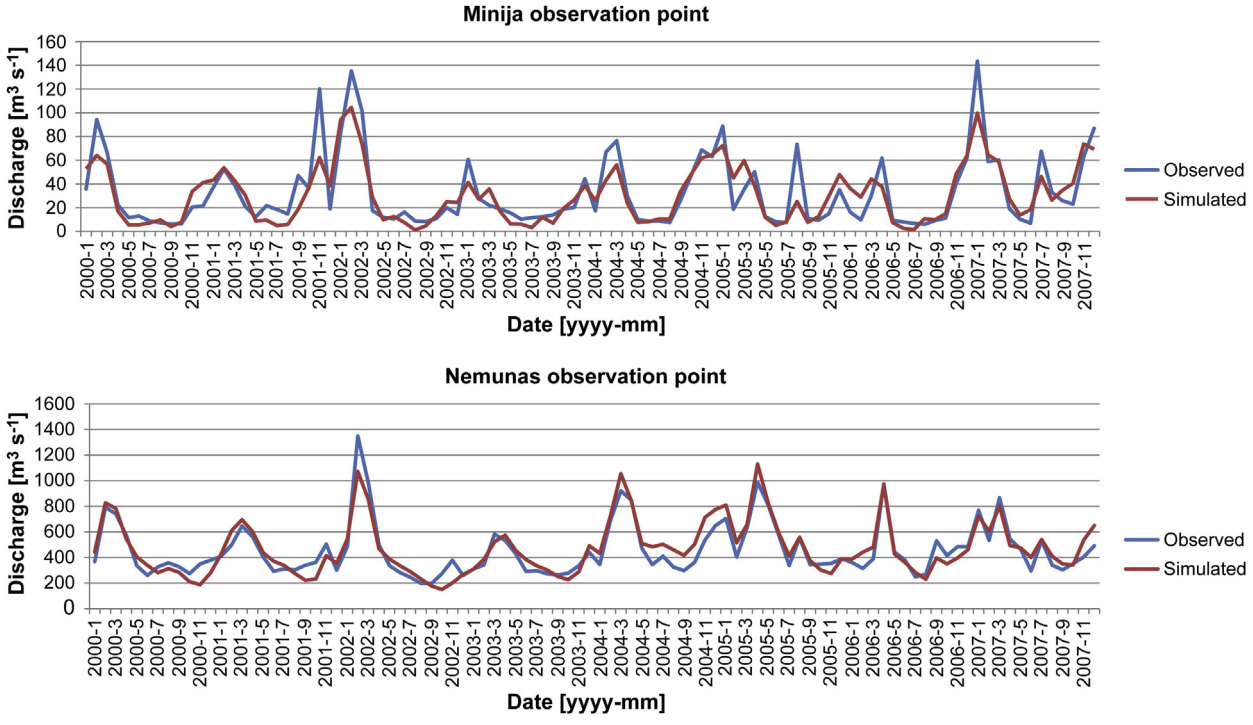

Figure 3 Calibration results for Minija and Nemunas river discharge.

Table 4 Statistics report for the calibration period (2000–2007) of the Curonian Lagoon drainage basin model.

Variable	*P*-factor	R^2	*NSE*	Mean (simulated) [$m^3 s^{-1}$]	StdDev (simulated) [$m^3 s^{-1}$]
FLOW_OUT (Minija)	0.28	0.77	0.76	32.61 (30.59)	29.99 (23.91)
FLOW_OUT (Nemunas)	0.38	0.85	0.84	455.91 (470.84)	204.85 (208.56)

this study, would benefit future developments of a Curonian Lagoon drainage-basin model.

2.4. Validation procedure

Validation results show whether the parameters were calibrated in such a way as to represent the modelled system adequately, in this case, the Curonian Lagoon's drainage area. The model's validation output can be analysed in the same way as the model calibration: a value for R^2 and *NSE* can be computed and the plot of the simulated flow, as compared to the observed flow, produced. After the successful validation of the model, it can be used for various purposes: monitoring seasonal and long-term trends, predicting any of the model's output elements under different conditions and scenarios and using outputs as inputs for other models.

Table 5 Fitted parameter values for the Curonian Lagoon drainage basin model.

Parameter[a]	Fitted parameter values	
	Nemunas sub-basin	Minija sub-basin
R[b]_CANMX.hru[c]	24.810646	−39.028244
R_CH_N2.rte	27.378458	37.603989
R_CN2.mgt	248.030533	−43.943916
R_SOL_ALB.sol	−0.964783	−19.724804
R_SOL_AWC.sol	−44.375572	−71.344315
R_SOL_BD.sol	−0.63497	−1.009578
R_SOL_K.sol	10.870995	−0.729487
R_SOL_Z.sol	1.501782	30.346178
R_SOL_ZMX.sol	36.707863	−35.845459
V_ALPHA_BF.gw	0.116285	1.178193
V_CH_K1.sub	199.661301	63.989532
V_CH_K2.rte	−11.417052	−53.535545
V_EPCO.bsn	0.651629	0.598089
V_ESCO.bsn	0.484453	0.799542
V_GW_DELAY.gw	279.003998	−72.274193
V_GW_REVAP.gw	0.143441	0.11155
V_GWHT.gw	14.892682	4.632501
V_GWQMN.gw	381.135162	803.918335
V_REVAPMN.gw	331.778961	18.785471
V_SMFMN.bsn	3.019845	9.110275
V_SMFMX.bsn	12.965604	9.025815
V_SMTMP.bsn	0.340758	0.831538
V_SURLAG.bsn	27.429886	8.502431
V_TLAPS.sub	2.980006	−8.614986

[a] Parameter definitions are given in Table 3.
[b] The qualifier (V_) refers to the substitution of a parameter by a value from the given range, while (R_) refers to a relative change in the parameter where the current value is multiplied by 1 plus a factor in the given range.
[c] The extension (.hru,.rte,.mgt,.sol,.gw,.sub,.bsn) refer to the SWAT file type where the parameter occurs.

The global Curonian Lagoon drainage area model validation results are $R^2 = 0.679$ and $NSE = 0.602$, which correspond to satisfactory values for the model at a monthly time-step. The validation result confirms that this area-specific hydrological model can produce sufficiently accurate predictions.

Although the required model performance objectives were met, validation results give an insight into possible errors in the output. The SWAT model was unable to predict the high amounts of run-off occurring in the spring months (for both observation points), and some peak flows were underestimated. The model failed to simulate the high amount of run-off that occurred in the late autumn and winter months (November–January) of 2008–2009 and 2009–2010 for both Minija and Nemunas (see Fig. 4). For improving the model's predictive accuracy, snowmelt and ice-formation parameter temperatures might be adjusted to account for early melting or late ice/snow formation.

2.5. Scenario formulation

Air temperature and the precipitation amount are the main climate elements directly affecting the total run-off of rivers. Prognostic air temperature, precipitation amount and humidity-change data, derived from the Intergovernmental Panel on Climate Change Fifth Assessment Report (IPCC AR5), were used with the SWAT for modelling river inflow changes.

Near-term projections from the General Circulation Model-Regional Climate Model (GCM-RCM) model chains for Europe were used for modelling precipitation and temperature changes. The analysis includes the following 10 GCM-RCM simulation chains for the Special Report on Emissions Scenarios' (SRES) A1B scenario (which includes the RCM group and GCM simulation): HadRM3Q0-HadCM3Q0, ETHZ-HadCM3Q0, HadRM3Q3-HadCM3Q3, SMHI-HadCM3Q3, HadRM3Q16- HadCM3Q16, SMHIBCM, DMI-ARPEGE, KNMI-ECHAM5, MPI-ECHAM5, DMI-ECHAM5 (Kirtman et al., 2013). The CMIP5 (Coupled Model Intercomparison Project, Phase 5) multi-model ensemble was used for the relative humidity change.

The current-condition scenario was carried out before implementation of the climate-change scenario simulations; the produced average monthly run-off values were considered as the baseline. In order to analyse the impacts of potential future climate change on the hydrology of the Curonian Lagoon drainage area, every scenario was implemented with downscaled, spatially variable climate inputs (air temperature precipitation, relative humidity) using the matching simulation period, which delivers a consistent foundation for comparison of the scenario outputs. The near-term change and projected changes described are for the period 2016–2035.

According to the summary of IPCC AR5, air temperature is going to increase by up to 1°C in winter, 0.5°C in spring and

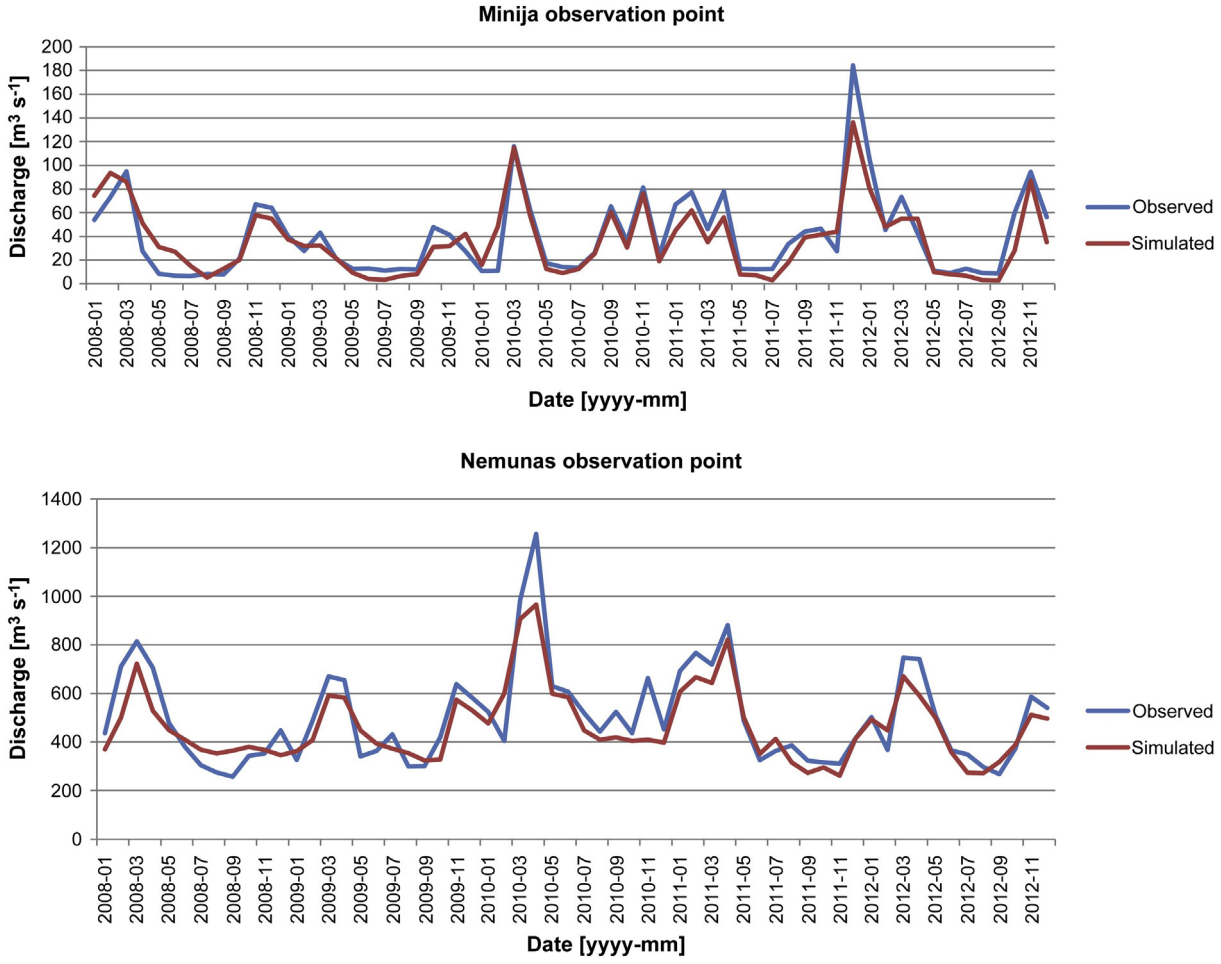

Figure 4 Validation result with the best fitted parameter value set for Minija and Nemunas river discharge.

autumn and 0.7°C in summer in the near-term; precipitation is expected to increase by 7.5% in winter, 5.0% in autumn and spring, and 2.5% in summer and humidity is likely to decrease slightly, by about 1% over most land areas (Kirtman et al., 2013). Two climate change scenarios, one pessimistic and one optimistic, were formulated (Table 6), and the effects of these scenarios on river run-off were explored. The pessimistic scenario includes high values for temperature and precipitation change, whereas the optimistic scenario's corresponding values were lower. Such scenarios were formulated for assessing the response of the study area to various conditions of climate change, and in order to determine the sensitivity of the modelled system.

3. Results

3.1. The pessimistic scenario's results

For the pessimistic scenario, high values of precipitation and temperature change were used to assess their effects on the Nemunas and Minija Rivers' run-off. For the Nemunas River, the projected changes in precipitation, temperature and

Table 6 Climate variable change in pessimistic and optimistic scenarios.

Scenario	Simulated changes in:						
	Temperature [°C]			Precipitation [%]			Relative humidity [%]
	DJF[a]	MAM, SON[b]	JJA[c]	DJF	MAM, SON	JJA	All seasons
Pessimistic	+2	+0.5	+0.7	7.5	5	2.5	−1
Optimistic	+0.6	+0.4	+0.3	3	1.5	0	−1

[a] "DJF" refers to winter months: December, January, February.
[b] "MAM" refers to spring months: March, April, May; "SON" refers to autumn months: September, October, November.
[c] "JJA" refers to summer months: June, July, August.

Table 7 Simulated inter-seasonal Nemunas and Minija river average (av), minimal (min), and maximal (max) discharge change for the pessimistic (^{P}) and optimistic (^{O}) scenario.

River	River discharge change [±%]											
	Winter			Spring			Summer			Autumn		
	av	min	max	av	min	max	av	min	max	av	min	max
^{P}Minija	22	21	23	−7	−28	−2	−18	−64	44	10	−10	23
^{P}Nemunas	17	20	1	−10	−24	−19	−8	−16	14	9	0.5	12
^{O}Minija	18	16	17	−5	−25	−8	−10	−65	−25	5	−18	20
^{O}Nemunas	10	8	1	−9	−32	−20	−2	−20	2	3	−3	2

humidity will result in a stronger inter-seasonal fluctuation of run-off. During the winter months, it is expected that the Nemunas River run-off will increase by 17% in the short term. The probable reason for this is the increased winter temperatures, which will result in earlier snowmelt. An increase in precipitation is also having a strong effect on run-off during the winter months. The peak run-off for the winter will experience no significant change, whereas the minimal run-off will increase by approximately 20% (see Table 7, Fig. 5), although the SWAT overestimated minimal run-off for the Nemunas River in some cases, so this percentage could be less.

For the Minija River, the effect of early snow melting is more prominent; the increase in discharge will be approximately 22%. Minimum and maximum discharges for the winter months will also increase by 21—23%. The strongest

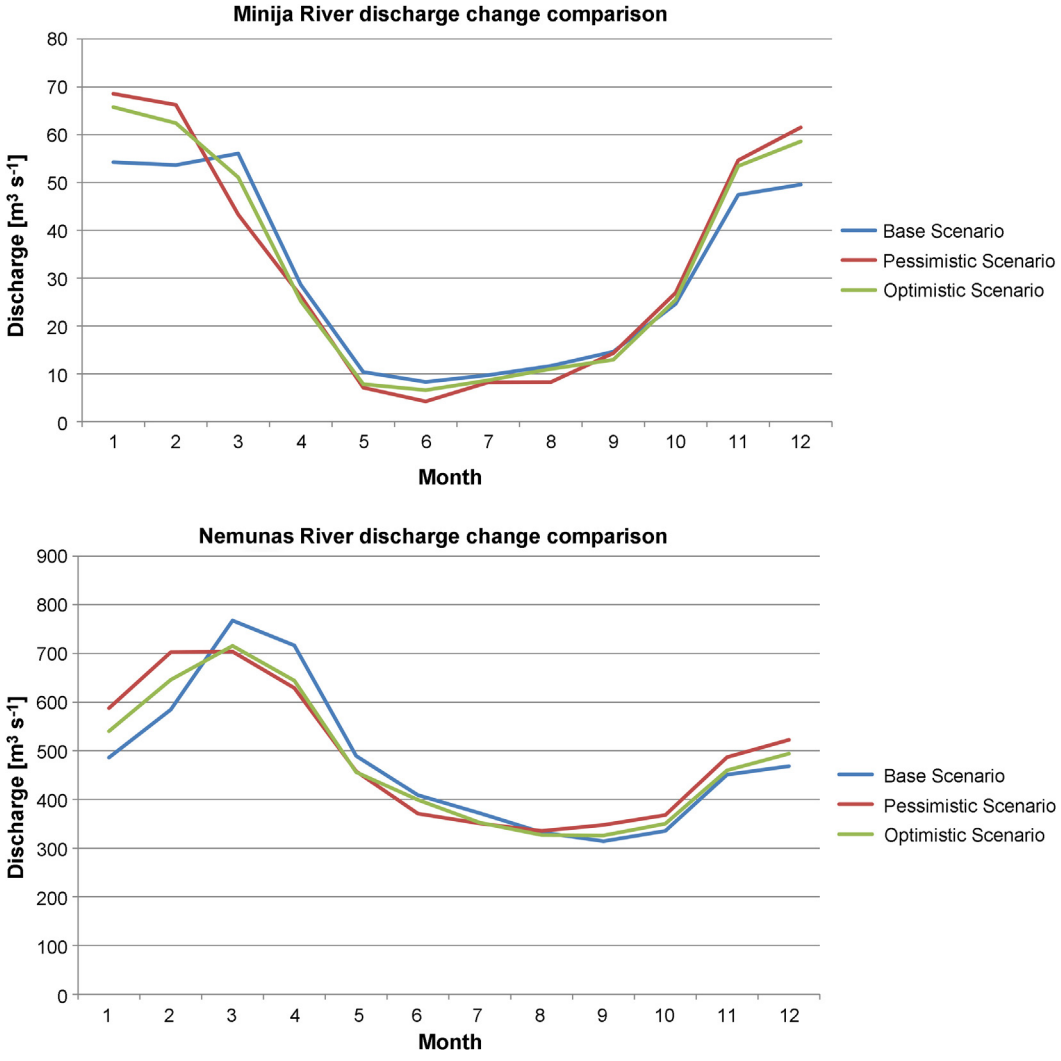

Figure 5 Monthly simulated discharges of base, optimistic, and pessimistic scenarios for Minija and Nemunas rivers.

increase of discharges for both rivers is observed in February, where the peak flow values are simulated to increase by more than 60%.

During spring months, a 10% decrease in run-off is expected for the Nemunas River and a 7% decrease is expected for the Minija River (Table 7, Fig. 5). This is caused by the ice-melting season moving to the winter months. The maximum spring discharges in Lithuanian rivers generally take place during March to April, but in the light of current climate change, these events will happen earlier. The strongest decrease in discharge during spring months is observed in May for Minija, whereas for Nemunas, it is observed in April.

The summer months are expected to be warmer; this has a significant negative impact on the discharge of rivers during this period. For Nemunas, it results in an 8% decrease in run-off, whereas for Minija, it results in an 18% decrease. The minimal and maximal discharge values vary: for Nemunas, peak flows during summer months will increase by 14%, but the minimal flow will decrease by 16%. For Minija, peak flows will increase by 44% and minimal flows will decrease by 64%. The highest discharge change is expected during June to July for Nemunas, and in July for Minija (see Fig. 5). Even if in some cases the model overestimated the values of peak flows and underestimated the minimal flows, the inter-seasonal differences between climate change and baseline scenarios are significant.

Discharge changes in the autumn months are less affected by climate change. During this period, the average discharge will increase by 10% for Minija and 9% for Nemunas. Maximal run-off will increase by 23% for Minija and by 12% for Nemunas. Minimal run-off will decrease by 10% for Minija and will not change significantly for Nemunas (Table 7). In the autumn months, the average discharge will increase for Nemunas during the whole season, with no distinct patterns. The Minija River's discharge, however, displays a decrease in the run-off during September, and a steady increase in the following months, reaching the highest increase during November (Fig. 5).

The annual discharge in the short term for the Nemunas River will increase by around 7%, and Minija's will increase slightly, by around 2—3%. These results confirm those of similar studies (Kriaučiunienė et al., 2008; Meilutytė-Barauskienė and Kovalenkovienė, 2007; Rogozova, 2006), which indicate a slight increase in annual river run-off in the near-term and a change in flood behaviour during the spring.

3.2. The optimistic scenario's results

For the optimistic scenario, low values of precipitation and temperature change were used to assess their effects on river run-off. As expected, results of the optimistic scenario show smaller changes than those of the pessimistic one, although their tendencies remain the same (see Table 7).

For both Nemunas and Minija, the expected river discharge will change mostly in the winter season: 18% for Minija and 10% for Nemunas. Minimal and maximal discharges during this season will increase by 16% and 17%, respectively, for the Minija River, while for Nemunas an increase of 8% in minimal discharge is expected, where the peak flows will remain at almost the same level. The increase in discharge is simulated during the entire season, with no distinct patterns for Minija. The strongest increase is observed during February for the Nemunas River.

During the spring months, a reduction in river flow is expected: 5% and 9% for Minija and Nemunas, respectively (Table 7). The maximal discharge will decrease by 8% and 20%, respectively, and the rivers' minimal discharges will decrease by even more: 25% and 32%. The strongest decrease in discharge is observed in April for Nemunas, and in May for Minija (Fig. 5).

During the summer months, a small increase in precipitation and a decrease in humidity were used in the optimistic scenario, with no change in the temperature. However, a decrease in the rivers' run-off was simulated: 10% for Minija and 2% for Nemunas (Fig. 5). This may be caused by the increased ET (evapotranspiration) and a higher water uptake by plants. The highest reduction in discharge is observed in the period of June to July for both rivers.

The autumn months will experience a small increase in river discharge: 5% for Minija and 3% for Nemunas. The peak and minimal flows will experience small fluctuations in both cases. A general decrease in run-off during September, compared to the baseline scenario, is simulated for Minija, with a gradual increase of flow in the following months. The Nemunas River's discharge displays a steady increase during September and October, with the highest values occurring in November. With this optimistic scenario, the annual discharge in the near-term for the Nemunas River will increase by around 5%, and by 2—3% for the Minija River.

4. Discussion

The SWAT is a very useful tool for investigating climate change's effects on the drainage basin, assessing management strategies on a catchment area's hydrological and water-quality response and other different scientific and practical uses. However, calibration and validation of the model is a key factor in reducing uncertainty and increasing confidence in its predicative abilities, thus making application of the model effective.

The Curonian Lagoon drainage basin model was successfully calibrated and validated, although some improvements to the results could be achieved in the future. During calibration, the model simulations generally underestimated high seasonal amounts of run-off for Minija, especially during the spring flood months of March to April. For both rivers, the model underestimated the amount of discharge during the months of June to August. This could be caused by some fitted parameters of groundwater or base-flow; an overestimation of plants' water uptake could also be the reason for these occurrences. Further improvements to the model could assess the influence of each parameter on the run-off separately, for acquiring a better understanding of the river-discharge governing processes for each sub-basin.

During the climate scenario evaluation, both optimistic and pessimistic scenario simulations produced similar general patterns in changes to river discharge: a strong increase in the winter months, especially in February, a decrease during spring and summer and a slight increase during autumn. It is noteworthy that even in the optimistic scenario, river discharges show a relatively high reduction during the spring months, meaning that the temperature threshold for

snowmelt can be reached even with a small increase in temperature (see Fig. 5).

Different climate-change factors have influenced the simulated changes in different ways. The relative humidity change has an impact on river discharges through an increase in water uptake by plants and ET. The share of the forested area in the Minija River's basin is approximately 21% (Kontautas and Matiukas, 2010), and about 35% for the Nemunas River's basin (Rimkus et al., 2013). Relative humidity can affect the flow of water through the plant: the higher the relative humidity, the more slowly transpiration occurs and vice versa. In the Curonian Lagoon drainage basin model, a reduction in relative humidity led to a reduction in river run-off during the summer months. This was the case even in the optimistic scenario, where higher precipitation values were used and the temperature values were not altered for this period. Relatively high absolute changes in minimal and maximal flows were simulated for the Minija River during the summer months, especially in the pessimistic scenario. Minija is a river dominated by rain floods in the run-off balance. This factor becomes even more distinct in the light of climate change, where heavy rain results in high local increases of generated discharge. Approximately half of the total run-off comes from rainwater; snow and groundwater comprise 22% and 25%, respectively, of the run-off. As a result of the earlier melting of snow, these values are projected to change accordingly.

A general tendency for potential hydrological droughts during the summer season is observed in both rivers. The Nemunas and Minija Rivers' basins lie under humid temperate climate conditions and cannot experience such water shortages as appear in the tropical and mid-latitudinal arid regions. Therefore, simulated dry periods and periods of low streamflow are interpreted here as droughts, because of the impact on wildlife and socio-economic factors (Rimkus et al., 2013) — a decrease in crop yields, a reduction in overall agricultural productivity, a massive increase in wildfires, an intensification of tree defoliation, etc.

The Minija River's sub-basin response to different climate-change factors was more significant than that of the Nemunas River, which displayed some robustness to projected changes. As smaller rivers in the Curonian Lagoon basin's western boundaries display a high correlation (0.76—0.97) in run-off and synchronicity in flood seasons (Meilutytė-Barauskienė and Kovalenkovienė, 2007), it is assumed that the changes in other, smaller rivers' sub-basins, such as the Deima River's sub-basin, will be similar to those simulated for the Minija River's sub-basin.

Possible future research directions may include improvement of the model's performance, a more thorough calibration and more detailed sensitivity and uncertainty analysis. In addition, the completed Curonian Lagoon drainage-basin model could be used to assess different climate-change, water-management and agricultural-management scenarios. The SWAT can be coupled with other models that require a hydrological input, in order to assess different management problems and scenarios.

As the SWAT model contains biogeochemical sub-models for nutrient transformation in its terrestrial and aquatic components, as well as plant growth and agricultural management operations, the model developed in this study can be upgraded to a full-featured drainage-basin model that can fill in the time-based gaps of monthly monitoring of the Nemunas River's outlet, giving an idea of what kind of variations occurred in the period of a month between two monitoring expeditions. With further research and additional calibration, this model can be used to simulate sediment, pesticide and nutrient transport in the basin. The model developed in this study can be linked to ecological-, biogeochemical- and sediment-transport models for the Curonian Lagoon. It can also support water-quality management studies of the Curonian Lagoon as well as scientific projects such as the ecological response of the Curonian Lagoon to different load conditions through the Nemunas River, or detailed studies of carbon, nitrogen and phosphorus budgets.

Acknowledgements

The authors wish to acknowledge the support of the Research Council of Lithuania for the project “Promotion of Student Scientific Activities” (VP1-3.1-ŠMM-01-V-02-003). The authors would also like to thank Klaipeda University's Open Access Centre for Marine Research for providing data and computational resources.

References

Abbaspour, K.C., 2011. SWAT-CUP2: SWAT Calibration and Uncertainty Programs Manual Version 2. User Manual. Department of Systems Analysis, Integrated Assessment and Modelling (SIAM), Eawag. Swiss Federal Institute of Aquatic Science and Technology, Duebendorf, Switzerland.

Arnold, J., Allen, P., Bernhardt, G., 1993. A comprehensive surface groundwater flow model. J. Hydrol. 142 (1—4), 47—69.

Arnold, J., Kiniry, J., Srinivasan, S., Williams, J., Haney, E., Neitsch, S., 2010. Soil and Water Assessment Tool Input/Output File Documentation, Version 2009. Texas Water Resourc. Inst. Tech. Rep. No. 365, 643 pp.

Arnold, J., Moriasi, D., Gassman, P., Abbaspour, K., White, M., Srinivasan, R., Santhi, C., Harmel, R., van Griensven, A., Liew, M.V., Kannan, N., Jha, M., 2012. SWAT: Model use, calibration and validation. Am. Soc. Agric. Biol. Eng. 55 (4), 1419—1508.

Balascio, C., Palmeri, D., Gao, H., 1998. Use of a genetic algorithm and multi-objective programming for calibration of a hydrologic model. Am. Soc. Agric. Biol. Eng. 41 (3), 615—619.

CGIAR — Consortium for Spatial Information. SRTM Data Search service, http://srtm.csi.cgiar.org/SELECTION/inputCoord.asp (accessed: February 2014).

Chaubey, I., Cotter, A., Costello, T., Soerens, T., 2005. Effect of DEM data resolution on SWAT output uncertainty. Hydrol. Process. 19 (3), 621—628.

Dubra, J., Červinskas, E., 1968. Freshwater balance of the Curonian Lagoon. Scientific Works of the High Schools. Geogr. Geol. 5, 19—26, (in Lithuanian).

ELLE, PAIC, 2012. Development of methodics and modelling system of nitrogen and phosphorus load calculation for surface waters of Lithuania. The 1st interim report of project, UAB Estonian, Latvian & Lithuanian Environment and SIA Procesu analīzes un izpētes centrs.

Gailiušis, B., Kovalenkovienė, M., Jurgelėnaitė, A., 1992. Water balance of the Curonian Lagoon. Energetika 2, 67—73.

Gassman, P., Reyes, M., Green, C., Arnold, J., 2007. The Soil and Water Assessment Tool: historical development, applications, and future research directions. Am. Soc. Agric. Biol. Eng. 50 (4), 1211—1250.

Ghaffari, G., 2011. The impact of DEM resolution on runoff and sediment modelling results. Res. J. Environ. Sci. 5 (8), 691—702.

Jakimavičius, D., 2012. Changes of water balance elements of the Curonian lagoon and their forecast due to anthropogenic and natural factors (Ph.D. thesis). Kaunas Univ. Technol.

Jakimavičius, D., Kovalenkovienė, M., 2010. Long-term water balance of the Curonian Lagoon in the context of anthropogenic factors and climate change. Baltica 23 (1), 33—46.

Kirtman, B., Power, S., Adedoyin, J., Boer, G., Bojariu, R., Camilloni, I., Doblas-Reyes, F., Fiore, A., Kimoto, M., Meehl, G., Prather, M., Sarr, A., Schar, C., Sutton, R., van Oldenborgh, G., Vecchi, G., Wang, H., 2013. Near-term climate change: projections and predictability. In: Climate Change 2013: The Physical Science Basis. Contribution of Working Group I to the Fifth Assessment Report of the Intergovernmental Panel on Climate Change. Cambridge University.

Kontautas, A., Matiukas, K., 2010. Environmental Problems and Challenges of the Minija River Towards a Sustainable Development of the River Basin. Watersketch Project Case Study Report. Coastal Research and Planning Institute, Klaipeda University.

Krause, P., Boyle, D.P., Base, F., 2005. Comparison of different efficiency criteria for hydrological model assessment. Adv. Geosci. 5, 89—97.

Kriaučiunienė, J., Meilutytė-Barauskienė, D., Rimkus, E., Kažys, J., Vincevičius, A., 2008. Climate change impact on hydrological processes in Lithuanian Nemunas river basin. Baltica 21 (1—2), 51—61.

Lin, S., Jing, C., Chaplot, V., Yu, X., Zhang, Z., Moore, N., Wu, J., 2010. Effect of DEM resolution on SWAT outputs of runoff, sediment and nutrients. Hydrol. Earth Syst. Sci. 7, 4411—4435.

Meilutytė-Barauskienė, D., Kovalenkovienė, M., 2007. Change of spring flood parameters in Lithuanian rivers. Energetika 53 (2), 26—33.

Moriasi, D., Arnold, J., Liew, M.V., Bingner, R., Harmel, R., Veith, T., 2007. Model evaluation guidelines for systematic quantification of accuracy in watershed simulations. Am. Soc. Agric. Biol. Eng. 50 (3), 885—900.

National Centers for Environmental Prediction. Climate Forecast System Reanalysis — Global weather database, http://globalweather.tamu.edu/ (accessed: November 2014).

Neitsch, S., Arnold, J., Kiniry, J., Williams, J., 2011. Soil and Water Assessment Tool. Theoretical Documentation. Version 2009. Texas Water Resourc. Inst. Theoretical Doc. 406, 618 pp.

Rimkus, E., Stonevčius, E., Korneev, V., Kažys, J., Valiuškevičius, G., Pakhomau, A., 2013. Dynamics of meteorological and hydrological droughts in the Neman river basin. Environ. Res. Lett. 8 (4), 045014.

Rogozova, S., 2006. Climate change impacts on hydrological regime in Latvian basins. In: Proceedings of the European Conference on Impacts of Climate Change on Renewable Energy Sources, 137—140.

Rouholahnejad, E., Abbaspour, K., Vejdani, M., Srinivasan, R., Schulin, R., Lehmann, A., 2012. A parallelization framework for calibration of hydrological models. Environ. Model. Softw. 31, 28—36.

United Nations Economic Commission for Europe, 2011. Second assessment of transboundary rivers, lakes and groundwaters: drainage basin of the Baltic Sea. Assessment report.

United Nations University. WaterBase project — Data for SWAT database, http://www.waterbase.org/download_data.html (accessed: November 2014).

Žilinskas, G., Jarmalavičius, D., Pupienis, D., Gulbinas, Z., Korotkich, P., Palčiauskaitė, R., Pileckas, M., Raščius, G., 2012. Curonian Lagoon coastal management study. Tech. Rep. Nature Heritage Fund, (in Lithuanian).

Oceanologia (2016) 58, 103—116

Available online at www.sciencedirect.com

ScienceDirect

journal homepage: www.elsevier.com/locate/oceano

ORIGINAL RESEARCH ARTICLE

Modeling the buoyancy-driven Black Sea Water outflow into the North Aegean Sea

Nikolaos Kokkos, Georgios Sylaios *

Department of Environmental Engineering, Democritus University of Thrace, Xanthi, Greece

Received 30 July 2015; accepted 29 December 2015
Available online 20 January 2016

KEYWORDS
Hydrodynamic model;
Remote sensing data;
Model validation;
Potential energy anomaly;
North Aegean Sea

Summary A three-dimensional numerical model was applied to simulate the Black Sea Water (BSW) outflux and spreading over the North Aegean Sea, and its impact on circulation and stratification—mixing dynamics. Model results were validated against satellite-derived sea surface temperature and in-situ temperature and salinity profiles. Further, the model results were post-processed in terms of the potential energy anomaly, ϕ, analyzing the factors contributing to its change. It occurs that BSW contributes significantly on the Thracian Sea water column stratification, but its signal reduces in the rest of the North Aegean Sea. The BSW buoyancy flux contributed to the change of ϕ in the Thracian Sea by 1.23×10^{-3} W m^{-3} in the winter and 7.9×10^{-4} W m^{-3} in the summer, significantly higher than the corresponding solar heat flux contribution (1.41×10^{-5} W m^{-3} and 7.4×10^{-5} W m^{-3}, respectively). Quantification of the ϕ-advective term crossing the north-western BSW branch (to the north of Lemnos Island), depicted a strong non-linear relation to the relative vorticity of Samothraki Anticyclone. Similar analysis for the south-western branch illustrated a relationship between the ϕ-advective term sign and the relative vorticity in the Sporades system. The ϕ-mixing term increases its significance under strong winds (>15 m s^{-1}), tending to destroy surface meso-scale eddies.

* Corresponding author at: Vas. Sofias 12, 67100 Xanthi, Greece. Tel.: +30 25410 79398; fax: +30 25410 79398.
E-mail address: gsylaios@env.duth.gr (G. Sylaios).
Peer review under the responsibility of Institute of Oceanology of the Polish Academy of Sciences.

Production and hosting by Elsevier

http://dx.doi.org/10.1016/j.oceano.2015.12.003

1. Introduction

The North Aegean Sea (NAS) (Fig. 1) acts as a dilution basin, directly affected by the buoyancy outflow of the low-salinity, nutrient-rich Black Sea Water (BSW) exported through the Dardanelles Strait, at the north-eastern part of the basin (Androulidakis and Kourafalou, 2011). Along the Dardanelles, a strongly-stratified two-layer system with opposing flows is formed, consisting of the exiting to the NAS surface BSW layer and the outflowing into the Sea of Marmara bottom layer (Ünlüata et al., 1990). The significant vertical shear stresses developed at the system's interface favor the upward entrainment, thus returning parts of NAS water back to the Aegean (Karnaska and Maderich, 2008). Recent estimates of the annual BSW discharge report values ranging between 38,820 $m^3 s^{-1}$ (Karnaska and Maderich, 2008) and 42,790 $m^3 s^{-1}$ (Tuğrul et al., 2002), with approximately 67% of its volume being directly transferred from the Marmara Sea and 33% attributed to NAS water entrainment. After its outflow, BSW occupies the first 50 m of the water column, overlying on the northward flowing warm and highly saline Levantine Intermediate Water (LIW), between a depth of 50 m and 400 m, and the North Aegean Deep Water (NADW) from 400 m to the bottom (Zervakis et al., 2000). Its impact on surface dynamics of NAS exhibits strong seasonality, especially during early spring, when the mean monthly outflux through the Dardanelles Straits reaches 450 km^3 per season (57,740 $m^3 s^{-1}$), as a result of the increased river runoff and precipitation over the Black Sea and the raised local entrainment fluxes at the Dardanelles (Tuğrul et al., 2002).

The exit of BSW from the Dardanelles produces a cyclonic flow, bifurcating at Lemnos Island, with the southern branch being stronger during the summer, under the influence of the annual northerly Etesian winds, and the northern branch covering the entire Thracian Sea continental shelf (Vlasenko et al., 1996; Zervakis and Georgopoulos, 2002). In winter BSW core concentrates at the northern coast of Lemnos Island, where it bifurcates primarily to the north-west and occasionally to the southwest, under the influence of north-easterly (bora-type) gales. The most prominent surface patterns in NAS include the thermohaline BSW-LIW frontal zone,

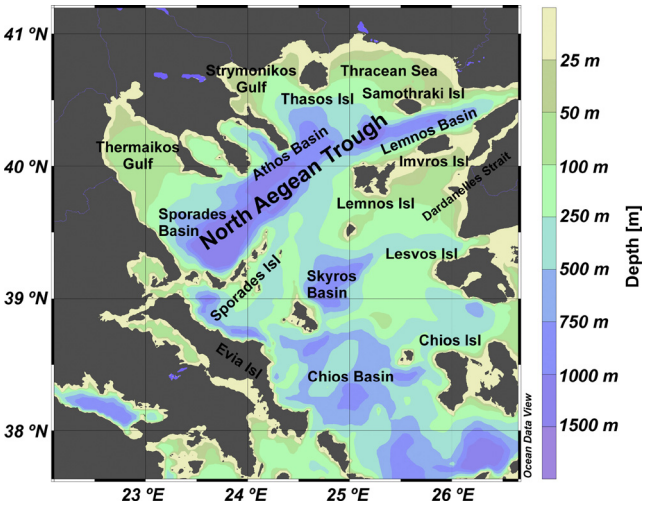

Figure 1 The North Aegean Sea and its physiographic basins.

affected strongly by seasonal meteorology (Sylaios, 2011), a semi-permanent anticyclone of variable strength and dimensions developed in the Thracian Sea, around Samothraki and possibly Imvros Islands (Cordero, 1999; Theocharis and Georgopoulos, 1993; Zervakis and Georgopoulos, 2002) and a rapidly changing cyclone–anticyclone system, covering the upper 200 m of the Sporades Basin. This latter system appears supplied either by the higher salinity waters moving from the southern Aegean Sea or by the fresher water of BSW (Kontoyiannis et al., 2003). Other eddy features of variable strength and size appear dependent on BSW discharge and Thermaikos Gulf freshwater outflows (Olson et al., 2007).

Several previous modeling efforts exist, using mostly the Princeton Ocean Model (POM), applied under variable spatial resolution grids and different boundary conditions for the BSW outflux. Zodiatis et al. (1996) used a two-dimensional vertically-integrated model to simulate the synoptic-scale flow patterns of the NAS and utilized NOAA-AVHRR thermal images for model validation. Korres et al. (2002) coupled a high resolution atmospheric model with POM and assessed model's skill in forecasting the satellite-recorded sea surface temperature (SST) field. Kourafalou and Barbopoulos (2003) used the modified sigma-coordinated POM in a high resolution mode (2.5 km × 2.5 km), nested at its southern boundary to a coarse grid Mediterranean model and a regional, intermediate resolution model. BSW discharge boundary condition was determined by the net monthly inflow-outflow budget at the Dardanelles, ranging from 5000 $m^3 s^{-1}$ in December to 15,000 $m^3 s^{-1}$ in June. Kourafalou and Tsiaras (2007) applied POM in a 1.6 km × 1.6 km grid imposing a two-layer (inflow-outflow) transport rate at the Dardanelles boundary. Tzali et al. (2010) applied POM in a series of BSW outflow scenarios, to assess the impact of BSW inflow rate on the established NAS circulation. Finally, Androulidakis and Kourafalou (2011) applied the Hybrid Coordinate Ocean Model (HYCOM) on a very high resolution grid (1/50° × 1/50°) and introduced a new mathematical scheme for BSW outflow rates. Model validation involved the comparison of model results to satellite and in situ data.

The present paper presents the results of a three-dimensional hydrodynamic model for the thermohaline NAS circulation, placing particular emphasis on (a) the model validation procedure, by comparing surface model results with extensive satellite datasets and CTD profiles from field campaigns, (b) the stratification–mixing conditions of BSW along its route over NAS, (c) the quantification of individual terms of the potential energy anomaly general equation, and (d) the description of the permanent and semi-permanent surface meso-scale patterns, developed in NAS and their inter-link to BSW buoyancy spreading.

2. Material and methods

2.1. Model description

The hydrodynamic Estuary and Lake Computer Model (ELCOM), a three-dimensional numerical model developed by the Centre for Water Research at the University of Western Australia (Hodges and Dallimore, 2001) was used for modeling the NAS. This model has mostly been used to simulate the hydrodynamics of lakes and reservoirs, but it has also been

applied in the modeling of buoyancy fluxes and geophysical flows at large-scale enclosed basins, estuaries and coastal seas, as the Persian Gulf (Alosairi et al., 2011), the Northern Adriatic Sea (Spillman et al., 2007) and the Red Sea (Barry et al., 2009). Kopasakis et al. (2012) modeled successfully NAS water circulation and pollutants accumulation, while Kamidis et al. (2011) validated the model to simulate the transport and diffusion processes in Nestos River plume. Further, Sylaios et al. (2013) utilized the above model-validated results to assess the along- and cross-shore circulation and the stratification-destratification processes in the shallow and elongated Thassos Passage (Thracian Sea).

ELCOM solves the Reynolds-Averaged Navier Stokes equations, using both the hydrostatic and the Boussinesq approximations. The numerical method applies a semi-implicit formulation on a finite-volume framework using rectangular Cartesian cells in an Arakawa-C grid stencil (Hodges, 2000). Horizontal grid spacing is fixed, whereas the vertical spacing may vary as a function of depth, but remains horizontally uniform and fixed over time. Free-surface evolution in each grid cell's column is solved by the vertical integration of the conservation of mass equation for incompressible flow applied to the kinematic boundary condition.

The numerical scheme follows the adapted TRIM approach (Casulli and Cheng, 1992) with modifications for scalar conservation, numerical diffusion, and implementation of a mixed-layer turbulence closure (Hodges, 2000). Convective terms are calculated using a third order Euler—Lagrange scheme, while the ULTIMATE-QUICKEST scheme is introduced for the advection of scalars. The model produces the dynamics of stratified water bodies with external environmental forcing, such as tidal forcing, wind stresses, surface thermal forcing as well as inflows and outflows (Hodges and Dallimore, 2001) and thus seems appropriate for application in NAS. Heat exchange through the water's surface is governed by standard bulk transfer models corrected for non-neutral atmospheric stability effects (Imberger and Patterson, 1990). The model does not follow the commonly-used eddy diffusivity approach, but adopts a unique 1D mixed-layer model for computing the vertical mixing of momentum and scalars (Laval et al., 2003), an approach particularly proper for stratified water bodies as NAS.

2.2. NAS model set-up

2.2.1. Bathymetry and computational domain

Model domain extends from 38.6°N to 41.0°N and from 22.5°E to 27.0°E, thus covering both shelf and deep areas of NAS (Fig. 1). The bottom bathymetry was digitized in a Geographic Information System (MapInfo v10.0), to develop a Digital Elevation Model (DEM) from the Hellenic Navy 1:200,000 bathymetric chart. Model's computational grid was developed using a spatial mapping tool (Vertical Mapper for MapInfo) and the application of linear triangulation interpolation. The modeled area was discretized into a uniform high resolution horizontal grid consisting of 1 km × 1 km orthogonal cells (0.009° × 0.009°), allowing the accurate representation of area's complex bathymetry and topography. The water column at each horizontal cell was divided into 20 exponentially stretched layers, consisting of thinner surface layers with gradually increasing thickness towards the bottom. All variables were located at fixed z-levels (z-coordinate model), thus producing a computational domain comprised by 3,109,280 rectangular finite-volumes.

2.2.2. Initial and boundary conditions

A constant initial condition over the grid domain (T = 10°C and S = 38.0 psu) was determined for the ambient water of NAS. Model boundary conditions involved hydrologic, meteorological and tidal forcing. Hydrologic forcing was determined on a mean monthly basis by applying river discharge and water temperature for all main rivers of Greece and Turkey, as reported by Skoulikidis et al. (1998). BSW buoyancy flux was considered seasonally variable, with a mean annual value of 42,222 $m^3 s^{-1}$ or 1331 $km^3 yr^{-1}$, as computed by Tuğrul et al. (2002). BSW daily temperature was extracted from MODIS SST satellite data for the Sea of Marmara. BSW salinity at the Dardanelles boundary varied seasonally, with a mean annual value of 28.03 psu, following Türkoğlu (2010).

Meteorological time-series for a four-year period (2005—2008) with a 3 hrs time-step were acquired from the NOAA database (http://ready.arl.noaa.gov/READYamet.php) at 1° × 1° spatial resolution, to describe the atmosphere-ocean boundary conditions. Datasets included wind speed and direction, atmospheric relative humidity, cloud cover, barometric pressure, atmospheric temperature, precipitation and solar radiation intensity.

Boundary temperature, salinity, currents and tidal elevations at the southern model boundary were obtained from daily MyOcean products (www.myocean.eu) using the Mediterranean Sea Physics Re-analysis database (1987—2012). Water temperature, salinity and velocity profiles were acquired at 72 layers with a daily time-step at a spatial resolution of 0.0625° along the southern boundary line of the model's computational grid. Initially, these profiles were vertically spline-interpolated to match the layered configuration of ELCOM model. At a second stage, a horizontal interpolation algorithm, applied to each layer, filled the gaps of horizontal model's discretization.

The NAS model was run for four consecutive years with a time-step of 3 min. Year one (2005) was used to develop and stabilize the flow field, especially due to BSW entry, while years 2006—2008 to obtain, compare and post-process model results. These consisted of the three-dimensional flow field, the temperature and salinity fields and the sea-surface height evolution.

2.3. Model validation procedure and criteria

Model validation was achieved in two manners: (a) by comparing sea-surface temperature model results at 44 regularly-spaced model grid cells with the SST data obtained by the International Group for High Resolution SST (GHRSST, www.ghrsst.org), a platform combining daily updates of near-real-time level 2 data (SSTs at observed pixels), level 3 data (gridded in space, but with no gap-filling) and level 4 data (gap-free objective analysis data), with a 0.25° × 0.25° spatial resolution (Martin et al., 2012); and (b) by comparing model produced temperature and salinity profiles with the 2006 CTD casts of summer NAS cruises (Sylaios, 2011; Sylaios, unpublished data).

To evaluate the validity of model results with satellite and in-situ data, a set of criteria was established (Jedrasik, 2005):

(a) the correlation coefficient, r, defined as:

$$r = \frac{\mathrm{cov}(o_i, m_i)}{\sigma_o \sigma_m} = \frac{\overline{o_i m_i} - \overline{o}\ \overline{m}}{\sigma_o \sigma_m}, \quad (1)$$

where o_i and m_i represent the observed and modeled paired values (with $i = 1, 2, \ldots, N$), respectively, and $\overline{o}$, $\overline{m}$ and σ_o and σ_m the respective means and standard deviations of the observed and modeled datasets. This is the non-dimensional measure of co-variation of the observed and modeled values, reaching its maximum at unity. Such criterion is insensitive to the total model bias.

(b) the mean squared error, MSE, defined as:

$$\mathrm{MSE} = \sigma_o^2 \left[(1 - r^2) + \left(\frac{\sigma_m}{\sigma_o} - r \right)^2 + \frac{(\overline{m} - \overline{o})^2}{\sigma_o^2} \right], \quad (2)$$

where the first term is the squared correlation coefficient; the second term describes the conditional model bias C, expressing the correlation between model error and the values simulated by the model; and the third term the unconditional model bias B, defined as the ratio of absolute bias to the squared standard deviation of the observations. For increased model reliability MSE should be minimum.

(c) the Nash-Sutcliffe effectiveness coefficient E, defined as:

$$E = 1 - \frac{\mathrm{MSE}}{\sigma_o^2}. \quad (3)$$

It is considered as a dimensionless transformation of MSE, also called a quadratic model score. Its value increases up to unity with increasing model quality.

(d) the special correlation coefficient:

$$R_s = \sqrt{1 - \frac{\mathrm{MSE}}{\sigma_o^2 + \overline{m}^2}}. \quad (4)$$

A perfect fit is reached when $R_s = 1$, meaning that MSE = 0. R_s better represents the fitting of model simulations to the observed ones, compared to the total square error (Jedrasik, 2005), and

(e) the mean modified model bias, defined as the ratio of the mean modeled to the mean observed counterpart, indicating the over- or under-estimation tendency of the simulations.

2.4. Model results post-processing

To assess the impact of BSW buoyancy flow path over the near-surface water column (0—200 m depth) of NAS, the potential energy anomaly ϕ (PEA, in J m^{-3}) was considered through model results. PEA-values express the stability of the water column, defined as the amount of energy per unit volume needed to vertically homogenize the water column, as (Simpson, 1981):

$$\phi = \frac{1}{h} \int_{-h}^{0} gz(\overline{\rho} - \rho)\, dz, \quad (5)$$

where g is the gravitational acceleration [m s^{-2}], z is the vertical coordinate pointing upward at the sea surface [m], $\overline{\rho}$ is the depth-averaged density [kg m^{-3}], ρ is the local density [kg m^{-3}] at depth z, and h is the total water depth [m]. By definition ϕ is depth independent, but it varies horizontally and in time. It occurs that ϕ is zero for a fully-mixed water column, and positive for stable stratification.

Although PEA explains the instant state of water column in terms of mixing and stratification, the temporal change of PEA may explain the interacted processes related to mechanical mixing (wind and tidal stirring) and stratifying mechanisms as the solar heat flux and the freshwater buoyancy flux (Simpson et al., 1991). Therefore, the change of PEA in time may be expressed as:

$$\left\{ \frac{\partial \phi}{\partial t} \right\}_{\mathrm{TOTAL}} = -\frac{\delta k_s \rho_a |W^3|}{h} - \frac{\epsilon k_b \rho_w |u_b^3|}{h} + \frac{\alpha g Q_S}{2 C_p} + \frac{1}{320} \times \frac{g^2 h^4}{N_Z \rho_w} \left(\frac{\partial \rho_w}{\partial x} \right)^2, \quad (6)$$

where the first term represents the wind stirring influence and the second term represents the tidal stirring effect, both tending to decrease ϕ over time. δ and ε are empirically determined mixing coefficients ($\delta = 0.039$ and $\varepsilon = 0.0038$) expressing the efficiency in the conversion of wind and the tidally-generated turbulent kinetic energy into potential energy (Lund-Hansen et al., 1996), k_s and k_b are the surface and bottom drag coefficients ($k_s = 6.4 \times 10^{-5}$ and $k_b = 2.5 \times 10^{-3}$), ρ_a is the air density (1.2 kg m^{-3}), ρ_w is the water density [kg m^{-3}], h is the water column depth [m] and W and u_b represent the wind speed [m s^{-1}] and bottom current velocity [m s^{-1}]. The third and fourth terms express the stratifying solar heat flux and freshwater buoyancy flux, respectively, tending to increase the ϕ-value in time. α and C_p are thermal expansion coefficients ($\alpha = 1.6 \times 10^{-4}$°C^{-1} at 9°C and $C_p = 4.0 \times 10^3$ J kg^{-1} °C^{-1}), g is the gravity acceleration [m s^{-2}], Q_S is the incident solar heat flux at the sea surface [W m^{-2}] and N_Z is the vertical eddy viscosity coefficient [m^2 s^{-1}], determined as $N_Z = \gamma h u$, where $\gamma = 3.3 \times 10^{-3}$ and u the depth-averaged tidal speed [m s^{-1}].

In order to derive the relative impact of each individual term on the change of the potential energy anomaly of NAS water column, the combined Eq. (6) was integrated in time, for a period of a month, using the mean daily values of respective parameters, thus:

$$\phi_{\mathrm{TOTAL}} = -\delta k_s \rho_a \left(\frac{1}{h} \right) \int_0^t |W|^3\, dt + \frac{\alpha g}{2 C_p} \int_0^t Q_S\, dt + \frac{1}{320} \times \frac{g^2 h^4}{N_Z \rho_w} \int_0^t \left(\frac{\partial \rho_w}{\partial x} \right)^2 dt - \epsilon k_b \rho_w \frac{1}{h} \int_0^t |u_b|^3\, dt, \quad (7)$$

where terms 1 to 4 refer to the relative impact of the wind, the incident solar radiation, the BSW buoyancy flux and the tide on the total potential energy anomaly of the water column. The term $(\partial \rho_w / \partial x)$ refers to the model-computed depth-averaged (0—200 m) density gradient between BSW exit point at the Dardanelles and each selected studied site throughout NAS. The impact of the tidal term was considered as negligible for the micro-tidal environment of NAS.

2.5. Relative contribution of PEA equation terms along a meridional transect

To comprehend the impact of advection of BSW pulses on NAS, the relative magnitude of each term in the general dynamic ϕ-equation was quantified, utilizing the ELCOM model results for the upper 130 m layer, corresponding to the upper 5 layers, along a meridional transect. The general ϕ-equation derived by Burchard and Hofmeister (2008) reads:

$$\frac{\partial\phi}{\partial t}=\underbrace{-\nabla_h(\overline{u}\phi)}_{A}+\underbrace{\frac{g}{h}\nabla_h\overline{\rho}.\int_{-h}^{0}\tilde{u}z\,dz}_{B}-\underbrace{\frac{g}{h}\int_{-h}^{0}\left(\eta-\frac{h}{2}-z\right)\tilde{u}\cdot\nabla_h\tilde{\rho}\,dz}_{C}$$
$$\underbrace{-\frac{g}{h}\int_{-h}^{0}\left(\eta-\frac{h}{2}-z\right)\tilde{w}\partial_z\tilde{\rho}\,dz}_{D}+\underbrace{\frac{\rho_0}{h}\int_{-h}^{0}P_b\,dz}_{E}-\underbrace{\frac{\rho_0}{2}(P_b^s+P_b^b)}_{F}$$
$$\underbrace{+\frac{g}{h}\int_{-h}^{0}\left(\eta-\frac{h}{2}-z\right)Q\,dz}_{G}+\underbrace{\frac{g}{h}\int_{-h}^{0}\left(\eta-\frac{h}{2}-z\right)\nabla_h(K_h\nabla_h\rho)\,dz}_{H}, \tag{8}$$

where $\overline{u}$ and $\tilde{u}$ are the depth-averaged and the deviation from the depth-mean horizontal velocity vectors, respectively [m s^{-1}], $\tilde{w}$ is the deviation from depth-mean vertical velocity [m s^{-1}], η is the elevation of sea surface above the mean [m], $\overline{\rho}$ and $\tilde{\rho}$ are the depth-averaged and the deviation from the depth-mean densities, respectively [kg m^{-3}], ρ_0 is the reference density [kg m^{-3}], Q is the source term for density due to heating [W m^{-2}], K_h is the horizontal eddy diffusivity [m^2 s^{-1}], P_b is the vertical buoyancy flux (=$(g/\rho_0)K_Z(\partial\rho/\partial z)$), while P_b^s and P_b^b are the surface and bottom buoyancy fluxes [m^2 s^{-3}], respectively, and ∇_h is the horizontal gradient operator.

In the above equation the described processes are: ϕ-advection (term A), representing the advection of potential energy anomaly by the depth-averaged horizontal velocity vector; the depth-mean straining (term B), representing the straining of the depth-averaged horizontal density gradient due to the deviation from the depth-mean velocity vector; the non-mean straining (term C), representing the straining produced by the deviation from the depth-averaged horizontal density gradient; the vertical advection (term D), produced by the deviation from the linear vertical velocity proceeding from the kinematic boundary conditions imposed on the water column surface and bottom; the vertical mixing (term E), expressed by the integrated vertical buoyancy flux; the surface and bottom density fluxes (term F), both increasing ϕ; the heating due to short-wave radiation (term G), representing inner sources or sinks of potential density; and the divergence of horizontal turbulent density fluxes (term H), increasing ϕ at the upper half of the water column.

For our analysis, only terms A, B, C, E, F and G were accounted for as the most important factors controlling the stratification–mixing dynamics of the area. Following Hoitink et al. (2011), contributions from the temporal and spatial variations of vertical velocity in the deviation of mean density (term D) and the impact on stratification from the horizontal divergence of horizontal turbulent density fluxes (term H) were considered as negligible.

Term E (vertical mixing) was simplified into:

$$\left(\frac{\partial\phi}{\partial t}\right)_{\text{Term-E}}=-C_d\Gamma\rho_0\frac{|\overline{u}^3|}{h}, \tag{9}$$

where C_d is the drag coefficient (=0.0025) and Γ is the mixing efficiency coefficient (=0.04).

Terms F and G involving inner sources of density due to absorption of solar radiation and the surface and bottom buoyancy fluxes appear dominated by surface heating. These terms could be parameterized according to Wiles et al. (2006), involving meteorological data (derived from NOAA database) as the incoming short wave radiation, relative humidity, wind speed and sea albedo for the derivation of the upward heat flux due to evaporation, the long-wave back radiation and the sensible heat transfer, as following:

$$\left(\frac{\partial\phi}{\partial t}\right)_{\text{Terms F\&G}}=\frac{\alpha g}{2C_p}(Q_S'T-Q_u), \tag{10}$$

where C_p is the heat capacity (=4.0 $\times$ 10^3 J kg^{-1}°C^{-1}), α is the thermal expansion coefficient (=1.51 $\times$ 10^{-4} K^{-1}), Q_S' is the sub-surface incident solar radiation, T is the heat released when radiation reaches the sea bottom, and Q_u is the sum of upward heat flux due to evaporation, long-wave back-radiation and sensible heat flux ($Q_u = Q_E + Q_B + Q_C$). Q_S' is determined by $Q_S' = Q_S(1-A)$, where A is the sea surface albedo (=0.15) and Q_S is the incident solar radiation. T is computed as a function of the effective diffusive attenuation coefficient for short wave radiation (k = 0.3) and total water depth, as:

$$T=1-\frac{2(1-\alpha_1)}{kh}(1-e^{-kh}), \tag{11}$$

where α_1 = 0.55, representing the fraction of heat absorbed at the thin surface layer. The upward heat flux terms were determined using relative humidity and wind velocity data from NOAA database combined with sea surface temperature data from the ELCOM model and applying the standard heat flux formulas (Gill, 1982). All calculations were performed in MATLAB 10.

3. Results

3.1. Model results validation

At the first validation stage, daily-averaged SST model results were compared to satellite recorded SST daily data obtained from the GHRSST dataset (n = 365 per year). For each station, the produced scatter points followed closely the diagonal in the simulated–observed data plots (Fig. 2a and b), providing quite successful statistical measures. The spatially-mean validation criteria, presented in Table 1, indicate that model's performance improves over time (years 2006–2008). Mean conditional and unconditional model biases of the mean squared error for all these years were computed at 0.040 and 0.099, respectively. From years 2006 to 2008 the mean modified model bias turns from over- to slight under-estimation of the satellite-derived SST (Table 1). This performance varies spatially and temporally. In the Thracian Sea slight winter and autumn over-estimation exists, changing to fair under-estimation in spring and summer (Fig. 2c). Summer under-estimation appears more prominent in the Sporades

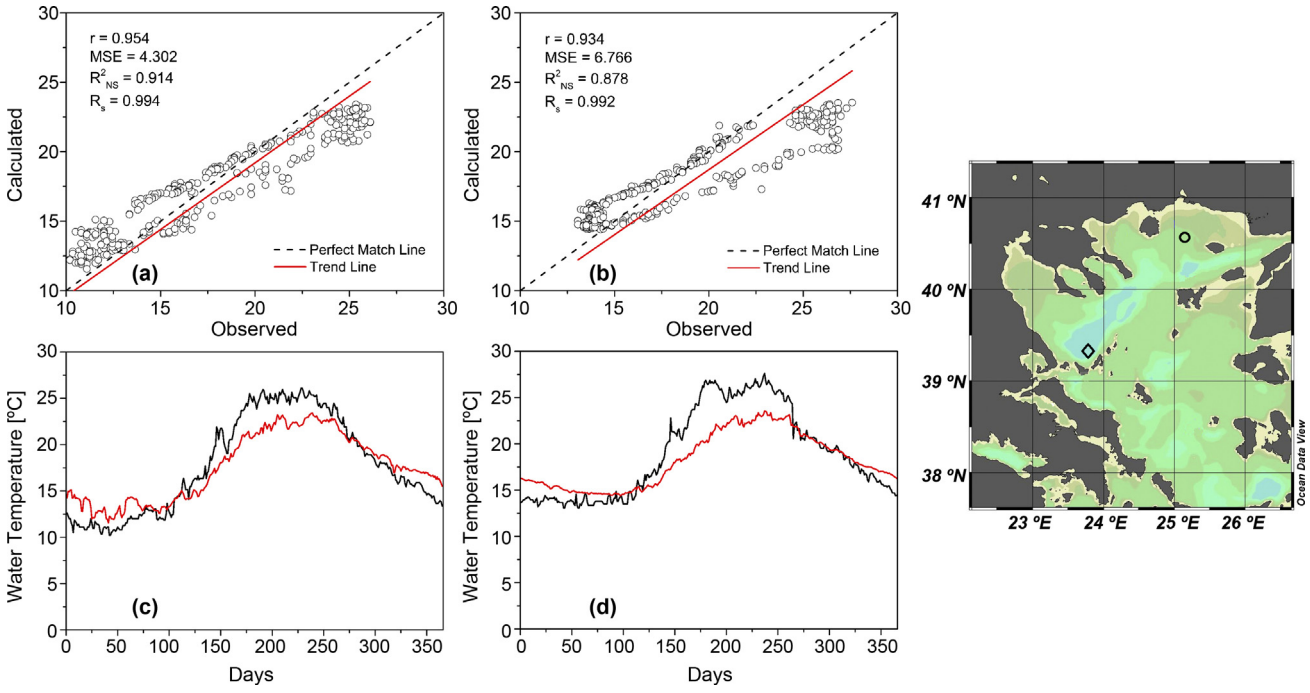

Figure 2 Scatter diagrams and temporal variability between the modeled and the GHRSST sea-surface temperature data during 2008. Subplots (a) and (c) compare data in the Thracian Sea (circle), and (b) and (d) in the Sporades Basin (diamond).

Basin (Fig. 2d). Such underestimation could also be attributed to the daily-averaging of modeled data, the impact of relatively poor meteorological conditions resolution and the fixed horizontal eddy viscosity and diffusivity coefficients. Fig. 3 illustrates the spatial variability in the model validation statistical measures for year 2008. Higher correlation coefficients were obtained in the Thracian Sea and Thermaikos Gulf, where the model slightly under-estimated observations. Lower correlation but improved modified bias was achieved in the central parts of NAS and in the Chios Basin.

Table 1 Spatially-mean statistical measures for ELCOM model validation in terms of SST.

Parameter	2006	2007	2008
Satellite-derived SST			
Correlation coefficient, r	0.917	0.924	0.941
Mean squared-error, MSE	4.985	5.060	3.838
Nash-Sutcliffe effectiveness coefficient, E	0.774	0.779	0.818
Special correlation coefficient, R_s	0.993	0.993	0.995
Modified model bias, MMB	1.063	1.024	0.966
	Temperature		Salinity
Year 2006 CTD casts			
Correlation coefficient, r	0.859		0.794
Mean squared-error, MSE	6.410		1.383
Nash-Sutcliffe effectiveness coefficient, E	0.402		0.138
Special correlation coefficient, R_s	0.990		0.999
Modified model bias, MMB	0.921		0.975

At the second validation stage, the model's ability to reproduce the vertical distribution of temperature and salinity fields was tested. Year 2006 CTD casts in NAS (103 sampling sites) were compared to temperature and salinity model results, up to 200 m depth. In-situ data were initially layer-averaged, to match model discretization, and then directly compared to model outputs (n = 457). Validation statistics shown in Table 1 indicate a rather good agreement and a fair under-estimation of in-situ observed variables. Indicative comparative profiles of water temperature and salinity for sites in Thracian Sea and Sporades Basin are shown in Fig. 4.

3.2. Model results description

The simulated surface flow exhibits similar patterns to those produced by other recent NAS models (Androulidakis and Kourafalou, 2011; Androulidakis et al., 2012; Kopasakis et al., 2012) and in-situ observations (Eronat and Sayin, 2014; Sayin et al., 2011; Sylaios, 2011). In winter (09 February 2008), the Dardanelles low salinity flow bifurcates around Lemnos Island, with its northern branch crossing the Lemnos-Imvros Passage, moving eastwards towards Chalkidiki Peninsula (Fig. 5). The flow around Athos Peninsula and into Singitikos Bay agrees to the Lagrangian observations of Olson et al. (2007). Under Ekman transport, the southern Dardanelles branch flows around the southern coasts of Lemnos Island, turning westwards to feed a weak anticyclone in the Sporades Basin. This pattern is consistent to the observations made by Olson et al. (2007) using drifters when reported on the enhanced westward Ekman drift associated with the strong northerly winds. A strong anti-cyclonic flow with a large diameter (~70 km) is formed in the vicinity of the BSW-LIW front, to the north-west of Lesvos Island.

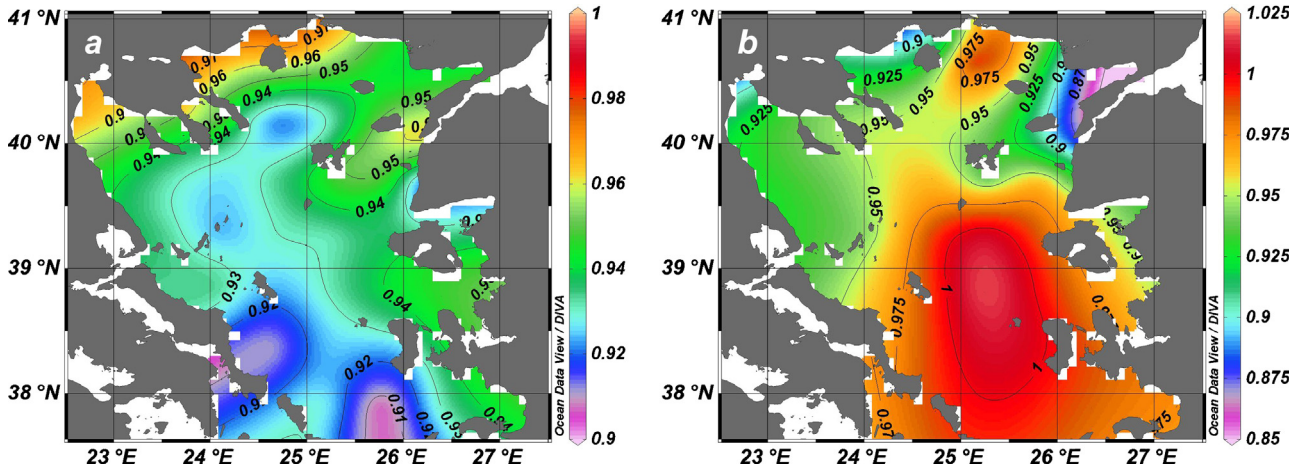

Figure 3 Spatial variability of (a) the correlation coefficient and (b) the modified model bias, between the modeled and the GHRSST sea-surface temperature datasets.

In spring (08 May 2008) the wind influence lessens and as BSW outflow remains at substantial levels (~50,000 $m^3 s^{-1}$), its northwestern branch achieves speeds up to 1 $m s^{-1}$, strongly affecting the Thracian Sea (Fig. 6). This low salinity water (~33.7–34.5) forms the Samothraki Anticyclone, a distinctive feature in Thracian Sea. Part of the BSW flow reaches the southwestern part of Thassos Island, and bifurcates into a branch moving towards Strymonikos Gulf and another towards Athos Peninsula. Similar features were also produced by the model of Androulidakis et al. (2012).

A circulation snapshot representing the summer conditions of moderate south-eastern winds and diminished BSW outflow is shown in Fig. 7 (05 July 2008). BSW flow follows a westward pathway between Lemnos and Imvros Islands, with speeds ranging from 0.7 to 0.95 $m s^{-1}$. As flow moves northwards towards Thassos Island, it separates developing a twin cyclonic–anti-cyclonic system to the west and north-west of Samothraki Island. This twin cyclone–anticyclone system was also simulated by Androulidakis et al. (2012) during the summer period (August 2003). The BSW-LIW frontal zone was found to the south and east of Lemnos Island, allowing the south-western water transfer towards Skiros Basin. Again, Androulidakis et al. (2012) points out the strong south-western propagation of surface waters and the presence of Sporades Anticyclone during the entire summer.

3.3. PEA distribution and change

The PEA quantifies the deficit in the potential energy due to stratification over a water column of 200 m depth, as

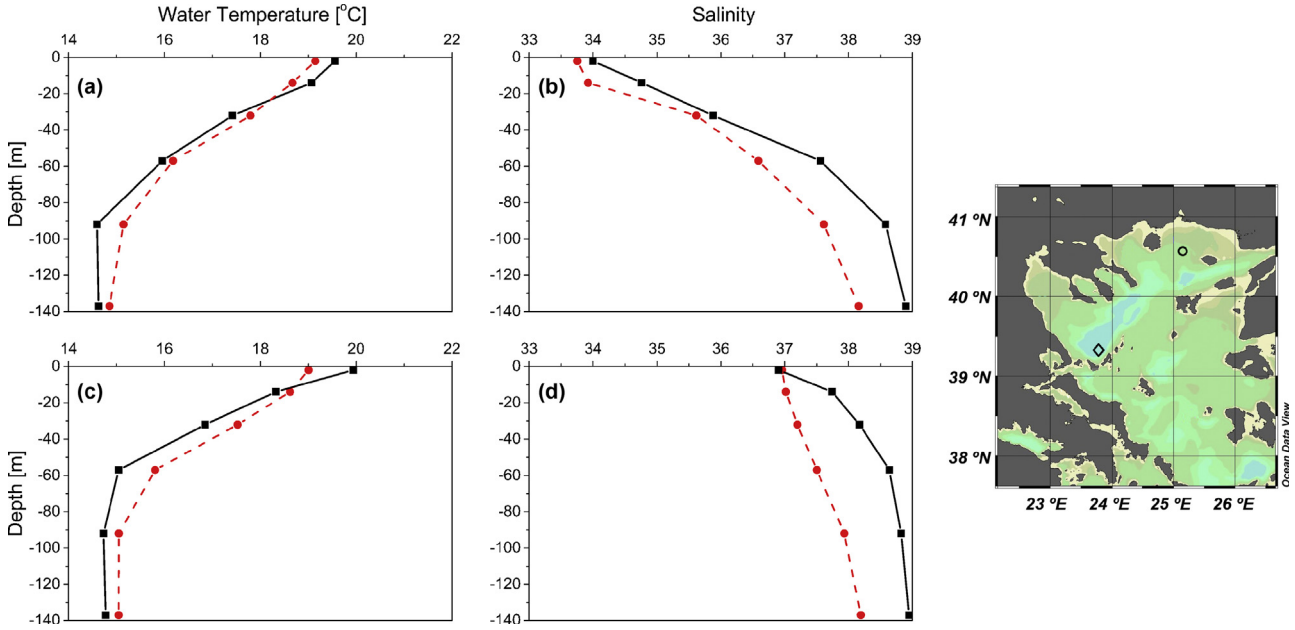

Figure 4 Modeled and observed profiles (surface to 200 m depth) in the Thracian Sea (circle) for (a) water temperature and (b) salinity and in the Sporades Basin (diamond) for (c) water temperature and (d) salinity, in summer 2006.

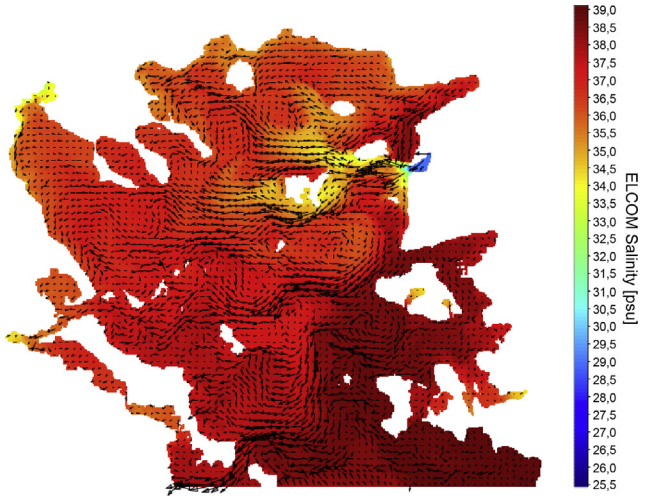

Figure 5 Surface flow and salinity patterns in the North Aegean Sea as produced by ELCOM model on 09 February 2008.

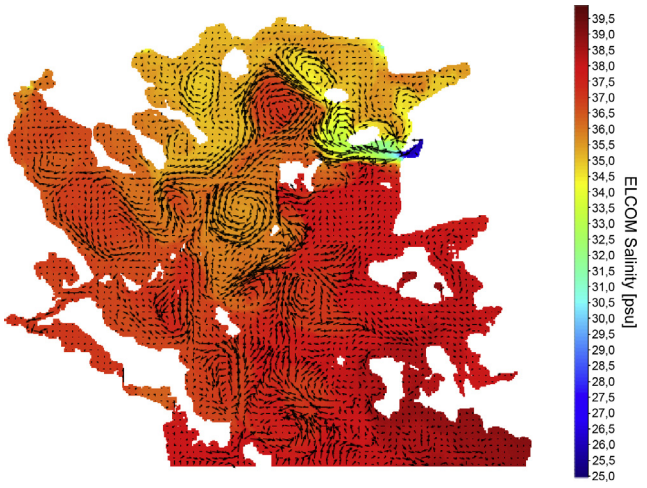

Figure 7 Surface flow and salinity patterns in the North Aegean Sea as produced by ELCOM model on 05 July 2008.

compared to that of the fully mixed water column. The PEA distribution in NAS increases due to the BSW buoyancy outflux and the solar radiation effect and diminishes under the wind mixing influence. Fig. 8 presents the PEA temporal variability at selected sites in the Thracian Sea, in Lemnos Basin, to the south of Lemnos Island and in Sporades Basin for year 2008. Results illustrate the PEA characteristic bell-shaped curve resulting from the incident heat flux seasonality. In the Thracian Sea and Lemnos Basin sites, the sudden PEA changes are attributed to increased BSW bulges reaching the site (positive change) and to wind impact and the LIW originated masses entrapped through eddies at the site (negative change). For example, the significant PEA reduction produced in the Thracian Sea and Lemnos Basin between 26 June 2008 and 04 July 2008 is attributed to the intrusion and entrapment of saltier Levantine origin water, while wind mixing ($\sim$10 m s^{-1}) is responsible for a similar sudden change on 12 October 2008. Moving to the south of Lemnos Island and towards Sporades Basin, the impact of BSW on the water column stratification reduces, and PEA values peak at 650 J m^{-3} and 580 J m^{-3}, respectively.

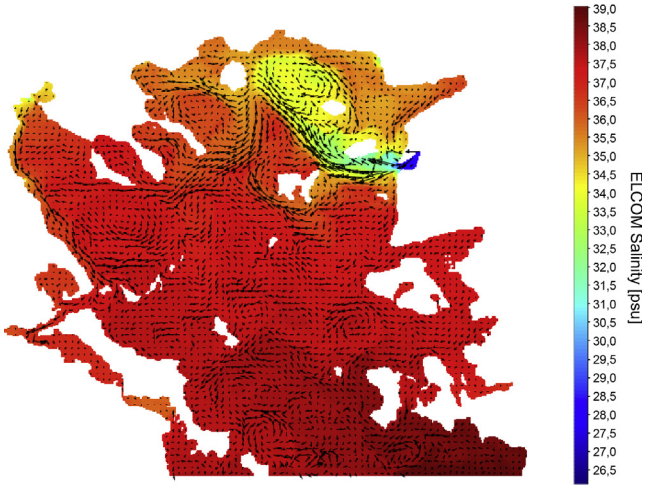

Figure 6 Surface flow and salinity patterns in the North Aegean Sea as produced by ELCOM model on 08 May 2008.

To understand the mechanisms responsible for the stratification—mixing dynamics over NAS, the individual terms of Eq. (6) were explored and their relative contribution on ϕ-change was accounted for. In the Thracian Sea, during January 2008, mean water column density of 1028.11 kg m^{-3}, mean density gradient of 1.41×10^{-5} kg m^{-4}, mean wind speed of 5.8 m s^{-1} and mean solar radiation of 92 W m^{-2} were considered. The wind impact on ϕ-change may be estimated at 3.62×10^{-6} W m^{-3}, the influence of solar radiation is an order of magnitude higher (1.41×10^{-5} W m^{-3}), while the buoyancy flux effect induced by BSW contributes the most (1.23×10^{-3} W m^{-3}). During July 2008, solar heat flux reached 330 W m^{-2} thus depth-averaged density reduced to 1026.80 kg m^{-3}, while the depth-averaged density gradient decreased slightly at 1.18×10^{-3} kg m^{-4}. As wind speeds decreased, the wind effect on ϕ-change reached 2.1×10^{-6} W m^{-3}, the influence of solar heat flux increased approximately by a factor of four (7.4×10^{-5} W m^{-3}), while the BSW impact almost halved compared to winter (7.9×10^{-4} W m^{-3}), but remained the dominant stratification mechanism.

Integrating the above results over a monthly period during 2006—2008, the relative contribution of each term on the total PEA may be examined. Table 2 presents the mean monthly ϕ-values for Thracian Sea, as obtained from calculated vertical density distribution and the use of Eq. (5), and the integrated monthly ϕ-values as obtained through Eq. (7). The results obtained by both methods appear rather comparative. Moreover, the relative contribution of each mechanism (solar radiation, buoyancy effect and wind impact) on the mean-monthly PEA value is also shown. The solar radiation contribution on the water column PEA depicts an average value of 130.79 J m^{-3}, ranging between 55.28 J m^{-3} in January and 55.86 J m^{-3} in December up to 208.02 J m^{-3} in July. These findings appear in agreement with the North Aegean sea-atmosphere heat fluxes analysis developed by Poulos et al. (1997) and Androulidakis et al. (2012). In the same month, the BSW buoyancy contribution

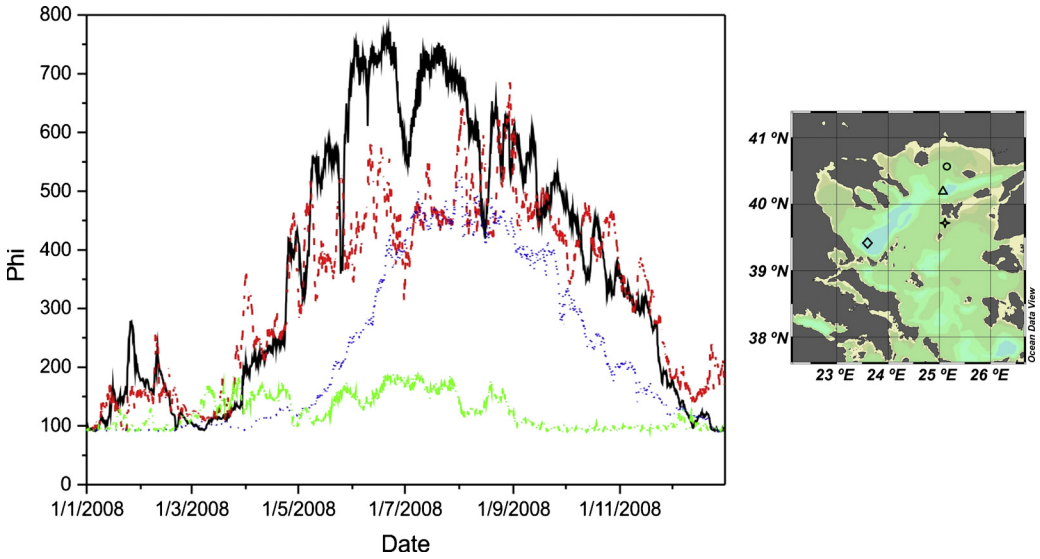

Figure 8 Temporal change of the potential energy anomaly at (a) the Thracian Sea (solid black line), (b) the Lemnos Basin (red dashed line), (c) the south of Lemnos Island (blue dotted line) and (d) the Sporades Basin (green dashed-dotted line) during 2008. The map shows the exact location of stations at the Thracian Sea (circle), the Lemnos Basin (triangle), the south of Lemnos Island (star) and the Sporades Basin (diamond). (For interpretation of the references to color in this figure legend, the reader is referred to the web version of this article.)

also receives its maximum value (611.98 J m^{-3}), leading to the most stratified water column having a ϕ-stratification value of 811.27 J m^{-3}. The wind impact reaches its maximum ϕ-contribution in January (22.19 J m^{-3}), producing a rather well-mixed water column in the Thracian Sea, since the ϕ_{TOTAL} value is limited to 94.94 J m^{-3}.

3.4. Quantification of PEA equation terms

Fig. 9 presents the temporal variation in the magnitude of the examined potential energy equation terms crossing the Northern Lemnos—the Thracian Sea meridional transect during 2008 (A: 40.475°N, 25.241°E; B: 40.022°N, 25.241°E). The $d\phi/dt$ term varies between -1.014×10^{-4} W m^{-3} and $+1.389 \times 10^{-4}$ W m^{-3} (Fig. 9a), while the ϕ-advective term, accounting for the effect of BSW buoyancy outflux crossing the transect in the east-to-west direction (positive values), ranges from -0.914×10^{-4} W m^{-3} to $+3.926 \times 10^{-4}$ W m^{-3}. Positive values prevail throughout the year, indicating that BSW is mostly transferred westward, towards the Thracian Sea (Fig. 9b). This westward transferred ϕ-advective flux appears related to the presence of Samothraki Anticyclone, an eddy system with 50—60 km diameter spread over the Thracian Sea. The depth-mean straining term, explained as the effect of tidal shear on the vertically constant horizontal density gradients appears of lower magnitude than the ϕ-advective term, ranging between -0.671×10^{-5} W m^{-3} and $+0.440 \times 10^{-5}$ W m^{-3} (Fig. 9c). Similarly, limited is the variability of the non-mean straining (term C), while the vertical mixing term (term E, Fig. 9e), expressed as

Table 2 The Thracian Sea mean monthly PEA, as computed by model results and monthly-integrated PEA and relative PEA-contribution of individual terms as derived from Eq. (7) during 2006—2008.

Months	Mean monthly PEA [J m^{-3}]	ϕ_{TOTAL} [J m^{-3}]	ϕ_{SOLAR} [J m^{-3}]	$\phi_{BOUYANCY}$ [J m^{-3}]	ϕ_{WIND} [J m^{-3}]
January	103.83	94.94	55.28	62.27	22.19
February	104.04	115.97	70.55	54.89	9.17
March	224.71	206.22	120.10	95.87	9.57
April	308.49	317.18	156.73	163.05	2.57
May	613.32	601.80	206.76	398.15	3.08
June	786.51	673.00	200.03	475.02	2.02
July	755.01	811.27	208.02	611.98	8.70
August	774.92	761.55	195.60	567.40	1.42
September	662.56	633.02	141.20	497.36	5.51
October	431.28	455.27	96.64	368.29	9.64
November	249.55	292.79	62.79	235.60	5.56
December	163.08	172.46	55.86	121.66	5.03

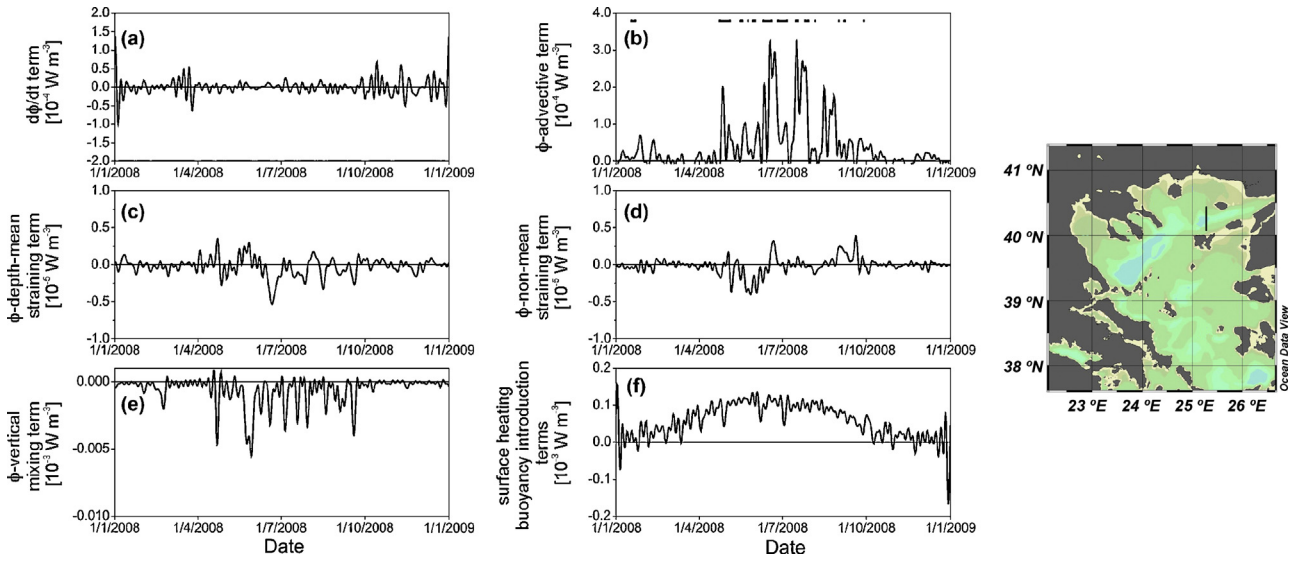

Figure 9 Temporal variability of (a) the $d\phi/dt$-term ($\times 10^{-4}$ W m^{-3}), (b) the ϕ-advective term ($\times 10^{-4}$ W m^{-3}), (c) the ϕ-depth-mean straining term ($\times 10^{-5}$ W m^{-3}), (d) the ϕ-non-mean straining term ($\times 10^{-5}$ W m^{-3}), (e) the ϕ-vertical mixing term ($\times 10^{-3}$ W m^{-3}) and (f) the surface heating buoyancy introduction terms ($\times 10^{-3}$ W m^{-3}), crossing the north-west BSW branch. All terms were smoothed using a low-pass-filter of 0.2 Hz cutoff frequency. Black lines in subplot (b) represent periods of Samothraki Anticyclone presence in Thracian Sea.

the integrated vertical buoyancy flux, fluctuates between near zero and -0.012×10^{-3} W m^{-3}, obtaining increased negative values under the influence of strong southern and north-eastern winds (15–20 m s^{-1}). The impact of solar heating, dominating terms G & F, increases during the summer obtaining a maximum value of 0.155×10^{-4} W m^{-3} and reduces to near zero values in the winter (Fig. 9f).

The variability of the ϕ-equation terms crossing an indicative meridional transect for the BSW south-western branch (C: 39.573°N, 25.241°E; D: 39.123°N, 25.241°E), is shown in Fig. 10. The positive sign in the ϕ-advective term (Fig. 10b) is related to the strengthening of the SW branch, with increased flow up to 0.6 m s^{-1} moving from the south-eastern cape of Lemnos towards Agios Efstratios Island. The Sporades anticyclone appears mostly supported by high positive ϕ-advective values, as on 09 March 2008 when $U_{SW\text{-}branch} = 0.72$ m s^{-1}, the $\phi_{advective}$ term $\sim 0.60 \times 10^{-4}$ W m^{-3} and an anticyclonic flow is formed in Sporades (Fig. 11a). Similar conditions prevail on 20 March 2008 ($\phi_{advective}$ term $\sim 0.83 \times 10^{-4}$ W m^{-3}), as shown in Fig. 11b. Under a negative sign, the SW branch of BSW is weak or completely absent, and the flow at the south of Lemnos Island is narrowed to the

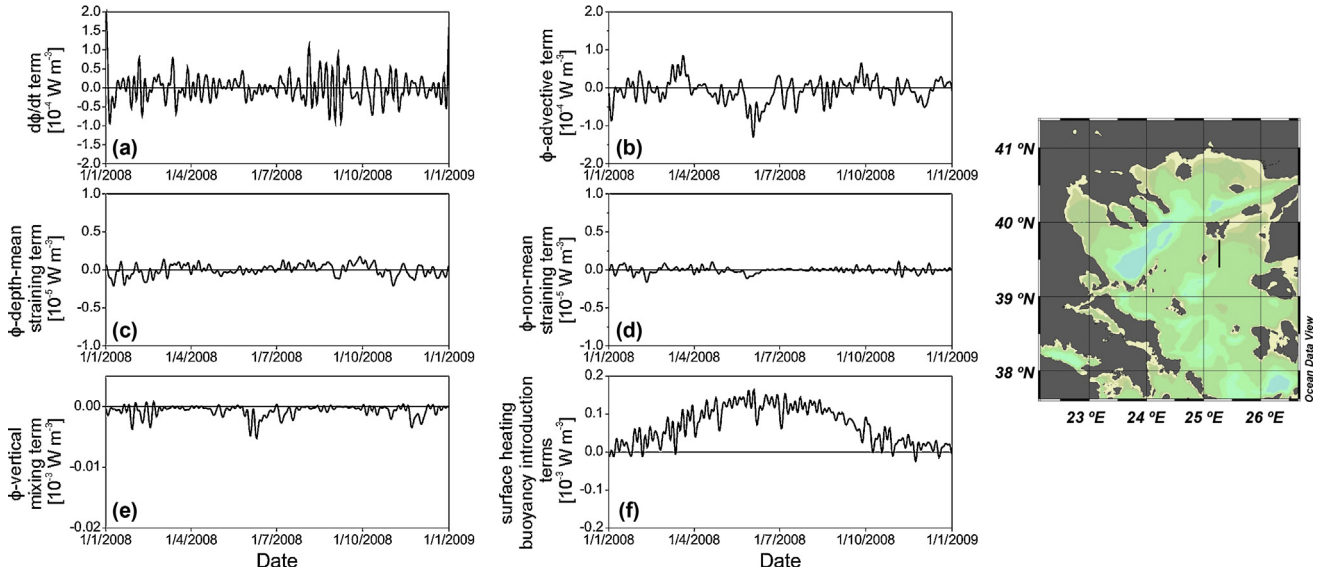

Figure 10 Temporal variability of (a) the $d\phi/dt$-term ($\times 10^{-4}$ W m^{-3}), (b) the ϕ-advective term ($\times 10^{-4}$ W m^{-3}), (c) the ϕ-depth-mean straining term ($\times 10^{-5}$ W m^{-3}), (d) the ϕ-non-mean straining term ($\times 10^{-5}$ W m^{-3}), (e) the ϕ-vertical mixing term ($\times 10^{-3}$ W m^{-3}) and (f) the surface heating buoyancy introduction terms ($\times 10^{-3}$ W m^{-3}), crossing the south-west BSW branch. All terms were smoothed using a low-pass-filter of 0.2 Hz cutoff frequency.

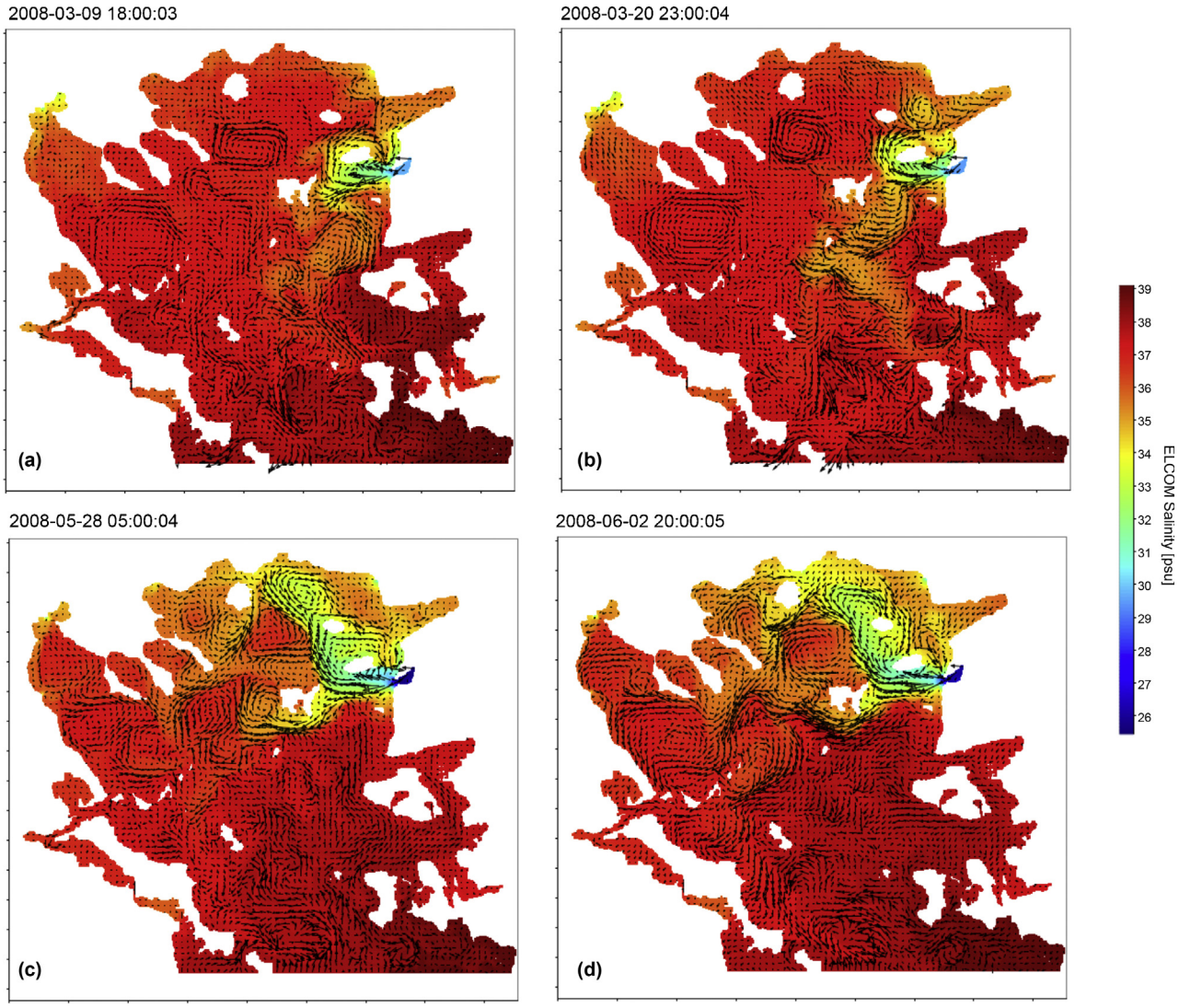

Figure 11 Surface water circulation in North Aegean Sea (a) on 09 March 2008, when the $\phi_{advective}$ term of SW-branch $\sim 0.60 \times 10^{-4}$ W m^{-3}, related to an anticyclone in Sporades Basin, (b) on 20 March 2008, when the $\phi_{advective}$ term of SW-branch $\sim 0.83 \times 10^{-4}$ W m^{-3}, related to an anticyclone in the Sporades Basin, (c) on 28 May 2008, when the $\phi_{advective}$ term of SW-branch $\sim -0.80 \times 10^{-4}$ W m^{-3}, related to a cyclonic flow in the Sporades Basin, and (d) on 2 June 2008, when the $\phi_{advective}$ term of SW-branch $\sim -1.30 \times 10^{-4}$ W m^{-3}, related to a cyclonic flow in the Sporades Basin.

coastal zone, with a westward direction. Strong negative $\phi_{advective}$ term values appear linked to the occurrence of a cyclonic flow in NE Sporades Basin, as on 28 May 2008 ($\phi_{advective} \sim -0.80 \times 10^{-4}$ W m^{-3}; Fig. 11c) and 02 June 2008 ($\phi_{advective} \sim -1.30 \times 10^{-4}$ W m^{-3}; Fig. 11d). Sudden changes in the ϕ-advective term sign occur mostly during August and September (Fig. 10b), leading to consequent changes on the vorticity sign of Sporades Basin flow.

4. Discussion

In this paper, ELCOM model rather successfully simulated the variability of surface circulation and water masses distribution in the North Aegean Sea, producing the rapidly changing surface meso-scale patterns and the water column dynamics under the BSW, meteorological and heat exchange influence. As seen from model results, the BSW bifurcation at the north and south of Lemnos Island and the relative strength of flow between these branches, determines the variability of the above described meso-scale patterns and the water column stratification-mixing processes, expressed by the potential energy anomaly of the studied system. The north-western BSW flow affects mostly the circulation in the Thracian Sea, feeding sub-basin scale gyres and flows along the Thracian coastline (the Coastal Current) and between Lemnos Basin and Chalkidiki Peninsula (the Rim Current). The strong south-western BSW flow enhances the horizontal density gradients across the BSW-LIW frontal zone and affects the Skiros and Sporades Basins inducing cyclonic–anti-cyclonic flows (the Sporades Eddy). The above described results appear in agreement to the circulation patterns described explicitly by Tzali et al. (2010), Androulidakis and Kourafalou (2011) and Androulidakis et al. (2012).

The potential energy anomaly variability illustrated the importance of BSW outflux in the stratification conditions of the water column. Our results suggest that during the winter the impact of BSW-induced buoyancy on water column stratification is higher by almost two orders of magnitude than that of solar radiation. During spring and summer, solar heat flux gradually increases, allowing BSW buoyancy impact as the dominant ϕ-change term, determining the water column stratification in the Thracian Sea, but only being an order of magnitude higher than the solar radiation effect. At the area of Sporades, solar radiation and buoyancy effects appear comparable during the summer period, while at Chios Basin ϕ-temporal variability shows limited mean-monthly fluctuation and solar radiation dominates the water column dynamics.

To comprehend the impact of BSW pulses advection on the North Aegean Sea, the general dynamic ϕ-equation, as derived by Burchard and Hofmeister (2008), was solved along a meridional transect in the Thracian Sea, utilizing the ELCOM model results for the upper 130 m. The ϕ-advective term crossing the NW branch appears mostly positive, implying the westward transport of the buoyant jet. The term fluctuates strongly in time and receives its highest values during spring and summer, related to the occurrence of a meso-scale eddy spread between Samothraki and Thassos Islands. Based on the modeled flow field, the relative vorticity of this system, known as Samothraki Anticyclone, was calculated, as:

$$\zeta = \frac{\partial v}{\partial x} - \frac{\partial u}{\partial y} \tag{12}$$

and then associated to the ϕ-advective term. Relative vorticity in the Thracian Sea exhibits negative values (mean $\zeta = -1.1 \times 10^{-5}\ s^{-1}$), indicating the anticyclonic nature of the circulation. A fifth-order polynomial regression between relative vorticity and cross-transect ϕ-advection is shown (Fig. 12), indicating that Samothraki Anticyclone was fed by the north-western branch of the BSW plume. A similar analysis was also performed by Soosaar et al. (2014) on the anticyclonic eddy of the southern Gulf of Riga and its relationship to the wind and horizontal density gradients. Results depicted that this anticyclone was mostly fed by the buoyancy field, being enhanced or reversed by the dominant

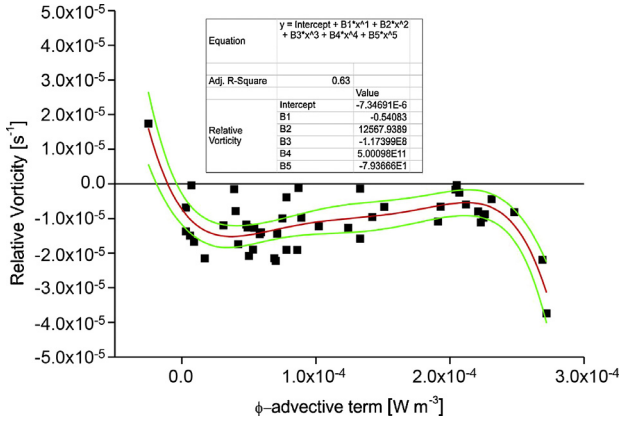

Figure 12 Non-linear regression between the ϕ-advective term crossing the north-west BSW branch and the relative vorticity of Samothraki Anticyclone.

winds. Sylaios (2011) explained that under northerly winds, the anticyclone was pushed towards the north-west of Lemnos Island, while under the influence of south to south-westerly winds, it moved to the north-west of Samothraki Island. As shown by the temporal variation of the ϕ—vertical mixing term (Fig. 9e), in the North Aegean Sea, strong winds ($>15\ m\ s^{-1}$) tend to destroy the anticyclonic pattern, promoting vertical water column mixing. Indeed, the negative peaks in the temporal variability of term-E (20 February 08; 21 April 08; 30 May 08; 18 June 08; 11 July 08; 20 July 08; 14 September 08) correspond to short-to-medium scale storms with wind speeds between 15 and 20 m s^{-1}.

Based on model results for the Thracian Sea, the baroclinic Rossby radius of deformation for Samothraki Anticyclone was computed, as:

$$R_1 = \frac{c_1}{|f|}, \tag{13}$$

where c_1 is the gravity baroclinic wave speed, estimated by:

$$c_1 = \frac{1}{\pi}\int_{-H}^{0} N(z)\, dz, \tag{14}$$

with $N(z)$ the Brunt-Väisälä frequency. The produced R_1 values during the occurrence of increased positive values in the cross-transect ϕ-advective term exhibits a mean value of 7.5 ± 0.3 km throughout 2008. This result is in agreement with the findings of Androulidakis and Kourafalou (2011), during their numerical experimental tests.

5. Conclusions

In this paper the three-dimensional model ELCOM was adapted, implemented and validated, aiming to derive the hydrodynamic field in the North Aegean Sea. The Black Sea Water outflow and spreading governs surface hydrodynamics, with two distinct branches (NW and SW) at Lemnos Island. Intensive post-processing on the validated model results was carried out, aiming to link BSW buoyancy transfer to NAS water column dynamics and surface meso-scale patterns.

The potential energy anomaly illustrated a significant spatial variability in NAS, due to the variable impact of BSW throughout the system's surface. PEA forcing analysis indicated that BSW induces buoyancy comparable to the solar heating impact on the winter water column stratification of the Thracian Sea. However, in spring and summer, the BSW influence in the Thracian Sea appears up to three times higher than the corresponding solar heating effect. In Sporades, solar radiation and buoyancy impact seem of equal importance for summer water column stratification. Analysis and quantification of the individual PEA terms exhibits the impact of BSW-induced buoyancy on the surface meso-scale patterns of NAS. Indeed, the ϕ-advective term crossing the NW branch exhibits strong relation to the occurrence of Samothraki Anticyclone. A non-linear regression between eddy's relative vorticity and the NW ϕ-advective term was developed, explaining the impact of BSW NW branch on Samothraki Anticyclone.

Similarly, a SW branch enhancement, indicated by the highly positive ϕ-advective values, appears related to the intensification of Sporades Anticyclone. On the contrary,

negative values in the ϕ-advective term appear related to the occurrence of a cyclone in Sporades Basin. This vorticity sign change occurred mostly during August and September 2008, associated to the sudden changes in the ϕ-advection term crossing the SW BSW branch. As shown by the variability of the ϕ—vertical mixing term, strong winds (>15 m s^{-1}) tend to destroy the above meso-scale eddy systems, thus promoting vertical water column mixing in NAS.

References

Alosairi, Y., Imberger, J., Falconer, R.A., 2011. Mixing and flushing in the Persian Gulf (Arabian Gulf). J. Geophys. Res. 116, C03029, 1—14, http://dx.doi.org/10.1029/2010JC006769.

Androulidakis, Y.S., Kourafalou, V.H., 2011. Evolution of a buoyant outflow in the presence of complex topography: the Dardanelles plume (North Aegean Sea). J. Geophys. Res. 116, C04019, http://dx.doi.org/10.1029/2010JC006316.

Androulidakis, Y.S., Krestenitis, Y.N., Kourafalou, V.H., 2012. Connectivity of North Aegean circulation to the Black Sea water budget. Cont. Shelf Res. 48, 8—26, http://dx.doi.org/10.1016/j.csr.2012.08.019.

Barry, M.E., Houdré, F.M., McAlister, A.B., Botelho, D.A., 2009. Three dimensional hydraulic and water quality modelling of the Red Sea: challenges and learnings. In: Proceedings of the 18th World IMACS Congress and MODSIM09 International Congress on Modelling and Simulation, "Interfacing Modelling and Simulation with Mathematical and Computational Sciences", 4142—4148.

Burchard, H., Hofmeister, R., 2008. A dynamic equation for the potential energy anomaly for analysing mixing and stratification in estuaries and coastal seas. Estuar. Coast. Shelf Sci. 77 (4), 679—687, http://dx.doi.org/10.1016/j.csr.2012.08.01910.1016/j.ecss.2007.10.025.

Casulli, V., Cheng, R.T., 1992. Semi-implicit finite difference methods for three dimensional shallow water flow. Int. J. Numer. Meth. Fluids 15, 629—648.

Cordero, S.G., 1999. The use of thermal satellite data in dense water formation studies in the Mediterranean Sea. J. Marine Syst. 20 (1—4), 175—186, http://dx.doi.org/10.1016/S0924-7963(98)00081-5.

Eronat, C., Sayin, E., 2014. Temporal evolution of the water characteristics in the bays along the eastern coast of the Aegean Sea: Saros, I¤zmir, and Gökova bays. Turkish J. Earth Sci. 23, 53—66, http://dx.doi.org/10.3906/yer-1307-4.

Gill, A.E., 1982. Atmosphere—Ocean Dynamics. Int. Geophys. Ser., vol. 30. Academic Press, London, 662 pp.

Hodges, B.R., 2000. Numerical Techniques in CWR-ELCOM (Code Release v.1). CWR Manuscript WP1422 BH. Cent. Water Res., Univ. Western Australia, Perth, 37 pp.

Hodges, B., Dallimore, C., 2001. Estuary and Lake Computer Model: ELCOM Science Manual Code Version 2.0.0. Cent. Water Res., Univ. Western Australia, Perth.

Hoitink, A.J.F., van Maren, D.S., Hoekstra, P., 2011. Mixing and stratification in a tropical tidal embayment subject to a distributed freshwater source. J. Marine Syst. 88 (1), 34—44, http://dx.doi.org/10.1016/j.jmarsys.2011.02.015.

Imberger, J., Patterson, J.C., 1990. Physical limnology. In: Wu, T. (Ed.), Advances in Applied Mechanics, vol. 27, 302—475.

Jedrasik, J., 2005. Validation of the hydrodynamic part of the ecohydrodynamic model for the southern Baltic. Oceanologia 47 (4), 543—566.

Kamidis, N., Sylaios, G., Tsihrintzis, V.A., 2011. Modelling Nestos River plume dynamics using ELCOM. Desalin. Water Treat. 33 (1—3), 22—35, http://dx.doi.org/10.5004/dwt.2011.2627.

Karnaska, Y., Maderich, V., 2008. Modelling of seasonal exchange flows through the Dardanelles Strait. Estuar. Coast. Shelf Sci. 79 (3), 449—458, http://dx.doi.org/10.1016/j.ecss.2008.04.019.

Kontoyiannis, H., Kourafalou, V.H., Papadopoulos, V., 2003. Seasonal characteristics of the hydrology and circulation in the Northwest Aegean Sea (eastern Mediterranean): observations and modeling. J. Geophys. Res. 108 (C9), 3302, http://dx.doi.org/10.1029/2001JC001132.

Kopasakis, K.I., Georgoulas, A.N., Angelidis, P.B., Kostovinos, N.E., 2012. Numerical modeling of the long-term transport, dispersion, and accumulation of Black Sea pollutants into the North Aegean coastal waters. Estuar. Coast. 35 (6), 1530—1550, http://dx.doi.org/10.1007/s12237-012-9540-9.

Korres, G., Lascaratos, A., Hatziapostolou, E., Katsafados, P., 2002. Towards an ocean forecasting system for the Aegean Sea. J. Atmos. Ocean Sci. 8 (2—3), 173—200.

Kourafalou, V.H., Barbopoulos, K., 2003. High resolution simulations on the North Aegean Sea seasonal circulation. Ann. Geophys. 21 (1), 251—265, http://dx.doi.org/10.5194/angeo-21-251-2003.

Kourafalou, V., Tsiaras, K., 2007. A nested circulation model for the North Aegean Sea. Ocean Sci. 3 (1), 1—16, http://dx.doi.org/10.5194/os-3-1-2007.

Laval, B., Imberger, J., Hodges, B.R., Stocker, R., 2003. Modeling circulation in lakes: spatial and temporal variations. Limnol. Oceanogr. 48 (3), 983—994, http://dx.doi.org/10.4319/lo.2003.48.3.0983.

Lund-Hansen, L.C., Skyum, P., Christiansen, C., 1996. Modes of stratification in a semi-enclosed bay at the North Sea—Baltic Sea transition. Estuar. Coast. Shelf Sci. 42 (1), 45—54, http://dx.doi.org/10.1006/ecss.1996.0004.

Martin, M., Dash, P., Ignatov, A., Banzon, V., Beggs, H., Brasnett, B., Cayula, J.-F., Cummings, J., Donlon, C., Gentemann, C., Grumbine, R., Ishizaki, S., Maturi, E., Reynolds, R.W., Roberts-Jones, J., 2012. Group for High Resolution Sea Surface temperature (GHRSST) analysis fields inter-comparisons. Part 1: A GHRSST multi-product ensemble (GMPE). Deep-Sea Res. Pt. II 77—80, 21—30, http://dx.doi.org/10.1016/j.dsr2.2012.04.013.

Olson, D.B., Kourafalou, V.H., Johns, W.E., Samuels, G., Veneziani, M., 2007. Aegean surface circulation from a satellite-tracked drifter array. J. Phys. Oceanogr. 37 (7), 1898—1917, http://dx.doi.org/10.1175/JPO3028.1.

Poulos, S.E., Drakopoulos, P.G., Collins, M.B., 1997. Seasonal variability in sea surface oceanographic conditions in the Aegean Sea (Eastern Mediterranean): an overview. J. Marine Syst. 13 (1—4), 225—244, http://dx.doi.org/10.1016/S0924-7963(96)00113-3.

Sayin, E., Eronat, C., Uçkaç, Ş., Beşiktepe, Ş.T., 2011. Hydrography of the eastern part of the Aegean Sea during the East Mediterranean Transient (EMT). J. Marine Syst. 88 (4), 502—515, http://dx.doi.org/10.1016/j.jmarsys.2011.06.005.

Simpson, J.H., 1981. The shelf sea fronts: implications of their existence and behavior. Philos. T. R. Soc. A 302, 531—546.

Simpson, J.H., Sharples, J., Rippeth, T.P., 1991. A prescriptive model of stratification induced by freshwater runoff. Estuar. Coast. Shelf Sci. 33, 23—35, http://dx.doi.org/10.1016/0272-7714(91)90068-M.

Skoulikidis, N.T., Bertahas, I., Koussouris, T., 1998. The environmental state of freshwater resources in Greece (rivers and lakes). Environ. Geol. 36 (1—2), 1—17.

Soosaar, E., Maljutenko, I., Raudsepp, U., Elken, J., 2014. An investigation of anticyclonic circulation in the southern Gulf of Riga during the spring period. Cont. Shelf Res. 78, 75—84, http://dx.doi.org/10.1016/j.csr.2014.02.009.

Spillman, C.M., Imberger, J., Hamilton, D.P., Hipsey, M.R., Romero, J.R., 2007. Modelling the effects of Po River discharge, internal nutrient cycling and hydrodynamics on biogeochemistry of the Northern Adriatic Sea. J. Marine Syst. 68 (1—2), 167—200, http://dx.doi.org/10.1016/j.jmarsys.2006.11.006.

Sylaios, G., 2011. Meteorological influence on the surface hydrographic patterns of the North Aegean Sea. Oceanologia 53 (1), 1—24, http://dx.doi.org/10.5697/oc.53-1.057.

Sylaios, G., Kamidis, N., Anastasiou, S., Tsihrintzis, V.A., 2013. Hydrodynamic response of Thassos Passage (N. Aegean Sea) to Nestos River discharge and meteorological forcing. Cont. Shelf Res. 59, 37—51, http://dx.doi.org/10.1016/j.csr.2013.04.003.

Theocharis, A., Georgopoulos, D., 1993. Dense water formation over the Samothraki and Limnos Plateaux in the north Aegean Sea (Eastern Mediterranean Sea). Cont. Shelf Res. 13 (8—9), 919—939, http://dx.doi.org/10.1016/0278-4343(93)90017-R.

Tuğrul, S., Beşiktepe, S.T., Salihoglu, I., 2002. Nutrient exchange fluxes between the Aegean and Black Seas through the Marmara Sea. Mediterr. Mar. Sci. 3 (1), 33—42, http://dx.doi.org/10.12681/mms.256.

Türkoğlu, M., 2010. Temporal variations of surface phytoplankton, nutrients and chlorophyll *a* in the Dardanelles (Turkish Straits System): a coastal station sample in weekly time intervals. Turkish J. Biol. 34 (3), 319—333, http://dx.doi.org/10.3906/biy-0810-17.

Tzali, M., Sofianos, S., Mantziafou, A., Skliris, N., 2010. Modelling the impact of Black Sea water inflow on the North Aegean Sea hydrodynamics. Ocean Dynam. 60 (3), 585—596, http://dx.doi.org/10.1007/s10236-010-0277-3.

Ünlüata, Ü., Oguz, T., Latif, M.A., Özsoy, E., 1990. On the physical oceanography of Turkish Straits. In: Pratt, L.J. (Ed.), The Physical Oceanography of Sea Straits. Kluwer Acad. Publ., Dordrecht, 25—60.

Vlasenko, V.I., Stashchuk, N.N., Ivanov, V.A., Nikolaenko, E.G., Uslu, O., Benli, H., 1996. Influence of the water exchange through Dardanelles on the thermohaline structure of the Aegean Sea. Bull. Inst. Oceanogr. Monaco, Spec. No. 17, 147—165.

Wiles, P., van Duren, L., Hase, C., Larsen, J., Simpson, J., 2006. Stratification and mixing in the Limfjorden in relation to mussel culture. J. Marine Syst. 60 (1—2), 129—143, http://dx.doi.org/10.1016/j.jmarsys.2005.09.009.

Zervakis, V., Georgopoulos, D., 2002. Hydrology and circulation in the North Aegean (eastern Mediterranean) throughout 1997 and 1998. Mediterr. Mar. Sci. 3 (1), 7—21.

Zervakis, V., Georgopoulos, D., Drakopoulos, P.G., 2000. The role of the North Aegean in triggering the recent Eastern Mediterranean climatic changes. J. Geophys. Res. 105 (C11), 26103—26116, http://dx.doi.org/10.1029/2000JC900131.

Zodiatis, G., Alexandri, S., Pavlakis, P., Jonsson, L., Kallos, G., Demetropoulos, A., Georgiou, G., Theodorou, A., Balopoulos, E., 1996. Tentative study of flow patterns in the North Aegean Sea using NOAA-AVHRR images and 2D model simulation. Ann. Geophys. 14 (11), 1221—1231, http://dx.doi.org/10.1007/s00585-996-1221-1.

Oceanologia (2016) 58, 117—123

Available online at www.sciencedirect.com

ScienceDirect

journal homepage: www.elsevier.com/locate/oceano

ORIGINAL RESEARCH ARTICLE

Spatial distribution and diet of larval snailfishes (*Liparis fabricii*, *Liparis gibbus*, *Liparis tunicatus*) in the Canadian Beaufort Sea☆

Wojciech Walkusz [a,b,*], Joclyn E. Paulic [a], Sally Wong [a], Slawomir Kwasniewski [b], Michael H. Papst [a], James D. Reist [a]

[a] *Fisheries and Oceans Canada, Freshwater Institute, Winnipeg, Canada*
[b] *Polish Academy of Sciences, Institute of Oceanology, Sopot, Poland*

Received 3 July 2015; accepted 8 December 2015
Available online 29 December 2015

KEYWORDS
Beaufort Sea;
Fish larvae;
Liparis;
Snailfish;
Diet

Summary This paper presents information on diet and distribution of larval snailfishes from the genus *Liparis* on the Canadian Beaufort Sea Shelf. In this study, 153 larval snailfishes of three species, *Liparis fabricii*, *L. gibbus* and *L. tunicatus*, were collected during 4 summer cruises (2003—2005, 2007). The majority of the larvae were either in flexion or post-flexion stage, and some were in pre-flexion stage. *Liparis* larvae appeared to be generalists in terms of diet and fed on a wide range of planktonic organisms. Pre-flexion larvae fed on small copepods (mainly adult stages of *Triconia borealis*). As larvae grew their diet shifted towards larger copepods (copepodids III/IV of *Calanus hyperboreus*, copepodids II—IV of *Calanus glacialis* and females of *Metridia longa*) and amphipods (*Themisto libellula*). Remarkably, larvaceans *Oikopleura* spp. and pelagic snails *Limacina helicina* made up a substantial part of the larval diet. This paper contributes to the knowledge on arctic larval fishes and to the ongoing efforts regarding Canadian Beaufort Sea ecosystem modeling.

☆ This study was financially supported by the NMCS program with contributions from the Polish Ministry of Science and Higher Education (grants: SPUB 289/W-NOGAP/2008/0 and SPUB 62/W-NOGAP/2009/0). The Polish—Canadian cooperation was based on an Interchange Canada Agreement for W. Walkusz. This project in its final phase (preparation of this paper) was partially funded by and is a contribution to the Beaufort Regional Environmental Assessment Marine Fish Project (AANDC) led by Fisheries and Oceans Canada (lead investigator: J. Reist).
* Corresponding author at: Fisheries and Oceans Canada, Freshwater Institute, 501 University Crescent, Winnipeg, MB R3T 2N6, Canada. Tel.: +1 204 984 7543; fax: +1 204 984 2401.
E-mail addresses: walwo@iopan.gda.pl (W. Walkusz), Joclyn.Paulic@dfo-mpo.gc.ca (J.E. Paulic), Sally.Wong@dfo-mpo.gc.ca (S. Wong), kwas@iopan.gda.pl (S. Kwasniewski), mhpapst@gmail.com (M.H. Papst), Jim.Reist@dfo-mpo.gc.ca (J.D. Reist).
Peer review under the responsibility of Institute of Oceanology of the Polish Academy of Sciences.

Production and hosting by Elsevier

http://dx.doi.org/10.1016/j.oceano.2015.12.001

1. Introduction

Of the more than 400 snailfish species known worldwide (www.fishbase.org), eight *Liparis* species are listed as present in the Arctic (Mecklenburg et al., 2013) but only four from this genus are regularly found on the shelves and upper slopes in the Arctic seas: *Liparis fabricii* (commonly known as Gelatinous Snailfish), *L. gibbus* (known as either Variegated or Dusky Snailfish), *L. tunicatus* (known as Kelp Snailfish) and *L. bathyarcticus* (known as Nebulous Snailfish) (Able, 1990; Evseenko et al., 2006; Chernova, 2008; Mecklenburg et al., 2011). These are distributed circumpolarly and all but one (*L. bathyarcticus*) were recorded previously in the Beaufort Sea (Chiperzak et al., 2003; Jarvela and Thorsteinson, 1999; Paulic and Papst, 2013; Wong et al., 2013). All four *Liparis* species were also found in the Chukchi Sea and Bering Strait (Mecklenburg et al., 2011; Mecklenburg et al., 2007; Norcross et al., 2010), while the former three species were also collected in Hudson Bay (Morin and Dodson, 1986; Ponton et al., 1993). Snailfishes, particularly adults during the spawning period, are found in the nearshore areas that have hard substrate and often kelp beds to which the fishes show an affinity (Byers and Prach, 1988; Dunton et al., 1982).

Little is known about the ecology of snailfishes, their significance in food webs and their importance in the Arctic ecosystems, though studies so far show that they are important food source for marine birds (Gaston, 1985) and seals (Falk-Petersen et al., 2004). Adult snailfishes feed mainly on bottom-associated amphipods, polychaetes and cumaceans (Atkinson and Percy, 1992; Byers and Prach, 1988), which suggests they occupy and thus feed in the benthic habitats. Apart from a few records of larval snailfish occurrence (e.g. Paulic and Papst, 2013; Suzuki et al., 2015; Wong et al., 2013) there is virtually no published information on their ecology in the Arctic.

When compared to the neighboring locations, e.g. the Canadian Arctic Archipelago (Stern and Gaden, 2015), the Canadian Beaufort Sea Shelf (<100 m depth) holds a relatively rich fish community. In the ice-free season it consists of approximately 25 species in both bottom and pelagic habitats (Lowdon et al., 2011; Majewski et al., 2009; Paulic and Papst, 2013; Wong et al., 2013). The spatial distribution of these fishes varies in relation to the oceanographic conditions that are mainly shaped by the Mackenzie River plume and sea currents (Paulic and Papst, 2013; Wong et al., 2013). Both the larval/juvenile and adult snailfishes rank relatively high in terms of their abundance (approx. 10% of total fish abundance; Lowdon et al., 2011; Paulic and Papst, 2013; Wong et al., 2013). Snailfishes, however, remain less abundant than Arctic Cod (*Boreogadus saida*; up to 60% of total fish abundance; Paulic and Papst, 2013) and Arctic Staghorn Sculpin (*Gymnocanthus tricuspis*, up to 13% of total fish abundance: Lowdon et al., 2011). Considering the role of fish as food for higher predators (e.g. whales), snailfishes and Arctic Cod are energetically similar prey due to their comparable weight at given length and high calorific content, which is greater than in Arctic Staghorn Sculpin, for example (Walkusz et al., 2012).

There is virtually no information existing on the feeding and growth of snailfishes in the Arctic. Although sometimes numerous in catches, snailfishes generally are an understudied component of the Arctic nearshore marine ecosystems. This motivated our research, results of which are summarized in this paper, the aim of which is to provide new information on spatial distribution and diet of the larval snailfishes in the Canadian Beaufort Sea.

2. Material and methods

Larval fishes were collected during 4 summer expeditions (August 9–20, 2003; August 6–20, 2004; August 3–26, 2005; July 24–August 18, 2007) to the Canadian Beaufort Sea (Fig. 1), aboard the Canadian Coast Guard Ship (CCGS) *Nahidik*. For the purpose of this paper all fish larvae collected during the 4 years were pooled together, however none of the stations was sampled twice over that time. Larval fishes were collected with a 500 μm Bongo net (60 cm diameter, 300 cm total length) towed obliquely for 15–20 min from the near-bottom to the sub-surface with the speed of 2 knots. All larvae were sorted from a sample and immediately preserved in a 4% solution of formaldehyde in seawater. After approximately one month from collection all fishes were identified to species (using primarily meristic characteristics from Fahay, 2007), weighed (0.0001 g accuracy; wet mass) and measured (0.01 mm accuracy; standard length) in the lab. Larvae that were found problematic for routine identification were re-examined in the Atlantic Reference Centre (Huntsman Marine Science Centre, St. Andrews, NB, Canada). The developmental stage of each larva was determined (based on Moser et al., 1984) and its digestive tract removed. All recognizable items from the stomach/intestines were identified to the lowest possible taxonomic level. Developmental stages of larger copepod species were determined for further biomass calculations. Lengths of all remaining food items were recorded. Since the majority of the material found in the guts was damaged due to swallowing/digestion, the wet weight of the food items was calculated based on the published information for particular species and developmental stage when applicable (Hanssen, 1997; Hay et al., 1991; Karnovsky et al., 2003; Mumm, 1991). ANOVA and Tukey HSD test were performed for statistical analysis of differences among species for larval stage sizes, weights and food mass.

Breadth of diet of each developmental stage of the three species was assessed with a Levin's standardized index (Hurlbert, 1978):

$$B_i = \frac{1}{n-1}\left(\frac{1}{\sum_j pij^2} - 1\right),$$

where B_i is the Levin's standardized index for predator i, pij is the proportion of diet of predator i that is made up of prey j, and n is the number of prey categories.

This index ranges from 0 to 1 with low values indicating diets dominated by few prey items and higher values indicating broader diets.

Diet overlap between the three *Liparis* species and their developmental stages was calculated (based on the average biomass percentage of food items) using Schoener's index (α) (Schoener, 1970):

$$\alpha = 1 - 0.5 \times \left(\sum |p_{xi} - p_{yi}|\right),$$

where α is the Schoener's index, p_{xi} the proportion of food category i in the diet of species x, and p_{yi} is the proportion of food category i in the diet of species y.

The Schoener's index ranges from 0 (no dietary overlap) to 1 (complete dietary overlap).

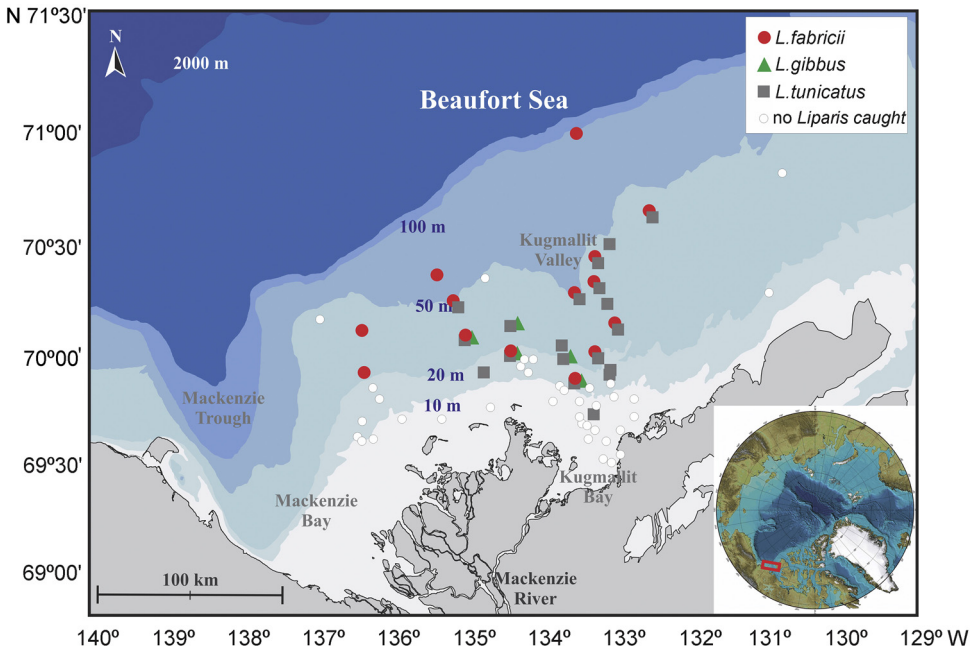

Figure 1 Map of the study area with occurrences of larval *Liparis* indicated. The general location of the study area (red rectangle) in the Arctic is presented in the insert (Arctic map source: www.ngdc.noaa.gov). (For interpretation of the references to color in this figure legend, the reader is referred to the web version of this article.)

3. Results

3.1. Distribution of larvae

Over the 4 years of sampling we visited 60 stations (Fig. 1). Overall, 1039 larval fishes were captured representing 12 taxa. *Liparis* larvae comprised 15% of the total with 153 individuals collected, including 83 individuals of *L. tunicatus*, 35 individuals of *L. fabricii* and 35 individuals of *L. gibbus* (Table 1). *Liparis* larvae were caught at 23 stations (Fig. 1; Table 2). With the exception of one station where *L. tunicatus* was captured, all *Liparis* larvae occurred in areas deeper than 10 m. Most stations where *Liparis* larvae were captured were between 20 and 50 m of depth. The three species were caught concurrently only at three stations. *Liparis fabricii* were captured over the greatest depth range (20–100 m) and

Table 1 Summary of weight and standard length (±SD) of the three *Liparis* larval species in different developmental stages. Average count of prey items and average food load mass for each developmental stage are presented. Numbers of larvae collected in each developmental stage are provided in parentheses.

Stage		Species		
		L. fabricii	*L. gibbus*	*L. tunicatus*
Pre-flexion	Weight [g]	0.016 ± 0.005 (3)	0.029 (1)	0.024 ± 0.006 (2)
	Standard length [mm]	12.7 ± 1.3 (3)	10.2 (1)	10.5 ± 4.4 (2)
	Av. food load abundance [ind. larvae^{-1}]	4 ± 4	5	1 ± 1
	Av. food load mass [mg dw larvae^{-1}]	0.02 ± 0.03	0.01	<0.001
Flexion	Weight [g]	0.063 ± 0.037 (10)	0.075 ± 0.034 (32)	0.130 ± 0.072 (30)
	Standard length [mm]	16.9 ± 4.1 (10)	16.3 ± 3.1 (32)	19.9 ± 2.7 (30)
	Av. food load abundance [ind. larvae^{-1}]	3 ± 3	8 ± 8	8 ± 9
	Av. food load mass [mg dw larvae^{-1}]	0.267 ± 0.548	0.880 ± 1.739	1.723 ± 2.805
Post-flexion	Weight [g]	0.154 ± 0.093 (22)	0.303 ± 0.191 (2)	0.266 ± 0.141 (48)
	Standard length [mm]	22.6 ± 4.9 (22)	22.7 ± 2.7 (2)	24.3 ± 3.7 (48)
	Av. food load abundance [ind. larvae^{-1}]	5 ± 6	13 ± 15	13 ± 16
	Av. food load mass [mg dw larvae^{-1}]	1.156 ± 2.227	3.899 ± 4.702	3.069 ± 3.521
Juvenile	Weight [g]	–	–	0.375 ± 0.095 (3)
	Standard length [mm]	–	–	28.4 ± 0.9 (3)
	Av. food load abundance [ind. larvae^{-1}]	–	–	21 ± 18
	Av. food load mass [mg dw larvae^{-1}]	–	–	6.636 ± 6.171

Table 2 Occurrences of larval *Liparis* species in relation to station depth.

Depth zone [m]	No. of stations in zone	No. of stations with		
		L. fabricii	*L. gibbus*	*L. tunicatus*
0–10	25	–	–	1
10–20	16	2	2	5
20–50	17	8	3	12
50–100	2	2	–	–

widest geographical area, with *L. tunicatus* being over the next greatest range (10–50 m) and area. *Liparis gibbus* were captured over the narrowest depth range (20–50 m) and geographical area.

3.2. Developmental characteristics of larvae

We found more larvae in post-flexion stage for *L. fabricii* and *L. tunicatus* than for *L. gibbus* – virtually all individuals of the latter species occurred in the flexion stage. Due to the low number of pre-flexion and juvenile larvae a statistical comparison of sizes and weights for these stages could not be performed. Larvae of *L. tunicatus* in the flexion stage were longer and heavier than larvae of the two other species (ANOVA, Tukey HSD test, $p < 0.01$). There were no differences between the length and weight of flexion larvae of *L. fabricii* and *L. gibbus*. There was no difference between *L. fabricii* and *L. tunicatus* post-flexion larvae in regards to their length (Table 1), however, *L. tunicatus* larvae were heavier (ANOVA, Tukey HSD test, $p < 0.01$). Both the sum of individual prey items and the food mass in an individual stomach increased with fish length in all species.

3.3. Diet of larvae

Overall, the diet of larval snailfishes contained 28 taxa/food categories (Fig. 2). There was no significant interspecific difference in total weight of gut contents at each developmental stage (ANOVA, Tukey HSD test, $p > 0.01$). The pre-flexion stage of all three species relied heavily on small cyclopoid copepods *Triconia borealis* and polychaete larvae. At the flexion stage, all three fish species fed on diverse food items, including the larvacean *Oikopleura* spp., the large-sized copepods *Metridia longa* and *Calanus glacialis* and the pelagic snail *Limacina helicina*. Once the larvae reached the post-flexion stage, their diet, apart from *Oikopleura* spp. and

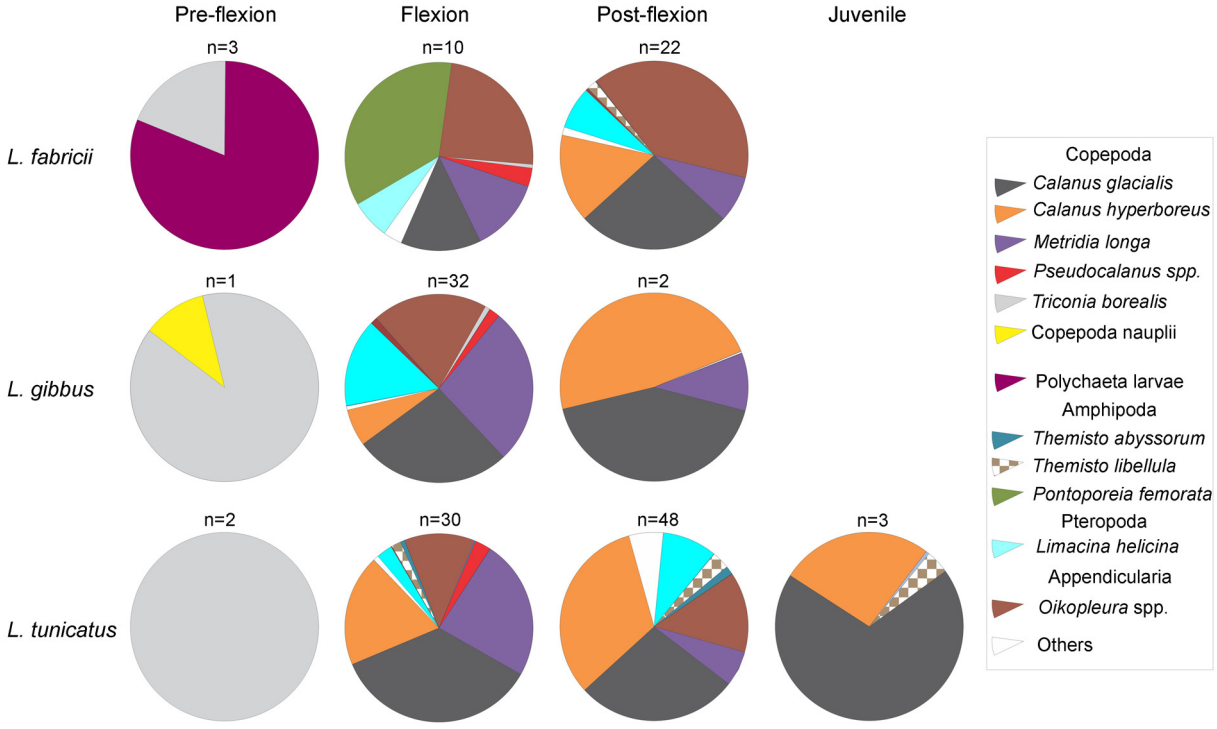

Figure 2 Weight composition of gut contents of the three larval *Liparis* species. The category "Others" includes the following taxa found in trace quantities: diatoms, *Podon leuckartii* (Cladocera), *Acartia* spp. (Copepoda), *Eurytemora herdmanii* (Copepoda), *Oithona similis* (Copepoda), *Microcalanus* spp. (Copepoda), *Jashnovia tolli* (Copepoda), *Paraeuchaeta glacialis* (Copepoda), *Scolecithricella minor* (Copepoda), Harpacticoida (Copepoda), *Onisimus glacialis* (Amphipoda), *Apherusa glacialis* (Amphipoda), *Sabinea septemcarinata* (Decapoda), Echinodermata larvae, Cirripedia nauplii/cypris and insects.

Table 3 Values of the Levin's index obtained from the diets of the particular developmental stages of the three *Liparis* species.

	L. fabricii	*L. gibbus*	*L. tunicatus*
Pre-flexion	0.018	0.010	0.000
Flexion	0.160	0.110	0.167
Post-flexion	0.250	0.070	0.147
Juvenile	—	—	0.076

Table 4 The Schoener overlap index calculated for the diets of the three *Liparis* species and their developmental stages. *Note*: sample sizes for pre-flexion larvae were too small for meaningful comparisons.

	Pair of species compared		
	L. fabricii/ *L. gibbus*	*L. fabricii*/ *L. tunicatus*	*L. gibbus*/ *L. tunicatus*
Pre-flexion	—	—	—
Flexion	0.51	0.41	0.68
Post-flexion	0.46	0.68	0.52

L. helicina, contained late copepodid stages of *C. glacialis* and *Calanus hyperboreus*. At post-flexion, larvae of *L. fabricii* and *L. tunicatus* fed also on the amphipod *Themisto libellula*. The juvenile *L. tunicatus* diet consisted almost exclusively of *Calanus* copepods and *T. libellula* while *L. helicina* and *Oikopleura* spp. were absent.

The diversity of diet items for all species, calculated here as a Levin's index, increased as the fish grew (Table 3). Also, overall *L. gibbus* had the least diverse diet while *L. fabricii* had the greatest diet breadth.

A low number of pre-flexion larvae collected precluded us from the diet overlap analysis for this stage. There was a moderate diet overlap amongst flexion and post-flexion stages of the three *Liparis* species investigated (Schoener index between 0.41 and 0.68; Table 4).

4. Discussion

Adult *Liparis* seem to depend, particularly during spawning, on the presence of a hard substrate and often kelp beds for successful reproduction (Byers and Prach, 1988; Dunton et al., 1982). There are, however, no reported kelp beds or rocky bottoms in the Mackenzie Shelf area of the Canadian Beaufort Sea. Therefore, the *Liparis* larvae found in this study are most likely expatriates from other areas, advected to this region. In the neighboring waters kelp beds were observed to the west in the Alaskan Beaufort Shelf (Dunton et al., 1982) and to the east in the Amundsen Gulf and Darnley Bay (Andrew Majewski, Fisheries and Oceans Canada, pers. comm.), and this is from where the larvae were most likely carried into the study area by currents (Pickart, 2004; Shadwick et al., 2011).

The larval distributions presented herein demonstrate co-occurrence of the three *Liparis* species in the study area. It appears that the *L. fabricii* larvae were more frequently present in the off-shore stations, while *L. tunicatus* were observed in areas that are more heavily influenced by the Mackenzie plume (Walkusz et al., 2010). Jarvela and Thorsteinson (1999) observed in large numbers only two larval snailfish species, *L. fabricii* and *L. gibbus*, in coastal waters of the Alaskan Beaufort Sea. On the other hand, Moulton and Tarbox (1987) did not find any of the aforementioned species but only collected adults of *L. tunicatus* in this area. Rand and Logerwell (2010) collected adults of only two species (*L. fabricii* and *L. gibbus*) further offshore in the Alaskan Beaufort Sea, which agrees with the more offshore presence of the *L. fabricii* in this study. This is likely due to the lower influence of the riverine plume in offshore waters. These observations suggest either a geographical separation of these species along an on- to off-shore gradient, differences in spawning timing that result in the larvae being present differentially at certain times of the year, or differences in sampling efficiency by different gear for adults (e.g. purse seine vs. otter-trawl, in Jarvela and Thorsteinson (1999) and Moulton and Tarbox (1987), respectively).

An increase in the prey diversity and prey size was observed for all three *Liparis* species as the larvae grew, demonstrated by the shift from the small copepod *T. borealis* (max. size of adults 0.7 mm), through younger stages of larger copepod species (2—3 mm) towards the adults of larger copepods and amphipods (4—6 mm). This transition has been already noted for Arctic Cod in the studied area and can be related to a larger gape size and increasing ability to catch more mobile prey as the larvae grow (Walkusz et al., 2011). Changing feeding focus from smaller to larger prey implies higher amounts of lipids are consumed to sustain rapid growth of larvae (10-fold weight increase between pre- and post-flexion). For example, the lipid content per individual copepodid increases approximately 50 times between the early and late life stages in *C. glacialis* (Falk-Petersen et al., 2009). Remarkably, the larvae of all three species fed heavily on larvacean *Oikopleura* spp. and pelagic snail *L. helicina* of which both may be an easy target due to their relatively slow motion. *Oikopleura* has been observed to be a key diet item of other larval fishes (e.g. Pacific herring (Foy and Norcross, 1999) or plaice (Shelbourne, 1962)). Madin et al. (1981) reported that tunicates, to which larvaceans belong, have high protein content (approx. 80% of organic content). Consuming this food, along with lipid-rich copepods, may help the *Liparis* larvae obtain the required energy supply and have a better balanced diet. Similarly, high lipid content found in *L. helicina*, particularly in the juvenile individuals (approx. 30% of dry mass; Gannefors et al., 2005), can explain notable frequency and biomass contribution of this food item to the larval snailfishes diet found in our study.

Diet overlap, particularly amongst the youngest larvae of *L. gibbus* and *L. tunicatus*, could suggest a shared dietary niche in early life history of these fishes. However, small sample size limits confidence in any conclusions. Nevertheless, Walkusz et al. (2013) showed the opposite habitat preferences for Polychaeta larvae and the copepod *T. borealis*, the potential planktonic food items of the larval fish, with the latter being affiliated with more saline (near bottom) water masses on the shelf. Thus, one could suggest that in the studied locations, pre-flexion *L. gibbus* and *L. tunicatus* are more associated with saline waters found deeper in

the water column as opposed to pre-flexion *L. fabricii*, which dietary preferences suggest feeding in the near-surface, fresher plume waters.

In summary, the *Liparis* larvae in the coastal Canadian Beaufort Sea were found to be generalists in terms of their feeding approach and relied on a broad spectrum of planktonic organisms (relatively high diversity of taxa as prey). A switch was observed in the diet, from small diet items in pre-flexion larvae (small copepods) towards larger items in flexion and post-flexion larvae (larger copepods and amphipods). This presumably results in the fish consuming food items having higher amounts of lipids, that provides the necessary amounts of energy required by larger snailfishes for proper development. The larval snailfishes in the study area fed also on larvaceans (*Oikopleura*) and pelagic snails (*L. helicina*) that can contribute significantly to the fish diet due to their high protein and lipid content, respectively. This study, along with many others, contributes to the current and future attempts of quantifying biomass/energy transfers in the Canadian Beaufort Sea. It can also be applied as baseline information in environmental assessments of the region.

Acknowledgements

This study was part of the Northern Coastal Marine Study (NCMS) program led by Donald Cobb. We thank Don for his leadership and for bringing the program to a successful conclusion. Our thanks also go to the captain and crew of the CCGS *Nahidik*, who made the sampling possible and created a good working atmosphere. We thank Lou Van Guelpen, Curator of Fishes and Collection Manager in the Atlantic Reference Centre (Huntsman Marine Science Centre, St. Andrews, NB, Canada) for help in identifying larvae that were found problematic during routine identification.

References

Able, K., 1990. A revision of Arctic snailfishes of the genus *Liparis* (Scorpaeniformes: Cyclopteridae). Copeia 1990 (2), 476—492, http://dx.doi.org/10.2307/1446352.

Atkinson, E.G., Percy, J.A., 1992. Diet comparison among demersal marine fish from the Canadian Arctic. Polar Biol. 11 (8), 567—573.

Byers, T., Prach, R.W., 1988. Diet of the kelpfish, *Liparis tunicatus*, in Jones Sound, Canadian High Arctic. Can. Field Nat. 102, 242—245.

Chernova, N.V., 2008. Systematics and phylogeny of fish of the genus *Liparis* (Liparidae, Scorpaeniformes). J. Ichthyol. 48, 831—852.

Chiperzak, D.B., Hopky, G.E., Lawrence, M.J., Schmid, D.F., Reist, J. D., 2003. Larval and post-larval fish data from the Canadian Beaufort Sea shelf, July to September, 1987. Can. Data Rep. Fish. Aquat. Sci. 1121 iv + 84 pp.

Dunton, K.H., Reimnitz, E., Schonberg, S., 1982. An Arctic kelp community in the Alaskan Beaufort Sea. Arctic 35 (4), 465—484, http://dx.doi.org/10.14430/arctic2355.

Evseenko, S.A., Andrianov, D.P., Mishin, A.V., Naumov, A.P., 2006. Species composition and distribution of ichthyoplankton in the White Sea in July 2003. J. Ichthyol. 46 (8), 640—652.

Fahay, M.P., 2007. Early Stages of Fishes in the Western North Atlantic Ocean, vol. II. Northwest Atlantic Fisheries Organization, Dartmouth, NS, Canada, 1696 pp.

Falk-Petersen, S., Haug, T., Nilssen, K.T., Wold, A., Dahl, T.M., 2004. Lipids and trophic linkages in harp seal (*Phoca groenlandica*) from the eastern Barents Sea. Polar Res. 23 (1), 43—50, http://dx.doi.org/10.1111/j.1751-8369.2004.tb00128.x.

Falk-Petersen, S., Mayzaud, P., Kattner, G., Sargent, J.R., 2009. Lipids and life strategy of Arctic *Calanus*. Mar. Biol. Res. 5 (1), 18—39, http://dx.doi.org/10.1080/17451000802512267.

Foy, R.J., Norcross, B.L., 1999. Spatial and temporal differences in the diet of juvenile Pacific herring (*Clupea pallasi*) in Prince William Sound, Alaska. Can. J. Zool. 77 (5), 697—706.

Gannefors, C., Boer, M., Kattner, G., Graeve, M., Eiane, K., Gulliksen, B., Hop, H., Falk-Petersen, S., 2005. The Arctic sea butterfly *Limacina helicina*: lipids and life strategy. Mar. Biol. 147 (1), 169—177, http://dx.doi.org/10.1007/s00227-004-1544-y.

Gaston, A.J., 1985. The diet of thick-billed murre chicks in the Eastern Canadian Arctic. The Auk 102 (4), 727—734.

Hanssen, H., 1997. Mesozooplankton of the Laptev Sea and the adjacent eastern Nansen Basin — distribution and community structure in late summer. Rep. Polar Res. 229, 1—131.

Hay, S.J., Kiørboe, T., Matthews, A., 1991. Zooplankton biomass and production in the North Sea during the Autumn Circulation Experiment, October 1987—March 1988. Cont. Shelf Res. 11 (12), 1453—1467, http://dx.doi.org/10.1016/0278-4343(91)90021-W.

Hurlbert, S.H., 1978. Measurement of niche overlap and some relatives. Ecology 59, 67—77.

Jarvela, L.E., Thorsteinson, L.K., 1999. The epipelagic fish community of Beaufort Sea coastal waters, Alaska. Arctic 52 (1), 80—94, http://dx.doi.org/10.14430/arctic912.

Karnovsky, N.J., Kwasniewski, S., Weslawski, J.M., Walkusz, W., Beszczynska-Möller, A., 2003. Foraging behaviour of little auks in a heterogeneous environment. Mar. Ecol. Prog. Ser. 253, 289—303.

Lowdon, M.K., Majewski, A.R., Reist, J.D., 2011. Fish catch data from Herschel Island, Yukon Territory, and other offshore sites in the Canadian Beaufort Sea, July and August 2008, aboard CCGS Nahidik. Can. Data Rep. Fish. Aquat. Sci. 1237 vi + 99 pp.

Madin, L.P., Cetta, C.M., McAlister, V.L., 1981. Elemental and biochemical composition of salps (Tunicata: Thaliacea). Mar. Biol. 63 (3), 217—226, http://dx.doi.org/10.1007/BF00395990.

Majewski, A.R., Reist, J.D., Park, B.J., Lowdon, M.K., 2009. Fish catch data from offshore sites in the Mackenzie River estuary and Beaufort Sea during the open water season, August 2006, aboard the CCGS Nahidik. Can. Data Rep. Fish. Aquat. Sci. 1218 vi + 37 pp.

Mecklenburg, C.W., Byrkjedal, I., Christiansen, J.S., Karamushko, O. V., Lynghammar, A., Møller, P.R., 2013. List of Marine Fishes of the Arctic Region Annotated with Common Names and Zoogeographic Characterization. Conservation of Arctic Flora and Fauna, Akureyri, Iceland.

Mecklenburg, C.W., Møller, P.R., Steinke, D., 2011. Biodiversity of arctic marine fishes: taxonomy and zoogeography. Mar. Biodivers. 41 (1), 109—140, http://dx.doi.org/10.1007/s12526-010-0070-z.

Mecklenburg, C.W., Stein, D.L., Sheiko, B.A., Chernova, N.V., Mecklenburg, T.A., Holladay, B.A., 2007. Russian—American long-term census of the Arctic: benthic fishes trawled in the Chukchi Sea and Bering Strait, August 2004. Northwest. Nat. 88, 168—187.

Morin, R., Dodson, J.J., 1986. The ecology of fishes in James Bay, Judson Bay and Hudson Strait. In: Martini, I.P. (Ed.), Canadian Inland Seas. Elsevier, New York, 293—325.

Moser, H.G., Richards, W.J., Cohen, D.M., Fahay, M.P., Kendall Jr., A. W., Richardson, S.L., 1984. Ontogeny and Systematics of Fishes. University of Kansas, Lawrence, 760 pp.

Moulton, L.L., Tarbox, K.E., 1987. Analysis of Arctic cod movements in the Beaufort Sea nearshore region, 1978—79. Arctic 40 (1), 43—49.

Mumm, N., 1991. On the summerly distribution of mesozooplankton in the Nansen Basin, Arctic Ocean. Rep. Polar Res. 92, 1—146, (in German).

Norcross, B.L., Holladay, B.L., Busby, M.S., Mier, K.L., 2010. Demersal and larval fish assemblages in the Chukchi Sea. Deep-Sea Res. Pt. II 57 (1—2), 57—70, http://dx.doi.org/10.1016/j.dsr2.2009.08.006.

Paulic, J.E., Papst, M.H., 2013. Larval and early juvenile fish distribution and assemblage structure in the Canadian Beaufort Sea during July—August, 2005. J. Mar. Syst. 127, 46—54, http://dx.doi.org/10.1016/j.jmarsys.2012.03.006.

Pickart, R.S., 2004. Shelfbreak circulation in the Alaskan Beaufort Sea: mean structure and variability. J. Geophys. Res. 109, C04024.

Ponton, D., Gagné, J.A., Fortier, L., 1993. Production and dispersion of freshwater, anadromous and marine fish larvae in and around river plume in subarctic Hudson Bay, Canada. Polar Biol. 13 (5), 321—331, http://dx.doi.org/10.1007/BF00238359.

Rand, K., Logerwell, E.A., 2010. The first survey of the abundance of benthic fish and invertebrates in the offshore marine waters of the Beaufort Sea since the late 1970s. Polar Biol. 34, 475—488, http://dx.doi.org/10.1007/s00300-010-0900-2.

Schoener, T.W., 1970. Non-synchronous spatial overlap of lizards in patchy habitats. Ecology 51, 408—418.

Shadwick, E.H., Thomas, H., Chierici, M., Else, B., Fransson, A., Michel, C., Miller, L.A., Mucci, A., Niemi, A., Papakyriakou, T.N., Tremblay, J.-E., 2011. Seasonal variability of the inorganic carbon system in the Amundsen Gulf region of the southeastern Beaufort Sea. Limnol. Oceanogr. 56 (1), 303—322, http://dx.doi.org/10.4319/lo.2011.56.1.0303.

Shelbourne, J.E., 1962. A predator—prey size relationship for plaice larvae feeding on *Oikopleura*. J. Mar. Biol. Assoc. U.K. 42 (2), 243—252, http://dx.doi.org/10.1017/S0025315400001326.

Stern, G.A., Gaden, A. (Eds.), 2015. From Science to Policy in the Western and Central Arctic: an Integrated Regional Impact Study (IRIS) of Climate Change and Modernization. University of Manitoba/ArcticNet, Winnipeg/Quebec City, 432 pp.

Suzuki, K.W., Bouchard, C., Robert, D., Fortier, L., 2015. Spatiotemporal occurrence of summer ichthyoplankton in the southern Beaufort Sea. Polar Biol. 38 (9), 1379—1389, http://dx.doi.org/10.1007/s00300-015-1701-4.

Walkusz, W., Paulic, J.E., Kwasniewski, S., Williams, W.J., Wong, S., Papst, M.H., 2010. Distribution, diversity and biomass of summer zooplankton from the coastal Canadian Beaufort Sea. Polar Biol. 33 (3), 321—335, http://dx.doi.org/10.1007/s00300-009-0708-0.

Walkusz, W., Paulic, J.E., Williams, W.J., Kwasniewski, S., Papst, M.H., 2011. Distribution and diet of larval and juvenile Arctic cod (*Boreogadus saida*) in the shallow Canadian Beaufort Sea. J. Mar. Syst. 84 (3—4), 78—84, http://dx.doi.org/10.1016/j.jmarsys.2010.09.001.

Walkusz, W., Williams, W.J., Harwood, L.A., Moore, S.E., Stewart, B.E., Kwasniewski, S., 2012. Composition, biomass and energetic content of biota in the vicinity of feeding bowhead whales (*Balaena mysticetus*) in the Cape Bathurst upwelling region (south eastern Beaufort Sea). Deep-Sea Res. Pt. I 69, 25—35, http://dx.doi.org/10.1016/j.dsr.2012.05.016.

Walkusz, W., Williams, W.J., Kwasniewski, S., 2013. Vertical distribution of mesozooplankton in the coastal Canadian Beaufort Sea in summer. J. Mar. Syst. 127, 26—35, http://dx.doi.org/10.1016/j.jmarsys.2012.01.001.

Wong, S., Walkusz, W., Hanson, M., Papst, M.H., 2013. The influence of the Mackenzie River plume on distribution and diversity of marine larval fish assemblages on the Canadian Beaufort Shelf. J. Mar. Syst. 127, 36—45, http://dx.doi.org/10.1016/j.jmarsys.2013.02.004.

Oceanologia (2016) 58, 124—134

Available online at www.sciencedirect.com

ScienceDirect

journal homepage: www.elsevier.com/locate/oceano

ORIGINAL RESEARCH ARTICLE

Scale-dependent environmental control of mesozooplankton community structure in three aquaculture subtropical bays of China☆

Dong Sun [a], **Zhensheng Liu** [a], **Chunsheng Wang** [a,b,*]

[a] *Laboratory of Marine Ecosystem and Biogeochemistry, Second Institute of Oceanography, State Oceanic Administration, Hangzhou, PR China*

[b] *State Key Laboratory of Satellite Ocean Environment Dynamics, Second Institute of Oceanography, State Oceanic Administration, Hangzhou, PR China*

Received 30 November 2014; accepted 9 November 2015
Available online 17 December 2015

KEYWORDS
Zooplankton;
Aquaculture;
Pollution effects;
Multivariate analysis;
Subtropical bays

Summary Most subtropical bays of China have been under heavy pollution since the late 1990s, mainly because of the rapid development of aquaculture and discharge of industrial and agricultural wastewater. Some projects were conducted to investigate the zooplankton community in these bays, but those studies were less focused on the relationship between spatial structure of mesozooplankton community and environmental variables in/among bays. The mesozooplankton community structures in relation to physical, chemical and biological variables were studied in three subtropical bays of China with seasons and different spatial scales during 2000 and 2002—2003. Data were collected on temperature (*T*), salinity (*S*), concentration of chlorophyll *a* (Chl *a*), pH, dissolved oxygen (DO), soluble reactive phosphate (SRP), dissolved inorganic nitrogen (DIN), chemical oxygen demand (COD), suspended particle material (SPM) and mesozooplankton taxonomic abundances. Correlation analysis showed that the main environmental factors correlated to the total abundance of mesozooplankton in these subtropical bays were Chl *a*, temperature, COD and SRP. Multivariate analysis indicated that DO, Chl *a* and temperature were the principal factors in influencing spatial differentiation of zooplankton

☆ This work was supported by the Global Change and Air-Sea Interaction Program (GASI-03-01-03-02), the China Ocean Mineral Resources Research and Development Association Program (DY125-11-E-03), National Natural Science Foundation of China (41406116), and Zhejiang Provincial Natural Science Foundation of China (LY12C03010).

* Corresponding author at: Laboratory of Marine Ecosystem and Biogeochemistry, Second Institute of Oceanography, State Oceanic Administration, Hangzhou 310012, PR China.
E-mail address: wang-sio@163.com (C. Wang).

Peer review under the responsibility of Institute of Oceanology of the Polish Academy of Sciences.

ELSEVIER Production and hosting by Elsevier

http://dx.doi.org/10.1016/j.oceano.2015.11.002

community structure in the inter-bay scale. At the within-bay scale, the influencing factors were different among bays; the main factors were physical variables for Xiangshan Bay and Sanmen Bay, while chemical variables for Yueqing Bay, respectively. The results revealed that the environmental variables that affected spatial structure of mesozooplankton community were different at inter-bay scale and within-bay scales, and zooplankton community was more influenced by chemical (e.g. nutrients/ammonia) variables when under serious eutrophication condition, while it would be more influenced by physical variables (temperature/salinity) when under less eutrophic conditions.

1. Introduction

Mesozooplankton always play an important role in various marine environments (Karsenti et al., 2011), and constitute a significant link between phytoplankton, microzooplankton and higher trophic levels, including many kinds of commercially marine animals (Tait and Dipper, 1998). Therefore, the aquatic environment and profits of aquaculture are always heavily influenced by the mesozooplankton community (Ayón et al., 2008; Bianchi et al., 2003). In estuarine areas, the spatial and temporal variation of the mesozooplankton community are always driven by several main factors, such as salinity and hydrographic facts (Hwang et al., 2010b; Mouny and Dauvin, 2002). While in coastal bays, the variation is mainly affected by many more environmental variables, such as temperature, salinity, oxygen, chlorophyll *a* concentration and other chemical factors (Li et al., 2005; Ning et al., 2004; Roman et al., 1993; Uriarte and Villate, 2005). The relationship is much more variable, since there are only weak or absolutely no constant decisive environmental gradients in these bays (Liu et al., 2012; Sun et al., 2011). Considering such weak environmental gradients, the relationship between environment and the zooplankton community in weak-influx coastal bays, are quite similar to the condition of adjacent continental shelf, where the influencing factors of zooplankton communities are strong spatial-temporal variation (Hwang et al., 2010a; Li et al., 2011, 2013).

The Zhejiang Province is one of the most industrialized and densely populated regions of China. In this area, with the rapid development of aquaculture and the discharge of ever increasing amounts of industrial and agricultural wastewater, the coastal waters have been heavily polluted since the late 1990s. Along the coastline of Zhejiang Province, there are three bays which are dominated by aquaculture: Xiangshan Bay, Sanmen Bay and Yueqing Bay. In recent years, several projects were conducted to assess the extent to which the marine ecosystem was influenced by human activities, and the carrying capacity of these bays, mainly based on the water quality parameters and plankton community characteristics (Cai et al., 2013; Ning and Hu, 2005). The mesozooplankton communities of those bays were reported in several studies from 2003 (Table 1). However, several aspects were

Table 1 Literatures reviewed about environmental variables which significantly affect the mesozooplankton community in these three bays.

Location	Season	Biological variable	Related environmental variable	Literatures
Xiangshan Bay	Four seasons	—	—	Wang et al. (2003)*
	Four seasons	—	—	Wang et al. (2009)*
	Winter	—	—	Liu et al. (2004)*
	Winter	Biomass	SPM, TOC	Du et al. (2011)[1]
		Abundance	S	
Yueqing Bay	Four seasons	Biomass	*T*, Chl *a*	Xu et al. (2012)[1]
		Abundance	*T*, Chl *a*, PCD	
	Spring	Abundance	S	Liu et al. (2005)[2]
	Summer	Abundance	S, TIN, SRP	
Sanmen Bay	Summer	Abundance	TIN	Liu et al. (2006)[2]
	Winter	Abundance	Chl *a*	
	Spring	Abundance	*T*, S, Chl *a*, TIN, SiO_3, DO	Liu et al. (2012)[1]
	Summer	Abundance	pH, DO	
	Autumn	Abundance	S, SiO_3	
	Winter	Abundance	COD	
	Four seasons	Abundance	*T*, S, Chl *a*	Xu et al. (2013)[3]

Statistical method: [1]Correlation analysis; [2]Linear regression analysis; [3]Canonical correspondence analysis (CCA); *no statistical method used. When no statistical method was used in cited studies, the biological variable and environmental variable were not shown.
Abbreviations: SPM — suspended particle material; TOC — total organic carbon; TIN — total inorganic nitrogen; SRP — soluble reactive phosphate; DO — dissolved oxygen; COD — chemical oxygen demand; *T* — temperature; *S* — salinity; PCD — phytoplankton cell density.

ignored in previous works until now. First, as mentioned above, there was no strong and constant environmental gradient in these bays. Additionally, the relationship between the environment and zooplankton community was more complex and with markedly seasonal variation. Hence, the relationship should be analyzed separately for each season. If that relationship between an environmental variable and a biotic parameter was reversed among different seasons, a potential significant effect in a certain season was likely to be counterbalanced using a linear regression analysis for whole year's data. Second, most studies focused only on the relationship between environment and biomass/abundance, but ignored the influencing factors of spatial variation of zooplankton community structure, and the scale-dependent effect of these influencing factors. Third, simple correlation analysis, instead of ordination analysis or other multivariate statistics analyses were used. In such case, the relationship between environmental variables and zooplankton spatial community structure might be underestimated in previous works (Table 1) (Šmilauer and Lepš, 2014).

Nutrients are key factors in most pelagic ecosystems, which indirectly influence the community structure and size structure of phytoplankton, and then indirectly influence the abundance and community structure of zooplankton (Graneli et al., 1999; McQueen et al., 1989; Zhou et al., 2008). Pollution always results in extremely high nutrient conditions for marine ecosystems in coastal waters (Li and Daler, 2004), and may significantly influence the mesozooplankton community structure (Marcus, 2004; Uriarte and Villate, 2005). Eutrophication may affect mesozooplankton via several possible pathways: bottom-up trophic dynamics, a limitation of hypoxia/anoxia and a toxic effect of ammonia (Roman et al., 1993; Sullivan and Ritacco, 1985; Uye et al., 1999). However, the effect of eutrophication on mesozooplankton is more complicated in coastal waters (Chen et al., 2011; Marcus, 2004), because the mesozooplankton are also under the influences of changing predation pressure, variation of food quality and hydrological conditions.

All three bays were heavily affected by aquaculture, but the differences in geometry and the exchange rate with open waters influenced their environmental characters. Among those three bays, Yueqing Bay is one of eight most critically polluted bays in China, especially characterized by extremely high nitrogen concentration (Chen et al., 2010; EBCWC, 2003). The water quality of Sanmen Bay is slightly better than the others, mainly because of its capacious geometry and much higher exchange rate (Ning and Hu, 2005) (Fig. 1).

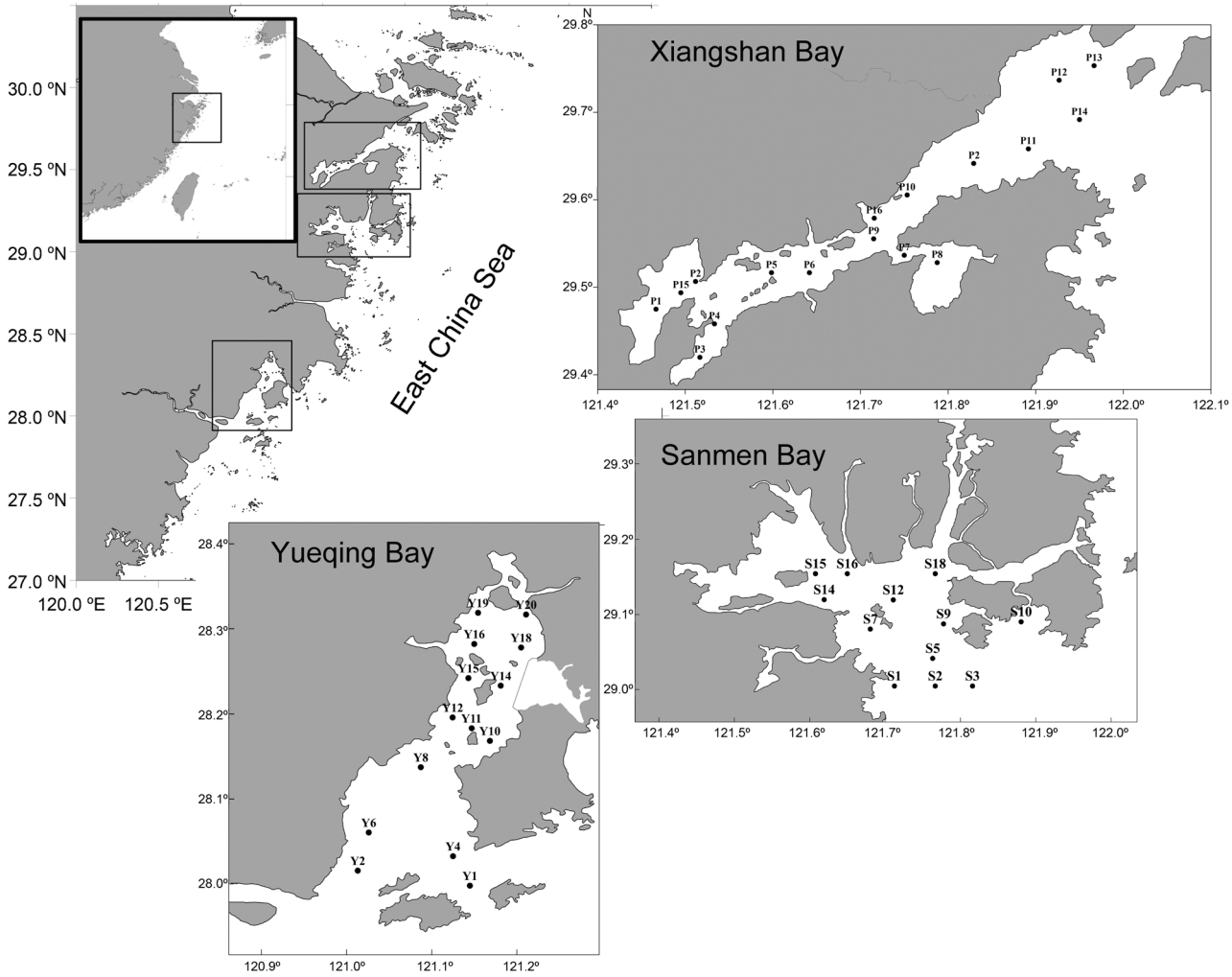

Figure 1 Map of Xiangshan Bay, Sanmen Bay and Yueqing Bay (located on the coast of Zhejiang Province, China, 28.0°N—29.9°N), showing sampling stations in the present study.

On the other hand, higher water exchange rate with the open sea might depress the gradient of chemical variables from pollution and their residence time (Wang et al., 2011).

Based on the three bays' environmental differences and a common effect of eutrophication on mesozooplankton community, we hypothesized that the zooplankton community would be more influenced by chemical (e.g. nutrients/ammonia) and biological (e.g. Chl *a*) variables when under serious eutrophic conditions, while it would be more influenced by physical variables (temperature/salinity) when under less eutrophic conditions.

2. Material and methods

2.1. Study area

This study was conducted in three subtropical bays: Xiangshan Bay, Sanmen Bay and Yueqing Bay, along the coast of Zhejiang Province, China (28.0°N–29.9°N) (Fig. 1). All three bays are semi-enclosed (with various magnitude of openness), without strong freshwater influx and have been heavily influenced by aquaculture since the 1990s. Xiangshan Bay is about 563 km^2 in area, 10 m in mean depth and 40 m in maximum depth. Xiangshan Bay is relatively narrow and long, with about 50 km in total length and 9.5 km in mouth width. Sanmen Bay is about 540 km^2 in area, 9 m in mean depth and above 60 m in maximum depth. There are several branches deep into land, which creates over one hundred square kilometers shoal in the area. Its total length is about 42 km and with 22 km wide in mouth. Yueqing Bay is about 464 km^2 in area, approximately 10 m in mean depth and over a hundred meters in maximum depth. This bay is 42 km in length, 21 km in mouth wide and 4.5 km in minimum width.

2.2. Sampling procedure

Sampling was conducted during twelve short-period investigations (four seasons × three bays). For Xiangshan Bay, investigations were conducted at twenty sampling sites in January, April, July and October 2000. For Sanmen Bay and Yueqing Bay, investigations were conducted at twelve and fourteen sampling sites respectively, in August, November 2002, May and February 2003.

Zooplankton samples were collected by vertical tows (505 μm mesh size and 0.8 m in diameter, equipped with a HYDRO-BIOS flowmeter fixed in the mouth to measure the volume of water filtered) from near-bottom to surface. Net collections were fixed with 5% (v/v) buffered formaldehyde (with seawater) immediately. In laboratory, 5% to 25% fractions of total mesozooplankton sample were identified and counted according to the individual number (Chen et al., 1974; Zheng et al., 1984). Zooplankton abundance was expressed as ind. m^{-3}. The fundamental data of wet biomass and abundance of mesozooplankton community collected from those investigations had been published (Liu et al., 2005, 2006; Wang et al., 2003), thus most of those detailed data were not shown again in the present study. The raw data on abundance of each species in every station were analyzed in the present study. Absolutely rare species (a single occurrence for all sampling sites) were eliminated from correlation analysis and ordination analysis below, and they were not shown in the list of species (Appendix Table 1).

The physical environmental parameters, including salinity and temperature were recorded at 0.5 m under surface by a SYA 2-2 salinometer and thermometer. The water samples for nutrient analysis were collected at a depth of 0.5 m by Go-Flo bottles. Nitrate and nitrite were determined by the pink azo dye method and ammonia by the hypobromite oxidation-pink azo dye method; soluble reactive phosphorus was determined by the molybdenum blue method immediately after sampling (Parsons et al., 1984). The detection limits of NO_3^-, NO_2^-, NH_4^+, PO_4^{3-} and SiO_3^{2-} are 0.02 μmol L^{-1}, 0.05 μmol L^{-1}, 0.05 μmol L^{-1}, 0.03 μmol L^{-1} and 0.07 μmol L^{-1}, respectively, for the present methods. The concentration of dissolved oxygen was measured using a direct spectrophotometry method (Pai et al., 1993). For the measurement of chlorophyll *a* (Chl *a*) concentration, a 500 mL water sample was gently filtered through a 0.22 μm cellulose filter and extracted in 90% acetone for 24 h in darkness and 4°C. The mean Chl *a* concentration was then determined fluorometrically (Turner Designs 10AU fluorometer) before and after acidification (Parsons et al., 1984). The concentration of suspended particle material (>0.45 μm) was only measured for Xiangshan Bay.

2.3. Data analysis

For the zooplankton abundance data and environmental data, we used unconstrained ordination, constrained ordination and correlation analysis to distinguish the main environmental variables which significantly affect the abundance of zooplankton and the zooplankton community structure, at different spatial scales and in different seasons. All analyses below were based on log-transformed abundance data and environmental data.

First, a Pearson correlation analysis was applied to find the relationship between abundance of zooplankton in three bays and environmental variables with seasons.

Second, the environmental variables which drive the heterogeneity of mesozooplankton community structure among the three subtropical bays in each season were distinguished. According to the methods by Šmilauer and Lepš (2014), DCA was used to find whether abundance data of zooplankton showed linear or unimodal responses to the underlying gradients in this region. For the data of spring, summer and autumn, the lengths of gradient were all less than 3, while the length of gradient was over 4 for the winter data. Thus, we conducted three redundancy analyses (RDA) for the spring, summer and autumn data, and a canonical correspondence analysis (CCA) for the data of winter. Explanatory environmental variables were chosen by the forward selection in RDA and CCA, and only those variables that significantly related to community structure according to Monte Carlo permutation tests ($p < 0.05$) were selected to be considered in RDAs and CCA, and to be shown in ordination diagrams. The variability explained for each environmental variable in CCA equals to λ value divided by total inertia.

Third, the environmental variables which affect the mesozooplankton community structure in each of the three subtropical bays in every season were distinguished. The model selection procedure was the same as above, and twelve separate RDAs were conducted. Also, only those variables

that significantly influence community structure according to Monte Carlo permutation tests ($p < 0.05$) were selected to be considered in RDAs. In the present analysis, chemical variables included DIN, SRP, PH, COD, NH_3; biological variable included Chl *a*; physical variables included temperature and salinity.

The correlation analysis was performed using SPSS v19.0 (IBM Corp., Somers, NY, USA), and ordination analysis was performed using CANOCO v4.5 (Microcomputer Power, Ithaca, NY, USA).

3. Results

3.1. Environmental and biotic characteristic

Environmental data obtained during this study were given in Fig. 2 and Appendix Table I. Surface temperature showed an obvious seasonal variation in those three bays, by winter cooling and summer warming. Surface salinity was higher in spring/summer and lower in autumn/winter in Xiangshan Bay and Sanmen Bay, while lower in spring/summer and higher in autumn/winter in Yueqing Bay. The concentration of Chl *a* was significantly lower in Xiangshan Bay, compared to the other two, and also showed significant seasonal variations (Fig. 2).

Similar to the environmental variables, the abundance of mesozooplankton in the three bays also showed a temporal and spatial variation. In Xiangshan Bay, the seasonal peak appeared in spring, while for the other two bays, the abundance reached the highest level in summer (Fig. 3). Compared to the other two bays, the mesozooplankton abundance in Xiangshan Bay was significantly higher in spring and autumn (one-way ANOVA, $p = 0.002$, and $p = 0.006$, respectively), and in Sanmen Bay it was significantly higher in summer (one-way ANOVA, $p = 0.001$). In winter, the abundance in Yueqing Bay was lower, but not statistically significant (one-way ANOVA, $p = 0.075$). The mesozooplankton community structures were also quite different among the three bays. In Xiangshan Bay, *Centropages abdominalis* was

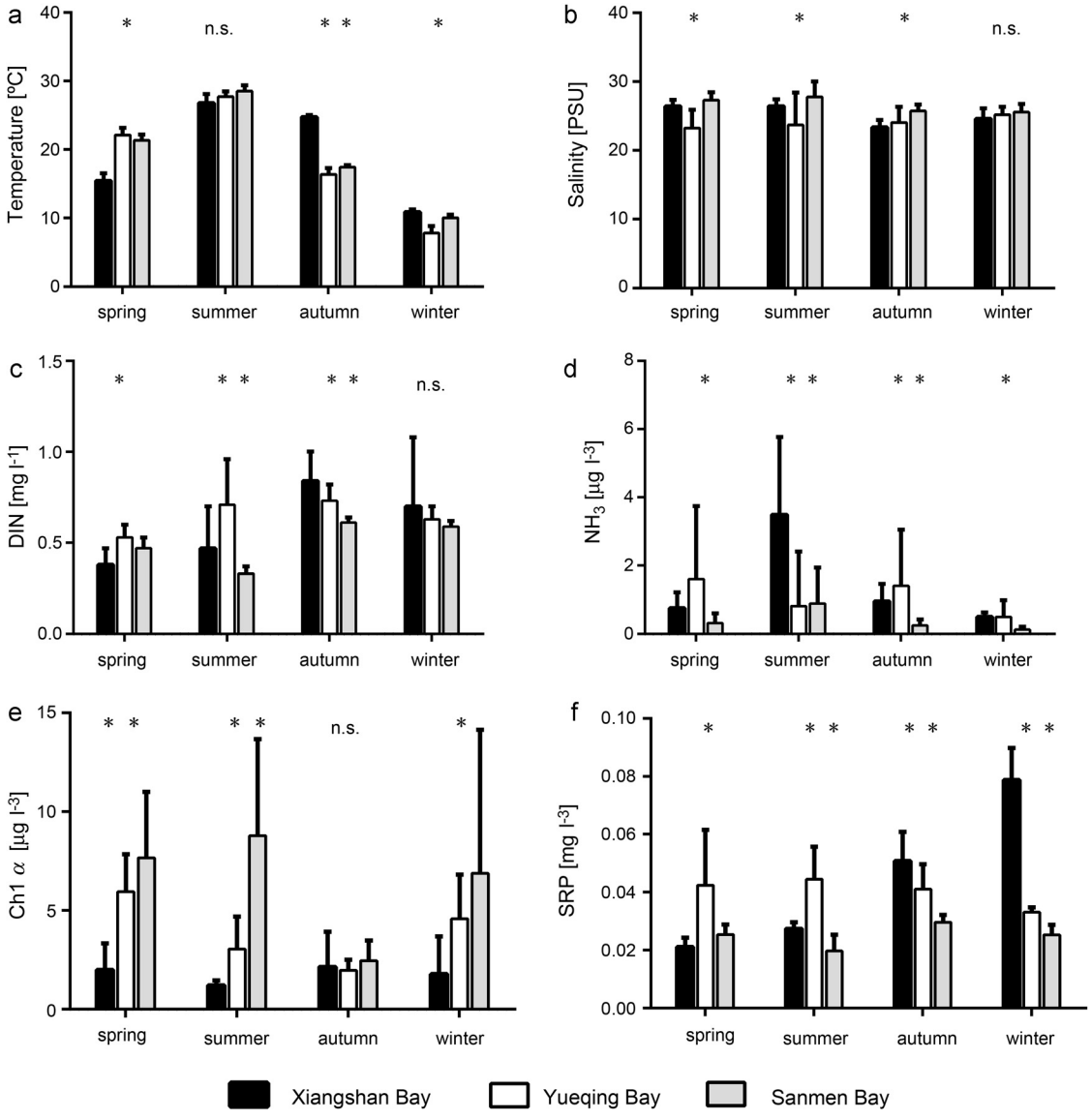

Figure 2 Environmental variables of Xiangshan Bay, Sanmen Bay and Yueqing Bay ($^{*}p < 0.05$; $^{**}p < 0.01$).

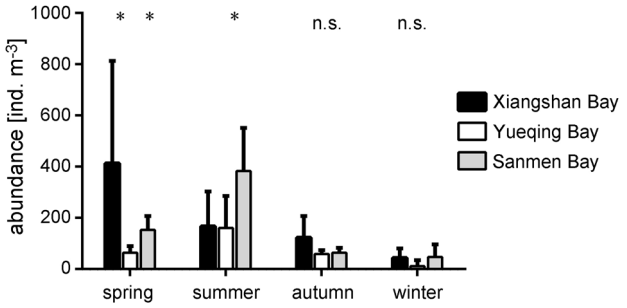

Figure 3 Abundance of mesozooplankton community of Xiangshan Bay, Sanmen Bay and Yueqing Bay ($^{*}p < 0.05$; $^{**}p < 0.01$).

one dominant species in spring, summer and winter, especially with an extremely high relative abundance in spring. And *Acartia pacifica* only dominated in warm seasons. In Yueqing Bay, *Labidocera euchaeta* was always the dominant species all the year round, especially in warm seasons. In Sanmen Bay, two main dominant species were *Calanus sinicus* and *Acrocalanus gibber* (Table 2).

3.2. Environmental factors—zooplankton community relationships

3.2.1. Seasonal variation of environmental factors correlated to zooplankton abundance

Pearson correlation analysis indicated that environmental factors correlated to the abundance of mesozooplankton in these subtropical bays differed with seasons. In spring, it was positively related to DO and negatively related to temperature, COD and SRP. In summer, it was positively related to Chl *a*, temperature and COD, and negatively related to SPR. In autumn, it was positively related to temperature, and negatively related to Chl *a*. While in winter, it was positively related to Chl *a* and negatively related to salinity (Table 3).

Table 3 Pearson correlation coefficients between abundance of mesozooplankton [ind. m^{-3}] and environmental variables in Xiangshan Bay, Yueqing Bay and Sanmen Bay in four seasons. The abbreviations of environmental variables were listed in Table 1.

Variables	Abundance			
	Spring	Summer	Autumn	Winter
Chl *a*	n.s.	0.666^{**}	-0.333^{*}	0.415^{**}
T	-0.436^{**}	0.376^{*}	0.329^{*}	n.s.
DO	0.512^{**}	n.s.	n.s.	n.s.
PH	n.s.	n.s.	n.s.	n.s.
S	n.s.	n.s.	n.s.	-0.452^{**}
NH_3	n.s.	n.s.	n.s.	n.s.
DIN	n.s.	n.s.	n.s.	n.s.
COD	-0.468^{**}	0.499^{**}	n.s.	n.s.
SRP	-0.413^{**}	-0.312^{**}	n.s.	n.s.

Note: n.s. — $p > 0.05$; $^{*}p < 0.05$; $^{**}p < 0.01$.

3.2.2. Environmental factors affecting the spatial differentiation of zooplankton community structure

RDAs and CCA showed that environmental factors affecting the spatial differentiation of zooplankton community structure were significantly different with seasons ($p < 0.05$, Monte Carlo permutation tests) (Fig. 4). In spring, the differentiation between the community of Xiangshan Bay and the others was mainly explained by DO (28%) and temperature (3%), while the differentiation between the community of Yueqing Bay and Sanmen Bay was mainly driven by salinity (11%). In summer, the differentiation between the community of Sanmen Bay and the others was mainly explained by Chl *a* (16%) and salinity (7%), while there was no significant differentiation between the community of Xiangshan Bay and Yueqing Bay (Fig. 4). In autumn, the differentiation between the community of Xiangshan Bay and the others was mainly explained by temperature (25%). And the differentiation between the community of Yueqing Bay and Sanmen Bay

Table 2 The dominant species of mesozooplankton community in Xiangshan Bay, Yueqing Bay and Sanmen Bay. The relative abundance of dominant species was given.

Seasons	Dominant species		
	Xiangshan Bay	Yueqing Bay	Sanmen Bay
Spring	*Centropages abdominalis* (76%)	Brachyura zoea larva (21%) *Labidocera euchaeta* (14%) *Zonosagitta bedoti* (12%)	*Calanus sinicus* (21%) Brachyura zoea larva (11%)
Summer	Brachyura zoea larva (29%) *Acartia pacifica* (17%) *Centropages abdominalis* (11%)	*Labidocera euchaeta* (25%) Brachyura zoea larva (14%)	*Acrocalanus gibber* (26%)
Autumn	*Paracalanus aculeatus* (20%) *Acartia pacifica* (20%) *Calanopia thompsoni* (11%)	*Labidocera euchaeta* (36%) *Acrocalanus gibber* (18%) *Acartia pacifica* (17%)	*Calanus sinicus* (20%) *Acrocalanus gibber* (12%)
Winter	*Centropages abdominalis* (42%) *Oikopleura dioica* (16%) *Tortanus derjugini* (15%)	Gastropoda post larva (42%) *Diastylis tricincta* (14%) *Labidocera euchaeta* (9%)	*Centropages abdominalis* (33%) *Tortanus derjugini* (17%) *Diastylis tricincta* (16%)

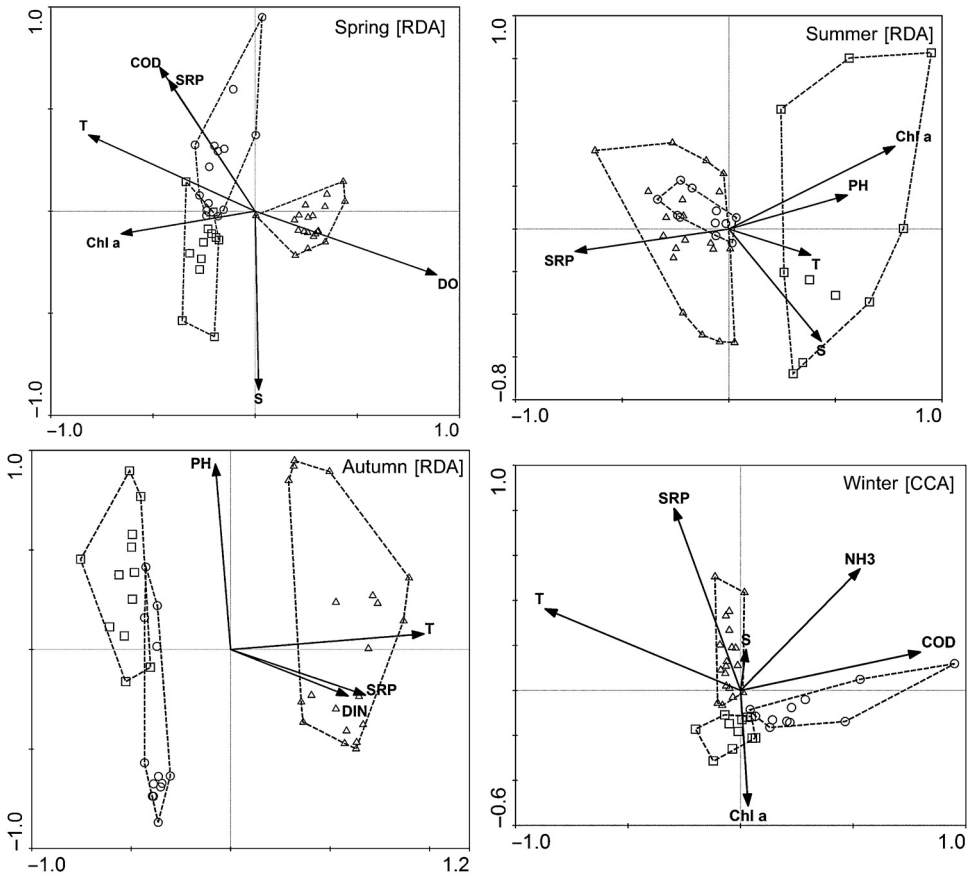

Figure 4 RDA and CCA ordination diagrams of site scores in three bays and selected environmental variables (represented by arrows) in four seasons. Only the significantly explanatory environmental variables retained by a forward selection procedure ($p < 0.05$, Monte Carlo permutation test) are presented. The data from spring, summer and autumn were analyzed under RDA model, while the data from winter were analyzed under CCA model (see more details in Methods). Symbol: triangle — Xiangshan Bay; circle — Yueqing Bay; square — Sanmen Bay.

could be explained by pH (12%), though there was a considerable degree of overlap between them under this axis. Finally, in winter, temperature (12%) explained the differentiation between the community of Yueqing Bay and the others, while NH_3 (9%) and salinity (7%) could influence the differentiation between the community of Xiangshan Bay and Sanmen Bay (Table 4).

3.2.3. Environmental factors affecting the zooplankton community structure in each bay

RDA showed that zooplankton community structure was significantly related to several environmental variables, and it was quite variable with sites and seasons. Specifically, salinity, temperature and Chl *a* were always the main factors affecting the community structure in Xiangshan Bay (Table 5). For Sanmen Bay, the primary factors were always salinity and NH_3 in spring, summer and autumn, but SRP and temperature in winter (Table 6). Finally, the primary environmental factors were extraordinarily variable in Yueqing Bay, which were temperature in spring, DIN in summer, SRP, Chl *a* and DIN in autumn and COD in winter (Table 7). For the full year, physical variables were the dominant influencing factors for the zooplankton community structure in Xiangshan Bay and Sanmen Bay, while chemical variables were more dominant in Yueqing Bay (Table 8).

4. Discussion

Generally, we found that the environmental variables which affected the abundance and spatial differentiation of zooplankton community structure were significantly variable with seasons and with different spatial scales in these adjacent subtropical bays of China. Consistent with our hypothesis, the zooplankton community structure of Sanmen Bay, which has lower pollution rate than the two other bays, was most influenced by the physical variables; while that of Yueqing Bay, which is heavily polluted, was most influenced by the chemical variables. In Xiangshan Bay, which is moderately polluted, the zooplankton was again most influenced by physical variables.

Eutrophication may affect herbivorous zooplankton through providing more food directly by phytoplankton or indirectly by complex microbial food loop (Calbet and Landry, 1999; Jones and Flynn, 2005). The concentration of Chl *a* was always an important environmental gradient related to the level of primary productivity in coastal bays. Although Chl *a* was widely used as a biological indicator of eutrophication in some monitoring methods (Nixon, 1995), the present results indicated that it was not associated with nutrient concentration in these bays. As in other shallow turbid systems, the phytoplankton seems not to be nutrient-limited, but light

Table 4 Ranking of environmental variables that significantly influenced the spatial differentiation of zooplankton community structure among three bays, based on Monte Carlo permutation test in redundancy analysis (RDA) (the data in spring, summer and autumn) and canonical correspondence analysis (CCA) (the data in winter) (499 samples, $p < 0.05$). The variability explained for each environmental variable in canonical correspondence analysis equals to λ value divided by total inertia. The abbreviations of environmental variables were listed in Table 1.

Explanatory variable	Variability explained	*p*-value	*F*-value
Spring (RDA)			
DO	0.28	0.002	16.93
S	0.11	0.002	7.8
COD	0.04	0.004	2.99
SRP	0.03	0.008	2.52
Chl *a*	0.03	0.024	2.08
T	0.03	0.028	2.1
Summer (RDA)			
Chl *a*	0.16	0.002	7.19
S	0.07	0.002	3.58
PH	0.05	0.01	2.63
SRP	0.05	0.006	2.75
T	0.04	0.04	2
Autumn (RDA)			
T	0.25	0.002	14.63
PH	0.12	0.002	8.12
DIN	0.04	0.008	2.66
SRP	0.03	0.012	2.2
Winter (CCA)			
T	0.12	0.002	5.12
NH_3	0.09	0.002	4.05
S	0.07	0.002	3.68
SRP	0.04	0.006	2.07
Chl *a*	0.04	0.044	2.05
COD	0.03	0.022	1.86

Table 5 Ranking of environmental variables that significantly influenced the community structure of mesozooplankton in Xiangshan Bay, based on Monte Carlo permutation test in redundancy analysis (RDA) (499 samples, $p < 0.05$).

Explanatory variable	Variability explained	*p*-value	*F*-value
Spring			
S	0.4	0.002	12.13
Chl *a*	0.13	0.002	4.71
Summer			
T	0.3	0.002	7.72
Chl *a*	0.14	0.002	4.3
Autumn			
S	0.28	0.002	7.15
T	0.18	0.002	5.51
DIN	0.07	0.012	2.36
Chl *a*	0.06	0.018	2.42
Winter			
S	0.37	0.002	10
Chl *a*	0.17	0.002	6.01
NH_3	0.09	0.006	3.8
PH	0.07	0.01	2.86

Table 6 Ranking of environmental variables that significantly influenced the community structure of mesozooplankton in Sanmen Bay, based on Monte Carlo permutation test in redundancy analysis (RDA) (499 samples, $p < 0.05$).

Explanatory variable	Variability explained	*p*-value	*F*-value
Spring			
S	0.23	0.002	3.05
NH_3	0.23	0.002	3.78
Summer			
S	0.35	0.002	4.28
Autumn			
S	0.25	0.002	3.34
Winter			
SRP	0.39	0.002	5.81
T	0.19	0.002	3.69

availability is likely to be the limiting factor (e.g. Domingues et al., 2011; Guinder et al., 2009; Zhu et al., 2009). In the present result, the concentration of Chl *a* was not the dominant influencing factor of zooplankton community structure in all three bays. Similar phenomenon was also found in other eutrophic coastal waters (Chen et al., 2011; Uriarte and Villate, 2005). These results indicated that direct trophic link between phytoplankton and mesozooplankton was relatively weak in these bays.

Typically, due to hydrographic features and a gradient of nutrient or transparency along geometrical features, the concentration of Chl *a* often showed a decreasing gradient from inside to mouth in temperate and subtropical bays, such as Xiangshan Bay and Jiaozhou Bay in China (Li et al., 2005; Liu et al., 1997). However, this stable gradient was not observed in Yueqing Bay and Sanmen Bay (Chen et al., 2010 and the present study). Multivariate statistics analysis indicated that the concentration of Chl *a* was only able to explain the spatial pattern of zooplankton community in Xiangshan Bay, but not in Yueqing Bay and Sanmen Bay. There were two possible reasons: one, a high Chl *a* concentration meant redundant food for mesozooplankton, thus Chl *a* was a limiting factor for them no longer (Chen et al., 2011); two, other more dominant influencing factors existed, which outstripped the contribution of Chl *a* variation (Uriarte and Villate, 2005), such as DIN from extreme heavy pollution in Yueqing Bay.

Copepods always dominated mesozooplankton community in coastal waters (Chang et al., 2010; Liu et al., 2012), and they were generally considered to be relatively sensitive to poor water quality (Uriarte and Villate, 2005). Buttino (1994) reported that the viability and reproduction rate of *Acartia clausi* would be significantly depressed under a NH_3 concentration of 0.12 ppm. We were not aware of the sensitivity of local zooplankton community to NH_3, considering that NH_3 concentration in Buttino's report was approximately two

Table 7 Ranking of environmental variables that significantly influenced the community structure of mesozooplankton in Yueqing Bay, based on Monte Carlo permutation test in redundancy analysis (RDA) (499 samples, $p < 0.05$).

Explanatory variable	Variability explained	*p*-value	*F*-value
Spring			
T	0.22	0.002	3.43
Summer			
DIN	0.4	0.002	6.06
Autumn			
SPR	0.39	0.002	7.05
Chl *a*	0.13	0.006	2.68
DIN	0.09	0.046	2.05
Winter			
COD	0.49	0.002	8.57

Table 8 The total variability explained by chemical/biological/physical variables on zooplankton community structure of each bay in four seasons (chemical variables: DIN, SRP, PH, COD, NH_3; biological variable: Chl *a*; physical variables: temperature, salinity; based on Tables 5–7).

	Variability explained		
	Chemical variable	Biological variable	Physical variable
Xiangshan Bay	0.23	0.5	1.53
Sanmen Bay	0.62	0	1.02
Yueqing Bay	1.37	0.13	0.22

orders of magnitude higher than those in the present study, thus the NH_3 concentration was likely to be the secondary factor in affecting the spatial structure of zooplankton community in the three bays.

The total abundance of mesozooplankton was not affected by DIN conditions in each season in our study, which was in accordance with other results in these three bays (Du et al., 2011; Xu et al., 2012, 2013), but it was negatively impacted by the SRP concentration in spring and summer. The exact mechanism of that relationship was unknown. Although all three bays exhibited eutrophic conditions, multivariate statistics analysis indicated that eutrophic conditions were the primary factor influencing the spatial structure of mesozooplankton community only in Yueqing Bay. The dominant species of the mesozooplankton communities were significantly different among the three bays, though the salinity and temperature were quite similar between Xiangshan Bay and Yueqing Bay. *L. euchaeta* is a common eurytopic and dominant species in the subtropical coast of China, distributed in a salinity range from 10 to 25 (Chen et al., 1995). A more recent study demonstrated that this species adapted to higher Chl *a* concentration and lower nutrient concentration in Hangzhou Bay (200 km north from Xiangshan Bay) (Sun et al., unpublished data). In summer and autumn, *L. euchaeta* was the first dominant species (the relative abundance is 25% and 36%, respectively) for the community in Yueqing Bay. Interestingly, RDA indicated that chemical variables also determined the spatial structure of community in these two seasons. A possible reason was that the lower nutrient condition for distribution area of *L. euchaeta* determined, to a great extent, the response of zooplankton community to DIN and SRP gradients in Yueqing Bay in summer and autumn. It also implied that the pelagic ecosystem of Yueqing Bay was under the most serious influence of pollution among the three bays.

Physical variables (temperature and salinity) were the main influencing factors for mesozooplankton community structure in Xiangshan Bay and Sanmen Bay. In contrast, chemical variables (DIN and SRP) were the main factors affecting community structure in Yueqing Bay during most of the year. These results indicated that salinity was usually still an important influencing factor for the mesozooplankton community structure of subtropical bays without strong freshwater influx and pollution, though it was no longer the only dominant factor, just as in typical estuary areas (Marques et al., 2006; Mouny and Dauvin, 2002). Moreover, this significant difference in influencing factors among different bays implied that the zooplankton community of Yueqing Bay was more heavily affected by pollution and aquaculture than Xiangshan Bay and Sanmen Bay.

5. Conclusions

The environmental variables influencing zooplankton community structure differed significantly with the seasons and spatial scales in subtropical bays of China which were heavily affected by pollution and aquaculture. DO, Chl *a* and temperature were the principal factors in affecting spatial differentiation of zooplankton community structure at the inter-bay scale. At within-bay scales, the influencing factors were different among adjacent bays: the main factors were physical variables for Xiangshan Bay and Sanmen Bay, while chemical variables for Yueqing Bay, respectively.

Acknowledgements

We would like to thank Ping Xia for providing a high resolution map of the research area and Renée McDonald for her valuable corrections of the English. We also thank four anonymous reviewers for their kind comments and constructive advice.

Appendix A. Supplementary data

Supplementary data associated with this article can be found, in the online version, at doi:10.1016/j.oceano.2015.11.002.

References

Ayón, P., Criales-Hernandez, M.I., Schwamborn, R., Hirche, H.-J., 2008. Zooplankton research off Peru: a review. Prog. Oceanogr. 79 (2–4), 238–255, http://dx.doi.org/10.1016/j.pocean.2008.10.020.

Bianchi, F., Acri, F., Aubry, F.B., Berton, A., Boldrin, A., Camatti, E., Cassin, D., Comaschi, A., 2003. Can plankton communities be considered as bio-indicators of water quality in the Lagoon of Venice? Mar. Pollut. Bull. 46 (8), 964–971, http://dx.doi.org/10.1016/S0025-326X(03)00111-5.

Buttino, I., 1994. The effect of low concentrations of phenol and ammonia on egg production rates, fecal pellet production and egg viability of the calanoid copepod *Acartia clausi*. Mar. Biol. 119 (4), 629—634, http://dx.doi.org/10.1007/BF00354327.

Cai, X., Pan, J., Yu, P., Liu, X., Sun, W., 2013. Study of the behavior of nutrients in different harbors in coastal waters of Zhejiang Province. Mar. Sci. Bull. 32, 488—493, (in Chinese with English abstract), http://dx.doi.org/10.11840/j.issn.1001-6392.2013.05.002.

Calbet, A., Landry, M.R., 1999. Mesozooplankton influences on the microbial food web: direct and indirect trophic interactions in the oligotrophic open ocean. Limnol. Oceanogr. 44 (6), 1370—1380, http://dx.doi.org/10.4319/lo.1999.44.6.1370.

Chang, W.-B., Dahms, H.-U., Tseng, L.-C., 2010. Copepods assemblages in an embayment of Taiwan during monsoonal transitions. Zool. Stud. 49 (6), 735—748.

Chen, M., Chen, B., Harrison, P., Liu, H., 2011. Dynamics of mesozooplankton assemblages in subtropical coastal waters of Hong Kong: a comparative study between a eutrophic estuarine and a mesotrophic coastal site. Cont. Shelf Res. 31 (10), 1075—1086, http://dx.doi.org/10.1016/j.csr.2011.03.011.

Chen, L., Xu, Z., Chen, S., Cai, S., Lv, B., Bao, X., 2010. Causal analysis and distribution of eutrophication index in the Yueqing Bay in spring-summer of 2007. J. Shanghai Ocean Univ. 19 (1), 91—97, (in Chinese with English abstract).

Chen, Y., Xu, Z., Wang, Y., Hu, F., Hu, H., Gu, G., 1995. An ecological study on zooplankton in plume front zone of Changjiang (Yangtze) River estuarine area. I. Biomass distribution of dominant species. J. Fish. Sci. China 2, 49—58, (in Chinese with English abstract).

Chen, Q., Zhang, S., Zhu, C., 1974. The planktonic copepods of the Yellow Sea and the East China Sea: II. Cyclopoida and harpacticoida. Stud. Mar. Sin. 9, 27—76, (in Chinese).

Domingues, R.B., Anselmo, T.P., Barbosa, A.B., Sommer, U., Galvão, H.M., 2011. Light as a driver of phytoplankton growth and production in the freshwater tidal zone of a turbid estuary. Estuar. Coast. Shelf Sci. 91 (4), 526—535, http://dx.doi.org/10.1016/j.ecss.2010.12.008.

Du, P., Liu, J., Xu, X., Chen, Q., Zeng, J., Jiang, Z., Wang, Q., 2011. A compare study of the ecologial characters of zooplankton community in different habitats of Xiangshan Bay in winter. Fish. Sci. Technol. Inf. 38, 92—99, (in Chinese with English abstract), http://dx.doi.org/10.3969/j.issn.1001-1994.2011.02.011.

EBCWC, 2003. The Environmental Bulletin of Coastal Waters of China in 2002. The State Environmental Protection Agency of China, 24 pp., (in Chinese).

Graneli, E., Carlsson, P., Turner, J.T., Tester, P.A., Béchemin, C., Dawson, R., Funari, E., 1999. Effects of N:P:Si ratios and zooplankton grazing on phytoplankton communities in the northern Adriatic Sea. I. Nutrients, phytoplankton biomass, and polysaccharide production. Aquat. Microb. Ecol. 18 (1), 37—54, http://dx.doi.org/10.3354/ame018037.

Guinder, V.A., Popovich, C.A., Perillo, G.M., 2009. Particulate suspended matter concentrations in the Bahía Blanca Estuary, Argentina: implication for the development of phytoplankton blooms. Estuar. Coast. Shelf Sci. 85, 157—165, http://dx.doi.org/10.1016/j.ecss.2009.05.022.

Hwang, J.-S., Kumar, R., Dahms, H.-U., Tseng, L.-C., Chen, Q.-C., 2010a. Interannual, seasonal, and diurnal variation in vertical and horizontal distribution patterns of 6 *Oithona* spp. (Copepoda: Cyclopoida) in the South China Sea. Zool. Stud. 49, 220—229.

Hwang, J.-S., Kumar, R., Hsieh, C.-W., Kuo, A.Y., Souissi, S., Hsu, M.-H., Wu, J.-T., Liu, W.-C., Wang, C.-F., Chen, Q.-C., 2010b. Patterns of zooplankton distribution along the marine, estuarine and riverine portions of the Danshuei ecosystem in northern Taiwan. Zool. Stud. 49, 335—352.

Jones, R.H., Flynn, K.J., 2005. Nutritional status and diet composition affect the value of diatoms as copepod prey. Science 307 (5714), 1457—1459, http://dx.doi.org/10.1126/science.1107767.

Karsenti, E., Acinas, S.G., Bork, P., Bowler, C., De Vargas, C., Raes, J., Sullivan, M., Arendt, D., Benzoni, F., Claverie, J.-M., 2011. A holistic approach to marine eco-systems biology. PLoS Biol. 9, e1001177, http://dx.doi.org/10.1371/journal.pbio.1001177.

Li, D., Daler, D., 2004. Ocean pollution from land-based sources: East China Sea, China. AMBIO 33 (1—2), 107—113, http://dx.doi.org/10.1579/0044-7447-33.1.107.

Li, K., Yin, J., Huang, L., Lian, S., Zhang, J., 2013. Spatio-temporal variations in the siphonophore community of the northern South China Sea. Chin. J. Oceanol. Limnol. 31 (2), 312—326, http://dx.doi.org/10.1007/s00343-013-2058-6.

Li, K., Yin, J., Huang, L., Zhang, J., Lian, S., Liu, C., 2011. Distribution and abundance of thaliaceans in the northwest continental shelf of South China Sea, with response to environmental factors driven by monsoon. Cont. Shelf Res. 31, 979—989, http://dx.doi.org/10.1016/j.csr.2011.03.004.

Li, C., Zhang, F., Shen, X., Yang, B., Shen, Z., Sun, S., 2005. Concentration, distribution and annual fluctuation of chlorophyll-*a* in the Jiaozhou Bay. Oceanol. Limnol. Sin. 36 (6), 499—506, (in Chinese with English abstract), http://dx.doi.org/10.3321/j.issn:0029-814X.2005.06.003.

Liu, Z., Ning, X., Shi, J., Cai, Y., 1997. Biomass and primary productivity of phytoplankton in shrimp enhancement area of Xiangshan Bay. Acta Oceanol. Sin. 19, 109—115, (in Chinese with English abstract).

Liu, Z., Wang, C., Yang, J., Zhang, J., Zhu, G., 2004. Distribution of zooplankton in the Xiangshangang Bay in winter. Donghai Mar. Sci. 22, 34—42, (in Chinese with English abstract).

Liu, Z., Wang, C., Zhang, Z., Cai, Y., Zhang, D., 2005. Seasonal dynamics and grazing rate of zooplankton in Yueqing Bay. Acta Ecol. Sin. 25, 1853—1862, (in Chinese with English abstract).

Liu, Z., Wang, C., Zhang, Z., Liu, C., Yang, G., 2006. Seasonal dynamics of zooplankton and microzooplankton grazing impact in Sanmen Bay, China. Acta Ecol. Sin. 26, 3931—3941, (in Chinese with English abstract).

Liu, Z., Zhang, Z., Wang, C., Jin, H., Du, M., Zhang, D., 2012. Changes in zooplankton community structure in Sanmen Bay, China. Acta Oceanol. Sin. 31 (6), 104—116, http://dx.doi.org/10.1007/s13131-012-0257-1.

Marcus, N., 2004. An overview of the impacts of eutrophication and chemical pollutants on copepods of the coastal zone. Zool. Stud. 43 (2), 211—217.

Marques, S.C., Azeiteiro, U.M., Marques, J.C., Neto, J.M., Pardal, M. Â., 2006. Zooplankton and ichthyoplankton communities in a temperate estuary: spatial and temporal patterns. J. Plankton Res. 28 (3), 297—312, http://dx.doi.org/10.1093/plankt/fbi126.

McQueen, D.J., Johannes, M.R., Post, J.R., Stewart, T.J., Lean, D.R., 1989. Bottom-up and top-down impacts on freshwater pelagic community structure. Ecol. Monogr. 59, 289—309, http://dx.doi.org/10.2307/1942603.

Mouny, P., Dauvin, J.-C., 2002. Environmental control of mesozooplankton community structure in the Seine estuary (English Channel). Oceanol. Acta 25 (1), 13—22, http://dx.doi.org/10.1016/S0399-1784(01)01177-X.

Ning, X., Hu, X., 2005. Study on the Impacts of Aquaculture Ecosystem and Assessment of the Aquaculture Carrying Capacity in Yueqing Bay and Sanmen Bay, China. China Ocean Press, Beijing, 275 pp.

Ning, X., Shi, J., Cai, Y., Liu, C., 2004. Biological productivity front in the Changjiang Estuary and the Hangzhou Bay and its ecological effects. Acta Oceanol. Sin. 26, 96—106, (in Chinese with English abstract).

Nixon, S.W., 1995. Coastal marine eutrophication: a definition, social causes, and future concerns. Ophelia 41 (1), 199—219.

Pai, S.-C., Gong, G.-C., Liu, K.-K., 1993. Determination of dissolved oxygen in seawater by direct spectrophotometry of total iodine. Mar. Chem. 41 (4), 343—351, http://dx.doi.org/10.1016/0304-4203(93)90266-q.

Parsons, T.R., Maita, Y., Lalli, C.M., 1984. A Manual of Chemical and Biological Methods for Seawater Analysis. Pergamon Press, Oxford, 208 pp.

Roman, M.R., Gauzens, A.L., Rhinehart, W.K., White, J.R., 1993. Effects of low oxygen waters on Chesapeake Bay zooplankton. Limnol. Oceanogr. 38 (8), 1603—1614, http://dx.doi.org/10.4319/lo.1993.38.8.1603.

Šmilauer, P., Lepš, J., 2014. Multivariate Analysis of Ecological Data Using CANOCO 5. Cambridge Univ. Press, 269 pp.

Sullivan, B.K., Ritacco, P., 1985. Ammonia toxicity to larval copepods in eutrophic marine ecosystems: a comparison of results from bioassays and enclosed experimental ecosystems. Aquat. Toxicol. 7 (3), 205—217, http://dx.doi.org/10.1016/s0166-445x(85)80006-0.

Sun, X., Sun, S., Li, C., Zhang, G., 2011. Seasonal and spatial variability in egg production, abundance and production of small copepods in and near Jiaozhou Bay, China. J. Plankton Res. 33 (5), 741—750, http://dx.doi.org/10.1093/plankt/fbq135.

Tait, R.V., Dipper, F.A., 1998. Elements of Marine Ecology, fourth ed. Butterworth-Heinemann, Oxford, 462 pp.

Uriarte, I., Villate, F., 2005. Differences in the abundance and distribution of copepods in two estuaries of the Basque coast (Bay of Biscay) in relation to pollution. J. Plankton Res. 27 (9), 863—874, http://dx.doi.org/10.1093/plankt/fbi059.

Uye, S., Iwamoto, N., Ueda, T., Tamaki, H., Nakahira, K., 1999. Geographical variations in the trophic structure of the plankton community along a eutrophic—mesotrophic—oligotrophic transect. Fish. Oceanogr. 8 (3), 227—237, http://dx.doi.org/10.1046/j.1365-2419.1999.00110.x.

Wang, K., Chen, J., Jin, H., Chen, F., Li, H., Gao, S., Lu, Y., 2011. The four seasons nutrients distribution in Changjiang River Estuary and its adjacent East China Sea. J. Mar. Sci. 29 (3), 18—35, (in Chinese with English abstract), http://dx.doi.org/10.3969/j.issn.1001-909X.2011.03.004.

Wang, C., Liu, Z., He, D., 2003. Seasonal dynamics of zooplankton biomass and abundance in Xiangshan Bay. J. Fish. China 27, 595—599, (in Chinese with English abstract).

Wang, X., Qiu, W., Qin, M., Wei, Y., 2009. Studies on ecological community distribution of zooplankton in Xiangshan Bay. Mar. Env. Sci. 28, 62—64, (in Chinese with English abstract).

Xu, X., Zeng, J., Chen, Q., Liu, J., Du, P., Wang, G., 2012. Seasonal variations of zooplankton community distribution and environmental impact factors in Yueqing Bay. J. Mar. Sci. 30, 34—40, (in Chinese with English abstract).

Xu, X., Zeng, J., Chen, Q., Liu, J., Du, P., Wang, G., 2013. Spatial niches of dominant zooplankton species in Sanmen Bay, Zhejiang Province of East China. Chin. J. Appl. Ecol. 24, 818—824, (in Chinese with English abstract).

Zheng, Z., Li, S., Xu, Z., 1984. Marine Planktology. China Ocean Press, Beijing, 653 pp.

Zhou, M.-j., Shen, Z.-l., Yu, R.-c., 2008. Responses of a coastal phytoplankton community to increased nutrient input from the Changjiang (Yangtze) River. Cont. Shelf Res. 28 (12), 1483—1489, http://dx.doi.org/10.1016/j.csr.2007.02.009.

Zhu, Z.-Y., Ng, W.-M., Liu, S.-M., Zhang, J., Chen, J.-C., Wu, Y., 2009. Estuarine phytoplankton dynamics and shift of limiting factors: a study in the Changjiang (Yangtze River) Estuary and adjacent area. Estuar. Coast. Shelf Sci. 84 (3), 393—401, http://dx.doi.org/10.1016/j.ecss.2009.07.005.

Oceanologia (2016) 58, 135—149

Available online at www.sciencedirect.com

ScienceDirect

journal homepage: www.elsevier.com/locate/oceano

ORIGINAL RESEARCH ARTICLE

Assessment of recent and chalcolithic period environmental pollution using *Mytilus galloprovincialis* Lamarck, 1819 from Yarimburgaz Cave, the northern Marmara Sea and Bosphorus coasts

Ipek F. Barut [a,*], **Engin Meriç** [b], **M. Baki Yokeş** [c]

[a] *Institute of Marine Sciences and Management, Istanbul University, Istanbul, Turkey*
[b] *Moda Hüseyin Bey Sokak, Istanbul, Turkey*
[c] *Dept. of Molecular Biology and Genetics, Haliç University, Istanbul, Turkey*

Received 5 August 2015; accepted 6 January 2016
Available online 5 February 2016

KEYWORDS
Chalcolithic period;
Geochemistry;
Mytilus galloprovincialis shells;
Northern Marmara Sea and Bosphorus coasts;
Yarimburgaz Cave

Summary Marine or freshwater mussel species are found in large quantities around populated areas and accumulate metals in aquatic systems. Therefore, these organisms are used to monitor environmental pollution. *Mytilus galloprovincialis* is a generally accepted bioindicator of metal pollution and is used in this study. The aim of this study is to determine the changes in the environmental conditions since antiquity. *M. galloprovincialis* shells were used to monitor Chalcolithic pollution levels in Yarimburgaz Cave, one of the oldest settlements in Europe. Recent samples were collected from 12 stations on the coasts of the Northern Marmara Sea and the Bosphorus between May—September 2004. The environmental pollution substantially changed over the last 7500 years. The comparison of the geochemical characteristics of the environmental pollution observed in the Chalcolithic period and today revealed that pollution from both household and industrial chemicals has increased in Istanbul.

* Corresponding author at: Institute of Marine Sciences and Management, Istanbul University, 34134 Vefa, Istanbul, Turkey. Tel.: +90 212 4400000/26035; fax: +90 212 5268433.
E-mail address: barutif@istanbul.edu.tr (I.F. Barut).
Peer review under the responsibility of Institute of Oceanology of the Polish Academy of Sciences.

ELSEVIER Production and hosting by Elsevier

http://dx.doi.org/10.1016/j.oceano.2016.01.001

1. Introduction

Previous studies have indicated that most marine species are not suitable for monitoring metal pollution. Thus, appropriate bioindicator species are required (Ikuta, 1990). Species with shells accumulate metals and trace elements in their shells and flesh, and are used as bioindicators in marine and coastal pollution analyses (Farrington et al., 1987; Maanan, 2007; Phillips, 1980; Widdows, 1985). Sedentary mollusca, such as *Mytilus galloprovincialis*, are preferred in environmental monitoring studies because they have long life spans, can be easily recognized, can be sampled in large quantities, and can tolerate the pollution (Argese et al., 2005; Goldberg, 1975; Kayhan, 2007; Kayhan et al., 2007; Serafim et al., 2002).

In a seasonal study performed in the Lagoon of Venice, a multiple biomarker approach was adopted to evaluate the natural and anthropic stresses influencing the biological responses of the mussel (*M. galloprovincialis*) and to assess the effects of the spatial rather than temporal variations (Da Ros et al., 2000, 2002; Nasci et al., 2002; Nesto et al., 2004). Bocchetti et al. (2008) investigated the natural variability of several biomarkers in *Tapes philippinarum* and *M. galloprovincialis* sampled from the Northern Adriatic, in which these organisms are sentinel species that are important for future environmental impact assessments. The results indicated a significant influence of the seasonal variability on several biomarkers and species-specific differences. This influence should be considered to discriminate anthropogenic disturbances.

Several compounds of environmental interest were investigated using a toxicity test for the early life stage of bivalve mollusca. Three pesticides (carbofuran, atrazine, and malathion), for which literature data are available only for species of oysters, were tested with *M. galloprovincialis* (Losso et al., 2004).

Rivaro et al. (2000) showed minimal evidence for a seasonal pattern, except for Cu, Zn, and V. Concentrations of these metals were a function of the sampling site and the reproductive cycle. Additionally, transplanted mussels can identify local anthropogenic sources of metals. In general, areas of known pollution display high concentrations of these metals; however, select areas not substantially influenced by human activities also showed high concentrations of several metals. Valve activity was measured in the Mediterranean mussel *M. galloprovincialis* in response to sub-lethal concentrations of four metals (Hg, Cu, Zn, and Cd) and two phosphate industry effluents from the Atlantic coasts of Morocco. Valve movements were monitored using a proximity inductive sensor which could display all activity from the full closure to wide opening of the shell valves (Fdil et al., 2006). Taleb et al. (2007) noted that the difference in the variations of the annual physical parameters found in Oran Harbor and found in the Maarouf corresponds to the influence of the domestic and industrial sewage discharged in the Algerian western coastal area. The damage caused to the lysosomal membrane and ADN appears to be a universal marker for the effects of stress on marine organisms such as bivalves.

In a monitoring study conducted by Risso-de Faverney et al. (2010), artificial tire reefs were deposited in a marine protected area (Vallauris-Golfe Juan Bay, France) located along the NW Mediterranean coast, and the potential toxic effects of the tire material were investigated by transplanting marine mussels (*M. galloprovincialis*). The metal accumulation (cadmium, copper, and zinc) and biomarker response in mussel tissues indicated a clear separation. The organisms were found to be significantly more affected by tire reefs than other anthropogenic pollutants.

In this study, the shells of the Mediterranean mussel, *M. galloprovincialis*, obtained from Yarimburgaz Cave excavations were used to detect paleo-environmental conditions. To determine the current environmental pollution levels with respect to past levels, the toxic, non-toxic and radioactive trace element content of these cave shells were compared to recent shells collected from the Sea of Marmara.

1.1. Regional geology of Yarimburgaz Cave

The study area, known as the Yarimburgaz Cave district, is located 2 km north of Altinsehir. The oldest rocks in this region are reefal limestones and clayey limestones of the Middle Eocene (Lutetian) age. Poorly cemented sediments from the Miocene (Sarmatian) age containing pebbles, sands, and clay are found on top of these formations (Dıgış, 1986; Meriç et al., 1991) (Fig. 1).

The Altinsehir formation (Fig. 2) has two members: the reefal limestone on the top (Yarimburgaz member) and the clayey limestone on the bottom (Ikitelli member). Yarimburgaz limestone (Tayk) (Middle Eocene) corresponds to deposits from the reef, and the Ikitelli member (Tai) corresponds to the deposits of the fore reef. Among the two, the hard and resistant Yarimburgaz limestone developed karstic features. Yarimburgaz Cave, which is one of the karstic formations, has revealed one of the earliest known horizons of human history. Mollusca were found in a grayish clayey lance of soil within layer 3. This pocket of earth was almost completely compacted with mollusc fragments and yielded some shards and bone. Mollusca were noted elsewhere within the deposit of layer 3. Accordingly, this mollusc bearing pocket of earth may also indicate a short break in occupation (Meriç et al., 1991).

Salvage excavations executed in this partly destroyed cave in 1986 revealed archeological levels dated to prehistoric periods (6500—7000 BP). The material yield of the assemblage enables an inference of the subsistence patterns and the environmental conditions of the period (Meriç et al., 1991).

1.2. Archeological and paleontological features of Yarimburgaz Cave

Being one of the oldest human footprints, Yarimburgaz Cave archeological findings are important for Istanbul and for the Near East and Europe (Steiner et al., 1998). The cave is found on Catalca Peninsula, located 22 km west of Istanbul and 1.5 km north of Lake Kucukcekmece. The entrances of the cave are narrow holes on the surface (Fig. 2). Geomorphological studies showed that the cave was formed by a water system, carving the karstic Eocene limestone (Fig. 1). The cave has two sections, the upper cave and lower cave, with entrances at 18.60 m and 11.46 m above sea level, respectively (Özdoğan et al., 1991). Both of the entrances face the Sazlidere Valley. The main corridor of the lower cave is separated into two branches after the 240th m. One branch

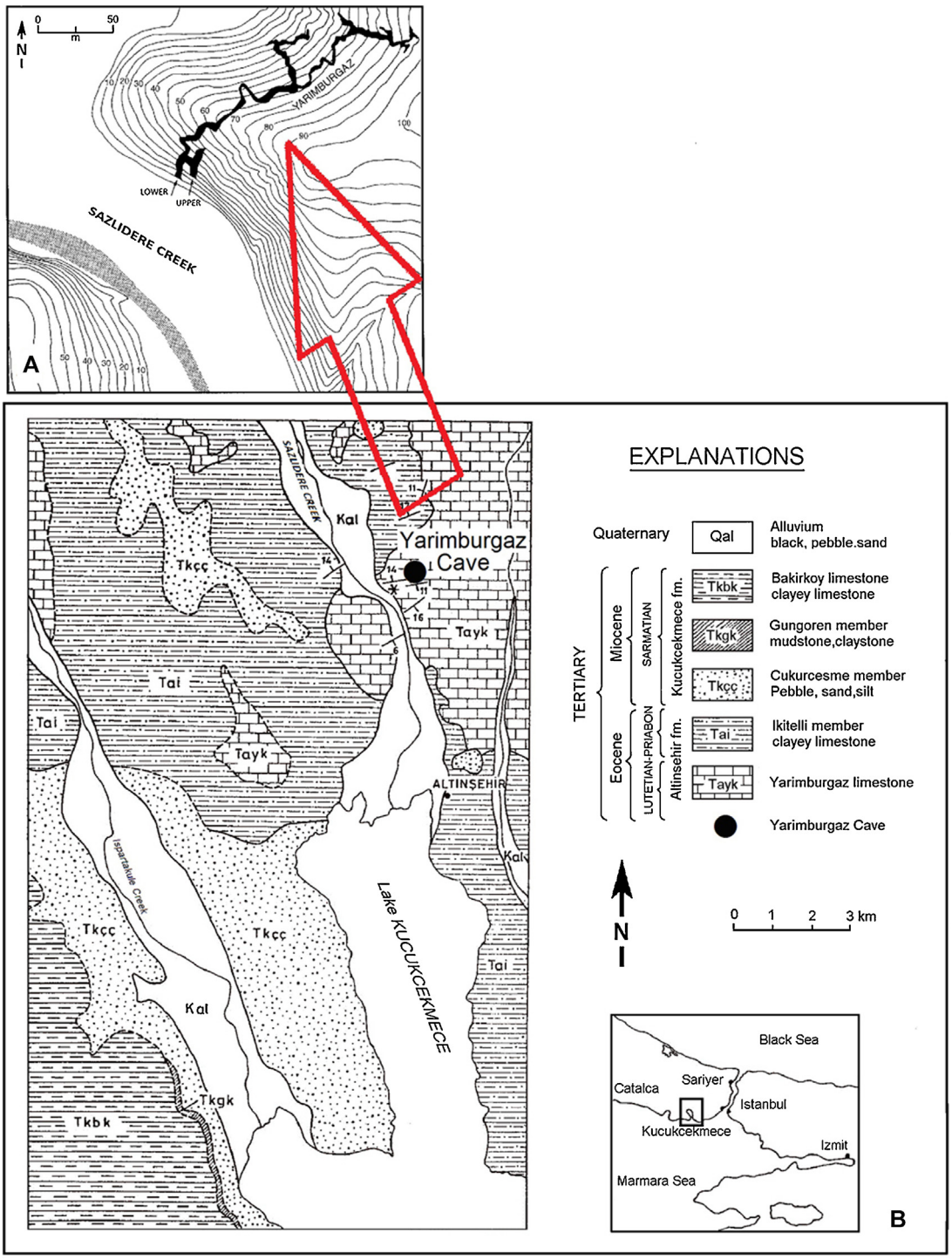

Figure 1 (A) Local topography map of the terrain surrounding Yarimburgaz Cave showing the valley interrupted by the Sazlidere River (from Farrand and McMahon, 1997). (B) The geological map of Yarimburgaz Cave (Kucukcekmece) and its surroundings (modified from Dıgış, 1986).

orients north, and the other points in the northeast direction. Both branches have a dead end. The longest branch is 600 m long. To determine the thickness of the cave walls, 5 m was dug, and the last 3 m was found to be culturally sterile. However, the main rock was not reached (Arsebük, 1993; Arsebük et al., 1990; Arsebük and Özbaşaran, 1995). A small spring named the "Little Danube Stream" is located near the cave.

Neolithic and Chalcolithic cultures detected in Yarimburgaz Cave were one of the first cultures to farm. Additionally, they are important in terms of their relations with the Balkans and Europe. The drawings of ships found on the walls

Figure 2 Entrances of the upper and lower of Yarimburgaz Cave. Photo: Dinçer (2005).

of the cave suggest that the cultures inhabiting the caves were involved in seamanship. Boats likely entered Lake Kucukcekmece for unloading and for shelter in hazardous weather (Arsebük and Özbaşaran, 1995). The entrance of the lake has narrowed and closed over time. Therefore, the lake lost its importance as a water way.

From archeological excavations, the people of that period were found to have used tools and equipment (stone tools, pottery, etc.) to combat environmental stresses. During archeological excavations in the third level of the Chalcolithic period, hand-made pottery was found in clayey material abundant with mollusc shells (Meriç et al., 1988, 1991; Özdoğan, 1999; Özdoğan and Koyunlu, 1986). These prehistoric shells were selected as the material to investigate the environmental conditions. Natural dyes are used in various fields such as textile fibers (wool, cotton, silk, leather, etc.) and wall paintings since the prehistoric. The use of natural dyestuffs after the discovery of synthetic dyes rapidly decreased in 1856 (Cristea and Vilarem, 2006). Compared with synthetic dyes, natural dyes usually do not cause environmental pollution. The natural dyes are less toxic and more hypoallergenic.

Layers found in Yarimburgaz Cave have been formed slowly, and no distinct cultural or paleontological boundaries have been noted between layers (Steiner et al., 1998). Tools and other cultural artifacts found in select layers covering a long period of time indicate that the cave has been used by humans. After a short break, stratification continued within the fourth cultural layer, or the Yarimburgaz layer, in 6800 BP. This culture is characterized by pottery with intricate carvings and incised decorations. The cave was uninhabited for three more cultural stages until 6300 BP.

Studies of the mollusca from Yarimburgaz Cave indicated that in 7000 BP, the sea was close to the cave. A close shoreline was likely present in the Holocene and displayed similar characteristics with other locations in the Middle-Late Pleistocene (Meriç et al., 1988). The age of the mollusc shells found in a hand-made clay pot from the third Chalcolithic period was found to be 6880 ± 80 years old (GrN. 15528) through a ^{14}C test (Meriç et al., 1991) (Fig. 3).

Ecological data suggests that the shoreline displayed cove characteristics in the Chalcolithic period. Later, the cove was filled with materials carried by the freshwater systems found to the north, forming the Kucukcekmece lagoon. Further rearrangements transformed the lagoon into a lake. The shoreline of the lake was suggested to be nearer to the cave approximately 7000 BP (Meriç et al., 1991).

During the Middle Pleistocene period, the Yarimburgaz layers were formed during use of the cave by humans. Teeth samples of an extinct cave bear were found in the layers belonging to the middle Pleistocene, and an electron spin resonance test revealed an age of 270,000–390,000 ± 40,000–60,000 years (Arsebük, 1995a, 1995b). In a multidisciplinary study (Steiner et al., 1998), a paleoecological and taxonomical approach was performed using isotopic osteometric methods. The cave was found to be inhabited by cave bears ((*Spelearctos*) *Ursus*) during the middle and last ice age. The cave was near the coast of an estuary.

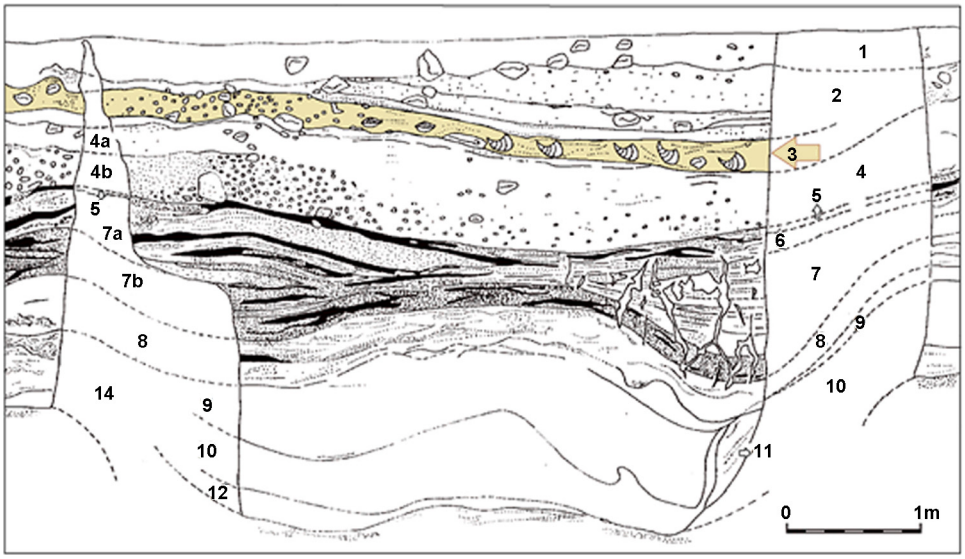

Figure 3 Archeological section of the northern sector of Yarimburgaz Cave, shells obtained from level 3 (after Özdoğan and Koyunlu, 1986).

2. Material and methods

2.1. Sample collection site

M. galloprovincialis shells found in the third layer of Yarimburgaz Cave (Fig. 3) were analyzed for metals and trace, radioactive and rare earth element contents. The shells were compared with recent samples collected from 12 different stations located on the northeast Marmara and Bosphorus between May 21—November 13, 2004 (Fig. 4, Table 1).

2.2. Chemical analysis of *M. galloprovincialis* shells

Firstly shells collected (Fig. 5) from Marmara and the Bosphorus were washed with purified sea water and kept at 40°C in an oven for drying.

For metal, trace, radioactive, and rare earth elements analyses were made. And the shells were pounded in an Agate mortar until a homogeneous mixture of powder was obtained. Each sample was separately packaged at the Istanbul University Marine Science and Management in the Laboratory of Marine Geology and sent to Acme Analytical Laboratories, Vancouver, Canada. The metal, trace, radioactive, and rare earth elements (REEs) analyses were performed by Acme Analytical Laboratories (Vancouver, Canada) in January 2008. The analysis was performed for 0.2 g samples using standard protocols (Method Cod: P150 Pulverize to 150 Mesh 13; Method Cod: 4B (Full Suite) $LiBO_2/Li_2B_4O_7$ fusion ICP-MS analysis). Rare earth and refractory elements are determined by ICP mass spectrometry following a lithium metaborate/tetrabortate fusion and nitric acid digestion of a 0.2 g sample. In addition a separate 0.5 g split is digested in Aqua Regia and analyzed by ICP Mass Spectrometry to report the precious and base metals (in highlight).

Elementary analysis: MDL (method detection limits) [$\mu g\ g^{-1}$]: Ba, Be, Sn, and Zn, 1; Co and Th, 0.2; Cs, Ta, Hf, Nb, Rb, U, Zr, Y, La, Ce, Mo, Cu, Pb, Ni, Cd, Sb, Bi, Tl, and Ag, 0.1; Ga and Sr, 0.5; V, 8; W, As, and Se, 0.5; Pr, Eu, and Ho, 0.02; Nd, 0.3; Sm, Gd, Dy, and Yb, 0.05; Tb, Tm, Lu, and Hg, 0.01; Er, 0.03; Au, [$ng\ g^{-1}$] 0.5.

Table 1 Coordinates of the selected 12 different stations at the northern Marmara Sea and Bosphorus coasts with the Yarimburgaz Cave.

Sample no.	Sample ID	Coordinates	
		Latitude	Longitude
	Yarimburgaz Cave	41°5.280′N	28°43.994′E
1	Selimpasa	41°3.444′N	28°19.017′E
2	Baltalimanı	41°5.727′N	29°3.328′E
3	Istinye	41°6.728′N	29°3.651′E
4	Anadolukavagi	41°10.762′N	29°5.164′E
5	Pasabahce	41°7.053′N	29°5.642′E
6	Kanlica	41°6.183′N	29°3.915′E
7	Kucuksu	41°4.735′N	29°3.845′E
8	Beylerbeyi	41°2.844′N	29°2.822′E
9	Kuzguncuk	41°2.265′N	29°1.715′E
10	Uskudar	41°0.186′N	29°0.087′E
11	Tubitak-MAM	40°46.334′N	29°27.802′E
12	Dil Iskelesi	40°46.370′N	29°30.671′E

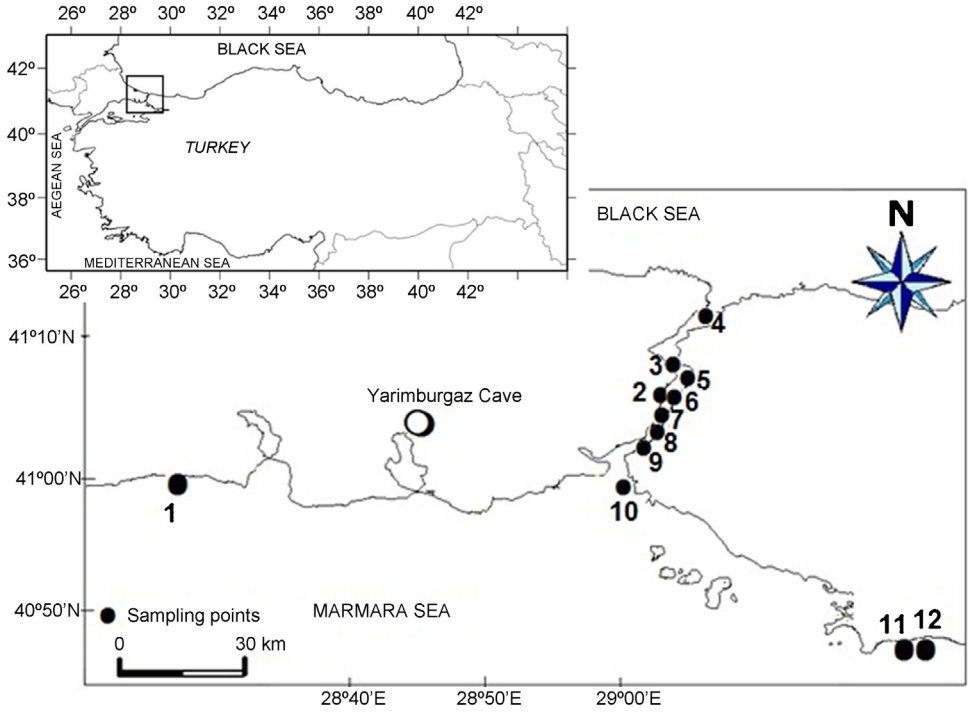

Figure 4 Location map of samples Yarimburgaz Cave, Northern Marmara Sea, and Bosphorus coasts.

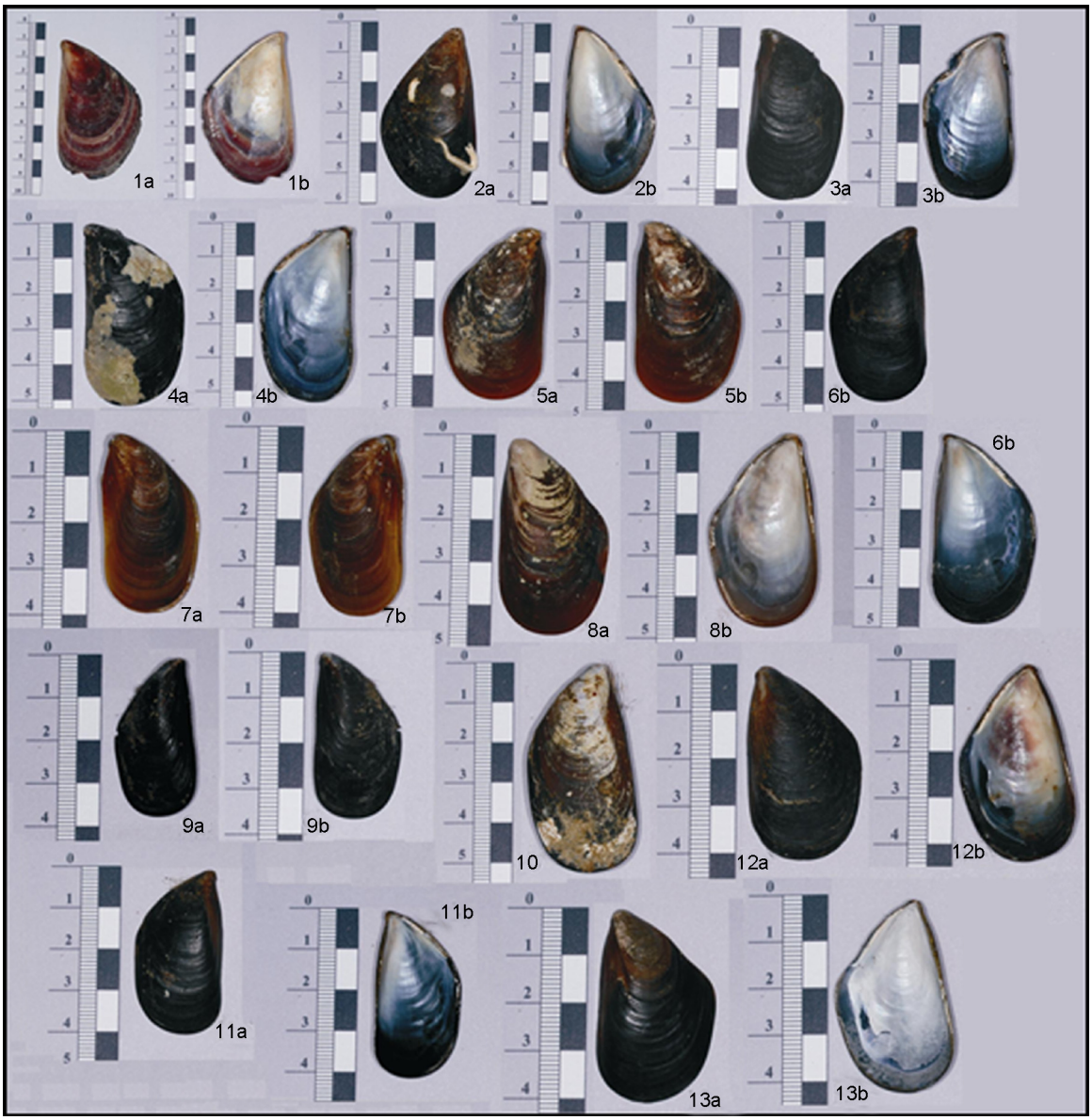

Figure 5 *Mytilus galloprovincialis* Lamarck, 1819. (1a and b) a: left valve, external view; b: left valve, internal view; Sample of Yarimburgaz Cave. (2a and b) a: right valve, external view; b: right valve, internal view; Sample 1. (3a and b) a: left valve, external view; b: left valve, internal view; Sample 2. (4a and b) a: left valve, external view; b: left valve, internal view; Sample 3. (5a and b) a: right valve, external view; b: left valve, external view; Sample 4. (6a and b) a: right valve, external view; b: right valve, internal view; Sample 5. (7a and b) a: left valve, external view; b: right valve, external view; Sample 6. (8a and b) a: left valve, external view; b: left valve, internal view; Sample 7. (9a and b) a: right valve, external view; b: left valve, external view; Sample 8. (10) right valve, external view; Sample 9. (11a and b) a: right valve, external view; b: right valve, internal view; Sample 10. (12a and b) a: left valve, external view; b: left valve, internal view; Sample 11. (13a and b) a: left valve, external view; b: left valve, internal view; Sample 12.

The quality control report shows that the 4B method was assigned the number of VAN 07002440.1 in the Acme Analytical Laboratories. Reference materials of "STD SO-18 Standard" were applied for Ba, Be, Co, Cs, Ga, Hf, Nb, Rb, Sn, Sr, Ta, Th, U, V, W, Zr, Y, La, Ce, Pr, Nd, Sm, Eu, Gd, Tb, Dy, Ho, Er, Tm, Yb, and Lu, whereas the "STD DS7 standard" was applied for Mo, Ni, Cu, Zn, Pb, Bi, Sb, As, and Cd. The 1DX method and a reference material "STD DS7" was applied for Ag, Au, Hg, Tl, and Se (Table 2).

2.3. Statistical analysis

The descriptive statistics analysis, *t*-test, ANOVA (analysis of variance), factor analysis, and correlation analysis were performed using Windows PASW Statistics 18.0 (SPSS (Hong Kong) Ltd., Hong Kong) and Statistics 6.0 (Statistics for Windows is developed by SPSS Inc.). To reduce the background noise, all of the chemical elements in the shells were considered in the statistical analyses. A correlation matrix

Table 2 The geochemical parameters of shell samples at the northern Marmara Sea and the Bosphorus on coasts with Yarimburgaz Cave (with standards, and according to Krauskopf values of crust, shale and seawater).

No.	Sample ID	Ba [$\mu g\ g^{-1}$]	Nb [$\mu g\ g^{-1}$]	Rb [$\mu g\ g^{-1}$]	Sr [$\mu g\ g^{-1}$]	Th [$\mu g\ g^{-1}$]	Zr [$\mu g\ g^{-1}$]	Y [$\mu g\ g^{-1}$]	La [$\mu g\ g^{-1}$]	Ce [$\mu g\ g^{-1}$]	Pr [$\mu g\ g^{-1}$]	Nd [$\mu g\ g^{-1}$]	Sm [$\mu g\ g^{-1}$]	Eu [$\mu g\ g^{-1}$]	Tb [$\mu g\ g^{-1}$]
	Yarimburgaz Cave	17	0.2	0.3	1464	0.3	1	0.4	1	1.9	0.26	1.1	0.16	0.05	0.02
1	Selimpasa	6	<0.1	0.2	1291	<0.2	0.4	<0.1	0.2	0.3	0.06	<0.3	<0.05	<0.02	<0.01
2	Baltalimanı	2	<0.1	0.1	1181	<0.2	0.3	<0.1	0.2	0.1	0.04	0.3	<0.05	<0.02	<0.01
3	Istinye	5	<0.1	<0.1	1238	<0.2	0.3	<0.1	0.2	<0.1	0.03	<0.3	<0.05	<0.02	<0.01
4	Anadolukavagi	2	<0.1	<0.1	1238	<0.2	<0.1	<0.1	0.4	0.2	0.04	<0.3	<0.05	<0.02	<0.01
5	Pasabahce	3	<0.1	<0.1	1113	<0.2	0.2	<0.1	0.3	0.1	0.03	<0.3	<0.05	<0.02	<0.01
6	Kanlica	6	<0.1	0.3	1251	<0.2	3.5	0.2	0.2	0.3	0.05	<0.3	0.05	<0.02	<0.01
7	Kucuksu	5	<0.1	0.2	1273	<0.2	0.3	<0.1	0.2	<0.1	0.04	<0.3	<0.05	<0.02	<0.01
8	Beylerbeyi	9	0.1	0.2	1168	<0.2	0.3	0.2	0.2	0.1	0.04	<0.3	<0.05	<0.02	<0.01
9	Kuzguncuk	2	<0.1	0.1	1026	<0.2	0.2	<0.1	0.2	<0.1	0.02	<0.3	<0.05	<0.02	<0.01
10	Uskudar	4	<0.1	0.3	1105	0.2	1	0.2	0.6	0.3	0.05	0.4	<0.05	<0.02	<0.01
11	Tubitak-MAM	11	<0.1	0.4	1108	<0.2	2.9	0.1	0.5	0.4	0.06	<0.3	<0.05	<0.02	<0.01
12	Dil Iskelesi	16	<0.1	0.3	1298	<0.2	3.6	0.2	0.3	0.3	0.06	0.3	<0.05	<0.02	<0.01
	Standard (STD SO-18)	518	21.2	28.6	451.6	10.5	294.2	33.2	12.7	27.2	3.53	14.1	2.93	90	52
	Standard (STD SO-18)	529	21.9	29	912.9	10.5	297.3	33.7	12.9	28	3.58	14.6	3	91	54
	Standard (STD DS7)														
	Standard (STD DS7)														
	Crust (Krauskopf, 1979)	500	20	90	375	8.5	165	35	35	70	8	30	7	1.2	1
	Shale (Krauskopf, 1979)	600	15	140	400	12	180	3.5	40	70	9	30	7	1.4	1
	Seawater (Krauskopf, 1979)	0.002	1×10^{-5}	0.12	8	1×10^{-5}	3×10^{-5}	1×10^{-6}	3×10^{-6}	1×10^{-6}	6×10^{-7}	3×10^{-6}	5×10^{-8}	1×10^{-8}	1×10^{-7}

No.	Sample ID	Dy [$\mu g\ g^{-1}$]	Er [$\mu g\ g^{-1}$]	Lu [$\mu g\ g^{-1}$]	Mo [$\mu g\ g^{-1}$]	Cu [$\mu g\ g^{-1}$]	Pb [$\mu g\ g^{-1}$]	Zn [$\mu g\ g^{-1}$]	Ni [$\mu g\ g^{-1}$]	As [$\mu g\ g^{-1}$]	Cd [$\mu g\ g^{-1}$]	Sb [$\mu g\ g^{-1}$]	Au [$\mu g\ g^{-1}$]	Hg [$\mu g\ g^{-1}$]	Se [$\mu g\ g^{-1}$]
	Yarimburgaz Cave	0.05	0.04	0.01	<0.1	1.3	0.9	6	4.9	<0.5	<0.1	<0.1	1.5	<0.01	<0.5
1	Selimpasa	<0.05	<0.03	<0.01	0.7	3.5	2.1	5	7.6	0.5	<0.1	0.4	1.4	<0.01	<0.5
2	Baltalimanı	<0.05	<0.03	<0.01	<0.1	1.6	2	8	5.6	1.1	<0.1	<0.1	<0.5	<0.01	<0.5
3	Istinye	<0.05	<0.03	<0.01	0.1	2.2	1.4	2	5.9	1.5	<0.1	<0.1	<0.5	<0.01	<0.5
4	Anadolukavagi	<0.05	<0.03	<0.01	<0.1	1.6	5.3	7	5.5	0.7	<0.1	<0.1	1.3	<0.01	<0.5
5	Pasabahce	<0.05	<0.03	<0.01	0.1	1.7	4.8	25	5.7	1	<0.1	<0.1	0.6	<0.01	0.5
6	Kanlica	<0.05	<0.03	<0.01	0.3	2.4	2.4	6	6.6	1.4	<0.1	<0.1	1.1	<0.01	0.7

Table 2 (*Continued*)

No.	Sample ID	Dy [μg g^{-1}]	Er [μg g^{-1}]	Lu [μg g^{-1}]	Mo [μg g^{-1}]	Cu [μg g^{-1}]	Pb [μg g^{-1}]	Zn [μg g^{-1}]	Ni [μg g^{-1}]	As [μg g^{-1}]	Cd [μg g^{-1}]	Sb [μg g^{-1}]	Au [μg g^{-1}]	Hg [μg g^{-1}]	Se [μg g^{-1}]
7	Kucuksu	<0.05	<0.03	<0.01	0.1	1.6	1.6	5	6.8	1.3	<0.1	0.2	2.1	<0.01	0.5
8	Beylerbeyi	<0.05	<0.03	<0.01	<0.1	1.8	2.3	15	8.3	1.6	0.1	<0.1	0.6	0.03	0.8
9	Kuzguncuk	<0.05	<0.03	<0.01	0.1	2	1.1	5	7.2	1.2	<0.1	0.1	<0.5	<0.01	0.5
10	Uskudar	<0.05	<0.03	<0.01	0.3	3.9	1	10	5.5	1	<0.1	<0.1	<0.5	<0.01	0.8
11	Tubitak-MAM	<0.05	<0.03	<0.01	0.2	2.3	3	14	4.6	1.8	<0.1	<0.1	<0.5	<0.01	0.8
12	Dil Iskelesi	<0.05	<0.03	<0.01	0.1	2.1	4.4	12	6.4	1.3	<0.1	<0.1	<0.5	<0.01	0.6
	Standard (STD SO-18)	304	183	28											
	Standard (STD SO-18)	307	187	28											
	Standard (STD DS7)				19.5	119.2	77.6	426	55.3	50.2	5.8	4.5	201	0.21	4
	Standard (STD DS7)				19.2	123.3	76	400	59.7	47.5	5.8	4.8	46	0.23	3.9
	Crust (Krauskopf, 1979)	6	3.5	0.6	1.5	50	12.5	70	75	1.8	0.15	0.2	0	0.02	0.05
	Shale (Krauskopf, 1979)	5	3.5	0.6	2	50	20	90	80	10	0.3	1.5	0	0.3	0.6
	Seawater (Krauskopf, 1979)	9×10^{-7}	8×10^{-7}	2×10^{-7}	0.01	5×10^{-4}	3×10^{-5}	0.049	0.0017	0.004	1×10^{-6}	2.4×10^{-4}	4×10^{-6}	3×10^{-5}	2×10^{-4}

(Pearson) was calculated for the transformed Chalcolithic era shells and recent shells elemental contents of Ba, Nb, Rb, Sr, Th, Zr, Y, La, Ce, Pr, Nd, Sm, Mo, Cu, Pb, Zn, Ni, As, Cd, Sb, Hg, Se, and Au.

2.4. Taxonomy of *Mytilus galloprovincialis* Lamarck, 1819

Mytilidae family (Mollusca, Bivalvia) has a wide distribution range. *M. galloprovincialis* Lamarck, 1819 is an important member of this family and is distributed in the Mediterranean and Black Sea. On the Turkish coastline, *M. galloprovincialis* is commonly found on the Black Sea coasts, the Sea of Marmara, the Biga Peninsula, the Gulf of Edremit and the coasts of Ayvalık. However, on the Mediterranean coasts, this mollusc is rarely observed. Mytilid shells have microstructures. The species living in subtropical regions have shells with two or three layers of aragonite and calcite, whereas the others have two layers of aragonite and nacre (Gosling, 1992).

3. Results

The measured values of Be, Co, Cs, Ga, Hf, Sn, Ta, U, V, W, Gd, Ho, Tm, Yb, Bi, Ag, and Tl in *M. galloprovincialis* shells were found to be below the MDL (method detection limits). Some rare earth elements (REEs) in the Lanthanide series, such as Eu, Tb, Dy, Er, and Lu were not found in the recent shells, but were measured in specimens from the Chalcolithic period in sample of Yarimburgaz Cave. Nevertheless, several elements (Mo, As, Cd, Sb, Hg, and Se) were not detected in specimens from the Chalcolithic period in this sample, but were measured in recent shells.

The measured values of Ba, Sr, Zr, Y, La, Ce, Pr, Nd, and Sm in samples from Yarimburgaz Cave were found to be higher than the values of recent shells. However, several metal, trace, and rare earth elements which are potential pollutants (Ag, As, Cr, Hg, Sb, Ba, Br, Ca, Co, Cs, Fe, Na, Sr, and Zn) were observed at higher quantities in recent samples. Pb, Zn, Ni, As, Au, and Se values measured in the samples from the middle of the Bosphorus Strait were found to be the highest of all samples measured.

In this study, the distribution of Ba and Sr (Fig. 6) in Yarimburgaz Cave shells was higher than in recent shells. Ba values were similar in recent shells from sample 12 and in ancient shells from sample of Yarimburgaz Cave. The lowest Ba content was noted in samples 2, 4, and 9. The highest Sr content was noted in the sample of Yarimburgaz Cave. The lowest Sr value was noted in sample 9 and the highest in sample 12.

The radioactive elements (Th: 0.3 μg g^{-1}, Y: 0.4 μg g^{-1}) were measured at higher levels in Yarimburgaz Cave shells than in recent shells. Th was measured only in sample 10 (Uskudar) shells (0.2 μg g^{-1}). The Y values were determined in samples 6, 8, 10, and 12 (0.2 μg g^{-1}) and in 11 (0.1 μg g^{-1}).

The distribution of trace elements is displayed in Fig. 7. Nb was found only in sample of Yarimburgaz Cave and 8 (Beylerbeyi), with a higher value in sample of Yarimburgaz Cave shells. Zr was not detected in sample 4 (Anadolukavagi) and was at its highest value in samples 6, 11, and 12. As was not detected in sample of Yarimburgaz Cave and was in the range of 0.5–1.8 μg g^{-1} in recent shells.

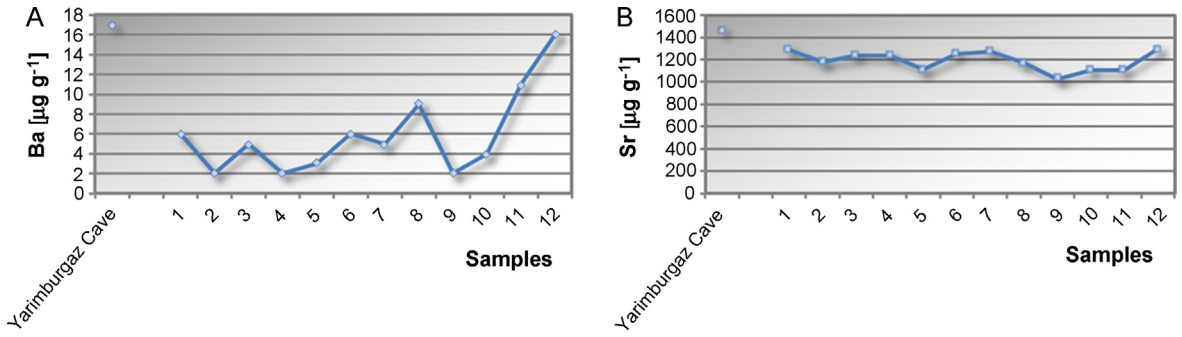

Figure 6 Distribution of Ba (A) and Sr (B) elements in samples from Yarimburgaz Cave, the northern Marmara Sea, and Bosphorus coasts.

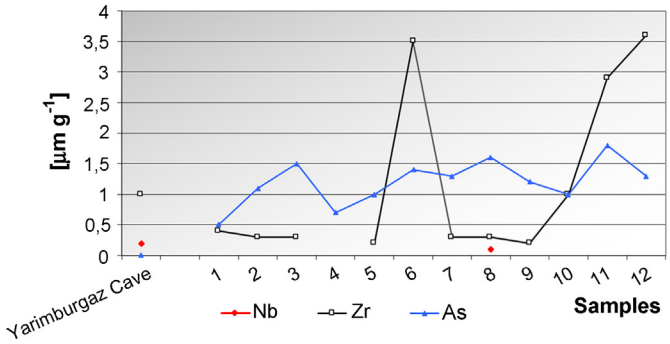

Figure 7 Distribution of trace elements in samples from Yarimburgaz Cave, the northern Marmara Sea, and Bosphorus coasts.

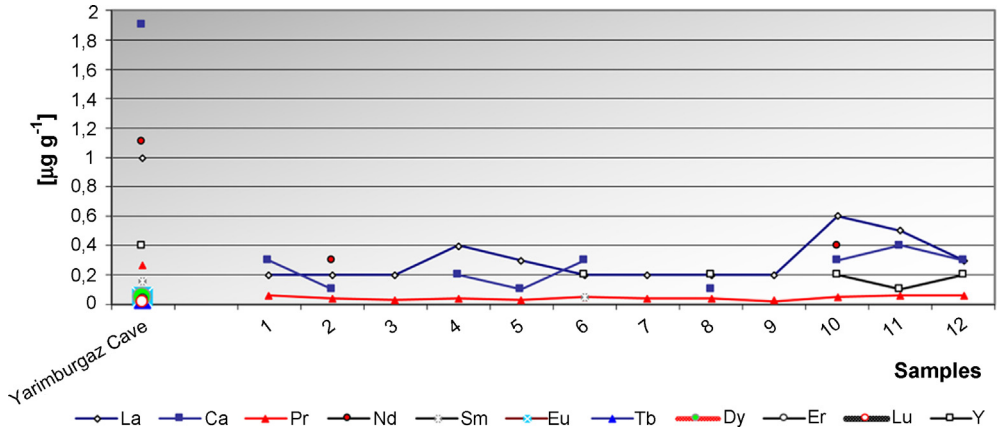

Figure 8 Distribution of rare earth elements in samples from Yarimburgaz Cave, the northern Marmara Sea, and Bosphorus coasts.

Au was detected in shells from the Chalcolithic period and from recent shells in samples 1 (Selimpasa), 4 (Anadolukavagi), 5 (Pasabahce), 6 (Kanlica), 7 (Kucuksu), and 8 (Beylerbeyi). The Au content from recent shells in samples 1 and 4 are similar to sample of Yarimburgaz Cave. The highest value was noted in sample 7 (Kucuksu) (Table 2).

The REE Eu, Tb, Dy, and Lu were only detected in Yarimburgaz Cave. La, Ce, Pr, Nd, Sm, and Y values are lower in the recent shells than in Yarimburgaz Cave (Fig. 8). The La value ranges over 0.2—0.6 $\mu g\ g^{-1}$ in the recent shells, but is 1 $\mu g\ g^{-1}$ in Yarimburgaz Cave. The Ce value is highest (1.9 $\mu g\ g^{-1}$) in Yarimburgaz Cave, ranging over 0.1—0.4 $\mu g\ g^{-1}$ in the recent shells. Nd was detected in recent shells in samples 2 (Baltalimanı) and 10 (Uskudar), and the Sm values is lower in sample 6 (Kanlica) than in shells from the Chalcolithic period. Y was detected off of the Bosphorus on the Asian side and eastern Marmara coast in samples 6, 8, 10, 11, and 12.

The heavy metals Cd and Hg were found only in sample 8 (Table 2). Cu, Pb, Zn, and Ni were measured in all samples. Mo, As, Cd, Sb, Hg, and Se were not observed in the Yarimburgaz Cave but were measured in some of the recent samples. The lowest value of Zn was observed in sample 3 (Istinye). Cu, Pb, and Ni were measured at high values in recent shells (except sample 11). The Ni value ranged over

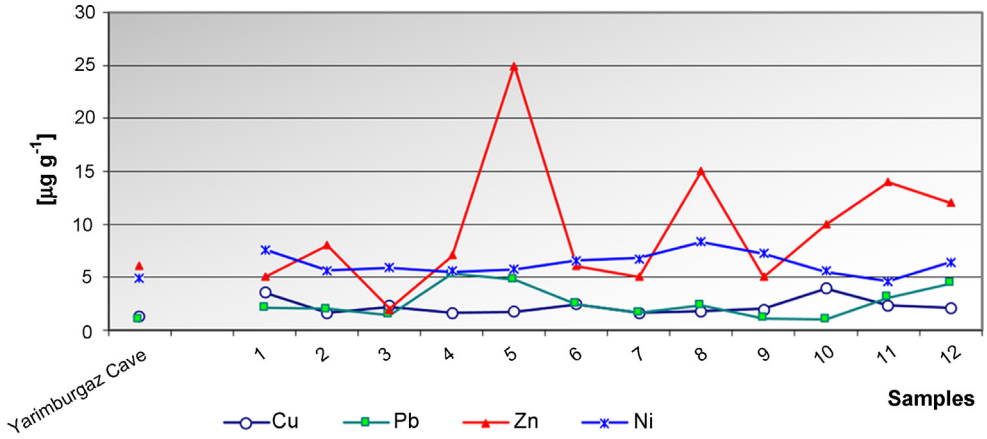

Figure 9 Distribution of heavy metals in samples from Yarimburgaz Cave, the northern Marmara Sea, and Bosphorus coasts.

4.6—8.3 $\mu g\ g^{-1}$, and the highest value was for recent shells in sample 8 (Beylerbeyi). The Ni values were also low in the Chalcolithic period sample and in the recent sample 11 (Tubitak-MAM) (Fig. 9).

The measured Zn values of the other recent samples 1, 7, and 9 were close to but lower than the value of sample of Yarimburgaz Cave. In sample 5, the highest toxic metals were found to be Pb and Zn; whereas in sample 8, Ni and Zn; in sample 1 (Selimpasa), Cu and Ni; and in sample 4 (Anadolukavagi), Pb display the highest metal content (Fig. 9).

The toxic metalloids were determined only in the recent shells and were in the range of 0.1—0.7 $\mu g\ g^{-1}$ for Mo, 0.5—0.8 $\mu g\ g^{-1}$ for Se, and 0.1—0.4 $\mu g\ g^{-1}$ for Sb. The maximum value of Mo and Sb were also determined in sample 1 (Selimpasa). The Se content was determined in the Bosphorus on the Asian side and in eastern Marmara coast in samples 5, 6, 7, 8, 9, 10, 11, and 12.

The Chalcolithic period shells and Selimpasa shells did not display Cd, Hg, and S. The values of Au are similar in all shells. Only Chalcolithic period shells displayed REEs such as Nb, Th, Y, Nd, Sm, Eu, Tb, Dy, and Lu. Only recent shells displayed Mo, As, and Sb. Other REEs and trace elements (Ba, Rb, Sr, Zr, La, Ce, Pr, Pb, and Au) are higher in the Chalcolithic period shell. Zn is higher in the Chalcolithic period shell, whereas other metals such as Cu, Pb, and Ni are higher in the recent shells.

A significant and positive Pearson correlation was found between the following: Nd and Th ($r = 0.99$, $n = 23$, $\alpha = 0.01$) in all shells, whereas no correlation was noted between Nb and Th ($r = -0.98$, $\alpha = 0.01$). The correlation between Cd and Hg was negative ($r = -1$, $n = 23$, $\alpha = 0.0$).

The relationship between the recent shells ($r = 1$, $n = 12$, $\alpha = 0.01$) was significantly positive, and a full linear relationship was obtained. A significant and strong positive correlation was found between the Chalcolithic period shells and recent shells ($r = 0.99$, $n = 13$). When the Chalcolithic period shells serve as a control group, a strong correlation is noted between Kuzguncuk and Selimpasa ($r = 0.97$), between Kuzguncuk and Kucuksu ($r = 0.97$), and between Istinye and Tubitak-MAM ($r = 0.87$).

The Cu and Pb and the Ni and Hg display a negative relationship, whereas the Pb and Zn, the Ni and Cd with Sb ($r = 0.71$, $\alpha = 0.05$), and the Pb and As ($r = 0.95$, $\alpha = 0.05$) display a positive correlation. The Zn (9.23) is an effective descriptive statistic within the group of heavy metals.

For the first sampling date, the variations of each metal concentration in the whole shell were tested by a one-way analysis of variance considering the site as a variable. When the ANOVA was significant, post hoc pairwise comparisons between the stations were conducted using Scheffe's test to determine which values differed significantly. We correlated the Chalcolithic period with recent shells and elemental groups using ANOVA. The group value was $p = 1$, showing no statistically significant difference between the relationships ($p > 0.05$). With all shells from the one-way ANOVA, the Chalcolithic period and the recent shells were found to display no significant difference ($F = 0.008$, $p = 1$; $p > 0.05$).

However, the one-way ANOVA table shows that the degree of significance is $p = 0.00$ among recent shells. The one-way ANOVA showed that the relationship between recent shells is significant at $p = 0.000$ ($p < 0.05$).

The groups were compared to determine the differences with each other. According to Tukey's test results in the table of Multiple Comparisons, the difference between the Chalcolithic era shells (X: 65.37) and the recent shells (values in the range of X: 45.54—58.58) were determined to be statistically significant. The Chalcolithic era shells ($X = 65.37$) was found to be significantly different from sample 9 (Kuzguncuk) ($X = 45.54$) and 10 (Uskudar) ($X = 49.38$).

For the recent shells in Dil Iskelesi, the shells ($X = 58.58$) showed significant differences from the other recent shells (values in the range of X: 45.54—57.44). Nevertheless, the Dil Iskelesi shells ($X = 58.58$) showed significant differences from Kuzguncuk (X: 45.54), Selimpasa (X: 57.44) and Uskudar shells (X: 49.38).

The Kaiser-Meyer-Olkin (KMO) test was performed to determine the reliability, displaying correlation eligibility values close to 1 (KMO measure of sampling adequacy 0.91). Six factors explain 91.13% of the total variance in practice. The first factor explains 37.82% of the variance. After rotation equalizing the relative importance of the factors, the contribution of factor 1 falls to 34.64%. The component values of each item was examined according to a Principal Component Analysis (PCA) component matrix divided into six components. Therefore, Ba, Nb, Sr, Th, Y, La, Ce, Pr, and Nd explain the first factor; Rb, Zr, Zn, As, Cd,

and Se explain the second factor; Rb, Mo, Cu, and Sb explain the third factor; Ni and Cd explain the fourth factor; Pb explains the fifth factor; Pb and Zn explain the sixth factor.

The variables influencing the factors were found when examining the component values of the Rotated Component Matrix used in the creation of the structure. The condition index of the shells was also included in the PCA. Data were normalized using a $\log(x + 1)$ transformation. Factors 3 and 4 have been mutually replaced. Factor 5 included Sr and Au. For another evaluation, Ba (variable) is effective in factors 1 and 2, Nd is in the first factor, Zr is in the second factor, Cd is in the third factor, Mo is in the fourth factor, Au is in the fifth factor, and Cu is in the fifth factor. Therefore, the factors contain effective and positive effects that do not differ.

4. Discussion

The *Mytilus galloprovincialis* shells were determined to be a combination of aragonite-calcite. The shell was composed of Ca (104,37.16 $\mu g\ g^{-1}$), Mg (74 $\mu g\ g^{-1}$), and Sr (36.17 $\mu g\ g^{-1}$) (Ökten, 2009). The Mg, Sr, Ba, and Si contents are high because they are structural elements of the shell. The abundance of these metals, therefore, exceeds other metals. Additionally, Mg, Ba, and Sr are important for the development, growth, and reproduction of the organism and are related to the temperature and salinity of the environment.

Nb is mainly found in niobite $[(Fe, Mn)(Nb, Ta)_2O_6]$ and niobite tantalite $[(Fe, Mn)(Ta, Nb)_2O_6]$ minerals in nature. Ba, Sr, La, and Pr were found in all of the shells analyzed, whereas Rb, Zr, Ce, Nd, and Sm were not observed in several of the recent samples (Table 2). The rare earth elements La and Pr were found in sample of Yarimburgaz Cave at its highest value. The measured values of these elements in coasts Marmara Sea as in samples 1 (Selimpasa), 11 (Tubitak-MAM) and 12 (Dil Iskelesi) were nearly identical.

High Ba content in sediments is normal. However, the high values of Au and Sr suggest that the sediment can be related to hydrothermal outlets. The most common and most widely used source of barium is naturally occurring sedimentary barite mines. The sediment has a layered structure because of the transportation by seas or rivers. Hot water outlets are usually seen in the region. The observed non-parallel relationship between the Ba, Pb, and Zn may indicate an anthropogenic origin of these elements (Apaydın and Erseçen, 1981; MTA, 2000).

An increase in the environmental pollution in the last 7500 years is prominent in the study field (Özdoğan, 1999; Özdoğan and Koyunlu, 1986). Marine pollution constitutes a major environmental problem in Turkey, which is surrounded by three seas. Marine transportation, tourism, disposal of industrial and domestic wastes without purification, petroleum derivatives released by accidents, and agricultural chemicals carried by water systems are the main causes of marine pollution that adversely affect the marine life.

The system in Marmara and the Bosphorus display unique hydrographic and ecological characteristics. These locations experience different pollution inputs from domestic, industrial, maritime transport (including tanker accidents) and from the Black Sea and Danube River. However, these pollutants flow to coasts Marmara Sea from the Black Sea and the Aegean Sea, notably from the increased concentrations of these pollutants in the Black Sea coasts.

As a result of urbanization and industrial activities, the limits of pollutants have been exceeded (Dethlefsen, 1988; Hammand and Beliles, 1980; Kaya et al., 1998; Şanlı, 1984). The Golden Horn and Gulf of Izmit is affected by physical and chemical pollutants, whereas, Bosphorus is polluted mainly by domestic and industrial wastes (Başsarı et al., 2000; Çağatay et al., 2006; Göksu et al., 2005; Topçuoğlu et al., 2004). In these studies, fish, algae species, and the organic parts of the mollusca have been used for to investigate the metals in the sea water.

Metals, such as Hg, Cd, Pb, Cu, Ni, Zn, Cr and As, accumulate in the food chain and display toxic effects on the biota. *M. galloprovincialis* is a filter feeder, filtering organic material and phytoplankton and accumulating toxic materials in its tissues and shell. In this study, the distribution of the elements in the shells was determined to be higher than the average of the sea water (Krauskopf, 1979) (Table 2).

The distribution of trace elements and REEs were affected by the geochemistry in the bottom sediments and in seawater of the terrigenous (terrestrial and anthropogenic) material in the Bosphorus and the Marmara Basin. In the Marmara Sea, the small and terrestrial inputs are higher. The trace elements (Ba, Sr, etc.) and lithophile elements (K, Rb, Li, La, Nb, etc.) originate from terrigenous sources. These metals are thought to originate from terrestrial erosional material, transported by the stream drainage network as suspended matter. The domestic and industrial discharges into the sea result in excessive organic matter in the sediments of the sea floor and a high metal pollution. Therefore, the form of the metal will change and precipitate, settling into the sediment in the basin. Thus, the bottom water is affected and can contaminate the shells.

The comparative toxicities of some of the metal and trace elements found in sea water can be shown as follows as from highest to lowest: Hg > Cd > Ag > Ni > Pb > As > Cr > Sn > Zn. The metal atoms can combine with organic molecules and be released to the environment when the organic molecules are degraded (Balkıs and Algan, 2005).

Atayeter (1991) showed that the Fe, Cu, Zn, Pb, and Al concentrations in the gills and digestive systems of the *M. galloprovincialis* specimens collected from Anadolukavagi (Bosphorus, Istanbul) vary throughout the year. In August, September, and November, the maximum accumulation of Zn is observed, followed by Fe, Cu, and Pb. However, the maximum accumulation was observed in Pb during January and February. Şentürk (1993) analyzed the Hg, Cd, and Pb concentrations in mollusc specimens collected from various parts of the Sea of Marmara, and found that the average concentrations of Hg, Cd, and Pb were 0.46 $\mu g\ g^{-1}$, 0.25 $\mu g\ g^{-1}$, and 0.304 $\mu g\ g^{-1}$, respectively. These concentrations are below the acceptable limits suggested for marine products. The Cu, Zn, Pb, and Cd concentrations of the soft tissues of *M. galloprovincialis* specimens collected from Sinop (Black Sea) were significantly different from the values observed in the coastal waters (Bat and Gündoğdu, 1999).

The Zn, Cu, Mg, and Fe contents of the inner and outer parts of the *M. galloprovincialis* shells have been compared in the samples from Napoli Bay, and only the Mg values have been found to vary (Cotugno et al., 1983). In a study performed on the coasts of NW Spain, the lead and nickel

concentrations observed in the shells and in the soft tissues of *M. galloprovincialis* have been compared with the values observed in the sediment. The shell of *M. galloprovincialis* was more reliable for monitoring the metal levels when compared to the soft tissues (Puente et al., 1996).

Mauri and Baraldi (2003) monitored the changes in metal concentrations in the shells and soft tissues. They transferred *M. galloprovincialis* specimens from the open sea to the Venice Lagoon, in which the pollution was well documented. They measured the Cr, Pb, Cu, Zn, Mn, and Fe concentrations periodically in the shell and other tissues. Initially in the lagoon and in the soft tissue of *M. galloprovincialis*, no difference was observed for Pb and Zn observed, and Cu, Cr, Mn, and Fe values displayed low levels. After a month, these metal levels increased in the *M. galloprovincialis*, but after two months, the values decreased. Except for the metal content of Cu in the shell, the Zn and Pb contents were determined to have decreased. They showed a considerable change in the metal concentrations three months after transfer.

The metal concentrations in the gills were found to be higher when compared to the other parts of the *M. galloprovincialis* specimens collected from the Danube Delta (Black Sea) (Roméo et al., 2005). A multivariate analysis (Duncan) showed that the highest accumulating metal in the shell was Fe, and the least accumulating metals were Cu, Mn, and Co (Tosyalı, 2005).

Aksu (2005) and Aksu et al. (2007) studied Cd, Cu, Ni, Pb, Zn, Mn, Fe, Cr [$\mu g\ g^{-1}$], and Hg [$ng\ g^{-1}$] in the edible parts of *M. galloprovincialis* specimens collected from the Bosphorus, Anadolukavagi, Beykoz, Uskudar, Baltalimanı, Buyukdere, and Ortakoy, in May, August, November 2003, and February 2004. The sampled specimens were separated into two groups according to their sizes: large ($\geq$10 cm) and small ($<$10 cm). The metal concentrations were higher in the small sized group. The distribution of metals was also found to differ between the stations. Cd, Mn, Ni, Pb, and Zn were higher in Beykoz samples. Cr and Hg were higher in Ortakoy samples. Cu was highest in the small sized group in Ortakoy and in the large sized group in Beykoz. However, Fe was the highest in the small sized group in Beykoz and in the large sized group in Buyukdere. The highest concentrations of the toxic and non-toxic metals have been observed during August and November 2003.

Another recent study by Yabanli et al. (2015), studied the low levels of toxic metals (Cd, Hg, Pb, Cr, Ni) found in tissues of *M. galloprovincialis*, comparing with the other studies including taken place in the inner part of the Gulf of Izmir. And this specimen can be used as a sensitive biomonitor for

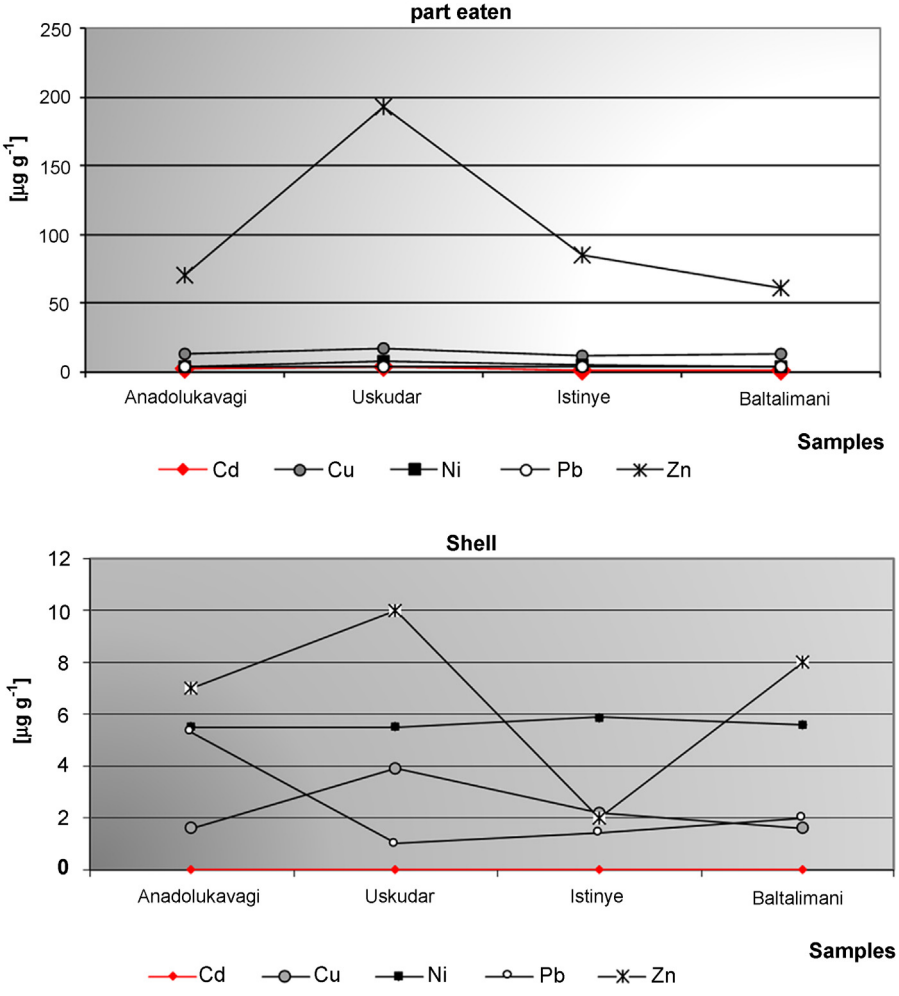

Figure 10 Distribution of metals in samples of the part eaten (after Aksu's (2005) data) with shells (our study).

the availabilities of studied elements in the inner Gulf of Izmir.

Cd, Cr, Ni, Pb, and Hg measurements were compared with the values [$\mu g\ g^{-1}$] reported in Aksu et al. (2007) obtained in May and August 2003 from Anadolukavagi, Uskudar, Istinye (Buyukdere), and Baltalimanı (Fig. 10). In the shells, Hg [$ng\ g^{-1}$] was only found in the Beylerbeyi samples, whereas in the organic material, Hg [$ng\ g^{-1}$] values were found to be high in all samples, notably in the Ortakoy sample. The Ni concentration was the highest in the shells, and the Cu was highest in the organic material. Pb was found to be lower both in the shells and in the organic materials when compared to other metals. Zn was measured at a minimum level in the shells; however, the Zn content was relatively higher in the organic material. The metal distribution agreed in all of the samples in the organic material, but not in the shells. Therefore, a linear relationship was not observed in the distribution of metals between the shell and the organic material (Fig. 10).

5. Conclusions

The results show that the recent *M. galloprovincialis* shells and the samples from the Chalcolithic period display considerable differences in the geochemical characteristics. The rare earth elements Eu, Tb, Dy, Er, and Lu were only observed in the Chalcolithic period shells, whereas the trace and rare earth elements Ba, Sr, and As were measured in all samples. The source of the Th is likely to be a type of granitic and gneissic rocks. A non-linear relation was observed in Ba, Pb, and Zn concentrations in the shells, suggesting an anthropogenic origin for these elements. A linear relation was observed neither between the metal concentrations nor in the metal contents of the shell with the soft tissues of the recent samples. Differences in the Cd, Pb, As, Sb, and Se contents were noted in the Chalcolithic period shells and recent shells. The source of metal pollution as a result of domestic and industrial activities can be explained by anthropogenic inputs. The resulting statistical value ($p = 1$) shows no statistically significant difference between the relationships noted in the shells.

Acknowledgments

The authors would like to thank Prof. Dr. Mehmet Özdoğan (Istanbul University) for supplying *M. galloprovincialis* shells from Chalcolithic age, and to Rıza Dervişoğlu (Bogazici University), Ünsal Karhan (Istanbul University) and Evren Varol (Bogazici University) for collecting the recent material. The authors especially thank Dr. Cengiz Keskin who delivered by hand to Acme Analytical Laboratories (Vancouver) and to Asst. Prof. Dr. Abdullah Aksu for contributions of chemical information.

References

Aksu, A., 2005. İstanbul Boğazı'nda Metal Kirliliğinin Midyelerle Takibi. (Msc. thesis). İstanbul Üniversitesi, İstanbul, 88 pp., (in Turkish with English abstract).

Aksu, A., Balkıs, N., Müftüoğlu, A.E., 2007. Metal pollution in the mussel (*Mytilus galloprovincialis*) in the Bosphorus. In: 38th CIESM Congress, 9–12 April 2007, İstanbul, Turkey, http://ciesm.org/online/archives/abstracts/pdf/38/CIESM_Congress_2007_Istanbul_article_0222.pdf.

Apaydın, N., Erseçen, N., 1981. Türkiye'nin Bilinen Maden Yatakları. MTA Yayınları, Ankara, (in Turkish).

Argese, E.C., Bettiol, C., Rigo, S., Bertini, S., Colomban, P., Ghetti, F., 2005. Distribution of arsenic compound in *Mytilus galloprovincialis* of the Venice Lagoon, Italy. Sci. Tot. Environ. 348 (1–3), 267–277, http://dx.doi.org/10.1016/j.scitotenv.2004.12.071.

Arsebük, G., 1993. Yarımburgaz: a lower paleolithic cave site near Istanbul. In: Frangipane, M., Hauptman, H., Liverani, M., Matthiac, D., Mellink, M. (Eds.), Between the Rivers and Over the Mountains. Univ. Rome, Grup. Editor. Internazion., 23–36.

Arsebük, G., 1995a. İnsan, İnsanlık ve Prehistorya. In: Halet Çambel İçin Prehistorya Yazıları. Graphis Yayınları, İstanbul, 11–26, (in Turkish).

Arsebük, G., 1995b. İnsan, Evrim, Alet. Bilim ve Teknik (TÜBİTAK) 332, 18–24, (in Turkish).

Arsebük, G., Howell, F.C., Özbaşaran, M., 1990. Yarımburgaz 1988. In: XI. Kazı Sonuçları Toplantısı TC Kültür Bakanlığı Anıtlar ve Müzeler Genel Müdürlüğü, Ankara, 9–38, (in Turkish).

Arsebük, G., Özbaşaran, M., 1995. İstanbul'un En Eski Yerleşim Merkezi: Yarımburgaz Mağaraları. Focus 2, 78–82, (in Turkish).

Atayeter, S., 1991. Anadolukavağı midye türünde (*Mytilus galloprovincialis* Lamarck, 1819) bazı ağır metal birikimlerinin belirlenmesi. (Msc. thesis). Ankara Üniv., Ankara, 37 pp., (in Turkish with English abstract).

Balkıs, N., Algan, O., 2005. Marmara Denizi yüzey sedimentlerinde metallerin birikimi ve denetleyen mekanizmalar. In: Güven, K.C., Öztürk, B. (Eds.), Deniz Kirliliği, Tüdav Yayınları, İstanbul, 177–204, (in Turkish).

Başsarı, A., Türkmen, G., Akyüz, T., 2000. İstanbul Boğazı'ndan toplanan *Mytilus galloprovincialis* örneklerinde eser ve toksik element düzeyleri. In: Marmara Denizi 2000 Sempozyumu, 11–12 Kasım 2000, İstanbul, 543–549, (in Turkish).

Bat, L., Gündoğdu, A., 1999. Copper, zinc, lead and cadmium concentrations in the Mediterranean mussel *Mytilus galloprovincialis* Lamarck, 1819 from the Sinop Coast of the Black Sea. Turk. J. Zool. (TUBITAK) 23, 321–326.

Bocchetti, R., Lamberti, C.V., Pisanelli, B., Razzetti, E.M., Maggi, C., Catalano, B., Sesta, G., Martuccio, G., Gabellini, M., Regoli, F., 2008. Seasonal variations of exposure biomarkers, oxidative stress responses and cell damage in the clams, *Tapes philippinarum*, and mussels, *Mytilus galloprovincialis*, from Adriatic Sea. Mar. Environ. Res. 66 (1), 24–26, http://dx.doi.org/10.1016/j.marenvres.2008.02.013.

Cotugno, M., Sansone, G., Rodriguez, M.U., Borriello, R., Biondi, A., 1983. Accumulation of heavy metals in biocrystals in the shell of *Mytilus galloprovincialis* from different zones of the Gulf of Naples. Boll. Soc. Ital. Biol. Sper. 59 (4), 514–519.

Cristea, D., Vilarem, G., 2006. Improving light fastness of natural dyes on cotton yarn. Dyes Pigments 70, 238–245, http://dx.doi.org/10.1016/j.dyepig.2005.03.006.

Çağatay, N., Balkıs, N., Sancar, Ü., Çakır, Z., Yücesoy-Eryılmaz, F., Eryılmaz, M., Sarı, E., Erel, L., Akçer, S., Biltekin, D., 2006. Marmara Denizi Çökel Jeokimyası Atlası. TÜBİTAK, ÇAYDAG, Ankara, vi + 81 pp., (in Turkish with English abstract).

Da Ros, L., Meneghetti, F., Nasci, C., 2002. Field application of lysosomal destabilisation indices in the mussel *Mytilus galloprovincialis*: biomonitoring and transplantation in the Lagoon of Venice (North-East Italy). Mar. Environ. Res. 54 (3–5), 817–822.

Da Ros, L., Nasci, C., Marigomez, I., Soto, M., 2000. Biomarkers and trace metals in the digestive gland of indigenous and transplanted mussels *Mytilus galloprovincialis*, in Venice Lagoon, Italy. Mar. Environ. Res. 50 (1–5), 417–423.

Dethlefsen, V., 1988. Status report on aquatic pollution problems in Europe. Aquat. Toxicol. 11 (3–4), 259–289.

Dıgış, A., 1986. Anbarli Samlar (Istanbul) arasindaki bölgenin jeolojisi. (Ph.D. thesis). Istanbul Üniversitesi, İstanbul, 28 pp., (in Turkish with English abstract).

Dinçer, B., 2005. Yarımburgaz Kazıları Işığında, Orta Pleistosen'de Doğal Çevre, http://paleoberkay.blogspot.com/2010/09/yarmburgaz-magaras-orta-pleistosen-kayd.html.

Farrand, W.R., McMahon, J.P., 1997. History of the sedimentary infilling of Yarimburgaz Cave, Turkey. Geoarchaeology 12 (6), 537–565, http://dx.doi.org/10.1002/(SICI)1520-6548(199709)12:6<537::AID-GEA3>3.0.CO;2-#.

Farrington, J.W., Davis, A.C., Tripp, B.W., Phelps, D.K., Galloway, W. B., 1987. 'Mussel Watch' — measurements of chemical pollutants bivalves as one indicator of coastal environmental quality. In: Boyle, T.P. (Ed.), New Approaches to Monitoring Aquatic Ecosystem. ASTM STP 940. American Soc. Testing Mater., Philadelphia, 125–139, http://dx.doi.org/10.1520/STP28585S.

Fdil, M.A., Mouabad, A., Outzourhit, A., Benhra, A., Maarouf, A., Pihan, J.C., 2006. Valve movement response of the mussel *Mytilus galloprovincialis* to metals (Cu, Hg, Cd and Zn) and phosphate industry effluents from Moroccan Atlantic coast. Ecotoxicology 15 (5), 477–486, http://dx.doi.org/10.1007/s10646-006-0083-3.

Göksu, M.Z.L., Akar, M., Çevik, F., Fındık, Ö., 2005. Bioaccumulation of some heavy metals in two bivalvia species. Turk. J. Vet. Anim. Sci. 29, 89–93.

Goldberg, E.D., 1975. The Mussel Watch — a first step in global marine monitoring. Mar. Pollut. Bull. 6, 111–117.

Gosling, E.M., 1992. Systematics and geographic distribution of *Mytilus*. In: Gosling, E. (Ed.), The Mussel *Mytilus*: Ecology, Physiology, Genetics and Culture. Elsevier, New York, 1–17.

Hammand, P.B., Beliles, R.P., 1980. Metals. In: Doull, J., Klaassen, C. D., Amdur, M.O. (Eds.), Toxicology. 2nd Edn. McMillan Publishing Co. Inc, New York, 409–462.

Ikuta, K., 1990. Comparisons of some heavy metal contents among four herbivorous gastropod mollusks in the same family. Miyazaki Univ. Bull. Fac. Agric. 37, 21–28.

Kaya, S., Pirinçci, İ., Bilgili, A., 1998. Çevre Bilimi ve Çevre Toksikolojisi. Medisan Yayın Serisi, İstanbul, (in Turkish).

Kayhan, F.E., 2007. Mercury levels of Mediterranean mussels (*Mytilus galloprovincialis*) from Bosphorus, İstanbul. Turk. J. Biol. Sci. 7 (2), 369–373, http://dx.doi.org/10.3923/jbs.2007.369.373.

Kayhan, F.E., Gulsoy, N., Balkıs, N., Yüce, R., 2007. Cadmium and lead levels of Mediterranean mussels (*Mytilus galloprovincialis*) from Bosphorus, İstanbul, Turkey. Pak. J. Biol. Sci. 10 (6), 915–919, http://dx.doi.org/10.3923/jbs.2007.915.919.

Krauskopf, K.B., 1979. Introduction to Geochemistry. McGraw-Hill, Singapore, 617 pp.

Losso, C., His, E., Ghetti, P.F., Volpi-Ghirardini, A., 2004. Sensitivity of embryotoxicity test with *Mytilus galloprovincialis* (Lmk) towards some compounds of environmental interest (copper and pesticides). Environ. Technol. 25 (7), 841–846, http://dx.doi.org/10.1080/09593330.2004.9619376.

Maanan, M., 2007. Biomonitoring of heavy metals using *Mytilus galloprovincialis* in Safi coastal waters, Morocco. Environ. Toxicol. 22 (5), 525–531, http://dx.doi.org/10.1002/tox.20301.

Mauri, M., Baraldi, E., 2003. Heavy metal bioaccumulation in *Mytilus galloprovincialis*: a transplantation experiment in Venice Lagoon. Chem. Ecol. 19 (2–3), 79–90, http://dx.doi.org/10.1080/0275754031000119852.

Meriç, E., Sakınç, M., Özdoğan, M., Açkurt, F., 1988. Yarımburgaz Mağarası kazılarında gözlenen mollusk kavkıları hakkında. Arkeoloji ve Sanat 40/41, 27–31, (in Turkish).

Meriç, E., Sakınç, M., Özdoğan, M., Açkurt, F., 1991. Mollusc shells found at the Yarimburgaz Cave. J. Islamic Acad. Sci. 4 (1), 6–9.

MTA, 2000. Türkiye Metalojeni Haritası. 1:1.000.000 Ölçekli. MTA Yayınları, Ankara, (in Turkish).

Nasci, C., Nesto, N., Monteduro, R.A., Da Ros, L., 2002. Field application of biochemical markers and a physiological index in the mussel, *Mytilus galloprovincialis*: transplantation and biomonitoring studies in the lagoon of Venice (NE Italy). Mar. Environ. Res. 54 (3–5), 811–816.

Nesto, N., Bertoldo, M., Nasci, C., Da Ros, L., 2004. Spatial and temporal variation of biomarkers in mussels (*Mytilus galloprovincialis*) from the Lagoon of Venice, Italy. Mar. Environ. Res. 58 (2–5), 287–291, http://dx.doi.org/10.1016/j.marenvres.2004.03.073.

Ökten, N.B., 2009. Marmara Denizi Güneyi Holosen Mollusk Kavkılarının Element Jeokimyası. (Msc. thesis). Ankara Üniv., Ankara, 84 pp., (in Turkish with English abstract).

Özdoğan, A., 1999. Çayönü. In: Özdoğan, M., Başgelen, N. (Eds.), Neolithic in Turkey. Arkeoloji ve Sanat Yayınları, İstanbul, 35–63.

Özdoğan, M., Koyunlu, A., 1986. Yarimburgaz Mağarası: 1986 yılı çalışmalarının ilk sonuçlar ve bazı gözlemler. Arkeoloji ve Sanat 32/33, 4–17, (in Turkish).

Özdoğan, M., Miyake, Y., Özbaşaran-Dede, N., 1991. An interim report on the Excavations at Yarımburgaz and Toptepe in Eastern Thrace. Anatolica XVII, 59–121.

Phillips, D.J.H., 1980. Quantitative Aquatic Biological Indicators: Their Use to Monitor Trace Metal and Organochlorine Pollution. Appl. Sci. Publ. Ltd., London, 488 pp.

Puente, X., Villares, R., Carral, E., Carballeira, A., 1996. Nacreous shell of *Mytilus galloprovincialis* as a biomonitor of heavy metal pollution in Galiza (NW Spain). Sci. Tot. Environ. 183 (3), 205–211, http://dx.doi.org/10.1016/0048-9697(96)05066-8.

Risso-de Faverney, C., Marielle, E., Guibbolini-Sabatier, M.E., Francour, P., 2010. An ecotoxicological approach with transplanted mussels (*Mytilus galloprovincialis*) for assessing the impact of tyre reefs immersed along the NW Mediterranean Sea. Mar. Environ. Res. 70 (1), 87–94, http://dx.doi.org/10.1016/j.marenvres.2010.03.007.

Rivaro, P., Abelmoschi, M.L., Leardi, R., Frache, R., 2000. Monitoring of heavy metals and butyltin compounds in coastal waters of Ligurian Sea: results of a mussel watch Project. Toxicol. Environ. Chem. 75 (1–2), 99–111, http://dx.doi.org/10.1080/02772240009358896.

Roméo, M., Frasila, C., Gnassia-Barelli, M., Damiens, G., Micu, D., Mustata, G., 2005. Biomonitoring of trace metals in the Black Sea (Romania) using mussels *Mytilus galloprovincialis*. Water Res. 39 (4), 596–604, http://dx.doi.org/10.1016/j.watres.2004.09.02.

Şanlı, L., 1984. Çevre Sorunlar ve Besin Kirlenmesi. Selçuk Üniv. Vet. Fak. Derg. Özel Sayı, 17–37, (in Turkish with English abstract).

Şentürk, F., 1993. Çeşitli yörelerden avlanmış mollusklarda civa, kadmiyum, kurşun düzeylerinin saptanması. (Msc. thesis). İstanbul Üniversitesi, İstanbul, 63 pp., (in Turkish with English abstract).

Serafim, M.A., Bebianno, R.M., Langstone, W.J., 2002. Effects of temperature and size on metallothionein synthesis and gill of *Mytilus galloprovincialis* exposed to Cd. Mar. Environ. Res. 54, 361–365.

Steiner, M.C., Achyuthan, H., Arsebük, G., Howell, F.C., Josephson, S.C., Juell, K.E., Pigati, J., Quade, J., 1998. Reconstructing cave bear paleoecology from skeletons: across-disciplinary study of middle Pleistocene bears from Yarimburgaz Cave, Turkey. Paleobiology 24 (1), 74–98, http://dx.doi.org/10.1017/S0094837300019989.

Taleb, Z.M., Benghali, S., Kaddour, A., Boutiba, Z., 2007. Monitoring the biological effects of pollution on the Algerian west coast using mussels *Mytilus galloprovincialis*. Oceanologia 49 (4), 543–564.

Topçuoğlu, S., Kırbaşoğlu, Ç., Balkıs, N., 2004. Heavy metal concentrations in marine algae from the Turkish Coast of the Black Sea, during 1979–2001. J. Black Sea/Medit. Environ. 10 (1), 21–44.

Tosyalı, C., 2005. *Mytilus galloprovincialis* (Lamarck, 1819) midyesinde pişirmenin çeşitli ağır metal düzeylerine etkisi. (Msc. thesis). Kahramanmaraş Sütçü İmam Üniversitesi, Kahramanmaraş, Turkey, (in Turkish with English abstract).

Widdows, J., 1985. Physiological procedures. In: Bayne, B.L., Brown, D.A., Burns, K., Dixon, D.R., Ivanovici, A., Livingstone, D.R., Lowe, D.M., Moore, M.N., Stebbing, A.R.D., Widdows, J. (Eds.), The Effects of Stress and Pollution on Marine Animals. Praeger Press, New York, 161—178.

Yabanli, M., Katalay, S., Yozukmaz, A., Inanan, B.E., 2015. Comparative study of heavy metals and selenium accumulation in the digestive gland and gills of *Mytilus galloprovincialis* (Lamarck, 1819) caught in Izmir Bay (Turkey). Turk. J. Biochem. 40 (2), 140—148, http://dx.doi.org/10.5505/tjb.2015.32448.

Oceanologia (2016) 58, 150—153

Available online at www.sciencedirect.com

ScienceDirect

journal homepage: www.elsevier.com/locate/oceano

SHORT COMMUNICATION

Addendum to "Sea spray aerosol flux estimation based on long-term variation of wave statistics": estimation based on long-term variation of wind statistics☆

Dag Myrhaug*, **Hong Wang, Lars Erik Holmedal**

Department of Marine Technology, Norwegian University of Science and Technology (NTNU), Trondheim, Norway

Received 1 July 2015; accepted 27 November 2015
Available online 23 December 2015

KEYWORDS
Sea spray aerosol flux;
Whitecap coverage;
Mean wind speed;
Wind statistics

Summary This note provides estimates of the mean whitecap coverage and the mean sea spray aerosol flux based on long-term wind statistics from the Northern North Sea. Here the improved sea spray aerosol production flux model by Callaghan (2013) is used. The results are compared with those in Myrhaug et al. (2015) based on long-term wave statistics from the Northern North Sea and the North Atlantic.

☆ This work was carried out as a part of the project "Air-Sea Interaction and Transport Mechanisms in the Ocean" funded by the Norwegian Research Council (221988). This support is gratefully acknowledged.
* Corresponding author at: Department of Marine Technology, Norwegian University of Science and Technology (NTNU), Otto Nielsens vei 10, NO-7491 Trondheim, Norway. Tel.: +47 73 59 55 27; fax: +47 73 59 55 28.
E-mail addresses: dag.myrhaug@ntnu.no (D. Myrhaug), hong.wang@ntnu.no (H. Wang), lars.erik.holmedal@ntnu.no (L.E. Holmedal).
DOI of original article: http://dx.doi.org/10.1016/j.oceano.2015.04.001.
Peer review under the responsibility of Institute of Oceanology of the Polish Academy of Sciences.

ELSEVIER Production and hosting by Elsevier

1. Introduction

Myrhaug et al. (2015) (hereafter referred to as MWH15) provided estimates of the mean sea spray aerosol flux based on long-term variation of wave statistics using the whitecap method applying the limiting steepness and threshold vertical acceleration criteria. Here the long-term wave statistics represented open ocean deep water waves in the Northern North Sea and the North Atlantic. This note is supplementary to MWH15 with the purpose of demonstrating how similar results for the mean sea spray aerosol flux can be obtained by using estimates of the whitecap coverage based on long-term variation of wind statistics. Moreover, the whitecap method used in MWH15 has been replaced by the Callaghan (2013) improved sea spray aerosol production flux model.

The whitecap coverage, which is defined as the area of whitecaps per unit sea surface, has often been used to

http://dx.doi.org/10.1016/j.oceano.2015.11.003

quantify the occurrence of breaking wind waves at sea. There are many parameterizations of whitecap coverage available in the literature; comprehensive reviews are given in Anguelova and Webster (2006), Massel (2007) and de Leeuw et al. (2011). Parameterizations are based on U_{10} and u_*. Here U_{10} [m s^{-1}] is the mean wind speed at the 10 m elevation, and u_* [m s^{-1}] is the friction velocity equal to the square root of the vertical flux of horizontal momentum at the sea surface. However, when plotting the whitecap coverage versus U_{10} and versus u_* it is often found that the data scatter is larger when plotted versus u_* than when plotted versus U_{10} (see e.g. Sugihara et al., 2007). This is attributed to the larger uncertainties in estimating u_* than measuring U_{10}. Therefore the parameterizations in the present study are based on U_{10}. Other important factors affecting the whitecap coverage are the stratification of the near-surface air boundary layer and the state of development of surface waves, see e.g. Sugihara et al. (2007) and Myrhaug and Holmedal (2008). Reviews of whitecap coverage at sea and how it is linked to marine aerosol production are given by Massel (2007), de Leeuw et al. (2011) and Callaghan (2013).

2. Whitecap coverage and sea spray aerosol flux estimation based on long-term variation of wind statistics

2.1. Whitecap coverage estimation

The following whitecap coverage (W_c) parameterizations will be considered here to demonstrate the use of wave statistics.

The Monahan and O'Muircheartaigh (1980) (hereafter referred to as MO80) parameterization is widely used and recognized (de Leeuw et al., 2011), given as fraction,

$$W_c = 3.84\times10^{-6}U_{10}^{3.41}. \tag{1}$$

The Callaghan et al. (2008) (hereafter referred to as C08) parameterization is based on data collected in the North East Atlantic inside a geographical area defined by 9.5°W, 13°W, 55.5°N and 57.5°N, given in percent,

$$\begin{aligned} W_c &= 0.00318(U_{10}-3.70)^3; \quad 3.70\,\mathrm{m\,s^{-1}} < U_{10} < 10.18\,\mathrm{m\,s^{-1}} \\ W_c &= 0.000482(U_{10}+1.98)^3; \; 10.18\,\mathrm{m\,s^{-1}} < U_{10} < 23.09\,\mathrm{m\,s^{-1}} \end{aligned}. \tag{2}$$

It should be noted that the wave statistics in BGGS07 (Bitner-Gregersen and Guedes Soares, 2007) Data Sets 1 to 5 used in MWH15 is from the same ocean area, i.e. from the North Atlantic.

According to Eqs. (1) and (2) the whitecap coverage is given for a known value of U_{10}. The long-term variation of the whitecap coverage can be obtained from available wind statistics, i.e. from long-term distributions of U_{10}. Different parametric models for the cumulative distribution function (*cdf*) or the probability density function (*pdf*) of U_{10} are given in the literature. A recent review is given in Bitner-Gregersen (2015), where the joint statistics of U_{10} with significant wave height H_s and spectral peak period T_p are presented. In the present article the long-term statistics of W_c are exemplified by using the *cdf* of U_{10} given by Johannessen et al. (2001), where wind measurements covering the years 1973–1999 from the Northern North Sea are used as a database. This database consists of composite measurements from the Brent, Troll, Statfjord and Gullfaks fields as well as the weather ship Stevenson. Model data from the Norwegian hindcast archive (WINCH, gridpoint 1415) have been filled in for periods where measured data were missing. Thus a 25-year long continuous time series has been used (see Johannessen et al. (2001) for more details), upon which the *cdf* of the 1-h values of U_{10} is described by the two-parameter Weibull model

$$P(U_{10}) = 1-\exp\left[-\left(\frac{U_{10}}{\alpha}\right)^{\beta}\right]; \quad U_{10}\geq 0, \tag{3}$$

with the Weibull parameters

$$\alpha = 8.426, \qquad \beta = 1.708. \tag{4}$$

It should be noted that the wave statistics in MGAU05 (Moan et al., 2005) used in MWH15 is from the same ocean area as the wind statistics, i.e. from the Northern North Sea.

If $x = U_{10}$ is defined for $x_1 \leq x \leq x_2$, then x follows the truncated Weibull *cdf* given by

$$P(x) = \frac{\exp\left[-\left(\frac{x_1}{\alpha}\right)^{\beta}\right]-\exp\left[-\left(\frac{x}{\alpha}\right)^{\beta}\right]}{\exp\left[-\left(\frac{x_1}{\alpha}\right)^{\beta}\right]-\exp\left[-\left(\frac{x_2}{\alpha}\right)^{\beta}\right]}; \quad x_1\leq x\leq x_2. \tag{5}$$

Now the long-term statistics of W_c can be derived by using this *cdf* of $x = U_{10}$. A statistical quantity of interest is the expected (mean) value of W_c given as

$$E[W_c(x)] = \int_0^{\infty} W_c(x)p(x)\,dx, \tag{6}$$

where $p(x)$ is the probability density function (*pdf*) of $x = U_{10}$ given by $p(x) = dP(x)/dx$ where $P(x)$ is given in Eq. (5). Then the integral in Eq. (6) can be calculated analytically by using the results in Abramowitz and Stegun (1972, Chs. 6.5 and 26.4)

$$\begin{aligned} E[x^n] &= \int_{x_1}^{x_2} x^n p(x)\,dx \\ &= \frac{\alpha^n}{N}\left\{\Gamma\left[1+\frac{n}{\beta}, \left(\frac{x_1}{\alpha}\right)^{\beta}\right]-\Gamma\left[1+\frac{n}{\beta}, \left(\frac{x_2}{\alpha}\right)^{\beta}\right]\right\}, \end{aligned} \tag{7}$$

$$N = \exp\left[-\left(\frac{x_1}{\alpha}\right)^{\beta}\right]-\exp\left[-\left(\frac{x_2}{\alpha}\right)^{\beta}\right], \tag{8}$$

where $\Gamma(s, t)$ is the incomplete gamma function, and n is a real number (not necessarily an integer). It should be noted that $\Gamma(s, 0) = \Gamma(s)$ where Γ is the gamma function, and $\Gamma(s, \infty) = 0$. Here the results are exemplified by using the parameterizations of W_c in Eqs. (1) and (2). The results are

$$\text{MO80}: \quad E[W_c] = 1.10\%, \tag{9}$$

$$\text{C08}: \quad E[W_c] = 0.76\%. \tag{10}$$

The estimate in Eq. (9) is obtained by integrating from zero to infinity, while the estimate in Eq. (10) is obtained by integrating from $x_1 = U_{10} = 3.70$ m s^{-1} to infinity, i.e. giving a 6% larger value than by integrating to $x_2 = U_{10} = 23.09$ m s^{-1}.

The corresponding results obtained in MWH15 (see the results for the MGAU05 data (Northern North Sea) and the

BGGS07 Data Sets 1 to 5 (North Atlantic) in Table 5) are denoted as $E[F_{cov}]$ by using the limiting steepness criterion (Criterion 1) and the threshold vertical acceleration criterion (Criterion 2). It appears that some of the example estimates based on the wind statistics agree well with some of the estimates based on the wave statistics, i.e. (1) the MO80 wind statistics estimate of 1.1% agrees well with the mean value of the estimate corresponding to BGGS07 Data Sets 1 to 5 using Criterion 2 of 1.2%; (2) the C08 wind statistics estimate of 0.76% agrees well with the estimate corresponding to MGAU05 using Criterion 1 of 0.77% (which is larger than the estimate using Criterion 2 of 0.58%).

2.2. Sea spray aerosol flux estimation

Rather than pursuing the method used in MWH15, a recent improved method given by Callaghan (2013) (hereafter referred to as C13) will be used. Thus, following C13, Eq. (1) in MWH15 should be rewritten to explicitly include the time scale of the decaying whitecap area as (i.e. using the notation in C13 by taking $\log r \equiv \log_{10} r$ and $r \equiv r_{80}$)

$$\frac{dF(r)}{d(\log r)} = \frac{dE(r)}{d(\log r)} \cdot \frac{W_c}{\tau}. \tag{11}$$

Here the term on the left hand side of the equation is the number of particles produced per unit ocean surface area and unit time per radius size bin. The first term on the right hand side of the equation is the number of particles produced per whitecap area per radius size bin, W_c is the whitecap per unit ocean surface area, and τ is a characteristic whitecap time scale which cannot be incorporated in the first term on the right hand side of the equation to produce an estimate of the rate of particle production per whitecap area. Here the droplet radius r is taken to represent r_{80}, i.e. the droplet radius in equilibrium with the atmosphere at a given ambient relative humidity of 80%. Moreover, following C13 the first term on the right hand side of Eq. (11) is given by

$$\frac{dE(r)}{d(\log r)} = 29419 r(1 + 0.057 r^{3.45}) \cdot \exp\left\{ \begin{matrix} 3.68 \exp[-5.33(0.433 - \log r)^2] \\ -4.7 \ln r [1 + \Theta r]^{-0.017 r^{-1.44}} \end{matrix} \right\}, \tag{12}$$

with the unit m^{-2}, where Θ is an adjustable parameter with 30 as a typically assigned value. The whitecap coverage in % is given in Eq. (2) (see C13 for more details).

Now it follows that

$$\frac{dF(r)}{dr} = \frac{r^{-1}}{\ln 10} \frac{dF(r)}{d(\log r)}, \tag{13}$$

with the unit $m^{-2}\,s^{-1}\,\mu m$, and consequently the total flux for particles with radii in the interval r_1 to r_2 is

$$F(r) = \int_{r_1}^{r_2} \frac{r^{-1}}{\ln 10} \frac{dF(r)}{d(\log r)} dr, \tag{14}$$

with the unit $m^{-2}\,s^{-1}$. The volume flux with unit $m\,s^{-1}$ is obtained by multiplying Eq. (14) by the factor $(4\pi/3)r^3$.

The total expected volume aerosol flux of $r = r_{80}$, $E[F(r)]$, can now be estimated based on the long-term wind statistics used in Section 2.1. The results are obtained by multiplying Eq. (14) with $E[W_c] = 0.76\%$ from Eq. (10) and dividing by $\tau = 5.3$ s (see C13). By integrating $r = r_{80}$ over the range 0.8–10 μm (as in MWH15) the result is

$$E[F(r)] = 0.83 \times 10^{-12}\,m\,s^{-1}. \tag{15}$$

The corresponding results obtained in MWH15 by using Criteria 1 and 2 (see the results for $E[f_{vol}^{(tot)}]$ corresponding to MGAU05 in Table 4) are $15.3 \times 10^{-12}\,m\,s^{-1}$ and $11.5 \times 10^{-12}\,m\,s^{-1}$, respectively. The mean values corresponding to BGGS07 Data Sets 1 to 5 are $34.2 \times 10^{-12}\,m\,s^{-1}$ and $23.9 \times 10^{-12}\,m\,s^{-1}$, respectively. Thus, it appears that the present result in Eq. (15) is significantly lower than those obtained in MWH15. This is mainly due to the inherent features of the improved sea spray aerosol production flux model by C13.

3. Summary

Estimate of the long-term sea spray aerosol flux based on long-term variation of wind statistics from the Northern North Sea is provided by adopting the improved Callaghan (2013) model. Overall, some of the example estimates of the mean whitecap coverage based on the wind statistics agree with those obtained in Myrhaug et al. (2015) based on wave statistics. However, the total mean volume aerosol flux based on the improved Callaghan (2013) give significantly lower value than those obtained in Myrhaug et al. (2015), which is mainly due to the inherent features of the first model.

Overall, this work provides a procedure which can be applied to calculate the whitecap coverage and sea spray aerosol flux based on long-term statistical information of the wind climate.

Acknowledgement

An anonymous reviewer is acknowledged for a thorough and constructive review of the first version of the paper.

References

Abramowitz, M., Stegun, I.A., 1972. Handbook of Mathematical Functions. Dover, New York, 1046 pp.

Anguelova, M.D., Webster, F., 2006. Whitecap coverage from satellite measurements: a first step toward modeling the variability of oceanic whitecaps. J. Geophys. Res. 111, C03017, http://dx.doi.org/10.1029/2005JC003158.

Bitner-Gregersen, E.M., 2015. Joint met-ocean description for design and operations of marine structures. Appl. Ocean Res. 51, 279–292, http://dx.doi.org/10.1016/j.apor.2015.01.007.

Bitner-Gregersen, E., Guedes Soares, C., 2007. Uncertainty of average steepness prediction from global wave databases. In: Proc. MARSTRUCT, Glasgow, UK, 3–10.

Callaghan, A.H., 2013. An improved whitecap timescale for sea spray aerosol production flux modeling using the discrete whitecap method. J. Geophys. Res. Atmos. 118, 9997–10010, http://dx.doi.org/10.1002/jgrd.50768.

Callaghan, A.H., de Leeuw, G., Cohen, L., O'Dowd, C.D., 2008. Relationship of oceanic whitecap coverage to wind speed and wind history. Geophys. Res. Lett. 35, L23609, http://dx.doi.org/10.1029/2008GL036165.

de Leeuw, G., Andreas, E.L., Anguelova, M.D., Fairall, C.W., Lewis, E.R., O'Dowd, C., Shultz, M., Schwartz, S.E., 2011. Production flux of sea spray aerosol. Rev. Geophys. 49, RG 2001, http://dx.doi.org/10.1029/2010RG000349.

Johannessen, K., Meling, T.S., Haver, S., 2001. Joint distribution for wind and waves in the Northern North Sea. In: Proc. 11th International Offshore and Polar Engineering Conference, vol. III, Stavanger, Norway, 19—28.

Massel, S.R., 2007. Ocean Waves Breaking and Marine Aerosol Fluxes. Springer, New York, 232 pp.

Moan, T., Gao, Z., Ayala-Uraga, E., 2005. Uncertainty of wave-induced response of marine structures due to long-term variation of extratropical wave conditions. Mar. Struct. 18 (4), 359—382, http://dx.doi.org/10.1016/j.marstruc.2005.11.001.

Monahan, E.C., O'Muircheartaigh, I., 1980. Optimal power law description of oceanic whitecap coverage dependence on wind-speed. J. Phys. Oceanogr. 10 (12), 2094—2099, http://dx.doi.org/10.1175/1520-0485(1980)010<2094:0PLDOO>2.0.CO;2.

Myrhaug, D., Holmedal, L.H., 2008. Effects of wave age and air stability on whitecap coverage. Coast. Eng. 55 (12), 959—966, http://dx.doi.org/10.1016/j.coastaleng.2008.03.005.

Myrhaug, D., Wang, H., Holmedal, L.E., 2015. Sea spray aerosol flux estimation based on long-term variation of wave statistics. Oceanologia 57 (3), 288—292, http://dx.doi.org/10.1016/j.oceano.2015.04.001.

Sugihara, Y., Tsumori, H., Ohga, T., Yoshioka, H., Serizawa, S., 2007. Variation of whitecap coverage with wave-field conditions. J. Mar. Syst. 66 (1—4), 47—60, http://dx.doi.org/10.1016/j.jmarsys.2006.01.014.

Oceanologia (2016) 58, 154—159

Available online at www.sciencedirect.com

ScienceDirect

journal homepage: www.elsevier.com/locate/oceano

SHORT COMMUNICATION

The quagga mussel (*Dreissena rostriformis bugensis* Andrusov, 1897) — another Ponto-Caspian dreissenid bivalve in the southern Baltic catchment: the first record from the Szczecin Lagoon☆

Adam Woźniczka [a,*], **Brygida Wawrzyniak-Wydrowska** [b], **Teresa Radziejewska** [b], **Anna Skrzypacz** [b]

[a] *National Marine Fisheries Research Institute, Research Station in Świnoujście, Świnoujście, Poland*
[b] *Institute of Marine and Coastal Sciences, University of Szczecin, Szczecin, Poland*

Received 22 May 2015; accepted 10 December 2015
Available online 11 January 2016

KEYWORDS
Dreissena rostriformis bugensis;
Baltic Sea;
Szczecin Lagoon;
Invasive species

Summary In 2014, a non-indigenous dreissenid bivalve, the quagga mussel (*Dreissena rostriformis bugensis* Andrusov, 1897) was for the first time recorded in the Szczecin Lagoon. This was also the first record of the species in the Baltic Sea catchment. The quagga mussel was found to accompany the zebra mussel (*Dreissena polymorpha*), a non-indigenous bivalve already firmly established in the Lagoon. As indicated by the new immigrant's estimated abundance (4000.0 ± 355.44 ind. m^{-2}) and the zebra mussel to quagga mussel abundance ratio (about 60:40), the immigration of *D. rostriformis bugensis* to the Lagoon can be regarded as successful. The quagga mussel has already formed a strong and reproducing population which co-occurs with that of the zebra mussel in the area.

☆ This study received support from the Polish National Science Centre grant No. N N305 397538, from funds for the statutory activities of the National Marine Fisheries Research Institute (P1-1, P9-10), and from funds for the statutory activities of the Palaeoceanology Unit, University of Szczecin.
* Corresponding author at: National Marine Fisheries Research Institute, Research Station in Świnoujście, Plac Słowiański 11, 72-600 Świnoujście, Poland. Tel.: +48 91 326 27 24.
E-mail address: awozniczka@mir.gdynia.pl (A. Woźniczka).
Peer review under the responsibility of Institute of Oceanology of the Polish Academy of Sciences.

Production and hosting by Elsevier

http://dx.doi.org/10.1016/j.oceano.2015.12.002

1. Introduction

In addition to the zebra mussel (*Dreissena polymorpha* Pallas, 1771), the quagga mussel (*Dreissena rostriformis bugensis* Andrusov, 1897) is another Ponto-Caspian dreissenid bivalve which has colonised freshwater reservoirs of Europe and North America (Karatayev et al., 2015; Nalepa and Schloesser, 2013; Orlova et al., 2004, 2005; Zhulidov et al., 2010). *Dreissena rostriformis bugensis* is a species native for the entire area of the southern Bug River and Dnieper River catchment in Ukraine (Orlova et al., 2004, 2005). The bivalve began expanding its range in eastern Europe as late as post 1940, when the first dam reservoirs were built on the Dnieper River. Between 1940—1990, *D. rostriformis bugensis* was seen to expand in three major direction: to the north, along the cascade of the Dnieper River dam reservoirs; to the east, via the River Don system, and thence to the north, through the reservoirs on the Volga; and to the north-west, through the Dniester River (Mills et al., 1996; Orlova et al., 2004, 2005; Zhulidov et al., 2010). In 2004, *D. rostriformis bugensis* was recorded in the Romanian part of the Danube River system (Micu and Telembici, 2004; Popa and Popa, 2006). Concurrently, in 1989, the species was first recorded in the Laurentian Great Lakes of North America (Benson, 2013; Mills et al., 1993). The quagga mussel invasion there closely followed that of the zebra mussel so the two species have been seen to expand their range in tandem (Benson, 2013; Karatayev et al., 2015). At present, the two species continue colonising the North American waters. In most of the newly colonised areas, the two congeners co-occur, but their within-water body distributions differ (Karatayev et al., 2015; Nalepa et al., 2010). The zebra mussel seems to be a more successful coloniser of the two, the number of water bodies it has colonised being 17 times higher than the number of water bodies colonised by the quagga mussel (Karatayev et al., 2015). In western Europe, the beginning of *D. rostriformis bugensis* expansion dates to 2006 when the species was recorded in the Rhine delta, in Hollandsch Diep in the Netherlands (Molloy et al., 2007; Schonenberg and Gittenberger, 2008). Subsequently, the species colonised the rivers Rhine and Mose (Haybach and Christmann, 2009; Imo et al., 2010; Karatayev et al., 2015; Matthews et al., 2014; Van der Velde and Platvoet, 2007). In 2007, the species was spotted in the River Main, a River Rhine tributary in Germany (Martens et al., 2007; Van der Velde and Platvoet, 2007), to be found — in 2011 — in the French part of the Mosel (Bij de Vaate and Beisel, 2011). In 2014, the species was first reported from the United Kingdom (Aldridge et al., 2014). At present, the quagga is observed to be spreading rapidly in inland waters of western Europe (Karatayev et al., 2015; Matthews et al., 2014). The western European population's site closest to the Baltic Sea catchment is in the Elbe, that of the eastern European population closest to the Baltic Sea inhabiting the Prypyat River (Schoell et al., 2012).

Here, we are reporting on finding the quagga mussel in the Szczecin Lagoon (Odra River estuary, southern Baltic Sea), thus providing the first record of the species in the Baltic Sea catchment.

The Szczecin Lagoon (Fig. 1), divided into two parts: the Small Lagoon (Kleines Haff) located almost entirely within Germany and the Great Lagoon (Wielki Zalew) on the Polish side of the Polish-German border bisecting the Lagoon, forms

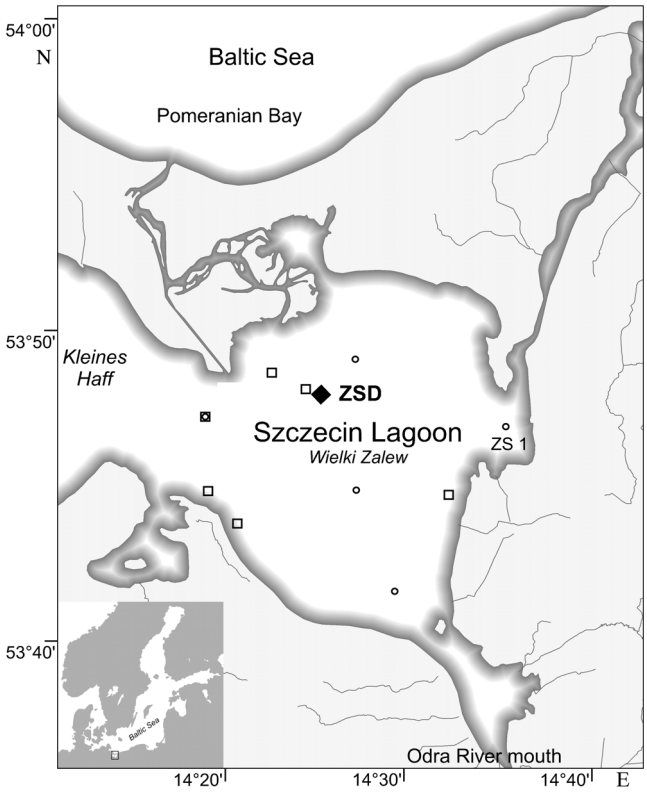

Figure 1 The study area and location of sampling sites. (□) sites of dredge and Van Veen grab sample collection on 10 October 2014; (○) sites sampled monthly within the project framework; (◆) Station ZSD, the site of the November 2014 sample.

a major part of the River Odra estuarine system. Fed by the Odra River from the south and connecting with the Pomeranian Bay (southern Baltic Sea) in the north, the Lagoon is a typical brackish transitional water body the hydrographic regime of which is shaped by an interplay of fresh water discharged by the Odra River and the periodic intrusions of about 7 PSU sea water from the Baltic Sea. As a result, the Lagoon's salinity ranges from 0.3 to 4—5 PSU and averages 1.4 PSU (Radziejewska and Schernewski, 2008). The Lagoon's mean and maximum natural depths are 3.8 and 8.5 m, respectively, a channel dredged along the length of the Great Lagoon being deeper (up to 10.5 m). The bottom in the central part of the Great Lagoon is covered by mud, usually found at depths of 4.5—5.5 m; the muddy parts are surrounded by a belt of sandy shallows 1—1.5 m deep which slope steeply towards the muddy bottom (Wolnomiejski and Witek, 2013). The shallows themselves, and their slopes in particular, support dense aggregations of the zebra mussel (*D. polymorpha*), one of the most important component of the Great Lagoon biota (Radziejewska and Schernewski, 2008; Wiktor, 1969; Wolnomiejski and Witek, 2013). There is no information on the timing of the zebra mussel's original settlement in the Szczecin Lagoon. The very first scientific publication about Lagoon's biota (Brandt, 1896) mentions only the “very dense aggregations” of the bivalve.

The Lagoon has been exposed to a heavy anthropogenic pressure manifested through a high level of eutrophication of the main basins, with all the negative consequences of the

process (Radziejewska and Schernewski, 2008). It is also an area of intensive ships' traffic, the ships using two large ports in Świnoujście and Szczecin (the latter accessed via the channel mentioned). The Odra River and a network of canals connect the Lagoon with the system of European waterways, including catchments of the rivers Vistula and Elbe and, indirectly, with those of the rivers Rhine and Danube. The consequence of the Lagoon's location and heavy ships' traffic is a high proportion of non-indigenous species in the biota (Gruszka, 1999; Radziejewska and Schernewski, 2008; Wawrzyniak-Wydrowska and Gruszka, 2005; Wolnomiejski and Witek, 2013; Woźniczka et al., 2011) which use the Lagoon as a gateway to the Baltic Sea basin (Gruszka, 1999).

2. Material and methods

Individuals identified as *D. rostriformis bugensis* were first encountered on 10 October 2014 in a sample of bivalves collected from the Lagoon to resolve doubts regarding the identity of unusual, non-typical zebra mussel-like individuals, found in earlier benthos samples from locations with bottoms covered by the zebra mussel and in fish trawls (B. Wawrzyniak-Wydrowska, A. Woźniczka, pers. obs.). Subsequently, qualitative samples were collected with a bottom dredge, quantitative samples being retrieved with an 0.1 m^2 Van Veen grab from areas known for the abundant presence of *D. polymorpha* (Fig. 1). The study was subsequently extended to include samples collected in the framework of a research project aimed at investigating historical and contemporary aspects of the Lagoon's sedimentary communities dynamics under the influence of intensive deposition of phytal organic material from the water column (Radziejewska et al., in prep.). The project involved monthly (April—November 2010—2014) sediment sampling at 5 stations located throughout the Lagoon (Fig. 1), differing in their hydrographic regime. In November 2014, additional samples were collected from Station ZSD (Fig. 1) in the northern part of the Lagoon to obtain enough material with which to check the earlier identification of *D. rostriformis bugensis*. Those samples were collected with a 625 cm^2 Van Veen grab. Contents of all grabs were sieved on an 0.5 mm mesh size sieve; the sieve residue was preserved in buffered 10% formalin and sorted in the laboratory. The quagga mussel individuals found were measured to 1 mm with a calliper.

3. Results

The individuals first identified as representing *D. rostriformis bugensis* were collected on 10 October 2014 in the northern part of the Szczecin Lagoon (sites denoted with squares in Fig. 1). They were present in all the samples and co-occurred there with the zebra mussel (*D. polymorpha*) to form mixed aggregations.

The identification of *D. rostriformis bugensis* was based on examination of shell characters (May and Marsden, 1992; Mills et al., 1996; Pathy and Mackie, 1993). The following features were regarded as diagnostic (cf. Fig. 2): the shell triangular in outline; distal part of the shell rounded; a rounded triangular carina between the ventral and dorsal surfaces; ventral side of the shell convex, without any sharp ventro-lateral ridge; dorsal side flat, also with a rounded margin, frequently with an ala-like distension; the two shells distinctly asymmetric; the proximal part of the right shell curved mid-ventrally; umbone (the thickest and oldest part of the shell) pointed and directed downward; byssus grove on the lower part of the shell very fine, located close to the

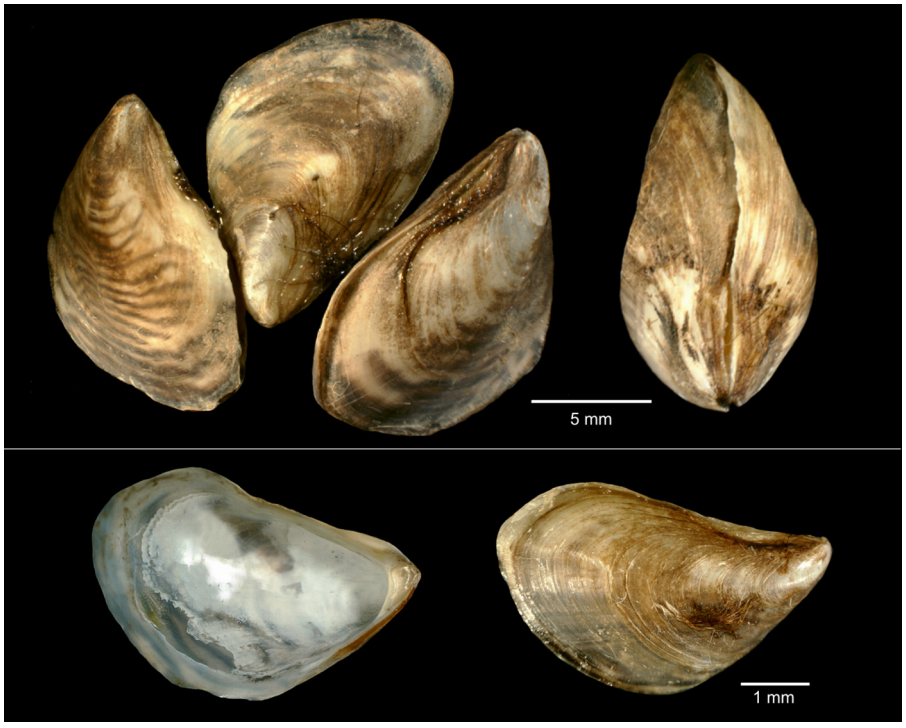

Figure 2 Quagga mussel individuals collected at Station ZSD (cf. Fig. 1) in the Szczecin Lagoon.

hinge; periostracum variously coloured (from light brown-yellow to totally black) with dark concentric rings variously shaped and sized and lighter-coloured rings found close to the hinge; shells of some individuals may differ in colouration of the latero-ventral and latero-dorsal side. The apical septum is located inside the proximal part of the shell; it serves as a myophore plate (an attachment site) for the anterior pedal retractor and the anterior shell adductor. The dorsal margin features two elongated scars left by the posterior adductor and posterior byssal retractor. In the proximal part, the shells are connected with the ligament. The hinge teeth are residual.

The samples collected in November 2014 made it possible to estimate the abundance and proportions of the two dreissenids and to determine the size structure of *D. rostriformis bugensis*. The ZSD samples yielded mixed aggregations of the dreissenids. The mean abundances of *D. polymorpha* and *D. rostriformis bugensis* in the area (+ standard deviation) were estimated at 6010.8 $\pm$ 446.05 and 4000.0 $\pm$ 355.44 ind. m^{-2}, respectively, and the zebra mussel to quagga mussel abundance ratio being estimated at about 60:40.

The *D. rostriformis bugensis* size structure was analysed on 1250 individuals collected at Station ZSD. The shell length was found to vary from 1.56—31.76 mm, 52.5% of the population being made up by small (shell length $<$7 mm) individuals.

4. Discussion

The data summarised above as well as observations made on other benthos samples and bivalves present in fish catches from the Lagoon allow to conclude that, at present, the quagga mussel is common and abundant throughout the Szczecin Lagoon (and the adjacent Kamieński Lagoon), and that it forms a strong, reproducing population there which co-occurs with that of *D. polymorpha*. It may be even argued that *D. rostriformis bugensis* has become a permanent component of the benthic biota in the Lagoon, and — together with *D. polymorpha* — it will play a major role in the functioning of the Lagoon's ecosystem. The high per cent contribution of *D. rostriformis bugensis* to the mixed dreissenid aggregations evidences the immigration success of the species and testifies to its being an able competitor for the stabilised zebra mussel population in the Lagoon. Interactions between the two species have been in the focus of numerous studies for some time (e.g., Karatayev et al., 2015; Nalepa et al., 2010; Quinn et al., 2014; Wilson et al., 2006). Both in the newly colonised reservoirs in North America and in the native central European locations, *D. rostriformis bugensis* has been observed to replace (in North America within a relatively short time of 5—10 years) the zebra mussel (Imo et al., 2010; Mills et al., 1996; Nalepa et al., 2010; Orlova et al., 2004; Ricciardi and Whoriskey, 2004; Zhulidov et al., 2004). A number of mechanisms have been put forth to explain the replacement in the Great Lakes. It has been suggested that one of the mechanisms involves genetic adaptations to new habitats, allowing expansion from deeper cold water to shallower, warmer habitats (Karatayev et al., 2011; Mills et al., 1996). Other authors suggest that *D. rostriformis bugensis* may begin to reproduce at temperatures lower than those needed by *D. polymorpha* to breed. Therefore breeding occurs earlier in the season, which confers a competitive advantage to the larval settlement (Claxton and Mackie, 1998; Roe and MacIsaac, 1997). Other hypotheses point to differences in filtration rates and in feeding and energy efficiency between the two species. According to Diggins (2001), *D. rostriformis bugensis* filtration rate is higher than that of *D. polymorpha*, again conferring a competitive advantage to the former, particularly when food resources are limiting. In addition, the energy efficiency of the quagga mussel is higher than that of the zebra mussel, which results in a higher growth rate at a high food concentration (Baldwin et al., 2002; Stoeckmann, 2003).

It is thus highly likely that *D. rostriformis bugensis* is well-equipped to substitute *D. polymorpha* in the Odra estuary. It is difficult to predict at present whether such replacement will in fact occur. Evidence from other areas (lakes) points to stabilisation of the co-occurrence of the two species in a lake on account of their depth-related spatial segregation (Karatayev et al., 2015). In reservoirs similar to the Szczecin Lagoon (shallow lakes and embayments) which support both species, the zebra mussel distribution is usually restricted to the littoral zone, while quagga mussel can be abundant in both the littoral and at larger depths (Karatayev et al., 2015). At the same time, the quagga mussel is known for its ability to settle on the muddy bottom, extremely inhospitable for the zebra mussel except for spots with hard elements enabling attachment (Karatayev et al., 2015). Therefore, taking into consideration the prevalence of muddy bottoms in the Szczecin Lagoon (Radziejewska and Schernewski, 2008), it may be expected that the quagga mussel will expand to the muddy bottom in the central part of the Lagoon, so far known only for occasional presence of the zebra mussel (Wiktor, 1969; Wolnomiejski and Witek, 2013). As a result, the dreissenid resources in the Szczecin Lagoon may be expected to increase, with potential consequences for the ecosystem functioning.

Observations made both in North America (Dermott et al., 2003; McMahon, 2011; Mills et al., 1993) and in Europe (Matthews et al., 2014) show that the domination of small individuals in *D. rostriformis bugensis* populations evidences an early stage of population growth. Bij de Vaate (2010) suggested individuals $>$18 mm found in the Rhine to have been at least 1 year old, while Imo et al. (2010) and Molloy et al. (2007) regarded the individuals they found in the Netherlands and in the Main, with shell lengths averaging 22.4 mm and reaching the maximum size of 27.5 mm, respectively, to have been at least 2 and 3 years old, respectively. As reported by Orlova et al. (2004) for the Volga River, *D. rostriformis bugensis* found in the area after it had colonised it in 1994 was represented by small ($<$2 mm) individuals; 4 years later (in 1996), however, the population included all the size classes up to the largest individuals with shells measuring 30 mm. As indicated by the shell length of the individuals found in the northern part of the Szczecin Lagoon (Station ZSD), they are about 3 years old, which means that the species arrived in the area at least 3 years prior to the first record. Examination of archived bivalve samples collected in 2010—2014 from the Skoszewska Cove in the eastern part of the Lagoon (Station ZS1 in Fig. 1) and stored in our laboratories revealed the presence of two quagga mussel individuals measuring 4.4 and 19.4 mm in an April 2013 sample, the November 2014 sample from that station yielding a

22.36 mm long individual. Thus, the data suggest that the bivalve is a recent immigrant in the area, the species being absent in samples collected from the Cove prior to 2013.

The vectors and mechanisms of the quagga mussel immigration into the Baltic Sea catchment are not known at present. An insight into the latter is expected from the genetic studies planned as the next step of the study. However, the most plausible is a hypothesis assuming quagga mussel dispersal from the sites it currently occupies in western Europe (Heiler et al., 2013; Matthews et al., 2014). It is also likely that the immigration proceeded via inland waterways (as was the case in *Hypania invalida*; Woźniczka et al., 2011) and from the sea, aided by ships. In the latter case, a reverse immigration from the Great Lakes cannot be ruled out (Heiler et al., 2013). Jump dispersal aided by ships operating in inland waterways and in the sea (Heiler et al., 2013) is most probable, because the nearest known sites supporting *D. rostriformis bugensis* are located in the Elbe River catchment (Heiler et al., 2013) and are beyond the potential of diffusive spread of the species. Considering the location of the Szczecin Lagoon with respect to various navigation routes, it may be assumed that the Lagoon will be a "stepping stone" for further expansion of the quagga mussel to areas populated at present by *D. polymorpha* (e.g., the Curonian Lagoon or the Neva Bay). Inland waters of central and eastern Europe may be another destination of a potential expansion. Owing to the high dispersal potential of the quagga mussel and serious effects the bivalve has produced in the water bodies it has colonised so far, including interactions with *D. polymorpha*, it seems necessary to monitor the species' progress in the Baltic Sea catchment.

Acknowledgements

We wish to thank Mieczysław Ziarkiewicz, Marcin Wroniecki, Agnieszka Szkudlarek-Pawełczyk, Adam Czugała, and the crew of RV Stynka II for their assistance in sampling. We are grateful to an anonymous reviewer for helpful comments which improved the manuscript.

References

Aldridge, D.C., Ho, S., Froufe, E., 2014. The Ponto-Caspian quagga mussel, *Dreissena rostriformis bugensis* (Andrusov, 1897), invades Great Britain. Aquat. Invasions 9 (4), 529–535, http://dx.doi.org/10.3391/ai.2014.9.4.11.

Baldwin, B.S., Mayer, M.S., Dayton, J., Pau, N., Mendilla, J., Sullivan, M., Moore, A., Ma, A., Mills, E.L., 2002. Comparative growth and feeding in zebra and quagga mussels (*Dreissena polymorpha* and *Dreissena bugensis*): implications for North American lakes. Can. J. Fish. Aquat. Sci. 59 (4), 680–694.

Benson, A.J., 2013. Chronological history of zebra and quagga mussels (Dreissenidae) in North America, 1988–2010. In: Nalepa, T.F., Schloesser, D.W. (Eds.), Quagga and Zebra Mussels: Biology, Impacts, and Control. 2nd ed. CRC Press, Boca Raton, 9–31.

Bij de Vaate, A., 2010. Some evidence for ballast water transport being the vector of the quagga mussel (*Dreissena rostriformis bugensis* Andrusov, 1897) introduction into Western Europe and subsequent upstream dispersal in the River Rhine. Aquat. Invasions 5 (2), 207–209, http://dx.doi.org/10.3391/ai.2010.5.2.13.

Bij de Vaate, A., Beisel, J.N., 2011. Range expansion of the quagga mussel (*Dreissena rostriformis bugensis* Andrusov 1897) in Western Europe: first observation from France. Aquat. Invasions 6 (Suppl. 1), 71–74, http://dx.doi.org/10.3391/ai.2011.6.S1.016.

Brandt, K., 1896. Ueber das Stettiner Haff. Wissenschaftliche Meeresuntersuchungen. Neue Folge Erster Band, Heft 2, 105–144.

Claxton, W.T., Mackie, G.L., 1998. Seasonal and depth variations in gametogenesis and spawning of *Dreissena polymorpha* and *Dreissena bugensis* in eastern Lake Erie. Can. J. Zool. 76 (1), 2010–2019.

Dermott, R., Bonnell, R., Carou, S., Dow, J., Jarvis, P., 2003. Spatial distribution and population structure of the mussels *Dreissena polymorpha* and *Dreissena bugensis* in the Bay of Quinte Lake Ontario, 1998 and 2000. Can. Tech. Report Fish. Aquat. Sci. 2479, 55 pp.

Diggins, T.P., 2001. A seasonal comparison of suspended sediment filtration by quagga (*Dreissena bugensis*) and zebra mussels (*D. polymorpha*). J. Great Lakes Res. 27 (4), 457–466.

Gruszka, P., 1999. The river Odra estuary as a gateway for alien species immigration to the Baltic Sea Basin. Acta Hydrochim. Hydrobiol. 27 (5), 374–382, http://dx.doi.org/10.1002/(SICI)1521-401X(199911)27:5<374::AID-AHEH374>3.0.CO;2-V.

Haybach, A., Christmann, K-H., 2009. Erster Nachweis der Quaggamuschel *Dreissena rostriformis bugensis* (Andrusov, 1897) im Niederrhein von Nordrhein-Westfalen. Lauterbornia 67, 69–72.

Heiler, K.C.M., Bij de Vaate, A., Ekschmitt, K., von Oheimb, P.V., Albrecht, C., Wilke, T., 2013. Reconstruction of the early invasion history of the quagga mussel (*Dreissena rostriformis bugensis*) in Western Europe. Aquat. Invasions 8 (1), 53–57, http://dx.doi.org/10.3391/ai.2013.8.1.06.

Imo, M., Seitz, A., Johannesen, J., 2010. Distribution and invasion genetics of the quagga mussel (*Dreissena rostriformis bugensis*) in German rivers. Aquat. Ecol. 44 (4), 731–740, http://dx.doi.org/10.1007/s10452-009-9311-2.

Karatayev, A.Y., Burlakova, L.E., Padilla, D.K., 2015. Zebra versus quagga mussels: a review of their spread, population dynamics, and ecosystem impacts. Hydrobiologia 746 (1), 97–112, http://dx.doi.org/10.1007/s10750-014-1901-x.

Karatayev, A.Y., Mastitsky, S.E., Padilla, D.K., Burlakova, L.E., Hajduk, M.M., 2011. Differences in growth and survivorship of zebra and quagga mussels: size matters. Hydrobiologia 668, 183–194, http://dx.doi.org/10.1007/s10750-010-0533-z.

Martens, A., Grabow, K., Schoolmann, G., 2007. Die Quagga-Muschel *Dreissena rostriformis bugensis* (Andrusov, 1897) am Oberrhein (Bivalvia: Dreissenidae). Lauterbornia 61, 145–152.

Matthews, J., Van der Velde, B., Bij de Vaate, A., Collas, F.P.L., Koopman, K.R., Leuven, R.S.E.W., 2014. Rapid range expansion of the invasive quagga mussel in relation to zebra mussel presence in The Netherlands and Western Europe. Biol. Invasions 16 (1), 23–42, http://dx.doi.org/10.1007/s10530-013-0498-8.

May, B., Marsden, J.E., 1992. Genetic identification and implications of another invasive species of dreissenid mussel in the Great Lakes. Can. J. Fish. Aquat. Sci. 49 (7), 1501–1506.

McMahon, R.F., 2011. Quagga mussel (*Dreissena rostriformis bugensis*) population structure during the early invasion of Lakes Mead and Mohave January–March 2007. Aquat. Invasions 6 (2), 131–140, http://dx.doi.org/10.3391/ai.2011.6.2.02.

Micu, D., Telembici, A., 2004. First record of *Dreissena bugensis* (Andrusov 1897) from the Romanian stretch of river Danube. In: Abstracts of the International Symposium of Malacology, August 19–22, 2004, Sibiu, Romania.

Mills, E.L., Dermott, R.M., Roseman, E.F., Dustin, D., Mellina, E., Corm, D.B., Spidle, A.P., 1993. Colonization, ecology, and population structure of the "quagga" mussel (Bivalvia: Dreissenidae) in the lower Great Lakes. Can. J. Fish. Aquat. Sci. 50 (11), 2305–2314.

Mills, E.L., Rosenberg, G., Spidle, A.P., Ludyanskiy, M., Pligin, Y., May, B., 1996. A review of the biology and ecology of the quagga mussel (*Dreissena bugensis*), a second species of freshwater dreissenid introduced to North America. Am. Zool. 36, 271–286, http://dx.doi.org/10.1093/icb/36.3.271.

Molloy, D.P., Bij de Vaate, A., Wilke, T., Giamberini, L., 2007. Discovery of *Dreissena rostriformis bugensis* (Andrusov 1897) in Western Europe. Biol. Invasions 9 (7), 871—874, http://dx.doi.org/10.1007/s10530-006-9078-5.

Nalepa, T.F., Fanslow, D.L., Pothoven, S.A., 2010. Recent changes in density, biomass, recruitment, size structure, and nutritional state of *Dreissena* populations in southern Lake Michigan. J. Great Lakes Res. 36, 5—19.

Nalepa, T.F., Schloesser, D.W. (Eds.), 2013. Quagga and Zebra Mussels: Biology, Impacts, and Control. 2nd ed. CRC Press, Boca Raton, 815 pp.

Orlova, M.I., Muirhead, J., Antonov, P.I., Shcherbina, G.K., Starobogatov, I., Biochino, G.I., Therriault, T.W., MacIsaac, H.J., 2004. Range expansion of quagga mussels *Dreissena rostriformis bugensis* in the Volga River and Caspian Sea basin. Aquat. Ecol. 38 (4), 561—573, http://dx.doi.org/10.1007/s10452-005-0311-6.

Orlova, M.I., Therriault, T.W., Antonov, P.I., Shcherbina, G.K., 2005. Invasion ecology of quagga mussels (*Dreissena rostriformis bugensis*): a review of evolutionary and phylogenetic impacts. Aquat. Ecol. 39 (4), 401—418, http://dx.doi.org/10.1007/s10452-005-9010-6.

Pathy, D.A., Mackie, G.L., 1993. Comparative shell morphology of *Dreissena polymorpha*, *Mytilopsis leucophaeta*, the 'quagga' mussel (Bivalvia: Dreissenidae) in North America. Can. J. Zool. 71 (5), 1012—1023.

Popa, O.P., Popa, L.O., 2006. The most westward European occurrence point for *Dreissena bugensis* (Andrusov 1897). Malacol. Bohemoslov. 5, 3—5.

Quinn, A., Gallardo, B., Aldridge, D.C., 2014. Quantifying the ecological niche overlap between two interacting invasive species: the zebra mussel (*Dreissena polymorpha*) and the quagga mussel (*Dreissena rostriformis bugensis*). Aquat. Conserv. 24 (3), 324—337, http://dx.doi.org/10.1002/aqc.2414.

Radziejewska, T., Schernewski, G., 2008. The Szczecin (Oder-) Lagoon. In: Schiewer, U. (Ed.), Ecology of Baltic Coastal Waters Series. Ecol. Stud., vol. 197. Springer, Berlin, 115—129, http://dx.doi.org/10.1007/978-3-540-73524-3_5.

Ricciardi, A., Whoriskey, F.G., 2004. Exotic species replacement: shifting dominance of dreissenid mussels in the Soulanges Canal, upper St. Lawrence River, Canada. J. N. Am. Benthol. Soc. 23, 507—514.

Roe, S.L., MacIsaac, H.J., 1997. Deepwater population structure and reproductive state of quagga mussels (*Dreissena bugensis*) in Lake Erie. Can. J. Fish. Aquat. Sci. 54 (10), 2428—2433.

Schoell, F., Eggers, T., Haybach, A., Gorka, M., Klima, M., Köning, B., 2012. Verbreitung von *Dreissena rostriformis bugensis* (Andrusov, 1897) in Deutschland (Mollusca: Bivalvia). Lauterbornia 74, 111—115.

Schonenberg, D.B., Gittenberger, A., 2008. The invasive quagga mussel *Dreissena rostriformis bugensis* (Andrusov, 1879) (Bivalvia: Dreissenidae) in the Dutch Haringvliet, an enclosed freshwater Rhine-Meuse estuary, the westernmost record for Europe. Basteria 72 (4—6), 345—352.

Stoeckmann, A., 2003. Physiological energetics of Lake Erie dreissenid mussels: a basis for the displacement of *Dreissena polymorpha* by *Dreissena bugensis*. Can. J. Fish. Aquat. Sci. 60 (2), 126—134.

Van der Velde, G., Platvoet, D., 2007. Quagga mussels *Dreissena rostriformis bugensis* (Andrusov, 1897) in the Main River (Germany). Aquat. Invasions 2 (3), 261—264.

Wawrzyniak-Wydrowska, B., Gruszka, P., 2005. Population dynamics of alien gammarid species in the River Odra estuary. Hydrobiologia 539 (1), 13—25, http://dx.doi.org/10.1007/s10750-004-3081-6.

Wiktor, J., 1969. Biology of *Dreissena polymorpha* (Pall.) and its importance on the Szczecin Lagoon. Stud. Mater. MIR., Gdynia, Ser. A, 88 pp., (in Polish).

Wilson, K.A., Howell, E.T., Jackson, D.A., 2006. Replacement of zebra mussels by quagga mussels in the Canadian nearshore of Lake Ontario: the importance of substrate, round goby abundance, and upwelling frequency. J. Great Lakes Res. 32 (1), 11—28.

Wolnomiejski, N., Witek, Z., 2013. The Szczecin Lagoon Ecosystem: The Biotic Community of the Great Lagoon and its Food Web Model. Versita Ltd., London, 293 pp.

Woźniczka, A., Gromisz, S., Wolnomiejski, N., 2011. *Hypania invalida* (Grube, 1960), a polychaete species new for the southern Baltic estuarine area: the Szczecin Lagoon and the River Odra mouth. Aquat. Invasions 6 (1), 39—46.

Zhulidov, A.V., Kozhara, A.V., Scherbina, G.H., Nalepa, T.F., Protasov, A., Afanasiev, S.A., Pryanichnikova, E.G., Zhulidov, D.A., Gurtovaya, T.Yu., Pavlov, D.F., 2010. Invasion history, distribution, and relative abundances of *Dreissena bugensis* in the Old World: a synthesis of data. Biol. Invasions 12 (7), 1923—1940.

Zhulidov, A.V., Pavlov, D.F., Nalepa, T.F., Scherbina, G.H., Zhulidov, D.A., Gurtovaya, T.Yu., 2004. Relative distributions of *Dreissena bugensis* and *Dreissena polymorpha* in the lower Don River system. Russ. Int. Rev. Hydrobiol. 89 (3), 326—333.